Physics of the Solid State, Vol. 45, No. 12, 2003, pp. 2213–2217. Translated from Fizika Tverdogo Tela, Vol. 45, No. 12, 2003, pp. 2113–2117.

METALS AND SUPERCONDUCTORS

Pressure-Induced Change of the Fermi Surface Topology in Al-Based Solid Solutions

A. S. Mikhaĭlushkin*, É. I. Isaev*, Yu. Kh. Vekilov*, and S. I. Simak**

**Moscow State Institute of Steel and Alloys (Technological University), Leninskiĭ pr. 4, Moscow, 119991 Russia*
e-mail: eyvaz_isaev@yahoo.com; isaev@trf.misis.ru
***Condensed Matter Theory Group, Uppsala University, Uppsala, S-75121 Sweden*

Received April 4, 2003

Abstract—An *ab initio* study of the electronic structure and the Fermi surface is carried out for random Al–Si and Al–Ge solid solutions. At a 10 at. % Si content, a topological transition of the neck-formation type is revealed, which can account for the experimentally observed peculiarities of the transport properties of the Al–Si system. A similar transition is also found in the Al–Ge system, and the appearance of the anomalous transport coefficients at Ge concentrations of about 10 at. % is predicted. In addition, it is shown that the increase in the concentration of the dopants gives rise to nesting of the Fermi surface sheets (superposition of electron–hole pockets). This peculiarity of the Fermi surface can be responsible for the enhancement of the superconductivity and the instability of the crystal structure observed in the $Al_{1-x}Si_x$ and $Al_{1-x}Ge_x$ solid solutions. *© 2003 MAIK "Nauka/Interperiodica".*

1. INTRODUCTION

It is well known that the physical properties of metals and alloys significantly depend on the topology of the Fermi surface, which is strongly affected by doping and external pressure. These factors give rise to different peculiarities in the electronic structure, for example, to electronic topological transitions, which, in turn, affect the physical properties of metals. In this paper, we study the influence of the external pressure and doping on the topology of the Fermi surface of metastable random solid solutions $Al_{1-x}Si_x$ and $Al_{1-x}Ge_x$.

Al–Si and Al–Ge solid solutions synthesized at high pressures exhibit unusual physical properties, such as enhanced superconductivity and anomalous transport coefficients at low temperatures. Under ambient conditions, the solubility of Si and Ge in aluminium is low: the solubility limit of these elements at 0.1 MPa is 1.6 and 2.8 at. %, respectively [1]. As the pressure is increased to 10 GPa, the solubility of Si and Ge increases to up to 20 and 18 at. %, respectively [2]. In this case, the temperature of the superconducting transition (T_c) of the metastable solid solutions increases from 1.18 K for pure aluminium [3] to 11 and 7.2 K for the $Al_{80}Si_{20}$ and $Al_{85}Ge_{15}$ alloys, respectively [2]. In addition, singularities in the phonon density of states have been revealed in these solid solutions [4]. Along with the increase in the electron–phonon interaction constant [4–6], these singularities lead to an increase in the superconducting transition temperature of these solid solutions [7, 8]. Moreover, peculiarities in the transport properties, such as thermopower and the Hall coefficient, have been revealed in the region of lattice instability [9–11]. It should also be noted that the $Al_{1-x}Si_x$ and $Al_{1-x}Ge_x$ solid solutions are a good model for studying the influence of pressure on a number of physical properties, because these solutions have a simple (face-centered cubic, FCC) crystal lattice, their Fermi surfaces consist of the *s* and *p* electron states, and the superconducting transition temperatures of these solutions are almost linear functions of the percentage of silicon. In this paper, we perform a theoretical study of the physical properties of the Al–Si and Al–Ge solid solutions by carrying out *ab initio* calculations of the electronic structure of the random binary alloys over wide concentration and pressure ranges. Two peculiarities of the electronic structure, which can result in different anomalous properties of the Al-based alloys, are found. One of them is the occurrence of an electronic topological transition induced by an increase in the Si or Ge concentration and pressure. It is shown that the electronic topological transition in Al–Si systems can be responsible for the experimentally observed anomalous transport properties [4–6]. The other peculiarity is associated with a nesting feature (Kohn anomaly), which occurs as the dopant content is increases. This anomaly seems to be responsible for the softening of the phonon spectrum and the increase in T_c of the $Al_{1-x}M_x$ (M = Si, Ge) solid solutions.

2. CALCULATION TECHNIQUE

The electronic structure of the $Al_{1-x}Si_x$ and $Al_{1-x}Ge_x$ random solid solutions, which have an FCC crystal lattice, was calculated using the Korringa–Kohn–Rostoker method within the coherent-potential and atomic-sphere approximations [12] and basis functions consisting of the *s*, *p*, and *d* orbitals. The exchange correlation

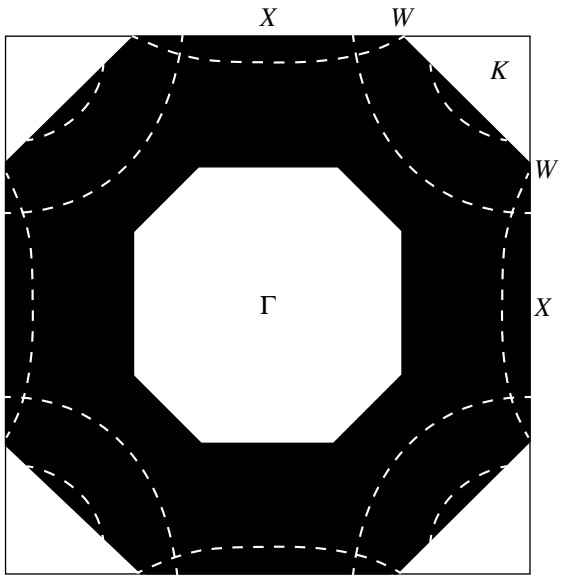

Fig. 1. Γ*XWK* section of the Fermi surface of pure Al at zero pressure.

effects were taken into account in the framework of the generalized gradient approximation [13]. The atomic-sphere radii for both elements were chosen to be equal to the average atomic-sphere radius of the Wigner–Seitz cell of the alloy, and the charge transfer was considered in the framework of the screened-impurity model with the Madelung screening factor $\beta = 0.6$ [14].

Integration over the irreducible part (1/48) of the Brillouin zone was carried out using 1500 special **k** points; the energy integrals were calculated using 25 points on the semicircular energy contour. The convergence criterion for the total energy was 0.001 mRy.

The total energy of the ground state of the solid solutions was calculated self-consistently for wide ranges of Si and Ge concentrations and different pressures. Then, the results obtained were used to approximate the dependence of the total energy on the unit cell volume using the Morse method [15]. The Fermi surface was determined for different values of the lattice parameters corresponding to various concentrations and pressures by finding the maxima of the Bloch spectral function $A(k, E_F)$; for this purpose, a very fine grid of **k** points in the Γ*XWK* plane of the Brillouin zone was used (a detailed description of this formalism can be found in [16]).

3. FERMI SURFACE AND ELECTRONIC TOPOLOGICAL TRANSITIONS

Under ambient conditions, the Fermi surface of pure aluminium consists of a large second hole zone and small third-zone toroidal electron pockets in the vicinity of the *K* point (Fig. 1). Silicon has an additional valence electron in comparison with aluminum; therefore, silicon doping leads to a growth in the size of the electron pocket near the *K* point. As the Si content increases and the pocket size grows, the electronic topological transition of the neck-formation type occurs near the *W* point at an Si concentration of approximately 10 at. % and zero external pressure (Fig. 2a). As expected, germanium doping also brings about the occurrence of an electronic topological transition of the neck-formation type, because the electronic structure of this element is similar to that of Si. However, the transition occurs at a Ge concentration of 11 at. % (Fig. 2b). In pure aluminium, the size of the electron pocket near the *K* point decreases as the pressure increases. Thus, the pressure and doping affect the Fermi surface of aluminum in different ways. Nevertheless, simultaneous doping and application of pressure facilitate the formation of the neck; the electronic topological transition is observed in this case at a pressure of about 10 GPa and Si and Ge concentrations of 8 (Fig. 2c) and 9 at. % (Fig. 2d), respectively. This is probably due to the strong broadening of the electron pocket near the point along the *WK* direction. It should be noted that, in the ranges of pressures and concentrations covered in this study, the change in shape of the second hole zone of the solid solutions is negligible.

According to the general theory of electronic topological transitions [17], these transitions can manifest themselves as peculiarities in different physical properties, above all, in transport properties, such as thermopower. Since these electronic topological transitions occur as the dopant content increases, they can be considered in the context of recent experiments in which the transport properties of the $Al_{1-x}Si_x$ solid solutions were studied as a function of the Si concentration [9–11]. These experiments revealed a peculiarity in the concentration dependence of thermopower at an Si concentration of 8–10 at. %, which is consistent with the calculated range of concentrations corresponding to the occurrence of the electronic topological transition in the system. In addition, the effect of the electronic topological transition on the concentration dependence of the transport coefficients of the Al–Si system was analyzed in [18] and it was shown that the anomalous transport properties observed in the Al–Si solid solutions are due to this transition. This is revealed in peculiarities in the relaxation time, which make a major contribution to the transport coefficients.

Unfortunately, there is no experimental data on the peculiarities in the transport properties exhibited by the Al–Ge solid solutions. Nevertheless, it can be argued that the electronic topological transition revealed in these solid solutions results in analogous peculiarities in the transport coefficients. On the other hand, from the microscopic theory of electronic topological transitions [17], it follows that these transitions do not influence the superconducting properties significantly, at least, in three-dimensional systems.

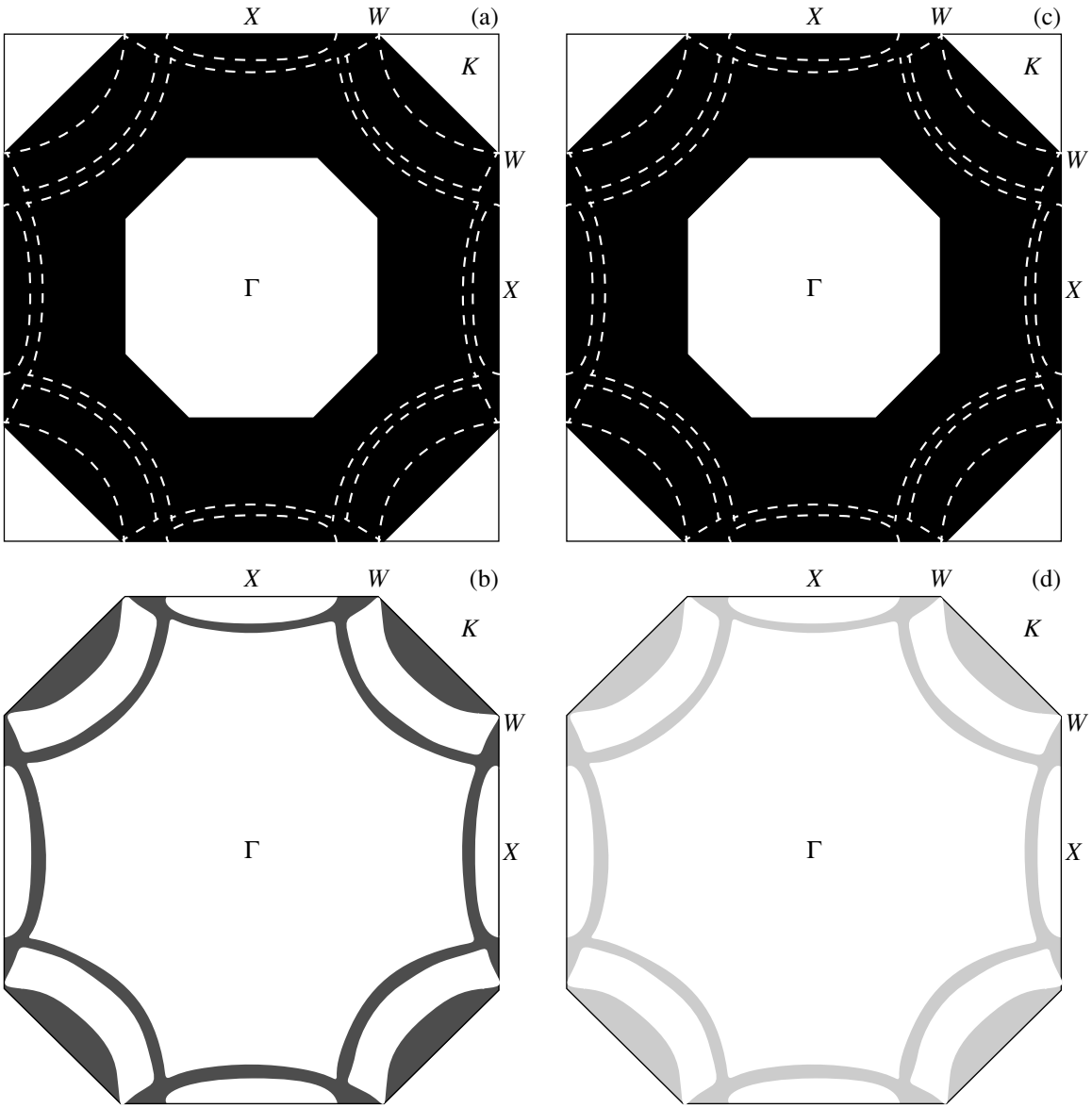

Fig. 2. Γ*XWK* section of the Fermi surface of the random solid solutions (a) $Al_{90}Si_{10}$ at zero pressure, (b) $Al_{89}Ge_{11}$ at zero pressure, (c) $Al_{92}Si_8$ under a pressure of 8 GPa, and (d) $Al_{91}Ge_9$ under a pressure of 10 GPa.

4. NESTING

It is well known that peculiarities in the Fermi surface, such as superposition (nesting) of electron–hole pockets and the presence of flat parts, give rise to different instabilities, for example, to instability with respect to the appearance of charge-density and spin-density waves. Kohn has shown [19] that, if the Fermi surface of a free electron gas has flat parts, then the phonon spectrum and susceptibility exhibit a nonanalytic dependence on the wave vector. Later on, these results were generalized to the case of an arbitrary band structure. This argues for the fact that the appearance of various instabilities can lead to an increase in the superconducting transition temperature in different compounds [20, 21]. The calculated spectral function $A(k, E_F)$ is the local density of states at the Fermi level for a given k point. Therefore, nesting can be determined by the approximate formula [22]

$$\chi \approx \int_{BZ} d^3kA(k, E_F)A(k + Q, E_F),$$

where χ is the susceptibility of the electron subsystem, E_F is the Fermi energy, k is the wave vector within the first Brillouin zone, and Q is the superposition (nesting) were vector of parts of the Fermi surface. For accurate quantitative analysis, however, a very fine grid of points should be taken in the Brillouin zone, even in the case

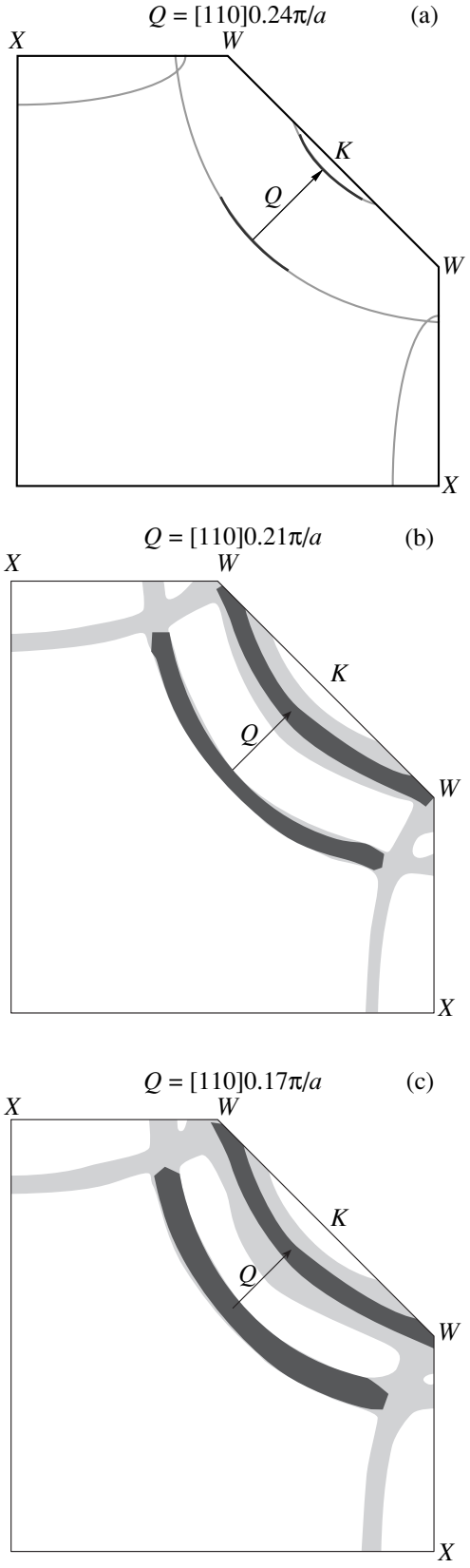

Fig. 3. Part of the Γ*XWK* section of the Fermi surface for (a) pure Al, an (b) $Al_{80}Si_{20}$ alloy, and (c) an $Al_{80}Ge_{20}$ alloy. The areas of the superposition of the third-zone electron pocket and the second-zone hole sheet are marked.

of a sufficiently simple Fermi surface similar to that of Al. Moreover, the Brillouin zone is asymmetrical with respect to the shift by vector Q in this case; therefore, we cannot restrict our consideration only to the irreducible part (1/48) of the Brillouin zone corresponding to an FCC lattice as we did while calculating the electronic structure. Both $A(k, E_F)$ and $A(k + Q, E_F)$ should be determined for the whole Brillouin zone, which significantly increases the calculation time. For this reason, we analyzed the possible appearance of nesting and studied the dependence of nesting on the Si content by calculating the product of the spectral functions, $F(Q) = A(k, E_F)A(k + Q, E_F)$, for pure Al and $Al_{1-x}Si_x$ and $Al_{1-x}Ge_x$ alloys in the interval of x from 0 to 0.2 at points k and $k + Q$. The quantity $F(Q)$ is determined by the local superposition of parts of the Fermi surface, when the Brillouin zone is shifted by vector Q. The calculation reveals a significant overlap of the hole second-zone sheet and the electron third-zone sheet of the Fermi surface in the system. Figures 3a–3c show the nesting vector Q connecting the hole second-zone sheet with the electron third-zone sheet of the Fermi surface in pure Al and in $Al_{80}Si_{20}$ and $Al_{80}Ge_{20}$ alloys, respectively. The following fact attracts attention: an increase in the dopant content results in more pronounced nesting of the Fermi surface. This is due to the increase in the size of the electron third-zone sheet and broadening of the Fermi surface caused by doping. It should be noted that nesting can result in softening of phonon modes and, therefore, in an enhancement of superconductivity in the $Al_{1-x}Si_x$ and $Al_{1-x}Ge_x$ substitutional solutions. From qualitative considerations, it follows that nesting is the most probable reason for the anomalous increase in susceptibility at nesting vectors Q, with a corresponding increase in the electron–phonon interaction.

5. CONCLUSIONS

Thus, we have calculated the electronic structure and Fermi surface of the $Al_{1-x}Si_x$ and $Al_{1-x}Ge_x$ random solid solutions. Pressure-induced electronic topological transitions of the neck-formation type were revealed to occur in these solutions. A nesting feature (superposition of electron–hole pockets of the Fermi surface) was established to take place and become more pronounced with Si or Ge doping. It was found that the anomalous transport properties of metastable solid solutions of aluminum are basically associated with the electronic topological transitions. The enhancement of the electron–phonon interaction near the lattice instability point could be the main factor responsible for the observed increase in the superconducting transition temperature.

ACKNOWLEDGMENTS

This work was supported by the Russian Foundation for Basic Research (project no. 02-02-16006) and the Royal Swedish Academy of Sciences.

REFERENCES

1. M. Hansen and K. Anderko, *Constitution of Binary Alloys* (McGraw-Hill, New York, 1958).
2. V. F. Degtyareva, G. V. Chipenko, I. T. Belash, *et al.*, Phys. Status Solidi A **89**, K127 (1985).
3. N. V. Douglass and R. Jr. Meservey, Phys. Rev., Sect. A **135**, 19 (1964).
4. A. I. Kolesnikov, O. I. Barkalov, I. T. Belash, *et al.*, J. Phys.: Condens. Matter **5**, 4737 (1993).
5. N. E. Sluchanko, V. V. Glushkov, S. V. Demichev, *et al.*, Phys. Rev. B **51**, 1112 (1995).
6. A. A. Gippius, N. E. Sluchanko, V. V. Glushkov, *et al.*, J. Phys.: Condens. Matter **12**, 1 (2000).
7. J. Chevrier, J. B. Suck, J. C. Lasjaunias, *et al.*, Phys. Rev. B **49**, 961 (1994).
8. J. Chevrier, J. B. Suck, J. J. Capponi, and M. Perroux, Phys. Rev. Lett. **61**, 554 (1988).
9. N. E. Sluchanko, V. V. Glushkov, S. V. Demishev, *et al.*, Fiz. Tverd. Tela (St. Petersburg) **41**, 3 (1999) [Phys. Solid State **41**, 1 (1999)].
10. N. E. Sluchanko, V. V. Glushkov, S. V. Demishev, *et al.*, Zh. Éksp. Teor. Fiz. **113**, 339 (1998) [JETP **86**, 190 (1998)].
11. N. E. Sluchanko, V. V. Glushkov, S. V. Demishev, *et al.*, Ferroelectrics **117**, 17 (1996).
12. I. A. Abrikosov and B. Johansson, Phys. Rev. B **57**, 14164 (1998).
13. J. P. Perdew, K. Burke, and M. Ernzerhof, Phys. Rev. Lett. **77**, 3865 (1996).
14. P. A. Korzhavyi, A. V. Ruban, I. A. Abrikosov, and H. L. Skriver, Phys. Rev. B **51**, 5773 (1995).
15. V. L. Moruzzi, J. F. Janak, and K. Schwarz, Phys. Rev. B **37**, 790 (1988).
16. N. V. Skorodumova, S. I. Simak, I. A. Abrikosov, *et al.*, Phys. Rev. B **57**, 14673 (1998).
17. A. A. Varlamov, V. S. Egorov, and A. V. Pantsulaya, Adv. Phys. **38**, 469 (1989).
18. D. V. Livanov, E. I. Isaev, S. I. Manokhin, *et al.*, Comput. Mater. Sci. **24**, 284 (2002).
19. W. Kohn, Phys. Rev. Lett. **2**, 393 (1959).
20. D. J. Scalapino, E. Loh, and J. E. Hirsch, Phys. Rev. B **35**, 6694 (1987).
21. L. P. Gorkov and O. N. Dorokhov, J. Low Temp. Phys. **22**, 1 (1976).
22. E. Bruno, B. Ginatempo, and E. S. Giuliano, Phys. Rev. B **63**, 174107 (2001).

Translated by A. Poushnov

Physics of the Solid State, Vol. 45, No. 12, 2003, pp. 2218–2224. Translated from Fizika Tverdogo Tela, Vol. 45, No. 12, 2003, pp. 2118–2123.

METALS AND SUPERCONDUCTORS

Density-Functional Study of Methanol Adsorption on the Al(100) Surface

A. L. Zaĭtsev*, F. Detraux, Yu. M. Pleskachevskiĭ*, and X. Gonze****

** Institute of Mechanics of Metal-Containing Polymer Systems, Belarussian Academy of Sciences, Gomel, 246050 Belarus*

*** Unite de Physico-Chimie et de Physique des Materiaux, Université Catholique de Louvain, Louvain-la-Neuve, B-1348 Belgium*

Received December 27, 2002; in final form, April 21, 2003

Abstract—The interaction of methanol (CH_3OH) molecules with the Al(100) surface is investigated in the framework of the density-functional theory. Numerical parameters, such as the decrease in the kinetic energy, number of special points used for integration over the Brillouin zone, broadening of the filling function, and number of atomic metal layers, are determined. The density-functional theory calculations with these parameters offer reliable data on the total energy and structural optimization of the system under consideration. The geometric characteristics of a methanol molecule in both isolated and adsorbed states on the metal surface are calculated. It is shown that the electron pseudodensity at the metal surface changes in the presence of an adsorbed molecule. The influence of the orientation of the methanol molecule (with respect to the metal surface and nearest neighbor methanol molecules) on the total energy of the system is analyzed. It is found that the total energy of the system is affected by the metal deformation and the interaction of adsorbed molecules with each other.

1. INTRODUCTION

Investigation into the electronic and geometric structures of organic molecules, including functional groups of polymers involved in the interaction with a solid surface, is an important problem in the physical chemistry of surfaces. The necessity of performing these investigations stems from recent progress achieved in the field of organic synthesis, heterogeneous catalysis, and polymer chemistry, which has made it possible to design a wide variety of polymer materials and adhesives for use in practice. In particular, the high strength of adhesive compounds of oxygen-containing polymers used for cementing metals is of special interest for mechanical engineering, aerospace industry, and automobile manufacturing. In this respect, the study of the interaction between simple molecules and a metal surface, which simulates the adsorption of functional groups of polymers, is of considerable importance from both the practical and scientific point of view [1–3].

In recent years, there have appeared a number of theoretical works concerned with first-principles calculations of the interaction between simple molecules and a metal surface with the use of available data on the sort of atoms involved in the system under investigation [4, 5]. *Ab initio* calculations have provided additional information, which, together with experimental data, permits one to develop a general concept of the interaction of molecules with a metal surface that will adequately account for the mechanism of formation of an adhesion bond.

The purpose of the present work was to calculate theoretically the total energy of the aluminum–methanol system, to optimize the geometry of this system, and to analyze the adsorption of methanol molecules on the Al(100) surface. This study of the Al–CH_3OH model system is the first step toward the description of the interaction of polyols with a metal surface, including dissociation and transition states of macromolecules on the metal surface.

2. COMPUTATIONAL TECHNIQUE

The calculations were performed in the framework of the density-functional theory [6–8]. This theory offers a more adequate description of the ground state of metals as compared to other quantum-chemical approaches. We used the ABINIT program [9] based on an efficient fast Fourier transform algorithm (for transforming wave functions between the real and reciprocal spaces), the conjugate-gradient band method [8], and the potential-based conjugate gradient algorithm, which made it possible to determine the self-consistent potential [10] and the total energy and to optimize the geometric configuration of the system.[1] The energy of the Al–CH_3OH system was calculated using the pseudopotential and plane-wave basis sets within the local-density approximation for determining the exchange and correlation energies [11]. The pseudopotentials were obtained according to the procedure described in [12, 13]. The geometry of the system was

[1] The ABINIT is a joint project of the Université Catholique de Louvain, Corning Inc., etc.

determined with the use of the structure optimization algorithm [14] included in the ABINIT program.

The system under consideration is represented by a repetitive supercell. The lattice parameter of the supercell along the *Z* axis is equal to 24.2988 Å. The supercell parameters along the *X* and *Y* axes are equal to 4.0496 Å, which corresponds to a ($\sqrt{2} \times \sqrt{2}$) surface unit cell in the (100) plane. The Al(100) surface was simulated by a set of plates involving from two to five atomic layers with an interlayer spacing of 2.0248 Å. One CH_3OH molecule was placed in each surface unit cell with an area of 16.3992 Å^2. The height of an adsorbed methanol molecule was taken to be equal to 4.813 Å. In this case, the mean density of the monolayer (0.673 g/cm^3) was close to the density of the liquid methanol (0.791 g/cm^3).

In the course of structure optimization, the spatial coordinates of atoms of a CH_3OH molecule and two Al atomic layers adjacent to this molecule relaxed, whereas the coordinates of the other Al atomic layers remained constant. Atoms at fixed positions had the following coordinates: (u, 0, –u), (0, u, –u), (0, 0, 0), (u, u, 0), (u, 0, u), and (0, u, u), where u = 2.0248 Å. The relaxation of the upper atomic layers of the aluminum plate (without a CH_3OH molecule) resulted in an insignificant (by less than 0.03 mHa) change in the total energy. The atomic positions considered led to good convergence. After the structure optimization, the residual forces acting on the atoms were less than 2.5×10^{-4} Ha/Bohr (1 Ha = 27.211 eV, 1 Bohr = 0.529177 Å).

The electron wave functions in the Brillouin zone were chosen according to the method of generating sets of special points proposed in [15]. The broadening of the filling function was equal to 0.025 Ha, and the filling numbers were determined by the cold-smearing method proposed by Marzari *et al.* [16, 17]. An analysis was performed for the convergence of the calculations with respect to both different values of the broadening and the numbers of special points *k* in the irreducible Brillouin zone (Fig. 1). We used five different sets of special points (Table 1).

For a clean Al(100) surface (in the absence of an adsorbed molecule), the higher the symmetry the smaller the necessary number of special points: sets **1** and **3** can be used instead of sets **2** and **4**, respectively. In the presence of a methanol molecule, the difference between the total energies obtained with sets **1** and **2** was equal to 0. 15 mHa. For sets **3** and **4**, this difference was 0.03 mHa. In our opinion, it is convenient to use sets **1**, **3**, and **5**. For the most part, the calculations were carried out with set **3** of special points and a broadening parameter of 0.025 Ha for the filling function, which made it possible to determine the total energies with an accuracy of 0.1 mHa (Fig. 1).

The required basis set of plane waves was specified by a parameter characterizing the decrease in the kinetic energy ranging from 20 to 30 Ha. In this case,

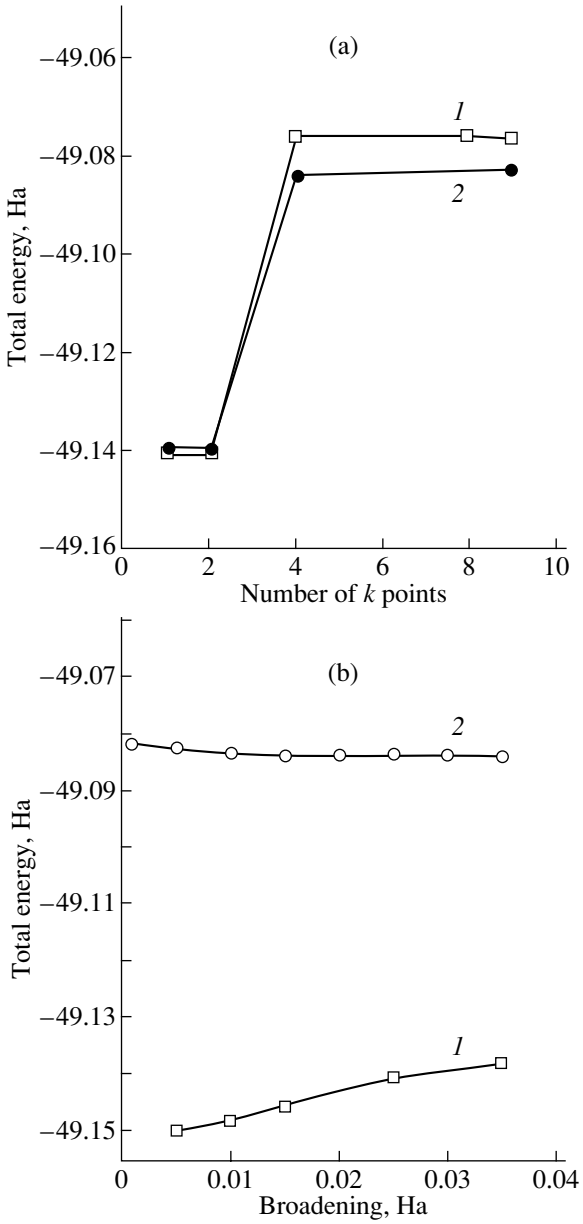

Fig. 1. Convergence of the results of calculations of the total energy in the local-density approximation as a function of (a) the number of special points and (b) the broadening of the filling function. Panel (a) illustrates the convergence of calculations for (*1*) parallel and (*2*) perpendicular orientations of the C–O bond with respect to the metal surface. Panel (b) shows the convergence upon integration over the irreducible Brillouin zone at (*1*) one and (*2*) four *k* points.

the basis set changed from 11494 to 21127 plane waves. For the chosen set of *k* points and broadening of the filling function, when the kinetic energy was decreased by 20, 25, and 30 Ha, the total energy of the system was equal to –49.083, –49.175, and –49.201 Ha, respectively. The above decrease in the kinetic energy by 20 Ha corresponds to the actual change in the total energy, provides a reasonable accuracy in estimating

Table 1. Special points for integrating over the irreducible Brillouin zone of the Al(100) surface

Set of points	Number of points	*X*	*Y*	*Z*	Set of points	Number of points	*X*	*Y*	*Z*
1	1	1/4	1/4	0			3/8	3/8	0
2	2	1/4	1/4	0			–3/8	3/8	0
		–1/4	1/4	0			–1/8	3/8	0
3	4	1/8	1/8	0	5	9	1/12	–3/12	0
		3/8	3/8	0			1/12	1/12	0
		–3/8	1/8	0			1/12	5/12	0
		–1/8	3/8	0			3/12	–5/12	0
4	8	1/8	1/8	0			3/12	–1/12	0
		3/8	1/8	0			3/12	3/12	0
		–3/8	1/8	0			5/12	–3/12	0
		–1/8	1/8	0			5/12	1/12	0
		1/8	3/8	0			5/12	5/12	0

Table 2. Coordinates of mobile atoms in a plate of pure aluminum and in a plate with the methanol molecule (coordinates of the lower six aluminum atoms are fixed)

System	Atom	*X*, Å	*Y*, Å	*Z*, Å
Plate of pure aluminum	Al(7)	2.02454	2.02454	4.05586
	Al(8)	0.00025	0.000256	4.05586
	Al(9)	2.02461	0.000184	6.07242
	Al(10)	0.00018	2.02461	6.07242
Plate of pure aluminum + CH_3OH	Al(7)	1.96550	2.04998	4.07469
	Al(8)	–0.04639	0.05666	4.08987
	Al(9)	1.92920	0.00926	6.23642
	Al(10)	–0.12090	2.14746	6.00057
	C	0.80377	0.11907	9.24271
	O	1.74405	0.73729	8.28364
	H(O)	1.30216	1.58354	7.91970
	H1	1.39405	–0.58140	9.85751
	H2	0.36147	0.90474	9.88030
	H3	–0.00077	–0.41846	8.69672

Table 3. Dependence of the total energy of the aluminum plate, the total energy of the Al–CH_3OH system, the adsorption energy, and the geometry of the methanol molecule on the number of atomic layers of aluminum

Number of atomic layers	E_{tot}, Ha		E_{ad}, mHa	Bond length, Å			C–O–H angle, deg
	plate	Al + CH_3OH		C–O	O–H	Al–O	
2	–9.644552	–34.468498	–10.392	1.4464	0.9886	3.2909	105.95
3	–14.527634	–39.340039	–18.848	1.4790	1.0247	2.1469	107.43
4	–19.398175	–44.208148	–16.416	1.4773	1.0198	2.1976	108.02
5	–24.272009	–49.083502	–17.936	1.4786	1.0217	2.1807	107.59

Table 4. Experimental and calculated geometric parameters of the methanol molecule in the adsorbed (Al + CH_3OH) state and in the free state

Bond, angle	Al + CH_3OH (calculation)	CH_3OH (free state)		Bond, angle	Al + CH_3OH (calculation)	CH_3OH (free state)	
		calculation	experiment [20]			calculation	experiment [20]
Bond length, Å				Bond angle, deg			
C–O	1.4786	1.4574	1.421	C–O–H	107.59	106.01	108.0
O–H	1.0217	0.9885	0.963	H1–C–H2	110.14	109.84	108.5
C–H1	1.1032	1.1052	1.094	H2–C–H3	109.75	107.51	108.5
C–H2	1.1043	1.1098	1.094	H1–C–H3	110.74	109.84	108.5
C–H3	1.1110	1.1098	1.094				

bond lengths (of the order of 0.5%), and makes it possible to perform the calculations more quickly.

The aforementioned parameters were used in the structure optimization of the atomic coordinates for an aluminum plate consisting of five atomic layers and an aluminum plate with a CH_3OH molecule in the case of relaxation of the atomic coordinates of the methanol molecule and the two upper layers of the aluminum plate. The results of the calculations are summarized in Table 2.

The results of our calculations illustrating the dependence of the total energy of the relaxed Al–CH_3OH system on the number of atomic layers in the repetitive supercell are given in Table 3. Moreover, Table 3 presents data on the difference between the total energy of the relaxed system and the sum of the total energies of an isolated methanol molecule and the aluminum plate and also data on the change in the adsorption energy and the geometry of the adsorbed molecule. The chemical structure of the methanol molecule changes only slightly when the calculations are performed with the inclusion of three or more atomic layers of aluminum. However, a decrease in the number of layers to two brings about a considerable decrease in the C–O and O–H bond lengths and the C–O–H bond angle and an increase in the Al–O bond length.

The surface energy, which is calculated from the total energy of crystalline aluminum (E_{tot} = –2.4321292 Ha/atom) and the total energy of the aluminum plates with different thicknesses, is approximately equal to 43.7 mHa per unit cell (or 0.59 eV per surface atom). With due regard for the computational error, the calculated energy is in reasonable agreement with the experimental value, which varies over a wide range (0.51–0.64 eV/atom) and depends on the experimental technique [18, 19].

3. RESULTS AND DISCUSSION

The optimized geometric configuration of the system under consideration (Fig. 2, Table 4) can be characterized as follows. The C–O bond in the methanol molecule forms an angle of 49.6° with the normal to the surface. The hydroxyl group is located in the vicinity of the Al(9) atom, which lies well above the surface. The O atom is located above the Al(9) atom, and the hydrogen atom is shifted toward the Al(7) atom of the lower layer. A comparison of the molecular structures of CH_3OH in the isolated and absorbed states (Table 3) shows that the adsorption brings about a change in the geometry of the CH_3OH molecule: the C–O and O–H bonds are lengthened by approximately 2% and the C–O–H bond angle increases by 1.5°. Furthermore, the adsorption leads to a change in the C–H bond lengths and the angles between them. The difference between the calculated and experimental parameters for the isolated methanol molecule does not exceed 2.0%.

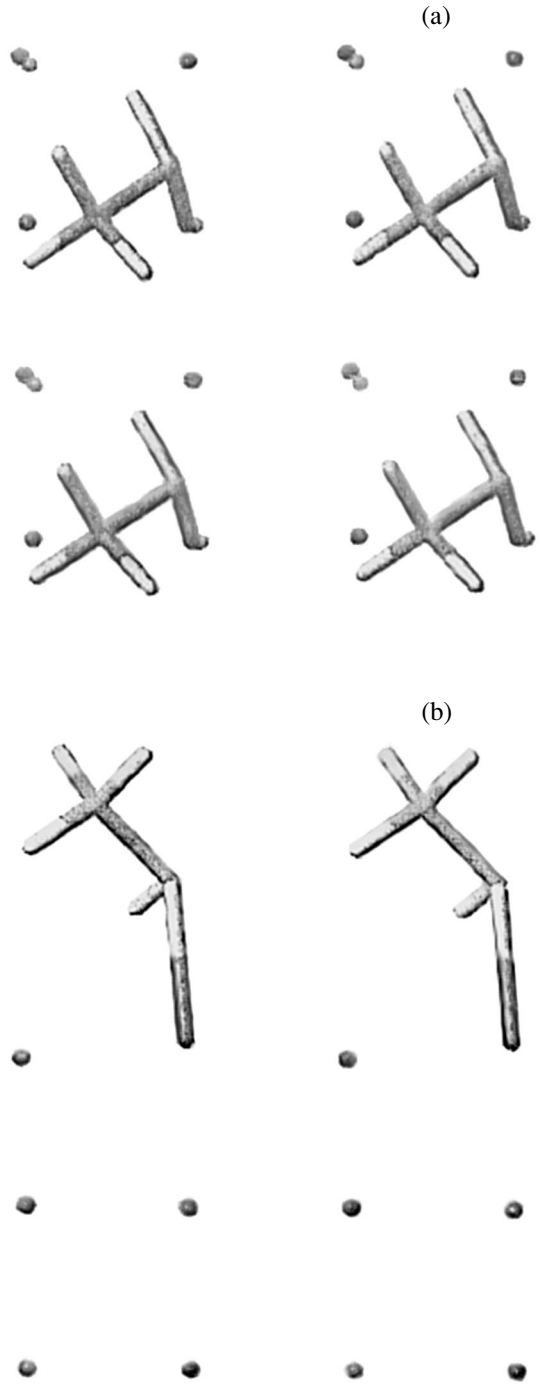

Fig. 2. Structure of the methanol molecule upon adsorption on the Al(100) surface: (a) projection on the *XY* plane and (b) projection on the *XZ* plane.

The results of calculations demonstrate that the adsorption of the methanol molecule is accompanied by a change in the topography of the surface of the plate consisting of ten Al atoms (Table 2). The Al(9) atom adjacent to the oxygen atom of the CH_3OH molecule is displaced upward along the *Z* axis by 0.236 Å with respect to the Al(10) atom of the same layer and by

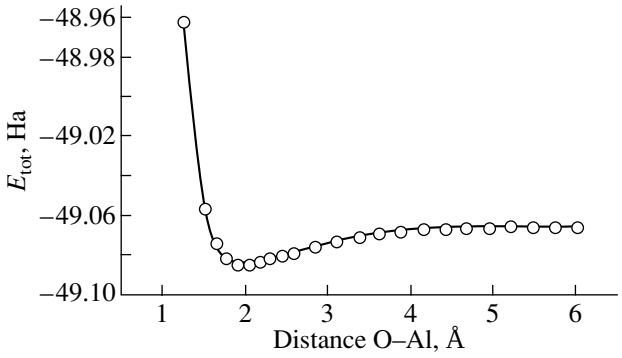

Fig. 3. Dependence of the total energy of the Al–CH_3OH system on the distance between the aluminum and oxygen atoms along the *Z* axis.

0.161 Å with respect to the clean Al plate. The displacement exceeds 10% of the interplanar distance in crystalline aluminum. In the absence of the methanol molecule, the Al(9) and Al(10) atoms are displaced by only 0.03% with respect to their equilibrium positions in the crystal. For the subsurface layer [the Al(7) and Al(8) atoms], the displacements with respect to the position in the crystal and in the Al plate are equal to 0.04 and 0.034 Å, respectively. Moreover, in the presence of the CH_3OH molecule, the Al(7)–Al(10) atoms are displaced in the plane of the (100) surface to a greater extent, which leads to the breaking of tetragonal symmetry.

The calculated dependence of the total energy of the system on the distance between the CH_3OH molecule and the aluminum surface is depicted in Fig. 3. In these calculations, the atomic coordinates did not relax; i.e., the atoms of aluminum and CH_3OH molecule were fixed in the course of displacement along the *Z* axis and their coordinates corresponded to the optimized configuration of the adsorbed CH_3OH molecule. As can be seen from Fig. 3, the total energy reaches a minimum when the difference between the *Z* coordinates of the O and Al(9) atoms is equal to 2.047 Å. The adsorption energy, which is estimated from the minimum energy of the system and the energy of the system at the maximum distance between the methanol molecule and the surface, is equal to 19.46 mHa (12.21 kcal/mol). Upon complete relaxation of the atomic coordinates, the adsorption energy is 17.94 mHa (11.26 kcal/mol). It can be seen that the difference between these two calculated energies is insignificant.

A comparison with the experimental and theoretical data obtained previously shows that the estimated adsorption energies differ substantially. For example, Whitten *et al.* [21] investigated the electron-stimulated desorption of methanol from the Al surface and found that the activation energy of desorption is close to 8.2 mHa (5.17 kcal/mol), whereas the bonding energy for oxygen-containing aluminum complexes is equal to 10 kcal/mol [22]. Sein and Jansen [23] theoretically

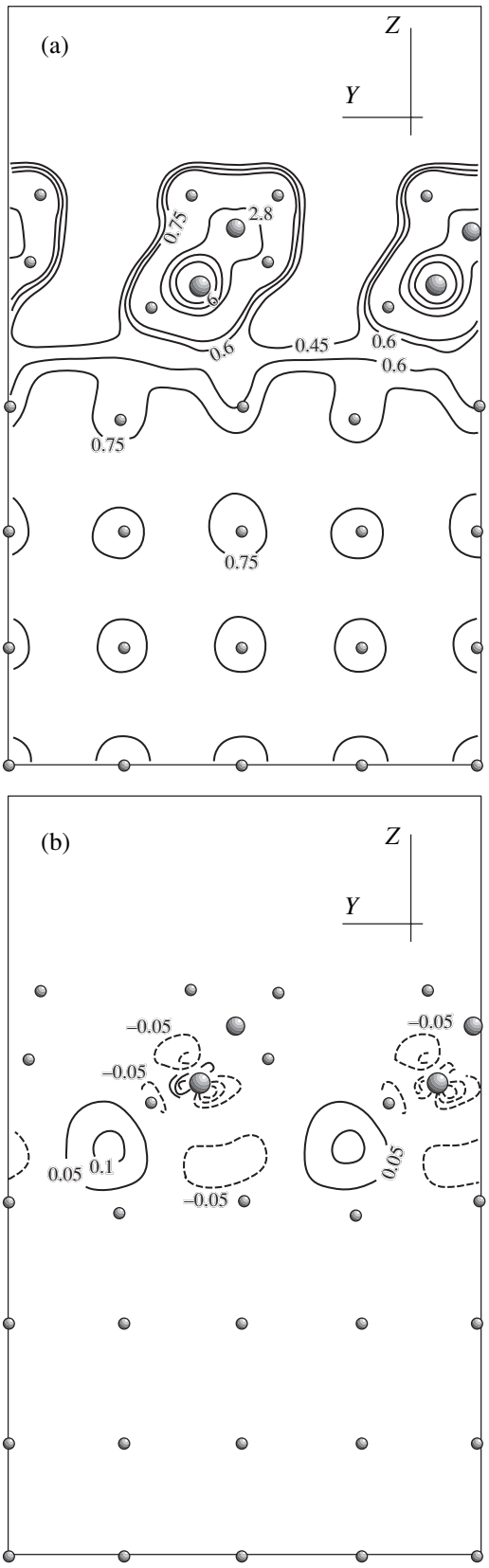

Fig. 4. Distribution of (a) the electron pseudodensity and (b) charge transfer (expressed in units of eV/Bohr^3) in the plane perpendicular to the Al(100) surface upon adsorption of methanol.

calculated the adsorption energy of $(CH_3O)^-$ radicals on the Al(100) surface and obtained a considerably higher adsorption energy: 90 mHa (56 kcal/mol).

An analysis of the distances between the Al and O atoms demonstrated that, for the optimum configuration of the methanol molecule, the Al–O bond length is equal to 2.18 Å. According to the experimental data for α-Al_2O_3 [24], the Al–O bond lengths fall in the range 1.72–1.75 Å. In transition oxides of aluminum, the Al–O bond length increases to approximately 2.02 Å and depends on the structural type of oxide [25, 26]. A comparison of the calculated bond length with the experimental data available in the literature gives grounds to believe that the adsorption bond is weaker than the standard chemical Al–O bond.

In order to elucidate the nature of the adsorption, we analyzed the distribution of the pseudodensity of valence electrons in a plane perpendicular to the aluminum surface (Fig. 4). It was found that the averaged density of valence electrons in the bulk of aluminum is substantially less than the electron density in the vicinity of the C–O bond (in Fig. 4, the changes in the density between the contour lines are irregular). In this case, it is clearly seen that the Al–O bond is absent. However, the estimates of the charge-density distribution demonstrated that the electron density between aluminum and hydrogen atoms increases. These estimates were obtained by subtracting the densities of valence electrons of the isolated methanol molecule and the aluminum plate from the pseudodensity of valence electrons of the Al–CH_3OH system with the same geometry.

With the aim of revealing other factors affecting the adsorption, we studied the change in the energy of the system upon rotation of the CH_3OH molecule about the tetragonal axis aligned parallel to the Z axis and passing through the point (u, 0, 0). The results of the calculations are presented in Fig. 5. The behavior of the system can be described in terms of the sum of two angular components of rotation. The first component leads to the breaking of twofold axial symmetry and is associated with the displacement of the Al(9) atom with respect to the tetragonal axis. The second component retains tetragonal symmetry and is most likely governed by the interaction of the CH_3OH molecule with nearest neighbor molecules (Fig. 2), the subsurface layer, and aluminum atoms in the bulk of the crystal. Upon rotation of the molecule through an angle of 180°, symmetry is absent (Fig. 5), because both components do not coincide in phase. The energies associated with each component are approximately equal to 4 mHa. Since this value amounts to 22% of the adsorption energy (17.94 mHa), it is necessary to investigate the tetragonal component in more detail. The analysis of the shorter distances between atoms in the nearest neighbor CH_3OH molecules revealed a correlation between these distances and the tetragonal extrema. The maxima are observed when the H(0)–H(3) bond

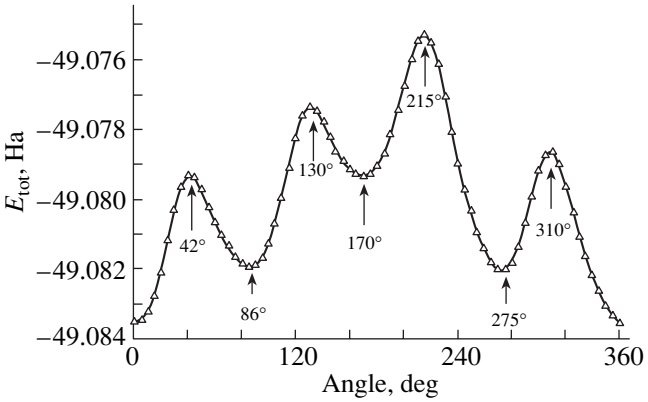

Fig. 5. Dependence of the total energy of the Al–CH_3OH system on the angle of rotation of the CH_3OH molecule with respect to the tetragonal axis of the aluminum crystal.

length is minimum and equal to 1.872 Å, even though this distance in the optimized geometric configuration is 2.548 Å.

From analyzing the component associated with the displacement of the Al(9) atom, we can infer that, in the case when organic molecules containing hydroxyl groups are adsorbed by the metal surface, the adsorption energy is substantially affected by lateral deformations of the metal surface, which result in the breaking of symmetry. These deformations can lead to a change in the surface activity of the metal with respect to adsorbed molecules.

4. CONCLUSIONS

Thus, the results obtained in the above investigation have demonstrated that the density-functional theory can be efficiently used in studying the interaction of hydroxyl-containing organic compounds with a metal surface. The proposed approach to the choice of numerical parameters (such as the decrease in the kinetic energy, number of special points used for integration over the Brillouin zone, broadening of the filling function, and number of atomic metal layers) provides a rapid convergence of the results of calculating the total energy and makes it possible to estimate the energy of adsorption and to optimize the structure of the model "CH_3OH–Al(100) surface" system.

It was shown that the redistribution of the charge density between the hydrogen atom of the hydroxyl group and the aluminum surface due to the adsorption of methanol on the surface is responsible for the character of the interaction at the interface. The adsorption energy was determined as a function of the distance between the methanol molecule and the aluminum surface. In the case where the atomic coordinates undergo relaxation, this energy differs only slightly (by 0.97 kcal/mol) from the adsorption energy of the immobile system (11.26 kcal/mol). It was found that the energy of the system under investigation changes

depending on the angle of rotation of the methanol molecule with respect to the tetragonal axis of the aluminum crystal. The effects of surface deformation of the metal and the influence of nearest neighbor molecules must be taken into account in studies of adsorption phenomena.

ACKNOWLEDGMENTS

This work was supported by the Republican Program for Basic Research "Surface-01" (Belarus) and the National Foundation for Scientific Research PAI/UAP P4-10 (Belgium).

REFERENCES

1. L. Martin and W. Brockmann, in *Proceedings of 3rd International Conference EURADH96, Cambridge, UK* (1996), p. 595.
2. W. Nitschke, Surf. Interface Anal. **16**, 247 (1990).
3. A. L. Zaitsev, Double Liason **495–496**, 9 (1994).
4. R. M. Dreizler and E. K. U. Gross, *Density-Functional Theory: An Approach to Approach to the Quantum Many-Body Problem* (Springer, Berlin, 1990).
5. H. Kuhlenbeck and H.-J. Freund, in *Metal–Ligand Interaction: From Atoms to Clusters, to Surface,* Ed. by D. R. Salahub and Nino Russo (Kluwer Academic, Dordrecht, 1992), pp. 37–70.
6. P. Hogenberg and W. Kohn, Phys. Rev., Sect. B **136**, 864 (1964).
7. W. Kohn and L. J. Sham, Phys. Rev., Sect. A **140**, 1133 (1965).
8. M. C. Payne, M. P. Teter, D. C. Allan, *et al.*, Rev. Mod. Phys. **64**, 1045 (1992).
9. http://www.pcpm.ucl.ac.be/ABINIT.
10. X. Gonze, Phys. Rev. B **54**, 4383 (1996).
11. D. M. Ceperley and B. J. Alder, Phys. Rev. Lett. **45**, 566 (1980).
12. N. Troullier and J. L. Martins, Phys. Rev. B **43**, 1993 (1991).
13. A. Khein and D. C. Allan, private communication; http://www.abinit.org/ABINIT/Psps/LDA_TM/lda.html.
14. W. K. Press, B. F. Flannery, S. A. Teukolsky, and W. T. Vettering, *Numerical Recipes. The Art of Scientific Computing* (Cambridge Univ. Press, Cambridge, 1989), p. 308.
15. H. J. Monkhorst and J. D. Pack, Phys. Rev. B **13**, 5188 (1976).
16. N. Marzari, PhD Dissertation (Univ. of Cambridge, 1996); http://www.physics.rutgers.edu/in~marzari/preprints.
17. N. Marzari, D. Vanderbilt, A. De Vita, and M. C. Payne, Phys. Rev. Lett. **82**, 3296 (1999).
18. V. Misşol, *Energia Powierzchni Rozdialu Faz w Metalach* (Ślăsk, Katowice, 1976; Metallurgiya, Moscow, 1978).
19. C. J. Smithells, *Metals: Reference Book*, 5th ed. (Butterworths, London, 1976; Metallurgiya, Moscow, 1980).
20. *Chemical Encyclopedia* (Bol'shaya Rossiĭskaya Éntsiklopediya, Moscow, 1992), Vol. 3.
21. J. E. Whitten, C. E. Young, M. J. Pellin, and D. M. Gruen, Surf. Sci. **282**, 97 (1993).
22. P. A. Hackett, S. A. Mitchell, D. M. Rayner, and B. Simard, in *Metal–Ligand Interaction, Structure, and Reactivity,* Ed. by D. R. Salahub and Nino Russo (Kluwer Academic, Dordrecht, 1992), Ser. C, Vol. 474, pp. 289–324.
23. L. T. Sein and S. A. Jansen, J. Phys. Chem. B **102**, 2415 (1998).
24. J. M. Wittbrodt, W. L. Hase, and H. B. Schlegel, J. Phys. Chem. B **102**, 6539 (1998).
25. H. Tachikawa and T. J. Tsuchida, Mol. Catal. A 277 (1995).
26. D. Farasiu and P. Lukinskas, J. Phys. Chem. A **103** (42), 8483 (1999).

Translated by O. Borovik-Romanova

Physics of the Solid State, Vol. 45, No. 12, 2003, pp. 2225–2231. Translated from Fizika Tverdogo Tela, Vol. 45, No. 12, 2003, pp. 2124–2130.

METALS AND SUPERCONDUCTORS

Temperature Dependences of the Low-Frequency Internal Friction and Shear Modulus in a Bulk Amorphous Alloy

N. P. Kobelev*, E. L. Kolyvanov*, and V. A. Khonik**

** Institute of Solid State Physics, Russian Academy of Sciences, Chernogolovka, Moscow oblast, 142432 Russia*
e-mail: kobelev@issp.ac.ru
*** Voronezh State Pedagogical University, ul. Lenina 86, Voronezh, 394043 Russia*

Received May 13, 2003

Abstract—The logarithmic decrement and shear modulus of a bulk amorphous $Zr_{52.5}Ti_5Cu_{17.9}Ni_{14.6}Al_{10}$ alloy were studied with an inverse torsion pendulum in the range from room temperature to the crystallization temperature and in the frequency range 5–40 Hz. The activation energy spectra of reversible and irreversible structural relaxation were estimated. The results obtained are discussed in the context of a two-energy-level model.

1. INTRODUCTION

In recent years, a significant number of metallic compositions (the so-called bulk metallic glasses) that exhibit a low critical cooling rate without crystallization (as low as 0.1 K/s) and provide amorphous samples 10 cm in diameter have been found [1, 2]. Apart from the fact that some of these alloys are applied in real practice, their discovery has extended the potential for investigating the nature of the amorphous state. In particular, the effect of the quenching rate on the properties of metallic glasses is of great interest. Moreover, the appearance of bulk amorphous materials in addition to amorphous ribbons enhances the instrumental possibilities for examining them.

Metallic glasses are in a nonequilibrium structural state; therefore, they undergo irreversible processes (structural relaxation), which substantially affect their physical properties. One of the efficient methods of studying relaxation processes in solids is the method of internal friction. Therefore, the purpose of this work is to investigate the temperature dependences of the low-frequency internal friction and shear modulus in a bulk metallic glass $Zr_{52.5}Ti_5Cu_{17.9}Ni_{14.6}Al_{10}$ in the range from room temperature to the crystallization temperature.

2. EXPERIMENTAL

The starting alloy of the given composition was prepared by vacuum induction melting under levitation conditions. To produce the metallic glass, we quenched the melt by ejecting it from a quartz crucible into an evacuated copper mold at room temperature [3]. The quenching rate was 10^2 K/s [3]. The ingots thus produced had dimensions $2 \times 5 \times 60$ mm. Samples for measurement were spark-cut and then mechanically polished to yield bars 30–50 mm long with a square or rectangular section having an area ranging from ~1 to 4 mm^2. The structural state (appearance of an amorphous state) was checked with x-ray diffraction analysis. At a heating rate of 2 K/min, the glass transition and crystallization temperatures of the alloy were 650 and 700 K, respectively (as follows from the data obtained earlier for similar samples).

The internal friction and shear modulus were measured on an inverse torsion pendulum in a vacuum of ~10^{-2} Pa in the temperature range 300–700 K. The measurements were performed in the frequency range from 5 to 40 Hz at a constant heating rate (2 K/min) and a deformation amplitude of ~10^{-5}.

3. EXPERIMENTAL RESULTS

Figure 1 shows the characteristic temperature dependences of the logarithmic decrement δ and the relative change in the squared resonance frequency f of the pendulum for several measurement frequencies. The shear modulus G is proportional to the squared resonance frequency of the torsion pendulum, the squared cross-sectional area of the sample, and a coefficient dependent on the shape of the cross section and is inversely proportional to the sample length [4]; therefore, we can assume that, to a first approximation, $f^2(T) \sim G/\rho$, where ρ is the material density. As can be seen from Fig. 1, the variation of the shear modulus with the temperature prior to crystallization (~700 K) is nonmonotonic; namely, the shear modulus exhibits a linear decrease in the range from room temperature to about 500 K, then becomes temperature-independent in the range from 500 to 600 K (slightly increasing near 600 K), and then exhibits a superlinear decrease above 600–650 K. Moreover, apart from the range above 600 K, the variation of the shear modulus with temperature is independent of the measurement frequency. At the same time, the logarithmic decrement increases

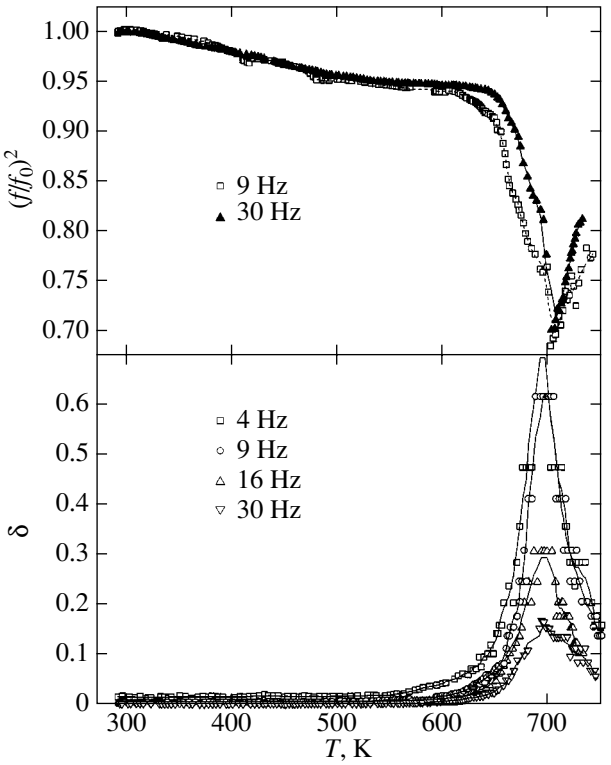

Fig. 1. Temperature dependences of the squared resonance frequency of the torsion pendulum and the logarithmic decrement in an Zr–Cu–Ni–Al–Ti alloy obtained upon heating at a rate of 2 K/min.

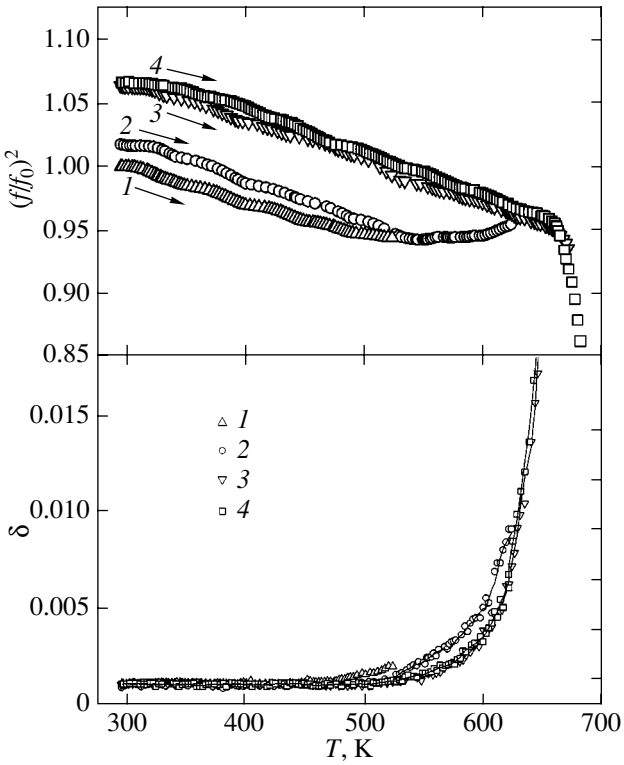

Fig. 2. Relative changes in the resonance frequency squared and the logarithmic decrement during four sequential cycles of heating to (*1*) 525, (*2*) 625, (*3*) 670, and (*4*) 700 K. The measurement frequency is 40 Hz.

with decreasing frequency. This indicates that, in this frequency range, the condition $\omega\tau > 1$ should be satisfied for relaxation processes (τ is the relaxation time) and the behavior of the shear modulus below 600 K cannot be related to the relaxation contribution to its effective value.

It should be noted that the change in the shear modulus *G* with temperature up to 400–450 K is reversible and that the logarithmic decrement does not exceed the background level. Heating of the sample to 500 K or above is accompanied by irreversible changes, namely, an increase in the shear modulus and a decrease in the logarithmic decrement, which is indicated by the results of temperature-cycling tests (Fig. 2). In the repeated heating, the linear temperature dependence of the shear modulus remains unchanged to about the maximum temperature of the previous cycle. Above this temperature, the logarithmic decrement again sharply increases. This process continues to 600–640 K. As the maximum temperature of heating increases further, the shear modulus virtually ceases to grow at room temperature after recovery and the temperature dependences of the logarithmic decrement and the shear modulus become reversible. However, heating of the sample to temperatures close to the onset of crystallization (above 650 K) or holding of the sample at temperatures above 600 K for some time again causes irreversible changes in the temperature dependences, namely, a more pronounced nonlinear dependence of the shear modulus in the range above 650 K (its decrease with a simultaneous increase in the logarithmic decrement) and a decrease in the crystallization temperature.

Thus, there are a few aspects in the behavior of the internal friction and shear modulus of the bulk Zr–Cu–Ni–Al–Ti metallic glass. We will consider them sequentially.

4. DISCUSSION OF THE RESULTS

The irreversible changes in the logarithmic decrement and the shear modulus in the temperature range 450–600 K can be qualitatively described in terms of a two-energy-level model. Let us assume that the metallic glass contains centers that can have two different energy states (as a result of insignificant changes in the interatomic configuration), which are separated by an energy barrier *E* and differ in the local symmetry of interatomic interaction. For example, in the simplest case, one state (*c*) has a spherical symmetry and the other (*s*) has an axial symmetry. Examples of such centers in a crystal structure can be interstitial sites (split and symmetrical configurations), interstitial defects, and so on [5]. The question as to the atomic structure of

such centers in amorphous materials remains open, although, e.g., in [6–8], a phenomenological theory was developed in which the properties of amorphous and liquid states are described using an interstitial model of their structures.

We will assume that the concentration of centers N is sufficiently low to neglect their interaction. In equilibrium, the relative concentrations of these energy states (n_c, n_s) are determined by the relations

$$\begin{aligned} n_c &= 1/(1 + \exp(E_c - E_s)/T), \\ n_s &= 1/(1 + \exp(E_s - E_c)/T). \end{aligned} \tag{1}$$

We will characterize the orientation of the s state by a unit vector s^α collinear to the symmetry axis. We introduce the angular concentration density of these states (in the isotropic case, its equilibrium magnitude is $n_s/4\pi$). For a small shear strain ε_{ij}, a variation of this density ν_s^α is specified by the kinetic equation

$$\tau\frac{\partial \nu_s^\alpha}{\partial t} + \nu_s^\alpha = n_s n_c V s_i^\alpha s_j^\alpha \varepsilon_{ij}/4\pi T, \tag{2}$$

where $\tau = \tau_0(n_s n_c)^{1/2}\exp(E/T)$, τ_0 is the characteristic time, and V is the deformation potential. A change in the free energy related to the first term of interaction between ν_s^α and ε_{ij} can be written as

$$\Delta F = -aN\nu_s^\alpha V s_i^\alpha s_j^\alpha \varepsilon_{ij}. \tag{3}$$

Using the thermodynamic definition of the elastic-stress tensor

$$\sigma_{ij} = [\partial F/\partial \varepsilon_{ij}]_{T,\nu} \tag{4}$$

and Eqs. (2) and (3), we can easily obtain an additional relaxation contribution from transitions between the s and c states to the shear modulus:

$$\Delta G = -aV^2\Omega N n_s n_c/T(1 + i\omega\tau), \tag{5}$$

where $\Omega = 1/15$ is the orientation factor. In general, when both energy states are characterized by anisotropic local interatomic interaction, Eq. (5) has the same form, where V is an effective quantity depending on the deformation potentials and the correlation factor between the anisotropy directions in these states.

Let us consider the case where $\omega\tau \gg 1$, which corresponds to the experimental data obtained for the frequency range under study. Then, the imaginary part of Eq. (5) specifies the logarithmic decrement and the relaxation contribution to the shear modulus is negligible.

It is natural to assume that the ratio between the concentrations of centers in these energy states in the quenched metallic glass is far from equilibrium (if the difference in their energy levels is a few times greater than T). At a fixed temperature, a deviation Δn from the equilibrium concentration changes in time following the law

$$\partial\Delta n/\partial t = -\Delta n/\tau. \tag{6}$$

At $\omega\tau \gg 1$, the variation in Δn in one oscillation period is negligible; therefore, the variation in ν_s^α with time can be considered to be reversible. Due to Δn, there appears an additional term $(\Delta n_s)n_s V s_i^\alpha s_j^\alpha \varepsilon_{ij}/4\pi T$ in the right-hand side of Eq. (2) and an additional ("nonequilibrium") contribution to the logarithmic decrement.

$$\delta = \pi a V^2 \Omega N|\Delta n(t)|n_c/(T\omega\tau). \tag{7}$$

It follows from Eq. (7) that the nonequilibrium contribution at a given temperature can be larger than the equilibrium value if the high-energy state has an axial symmetry.

Now, we analyze the variation of this contribution to the logarithmic decrement with temperature under the assumption that N (concentration of the centers) remains unchanged in the temperature range under study. First, we examine how Δn varies with temperature. Under the assumptions made above, the quantity τ in Eq. (6) can be written as $\tau = \tau_0\exp(E_0/T)$, where $E_0 = E - |E_s - E_c|$. Assuming that the nonequilibrium concentration is substantially higher than the equilibrium one when a sample is heated at a constant rate, we can rewrite Eq. (6) in the form

$$\partial\Delta n/\partial T = -\Delta n\exp(-E_0/T)/(\tau_0\theta). \tag{8}$$

We assume that τ_0^{-1} characterizes atomic frequencies (10^{13}–10^{15} s^{-1}) and that the conditions $T/\tau_0\theta \gg 1$, $T/E_0 \ll 1$, and $T^2/(E_0\tau_0\theta) \gg 1$ are satisfied. It can be shown that, under these conditions (which are indeed satisfied, as will be shown below), an approximate solution to Eq. (8) has the form

$$\Delta n(T) = \Delta n_0\exp(-T^2\exp(-E_0/T)/E_0\tau_0\theta). \tag{9}$$

Figure 3 shows the temperature dependence of $\Delta n/\Delta n_0$ calculated at $E_0 \approx 1.9$ eV, $\tau_0 \sim 10^{-13}$ s, and $\theta = 2$ K/min. As is seen, the relaxation of the nonequilibrium state in the case of a single activation energy proceeds in a relatively narrow temperature range. Figure 3 also shows the temperature dependence of $\partial(\Delta n/\Delta n_0)\partial T$, which has the shape of a sharp asymmetric peak; the position of the maximum of this peak corresponds to the condition $E_0/T = \ln(T^2/E_0\tau_0\theta)$. A comparison of Eqs. (7) and (8) yields

$$\delta \sim |\partial\Delta n/\partial T|/(T\omega/\theta). \tag{10}$$

Since $1/T$ varies only weakly as compared to $\partial\Delta n/\partial T$, the temperature dependence of the logarithmic decrement should be similar to $\partial\Delta n/\partial T$.

Figure 4 shows the temperature dependences of the irreversible contribution to the logarithmic decrement

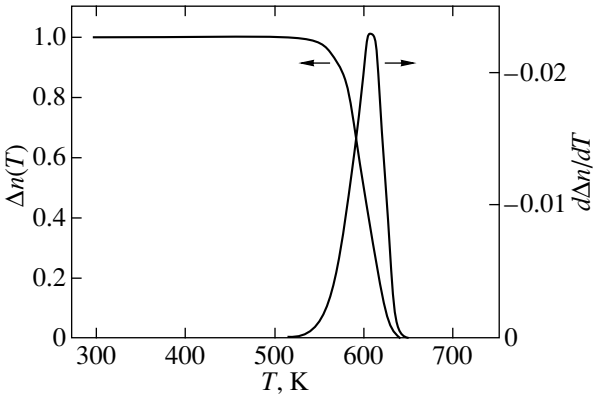

Fig. 3. Temperature dependences of the concentration of nonequilibrium states and its derivative with respect to temperature as calculated using Eqs. (8)–(10) at E_0 = 1.9 eV, $\tau_0 = 10^{-13}$ s, and a heating rate of 2 K/min.

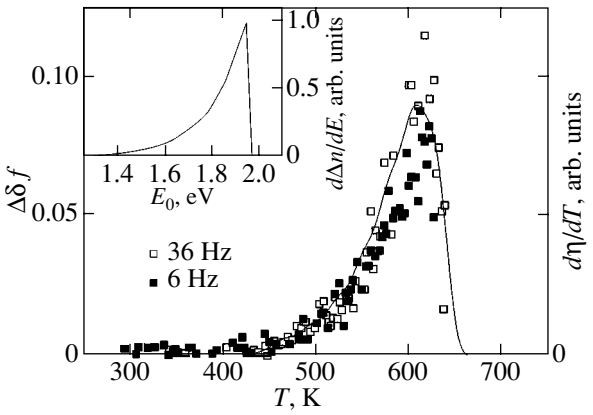

Fig. 4. Temperature dependences of the irreversible contribution to the logarithmic decrement multiplied by frequency. The solid line shows the temperature dependence of damping calculated using Eqs. (10) and (11) for the activation-energy spectrum given in the inset.

(multiplied by frequency) found from the experimental data for two measurement frequencies. As follows from these data, the irreversible contribution to damping is indeed inversely proportional to the frequency to within the limits of experimental error. It is also seen that the experimental dependences agree qualitatively with those calculated from the model proposed here. However, the experimental peaks in damping have a less pronounced dependence on T in the low-temperature range. This is not surprising, since a real metallic glass should have dispersed activation energies [9]. This behavior can be caused by several factors, which are actually interrelated. One factor is the variation in the elemental composition of the nearest environment of a center. A second factor is the presence of random elastic stress fields. In this case, the activation-energy spectrum should broaden toward low energies, since it is obvious that shear stresses effectively decrease the activation energy. Another possible cause of the broadening of the activation-energy spectrum can appear at a high density of nonequilibrium states because of their interaction. This factor should also result in broadening of only the low-temperature part of the damping peak, since the concentration of nonequilibrium states decreases with increasing temperature. Moreover, it can be shown that, since the nonequilibrium concentration arises during quenching (rapid cooling), the low-temperature part of the spectrum of nonequilibrium states must drop almost exponentially, with its decay rate determined by the quenching rate and the value of ΔE.

Thus, the actual temperature dependence of the concentration of nonequilibrium states $\eta(T)$ is expressed as

$$\eta(T) = \int(\partial\Delta n_0/\partial E_0) \times \exp(-T^2\exp(-E_0/T)/E_0\tau_0\theta)dE_0. \quad (11)$$

It should be noted, however, that relation (10) between the logarithmic decrement and the temperature derivative of the concentration is valid in this case as well. This allows one to reconstruct the activation-energy spectrum from the temperature dependence of the logarithmic decrement. Unfortunately, the experimental data are not accurate enough for us to try to perform such a reconstruction. Therefore, we simply took a spectrum characterized by exponential growth of the activation energy to a certain maximum value (see inset to Fig. 4) and used it to calculate the temperature dependence of $\partial(\Delta n/\Delta n_0)\partial T$ with Eqs. (10) and (11). The dependence thus constructed is seen from Fig. 4 to agree satisfactorily with the experimental data.

Let us consider the temperature dependence of the irreversible contribution to the shear modulus, which is

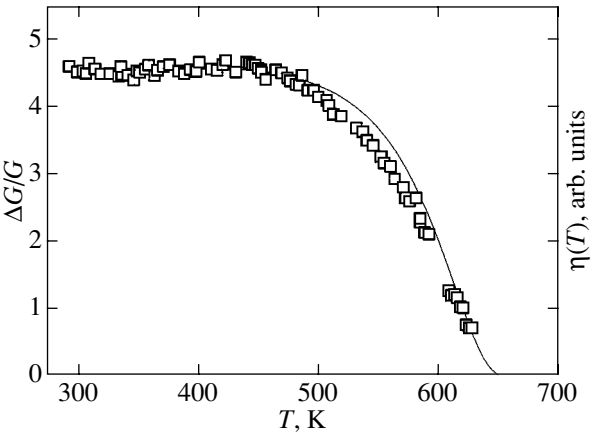

Fig. 5. Experimental temperature dependence of the irreversible contribution to the shear modulus at a frequency of 6 Hz and the calculated temperature dependence of the concentration of nonequilibrium states (solid line) for the activation-energy spectrum given in Fig. 4.

seen from Fig. 5 to be similar to that of the concentration of nonequilibrium states. Moreover, the $\eta(T)$ dependence calculated by Eq. (11) for the same activation-energy spectrum virtually coincides with the experimental temperature dependence of the irreversible contribution to the shear modulus. This suggests that the observed irreversible changes in the shear modulus are specified by the concentration of nonequilibrium states. Such a (nonrelaxation) contribution to the elastic moduli can indeed exist and is caused by the terms proportional to the concentration of nonequilibrium states and the related strains squared in the expression for the free energy. Actually, this signifies inclusion of the nonlinearity of the elastic properties of a material. If we take into account only the difference in the values of dilatation corresponding to different energy states, this contribution to the shear modulus should be equal to $N\Delta n\beta\phi$, where β is the ratio of the corresponding third-order modulus to the shear modulus and ϕ is the relative change in volume of the material per unit of atomic concentration of nonequilibrium states. The value of β in crystalline materials is about –10 [10]. For metallic glasses, this value is usually several times larger. For example, for the alloy under study, $\partial G/\partial T$ in the range of the linear temperature dependence in the amorphous state is about three times greater than that after crystallization; therefore, we can assume that $\beta = -30$. According to our estimations, the increase in the material density after annealing at about 600 K is 0.1–0.3%, which means that the change in the shear modulus should be 3–10% (which agrees with the experimental data). We can also estimate the order of the change in the dilatation per center when its energy state changes. Assuming that $N \sim 10^{-1}$ [6–8] and $\Delta n \sim$ 0.1–0.3, we obtain $\phi \sim 0.1$, which is rather realistic. Apparently, shear strains that appear during a change in the energy state of a center can also contribute to the shear modulus. In this case, the change in the shear modulus should be proportional to the squared change in the shear strains and to the corresponding fourth-order modulus. Unfortunately, we cannot conduct the corresponding estimations now.

Thus, the obtained experimental data on the character of the irreversible changes in the logarithmic decrement and the shear modulus at temperatures below the glass transition temperature can be described consistently in the context of the two-level center model with anisotropic local interatomic interaction (at least, in the high-energy state).

As follows from the experimental data given above, the temperature dependence of the shear modulus in the equilibrium state (up to ~600 K) remains linear; that is, this dependence can be described in terms of the variation of the mean interatomic distance with temperature due to the anharmonicity of interatomic interaction (we will return to the temperature range above 600 K further on). At the same time, the logarithmic decrement at temperatures above 500 K remains considerable. Figure 6 shows the dependences of the logarithmic decrement on the reciprocal temperature (in the logarithmic coordinates) obtained in the repeated cycle after preliminary heating of the sample to 640 K at three different measurement frequencies. Within the limits of experimental error, they are satisfactorily described by the sum of two exponents $\exp(-U/T)$ with activation energies of ~2.1 and ~0.7 eV. It should be noted that the activation energy of the high-temperature part of the internal friction is rather close to the characteristic energies in the activation-energy spectrum of the irreversible contribution to damping (Fig. 4). Therefore, it is natural to suppose that this portion of damping is caused by a reversible ("equilibrium") relaxation process related to transitions between different energy states (see Eq. (5)). Analysis of the temperature dependences of the logarithmic decrement and the shear modulus indicates that, up to ~600 K, this contribution to damping is significantly lower than the irreversible part of damping. However, at higher temperatures, the value of this equilibrium contribution to damping becomes substantially larger than that of the irreversible contribution to damping. This fact indicates that the equilibrium concentration of excited states becomes comparable to or even higher than the nonequilibrium one. This can explain the drop in the irreversible portion of damping above 600 K (Fig. 4), since, in this case, we have to include the term proportional to the rate of variation of the equilibrium excitation concentration with temperature in the right-hand side of Eq. (8). Qualitative estimations indicate that, when the nonequilibrium concentration drops to a level of about $E_0/\Delta E$ times less than the equilibrium concentration, the irreversible contribution to damping vanishes.

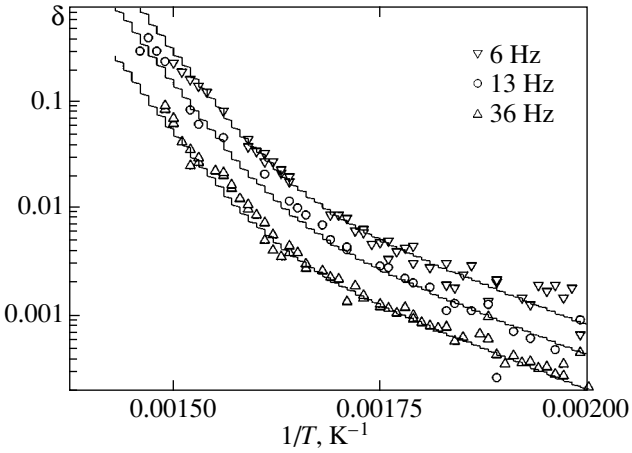

Fig. 6. Dependences of the reversible contribution to damping on the reciprocal temperature for three measurement frequencies. The solid lines show the sums of two exponential dependences with activation energies of 2.1 and 0.7 eV.

At low temperatures, the reversible internal friction with a low effective activation energy (~0.7 eV) can be adequately described in terms of a relaxation process with distributed activation energies. Analysis of the

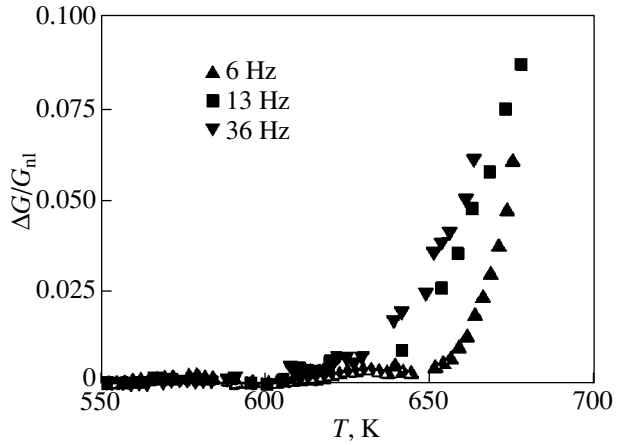

Fig. 7. Temperature dependences of the superlinear portion of the variation of the shear modulus for three measurement frequencies.

experimental data shows that, at $\tau_0 = 10^{-13}$ s, this process can be described using a spectrum of activation energies ranging from 0.9 to 1.3 eV with an exponentially growing energy-state density ($\partial n/\partial E \sim \exp(E/U)$, where $U \sim 0.1$ eV) in this range. Unfortunately, the experimental data are too scarce to draw a conclusion about the character of the energy spectrum in the range from 1.3 to 2.1 eV. To accomplish this, a significantly broader frequency range should be covered.

What processes can determine the low-energy portion of the spectrum? One of the possible mechanisms is the reorientation of centers of elastic-dipole type [5]. As was already noted, analogs of such dipoles in crystal structures can be defects, such as split interstitial sites, Snoek defects, etc. We assume that such dipoles are the dipoles that were considered earlier rather than new centers and that the low-energy states are also anisotropic.

Let us discuss the behavior of the shear modulus in the temperature range above 600 K. Here, the temperature dependence becomes nonlinear, although the behavior of the shear modulus still remains almost completely reversible (up to at least 650–670 K). Figure 7 shows the temperature dependence of the superlinear contribution to the shear modulus (the difference between the extrapolation of the linear dependence to temperatures above 600 K and the corresponding values of shear modulus in this temperature range) at three measurement frequencies. This portion of the variation of the shear modulus is seen to be frequency-dependent. At first glance, the changes are too large to be related to relaxation processes. The logarithmic decrement is inversely proportional to the frequency even in this temperature range; i.e., $\omega\tau > 1$. Therefore, the possible relaxation contribution, as calculated from the conventional relaxation relations between modulus changes and the logarithmic decrement, does not exceed 1%. However, we have to take into account that, for damping in the band 0.9–1.3 eV, the condition $\omega\tau > 1$ is invalid. For each activation energy in this band, damping has the form of a relaxation peak with a maximum at the corresponding temperature and the observed temperature dependence is an integrated characteristic of the spectrum. At the same time, the contribution to the modulus change at $\omega\tau < 1$ levels off rather than decreases. Estimations show that even the examined portion of the spectrum (0.9–1.3 eV) is sufficient to provide a 5–15% change in the shear modulus. For more precise estimations, we need to know the character of the spectrum at higher activation energies.

Thus, both the reversible portion of the internal friction and the change in the shear modulus can be qualitatively described within the framework of the two-energy-level model.

Let us consider how the model proposed explains the appearance of the irreversible changes in the logarithmic decrement and in the shear modulus in the temperature range prior to the onset of crystallization. We can assume that the low-energy states of a center are localized; that is, a change in the orientation (the direction of the anisotropy axis) is not accompanied by a change in the center of gravity and by mass transfer. Therefore, the glass remains in the reversible (equilibrium) state up to temperatures where processes with higher activation energies begin to manifest themselves. A transition to a high-energy state and vice versa can result in a displacement of the center in space. From this standpoint, the appearance of transitions to a high-energy state in the activation-energy spectrum means the onset of diffusion processes, which can cause irreversible rearrangements.

4. CONCLUSIONS

Thus, we have qualitatively explained all detected experimental phenomena in terms of the two-energy-level model. Naturally, the model proposed here is fairly conventional and requires further investigations in order to refine it. In particular, it is of interest to study the time dependence of the variation in the shear modulus and the logarithmic decrement at temperatures below and above the glass transition temperature, to broaden the measurement frequency range, and to study the effect of the deformation amplitude on the behavior of the shear modulus and the logarithmic decrement in various temperature ranges.

ACKNOWLEDGMENTS

This work was supported in part by the U.S. Civilian Research and Development Foundation (grant no. RPI-2320-VO-02) and the Russian Foundation for Basic Research (project no. 01-02-16461).

REFERENCES

1. A. Inoue, Acta Mater. **48**, 279 (2000).

2. W. L. Johnson, MRS Bull. **24**, 42 (1999).
3. A. E. Berlev, O. P. Bobrov, K. Csach, *et al.*, J. Appl. Phys. **92**, 5898 (2002).
4. W. Nowacki, *Teoria Spreżyštosci* (PWN, Warszawa, 1970; Mir, Moscow, 1975).
5. A. S. Nowick and B. S. Berry, *Anelastic Relaxation in Crystalline Solids* (Academic, New York, 1972; Atomizdat, Moscow, 1975).
6. A. V. Granato, Phys. Rev. Lett. **68**, 974 (1992).
7. A. V. Granato, J. Phys. Chem. Solids **55**, 931 (1994).
8. A. V. Granato, J. Non-Cryst. Solids **307–310**, 376 (2002).
9. A. E. Belyavskiĭ, O. P. Bobrov, A. T. Kosilov, and V. A. Khonik, Fiz. Tverd. Tela (St. Petersburg) **38**, 30 (1996) [Phys. Solid State **38**, 16 (1996)].
10. R. Truell, C. Elbaum, and B. B. Chick, *Ultrasonic Methods in Solid State Physics* (Academic, New York, 1969; Mir, Moscow, 1972).

Translated by K. Shakhlevich

Physics of the Solid State, Vol. 45, No. 12, 2003, pp. 2232–2236. Translated from Fizika Tverdogo Tela, Vol. 45, No. 12, 2003, pp. 2131–2135.

METALS AND SUPERCONDUCTORS

Control of the Perturbation-Wave-Vector Range of Modulation Instability of Dispersive Electromagnetic Waves in the Nonlocal Josephson Electrodynamics of a Thin Superconducting Film

A. I. Lomtev

Donetsk Physicotechnical Institute, National Academy of Sciences of Ukraine, Donetsk, 83114 Ukraine
e-mail: lomtev@kinetic.ac.donetsk.ua

Received April 22, 2003

Abstract—Modulation instability of dispersive electromagnetic waves propagating through a Josephson junction in a thin superconducting film is investigated in the framework of the nonlocal Josephson electrodynamics. A dispersion relation is found for the time increment of small perturbations of the amplitude. For dispersive waves, it is first established that spatial nonlocality suppresses the modulation instability in the range of perturbation wave vectors $0 \le Q \le Q_{B1}(k)$, i.e., in the long-wavelength range of experimental interest. The modulation instability range $Q_{B1}(k) < Q < Q_{B2}(k, A, L)$ can be controlled (which is a unique possibility) by varying a dispersion parameter, namely, the wave vector **k** [or the frequency $\omega(k)$] of linear-approximation waves. In the wave-vector ranges $0 \le Q \le Q_{B1}(k)$ and $Q \le Q_{B2}(k, A, L)$, waves are shown to be stable. © *2003 MAIK "Nauka/Interperiodica".*

1. Continued attention has been focused on a wide range of instabilities of waves in various nonlinear systems and media [1, 2]. It is well known that compression of a nonlinear wave can occur both in the cross section and in the direction of propagation of the wave beam. Examples are the self-focusing of light predicted by Askar'yan [3, 4] and the instability of waves to breaking up into wave packets and the self-compression of wave packets (modulation instability) first studied by Lighthill [5]. Modulation instability of electromagnetic waves observed in optical fibers corresponds to the instability of solutions to a nonlinear Schrödinger equation [6], and that observed in distributed Josephson junctions, to the instability of solutions to the sine-Gordon equation [7, 8]. Modulation instability is of interest from the fundamental point of view and for practical applications. For example, this phenomenon is used for generating series of ultrashort optical pulses with a high repetition frequency [6] and for developing novel logic units [9].

In many cases, spatially nonlocal modifications of the nonlinear Schrödinger equation [10] and of the sine-Gordon equation [11–22] should be used in studying modulation instability. For example, it was shown in [11, 12] that spatial nonlocality can be significant even in junctions of bulk superconductors of large thickness $d \gg \lambda$ (λ is the London penetration depth) along the magnetic field (vortex lines), i.e., in the cases where the local approximation was used earlier. For junctions in thin films of $d \ll \lambda$, there is no local limit and the spatial nonlocality is significant and becomes a determining factor. The corresponding equations were derived and investigated in [13–16]. It has been shown [17–19] that, in the Josephson electrodynamics of thin films of magnetic (two- and three-dimensional) superconductors, not only spatial nonlocality but also retardation effects must be taken into account. The Josephson junction at the interface between two superconducting layers of finite thickness along a direction perpendicular to the magnetic vortex field was studied in [20]. In [21, 22], a butt junction and a tilted (tapered) junction (having, therefore, a finite thickness along the magnetic field of vortices) were considered for arbitrary values of the ratio d/λ.

Due to the difference in geometry of the problems considered in the papers mentioned above [11–22], the equations for the Josephson electrodynamics in them differ in the form of the kernel of the integral operator describing the spatial nonlocality. However, in all those papers, the spatial nonlocality of the equations for the phase difference is due to the nonlocal relation between the fields at the interface and in the superconductor. This origin of spatial nonlocality is universal for the electrodynamics of Josephson junctions; therefore, the nonlocality itself is the rule rather than the exception.

In the framework of the spatially nonlocal Josephson electrodynamics of the junction at the interface between bulk superconductors, the modulation instability was first considered in [11]. It was shown that increasing small perturbations of the amplitude and phase correspond to the development of modulation instability in the electromagnetic wave with a finite constant amplitude; the instability is characterized by a nonlinear shift in frequency and by the dispersion law of waves in the linear approximation. It was also found that spatial nonlocality suppresses the modulation

instability. Abdullaev [23] also considered the Josephson junction at the interface of bulk superconductors and investigated the modulation instability of a plane nonlinear uniform (dispersionless) electromagnetic wave with a finite amplitude and with a frequency equal to the Josephson frequency. It was shown that the instability causes small perturbations of the amplitude to increase and brings about the breaking up of the wave into wave packets.

In both [11] and [23], it was shown that the modulation instability occurs in the perturbation wave-vector **Q** range $0 < Q < Q_B$, where Q_B is a certain limiting wave vector. Thus, in the long-wavelength range of experimental interest ($Q \longrightarrow 0$), modulation is always unstable in the cases considered in [11, 23].

In this paper, we show that the spatial nonlocality in the equation for the Josephson electrodynamics that describes the propagation of dispersive waves in thin films suppresses the modulation instability to increasing small-amplitude perturbation in the long-wavelength range $0 \le Q \le Q_{B1}(k)$. Therefore, it is of interest to investigate the modulation instability of dispersive electromagnetic waves propagating in thin two-dimensional superconducting films (which has not been done yet) in the framework of the nonlocal Josephson electrodynamics.

2. As an example of a nonlinear system exhibiting modulation instability, we consider a Josephson junction in an ultrathin superconducting film of thickness $d \ll \lambda$.

For a Josephson junction consisting of thin superconducting films of thickness $d \ll \lambda$, the dynamics of the phase difference $\varphi(x, t)$ of the condensate wave functions at the junction banks in the dissipationless limit is described by the nonlinear nonlocal sine-Gordon equation [16]

$$\frac{1}{\omega_J^2}\frac{\partial^2\varphi(x,t)}{\partial t^2} + \sin\varphi(x,t) = L_J\int_{-\infty}^{\infty} dx' K\left(\frac{x-x'}{2\lambda_{\text{eff}}}\right)\frac{\partial^2\varphi(x',t)}{\partial x'^2}. \quad (1)$$

Here, $L_J = \lambda_J^2/\lambda$, ω_J is the Josephson frequency, λ_J is the Josephson length, $\lambda_{\text{eff}} = \lambda^2/d$ is the Pearl length, and the nonlocal kernel $K\left(\frac{x-x'}{2\lambda_{\text{eff}}}\right)$ has the form

$$K\left(\frac{x-x'}{2\lambda_{\text{eff}}}\right) = \frac{2\lambda_{\text{eff}}}{\pi}\int_0^{\infty} dq \frac{J_0 q(x-x')}{1+2q\lambda_{\text{eff}}}, \quad (2)$$

where $J_0(x)$ is the zero-order Bessel function.

Using Eq. (1) and the approximation $\sin\varphi(x, t) \approx \varphi(x, t)$, we find that, in the linear approximation, dispersive waves with an infinitely small amplitude

$$\varphi(x,t) = \varphi_0 \exp[i(kx-\omega t)], \quad |\varphi_0| \ll 1 \quad (3)$$

propagating with frequency ω and wave vector **k** along the Josephson junction possess a real spectrum,

$$\frac{\omega(k)}{\omega_J} = \left[1 + \frac{L}{\pi}(2k\lambda_{\text{eff}})^2 J(2k\lambda_{\text{eff}})\right]^{1/2}, \quad (4)$$

where $L = L_J/2\lambda_{\text{eff}}$ and $J(q) = 2\int_0^{\infty} dx[q\cosh x + 1]^{-1}$; this integral can be evaluated to be

$$J(q) = \frac{1}{\pi\sqrt{1-q^2}}\ln\frac{1+\sqrt{1-q^2}}{1-\sqrt{1-q^2}}, \quad q \le 1,$$
$$J(q) = \frac{4}{\pi\sqrt{q^2-1}}\arctan\frac{\sqrt{q^2-1}}{q+1}, \quad q \ge 1. \quad (5)$$

Let us consider the evolution of nonlinear dispersive electromagnetic waves with a small, but finite, amplitude propagating through the junction. The phase change $\varphi(x, t)$ can be represented in the form

$$\varphi(x,t) = u(x,t)\exp\{i[kx-\omega(k)t]\} + u^*(x,t)\exp\{-i[kx-\omega(k)t]\}, \quad |u(x,t)| \ll 1, \quad (6)$$

where the carrier wave is a dispersive wave in the linear approximation described by Eq. (3) with spectrum (4).

After substituting Eq. (6) and the approximation $\sin\varphi(x, t) \approx \varphi(x, t) - \varphi^3(x, t)/3!$ into Eq. (1) [24], we retain only the lowest order nonlinear term at the fundamental (carrier) frequency and restrict ourselves to the approximation in which the amplitude $u(x, t)$ varies slowly in time and, therefore, the condition $|\partial^2 u(x, t)/\partial t^2| \ll 2\omega(k)|\partial u(x, t)/\partial t|$ is satisfied. As a result, we obtain the following equation for the amplitude $u(x, t)$ from Eq. (1):

$$i2\frac{\omega(k)}{\omega_J^2}\frac{\partial u(x,t)}{\partial t} + \left[\frac{\omega(k)^2}{\omega_J^2} - 1 + \frac{1}{2}|u(x,t)|^2\right]u(x,t) + L_J\int_{-\infty}^{\infty} K\left(\frac{(x-x')}{2\lambda_{\text{eff}}}\right)\left[\frac{\partial^2 u(x',t)}{\partial x'^2} + 2ik\frac{\partial u(x',t)}{\partial x'} - k^2 u(x',t)\right]\exp[-ik(x-x')]dx' = 0. \quad (7)$$

This nonlinear nonlocal equation has an exact solution in the form of a plane nonlinear wave with a uniform amplitude A and with a shift in frequency,

$$u_0(t) = A\exp[i\omega_J^2 A^2 t/4\omega(k)], \quad A \ll 1. \quad (8)$$

In order to investigate the stability of this solution, we introduce a small perturbation $\psi(x, t)$ of the amplitude:

$$u(x, t) = [A + \psi(x, t)]\exp[i\omega_J^2 A^2 t/4\omega(k)], \quad |\psi(x, t)| \ll A. \tag{9}$$

It follows from Eq. (7) that the small perturbation $\psi(x, t)$ satisfies the linear equation

$$i\frac{2\omega(k)}{\omega_J^2}\frac{\partial\psi(x, t)}{\partial t} + \left[\frac{\omega^2(k)}{\omega_J^2} - 1\right]\psi(x, t) + \frac{A^2}{2}[\psi(x, t) + \psi^*(x, t)] + L_J\int_{-\infty}^{\infty} K\left(\frac{x-x'}{2\lambda_{\text{eff}}}\right) \times\left[\frac{\partial^2\psi(x', t)}{\partial x'^2} + i2k\frac{\partial\psi(x', t)}{\partial x'} - k^2\psi(x', t)\right] \times\exp[-ik(x-x')]dx' = 0. \tag{10}$$

Substituting $\psi(x, t) = v(x, t) + iw(x, t)$ into Eq. (10), we obtain the following equations for the real and imaginary parts of the perturbation:

$$\begin{aligned}&\frac{2\omega(k)}{\omega_J^2}\frac{\partial v(x, t)}{\partial t} + \left[\frac{\omega^2(k)}{\omega_J^2} - 1\right]w(x, t)\\ &+ L_J\int_{-\infty}^{\infty} K\left(\frac{x-x'}{2\lambda_{\text{eff}}}\right)\left[\frac{\partial^2 w(x', t)}{\partial x'^2} + 2k\frac{\partial v(x', t)}{\partial x'} - k^2 w(x', t)\right]\exp[-ik(x-x')]dx' = 0,\\ &-\frac{2\omega(k)}{\omega_J^2}\frac{\partial w(x, t)}{\partial t} + \left[\frac{\omega^2(k)}{\omega_J^2} - 1 + A^2\right]v(x, t)\\ &+ L_J\int_{-\infty}^{\infty} K\left(\frac{x-x'}{2\lambda_{\text{eff}}}\right)\left[\frac{\partial^2 v(x', t)}{\partial x'^2} - 2k\frac{\partial w(x', t)}{\partial x'} - k^2 v(x', t)\right]\exp[-ik(x-x')]dx' = 0.\end{aligned} \tag{11}$$

An arbitrary perturbation can be represented as a superposition of the waves

$$\begin{aligned}v(x, t) &= V(Q, \Omega)\exp[i(Qx - \Omega t)],\\ w(x, t) &= W(Q, \Omega)\exp[i(Qx - \Omega t)]\end{aligned} \tag{12}$$

propagating with a wave vector **Q** and a frequency Ω along the Josephson junction. From Eqs. (11), we obtain the dispersion relation $\Omega = \Omega(Q)$ for these waves:

$$\begin{aligned}\tilde{\Omega}(\tilde{Q}) &= \frac{L\tilde{Q}\tilde{k}}{\pi\tilde{\omega}(\tilde{k})}J(\tilde{Q} + \tilde{k}) \pm \frac{1}{2\tilde{\omega}(\tilde{k})}\\ &\times\left[\tilde{\omega}^2(\tilde{Q} + \tilde{k}) - \tilde{\omega}^2(\tilde{k}) - \frac{2L}{\pi}\tilde{Q}\tilde{k}J(\tilde{Q} + \tilde{k})\right]^{1/2}\\ &\times\left[\tilde{\omega}^2(\tilde{Q} + \tilde{k}) - \tilde{\omega}^2(\tilde{k}) - \frac{2L}{\pi}\tilde{Q}\tilde{k}J(\tilde{Q} + \tilde{k}) - A^2\right]^{1/2}.\end{aligned} \tag{13}$$

Here, $\tilde{\Omega} = \Omega/\omega_J$, $\tilde{k} = 2k\lambda_{\text{eff}}$, $\tilde{Q} = 2Q\lambda_{\text{eff}}$, $\tilde{\omega} = \omega/\omega_J$, and $\tilde{\omega}(\tilde{k})$ is given by Eqs. (4) and (5). The time increment is defined as $\tilde{\gamma}(\tilde{Q}) = \text{Im}\tilde{\Omega}(\tilde{Q}) = \text{Im}\Omega(\tilde{Q})/\omega_J$.

Equation (13) always has a solution $\tilde{\Omega}(\tilde{Q}) = \text{Re}\tilde{\Omega}(\tilde{Q}) + i\text{Im}\tilde{\Omega}(\tilde{Q})$ with a positive imaginary part, for which small amplitude perturbations (12) with wave vector Q will increase in time with time increment $\gamma(Q)$. Therefore, modulation instability takes place for a wave of uniform amplitude with a shift in frequency defined by Eq. (8) and with the linear-approximation dispersion law given by Eq. (4). We note that the time increment $\gamma(Q)$, as calculated from Eq. (13), is determined by the linear-approximation spectrum (4) rather than by the derivative of the group velocity $\partial^2\omega(k)/\partial k^2$ as in [11].

3. For dispersionless waves characterized by spectrum (4) with $k = 0$, we have $\omega(k) \equiv \omega_J$ and dispersion relation (13) takes the form

$$\tilde{\Omega}(\tilde{Q}) = \pm i\frac{L^{1/2}}{2\pi^{1/2}}\tilde{Q}J^{1/2}(\tilde{Q})\left[A^2 - \frac{L}{\pi}\tilde{Q}^2 J(\tilde{Q})\right]^{1/2}. \tag{14}$$

This equation for the time increment of perturbations in combination with Eq. (5) has a positive solution $\tilde{\gamma}(\tilde{Q}) > 0$ in the wave-vector range $0 < \tilde{Q} < \tilde{Q}_B$. In this range, small amplitude perturbations (12) will increase with time; that is, the plane nonlinear electromagnetic wave (3) with spectrum $\tilde{\omega}(\tilde{k} \equiv 0) \equiv 1$ will exhibit modulation instability. In the wave-vector range $\tilde{Q} \geq \tilde{Q}_B$, we have $\tilde{\gamma}(\tilde{Q}) \equiv 0$ and the wave is stable. The wave vector $\tilde{Q}_B$ can be found from the equation

$$\tilde{Q}_B^2 J(\tilde{Q}_B) = \frac{\pi A^2}{2L}. \tag{15}$$

The maximum value of the time increment of perturbations is equal to

$$\tilde{\gamma}_{\max}(\tilde{Q}_m) = A^2/4 \tag{16}$$

and is reached at the wave vector $\tilde{Q}_m$ that is a root of the equation

$$\tilde{Q}_m^2 J(\tilde{Q}_m) = \frac{\pi A^2}{4L}. \quad (17)$$

The results obtained in this section support the results reported in [25].

4. The inclusion of dispersion of linear-approximation carrier waves (3) with spectrum (4) radically changes the dependence of the time increment $\tilde{\gamma}(\tilde{Q})$ on wave vector $\tilde{Q}$ and the wave-vector range over which $\tilde{\gamma}(\tilde{Q})$ is nonzero and positive. For dispersive waves with $k \neq 0$, the dispersion relation (13) in combination with Eq. (5) can be solved only numerically. In the wave-vector range where $2k\lambda_{\text{eff}} \approx 1$ and, hence, the spatial nonlocality is significant, numerical analysis in the case of $L \ll 1$ shows that the waves are stable over the ranges $0 \leq Q \leq Q_{B1}(k)$ and $Q \geq Q_{B2}(k, A, L)$ and are unstable over the range $Q_{B1}(k) < Q < Q_{B2}(k, A, L)$. The region of modulation instability is defined as the range of the wave vectors of small amplitude modulation within which the time increment of modulation $\tilde{\gamma}(\tilde{Q})$ is nonzero and positive.

Figure 1 shows the regions of modulation instability for fixed values of amplitude A and parameter L and four values of the reduced wave vector $\tilde{k}$. It can be seen from Fig. 1 that there is a unique possibility to control the region of modulation instability by varying the wave vector $\tilde{\mathbf{k}}$ [or the corresponding frequency $\tilde{\omega}(\tilde{k})$] of the carrier wave in the linear approximation. As this wave vector is increased, the region of instability shifts as a whole to larger values of $\tilde{Q}$. For this reason, modulation of dispersive waves (with $\tilde{k} \neq 0$) is always stable in the wave-vector range $0 \leq \tilde{Q} \leq \tilde{Q}_{B1}(k)$ of experimental interest.

Figure 2 shows the regions of modulation instability for fixed values of wave vector $\tilde{k}$ and amplitude A and four values of parameter L. It can be seen that, as the parameter L increases, the wave-vector $\mathbf{Q}$ range of modulation instability narrows and the maximum time increment slightly decreases.

Figure 3 shows the regions of modulation instability for fixed values of wave vector $\tilde{k}$ and parameter L and for values of amplitude A. It is seen that, as the amplitude A increases, the region of modulation instability becomes wider and the maximum time increment increases.

5. Thus, the nonlocality of the equation for the phase change is very significant for plane nonlinear dispersive waves with a uniform amplitude and with a nonlinear shift in frequency. First, a dispersive wave is stable against large-scale perturbations of the amplitude, which are of experimental interest. Second, there is a unique possibility to control the region of modulation instability by varying a dispersion parameter, namely, the wave vector $\mathbf{k}$ or frequency $\omega(k)$. This possibility is of great importance to experimental studies of such waves.

In studying Josephson junctions theoretically, it is important to keep in mind that the frequency $\omega(k)$ must not exceed a certain limiting value [26] determined by the band gap width $\Delta(T)$.

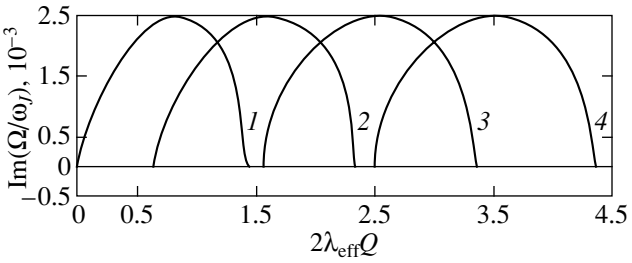

Fig. 1. Regions of modulation instability of plane dispersive nonlinear electromagnetic wave (8) for amplitude $A = 10^{-1}$, parameter $L = 10^{-2}$, and various values of reduced wave vector $\tilde{k}$: (*1*) 0, (*2*) 1, (*3*) 2, and (*4*) 3.

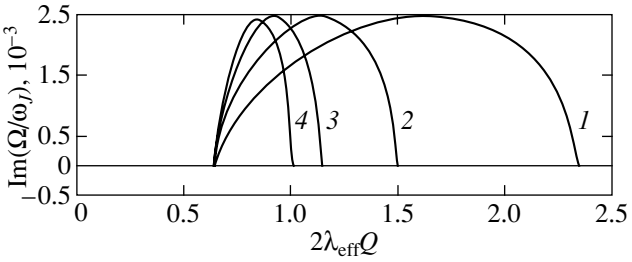

Fig. 2. Regions of modulation instability of plane dispersive nonlinear electromagnetic wave (8) for wave vector $\tilde{k} = 1$, amplitude $A = 10^{-1}$, and various values of parameter L: (*1*) 10^{-2}, (*2*) 2.5×10^{-2}, (*3*) 5×10^{-2}, and (*4*) 7.5×10^{-2}.

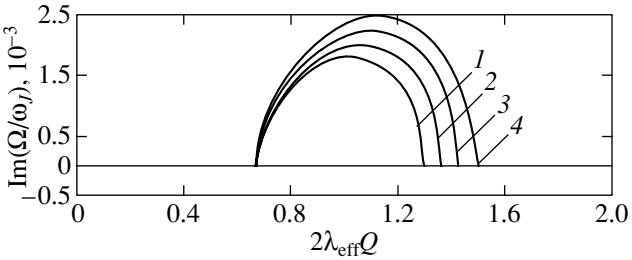

Fig. 3. Regions of modulation instability of plane dispersive nonlinear electromagnetic wave (8) for wave vector $\tilde{k} = 1$, parameter $L = 2.5 \times 10^{-2}$, and various values of amplitude A: (*1*) 0.85×10^{-1}, (*2*) 0.9×10^{-1}, (*3*) 0.95×10^{-1}, and (*4*) 10^{-1}.

Experimentally, modulation instability can be observed in long Josephson junctions consisting of ultrathin superconducting films when dispersive waves with a weakly modulated finite amplitude are excited in them. As the modulation instability develops, a dispersive plane nonlinear wave with a uniform amplitude and a nonlinear shift in frequency breaks up into a sequence of pulses (wave packets), whose repetition frequency is determined by the amplitude modulation period of the initial wave $L_0 = 2\pi/Q$, where the wave vector $\mathbf{Q}$ lies in the range $Q_{B1}(k) < Q < Q_{B2}(k, A, L)$. Since we have considered the case where there is no phase modulation and only amplitude modulation takes place, the wave packets will not undergo self-compression in this case.

The behavior of the regions of modulation instability of dispersive waves predicted in this paper may also be expected in Josephson junctions of bulk superconductors of thickness $d \gg \lambda$.

ACKNOWLEDGMENTS

The author is grateful to Yu.V. Medvedev and I.B. Krasnyuk for useful discussions and encouragement.

REFERENCES

1. V. I. Karpman, *Non-Linear Waves in Dispersive Media* (Nauka, Moscow, 1973; Pergamon, Oxford, 1975).
2. B. B. Kadomtsev, *Collective Phenomena in Plasmas* (Nauka, Moscow, 1976).
3. G. A. Askar'yan, Zh. Éksp. Teor. Fiz. **42** (6), 1567 (1962) [Sov. Phys. JETP **15**, 1088 (1962)].
4. V. I. Bespalov and V. I. Talanov, Pis'ma Zh. Éksp. Teor. Fiz. **3** (12), 471 (1966) [JETP Lett. **3**, 307 (1966)].
5. M. J. Lighthill, J. Inst. Math. Appl. **1** (2), 269 (1965); Proc. R. Soc. London, Ser. A **229** (1), 28 (1967).
6. A. Hasegawa, Opt. Lett. **9** (3), 288 (1984).
7. N. N. Akhmediev, V. M. Eleonskiĭ, and N. E. Kulagin, Izv. Vyssh. Uchebn. Zaved., Radiofiz. **31** (2), 244 (1988).
8. N. M. Ercolani, M. G. Forest, and D. W. McLaughkin, Lett. Appl. Math. **23** (1), 149 (1986).
9. M. Islam, *Ultra Fast Optical Devices* (Oxford Univ. Press, Oxford, 1993).
10. M. Alfimov, V. M. Eleonsky, and N. E. Kulagin, Chaos **2** (4), 454 (1992).
11. Yu. M. Aliev, V. P. Silin, and S. A. Uryupin, Sverkhprovodimost: Fiz., Khim., Tekh. **5** (2), 228 (1992).
12. A. Gurevich, Phys. Rev. B **46** (5), 3187 (1992).
13. Yu. M. Ivanchenko and T. K. Soboleva, Pis'ma Zh. Éksp. Teor. Fiz. **51** (2), 100 (1990) [JETP Lett. **51**, 114 (1990)].
14. Yu. M. Ivanchenko and T. K. Soboleva, Phys. Lett. A **147** (1), 65 (1990).
15. Yu. M. Ivanchenko and T. K. Soboleva, Fiz. Tverd. Tela (Leningrad) **32** (7), 2029 (1990) [Sov. Phys. Solid State **32**, 1181 (1990)].
16. R. G. Mints and I. B. Snapiro, Phys. Rev. B **51** (5), 3054 (1995).
17. A. I. Lomtev, Pis'ma Zh. Éksp. Teor. Fiz. **69** (2), 132 (1999) [JETP Lett. **69**, 148 (1999)].
18. A. I. Lomtev, Fiz. Tverd. Tela (St. Petersburg) **42** (1), 16 (2000) [Phys. Solid State **42**, 15 (2000)].
19. A. I. Lomtev, Zh. Tekh. Fiz. **70** (9), 63 (2000) [Tech. Phys. **45**, 1159 (2000)].
20. I. O. Kulik and I. K. Yanson, *Josephson Effect in Superconducting Tunnel Structures* (Nauka, Moscow, 1970).
21. Yu. E. Kuzovlev and A. I. Lomtev, Zh. Éksp. Teor. Fiz. **111** (5), 1803 (1997) [JETP **84**, 986 (1997)].
22. A. I. Lomtev, Zh. Éksp. Teor. Fiz. **113** (6), 2256 (1998) [JETP **86**, 1234 (1998)].
23. F. Kh. Abdullaev, Pis'ma Zh. Tekh. Fiz. **23** (2), 8 (1997) [Tech. Phys. Lett. **23**, 52 (1997)].
24. R. K. Dodd, J. C. Eilbeck, J. Gibbon, and H. C. Morris, *Solitons and Nonlinear Wave Equations* (Academic, New York, 1982; Mir, Moscow, 1988).
25. A. I. Lomtev, Pis'ma Zh. Tekh. Fiz. **29** (8), 72 (2003) [Tech. Phys. Lett. **29**, 342 (2003)].
26. A. I. Larkin and Yu. N. Ovchinnikov, Zh. Éksp. Teor. Fiz. **51** (5), 1535 (1966) [Sov. Phys. JETP **24**, 1035 (1967)].

Translated by Yu. Epifanov

Physics of the Solid State, Vol. 45, No. 12, 2003, pp. 2237–2241. Translated from Fizika Tverdogo Tela, Vol. 45, No. 12, 2003, pp. 2136–2140.

METALS AND SUPERCONDUCTORS

Anisotropy of the Heat Capacity of a Mixed-State Superconducting $Nd_{1.85}Ce_{0.15}CuO_4$ Single Crystal for Various Magnetic Field Orientations with Respect to the Crystallographic Axes

G. Kh. Panova*, A. A. Shikov*, N. A. Chernoplekov*, A. A. Zhokhov, A. N. Maljuk***, and C. T. Lin*****

**Russian Research Center "Kurchatov Institute", pl. Kurchatova 1, Moscow, 123182 Russia*
e-mail: shikov@isssph.kiae.ru
***Institute of Solid State Physics, Russian Academy of Sciences, Chernogolovka, Moscow oblast, 142432 Russia*
****Max-Planck-Institut für Festkörperforschung, Heisenbergstrasse 1, D-70569 Stuttgart, Germany*
Received May 16, 2003

Abstract—The anisotropy in the superconducting properties of single-crystal $Nd_{1.85}Ce_{0.15}CuO_4$ was studied from measurements of the heat capacity within the temperature interval 2–40 K in zero magnetic field and in a magnetic field of 8 T. We report on the first observation of heat capacity jumps occurring at the superconducting transition for various magnetic field orientations with respect to the crystallographic axes and on a strong anisotropy of the magnetic contribution to heat capacity in magnetic fields oriented in the *a*–*b* plane and perpendicular to it. These measurements yielded the anisotropy in the electronic heat capacity coefficient $\gamma_n(H)$ and in the superconducting transition temperature $T_c(H)$. The angular dependence of the Sommerfeld coefficient γ_n in the *a*–*b* plane observed in a magnetic field of 8 T exhibits four-lobe symmetry and zero gap direction of the order parameter. A comparison of the results obtained on the $Nd_{1.85}Ce_{0.15}CuO_4$ single crystal with the data available for $La_{1.85}Sr_{0.15}CuO_4$ permits one to conclude that the mechanisms of superconductivity in the electron- and hole-doped superconductors are similar. © *2003 MAIK "Nauka/Interperiodica".*

1. INTRODUCTION

Knowledge of the symmetry of the superconducting order parameter in high-temperature superconductors (HTSC) provides unique information on the mechanism of superconductivity. Although scientific literature abounds in statements that the symmetry of the superconducting order parameter in HTSCs has been fully established [1], the reason for the discrepancies observed between the results of various experiments remains unclear. All relevant experimental techniques can be judiciously divided into two classes, "volume sensitive" and "surface sensitive." The conclusion concerning the symmetry of a superconducting state can be obviously drawn only from volume-sensitive experiments, because on the surface this symmetry may turn out to be totally different for a number of reasons.

The angular dependence of the electrical resistivity $\rho(\theta)$ of the electronic superconductor $Nd_{1.85}Ce_{0.15}CuO_4$ in a magnetic field applied in the *a*–*b* plane was measured in [2]. It was found that $\rho(\theta)$ has a two-lobe anisotropy, with a sharp drop of the resistivity for fields directed along the [100] or [010] axes. The absence of four-lobe symmetry in the *a*–*b* plane was maintained as proof that the $Nd_{1.85}Ce_{0.15}CuO_4$ system does not have *d*-wave pairing symmetry. However, the angular dependence of the electrical resistivity $\rho(\theta)$ itself indicates the crystal symmetry only.

The actual symmetry of the superconducting order parameter can be judged only from the anisotropy of such superconducting properties as the upper critical magnetic field $H_{c2}(T)$, the superconducting transition temperature $T_c(H)$, and the Sommerfeld coefficient $\gamma_n(H)$. The anisotropy in the superconducting properties of single-crystal $Nd_{1.85}Ce_{0.15}CuO_4$ was studied by us earlier from the resistivity in the temperature interval 2–30 K measured in magnetic fields of 0, 1, 2, 4, and 6 T in the *a*–*b* plane [3]. Those measurements provided the first evidence of a strong anisotropy in $T_c(H)$ and $H_{c2}(T)$ for various magnetic-field orientations in the *a*–*b* plane, with a two-lobe symmetry of $T_c(H)$ and $H_{c2}(T)$ in this plane. The $T_c(H)$ and $H_{c2}(T)$ relations dropped to a minimum at an angle $\theta = 29°$ to the *a* axis, which defines the zero gap direction in the order parameter. The observed symmetry is apparently associated with a change in the local environment of the copper atoms, which brings about a lowering of symmetry from tetragonal to orthorhombic in the low-temperature region; this phenomenon has studied in considerable detail in [4–6] by using neutron diffraction on $Nd_{1.85}Ce_{0.15}CuO_4$ samples.

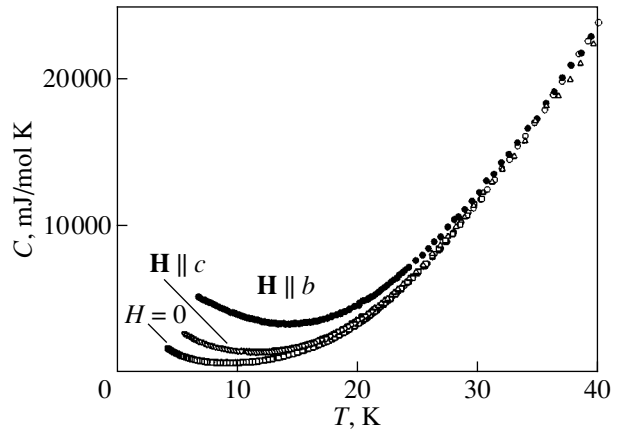

Fig. 1. Temperature dependence of the specific heat of single-crystal $Nd_{1.85}Ce_{0.15}CuO_4$ in the range 2–40 K measured in zero field and in a field of 8 T for two magnetic field directions, namely, in the *a*–*b* plane along the *b* axis and perpendicular to it, along the *c* axis.

Because a conclusion concerning the symmetry of the superconducting order parameter can be reached only from an analysis of volume-sensitive experiments, measurements of the heat capacity appear to be of particular interest in this respect. The fact that the heat capacity is a volume thermodynamic characteristic of a substance makes its measurement an important direct method of probing the properties of superconductors, because it offers the possibility of obtaining information that can be compared unambiguously with various theoretical models.

The low-temperature course of various thermodynamic and transport properties depends on the behavior of the density of states of the electronic quasiparticle energy spectrum of a superconductor near the Fermi surface. Because of the presence of zeroes in the order parameter, the $N(E)$ function changes radically within a narrow energy interval in the vicinity of E_F for a superconductor in a mixed state ($H_{c1} < H < H_{c2}$); this is what gives rise to temperature anomalies in the properties of a superconductor. In this connection, studies of the anisotropy in the electronic density of states for various magnetic field orientations relative to the crystallographic axes are of particular interest, because features in the temperature and field dependences of the heat capacity are very important criteria for the nontrivial nature of the superconducting energy gap. Unfortunately, this anisotropy is confined to the region of low temperatures and high magnetic fields and is difficult to probe experimentally. The presence of magnetic contributions to the heat capacity adds to the challenge of revealing this anisotropy.

The purpose of this study was to determine the symmetry of the superconducting order parameter from measurements of the field and temperature dependences of the heat capacity of a high-quality bulk superconducting $Nd_{1.85}Ce_{0.15}CuO_4$ single crystal at temperatures from 2 to 40 K and in a magnetic field of 8 T.

2. PREPARATION OF SAMPLES AND THEIR CHARACTERIZATION

The $Nd_{1.85}Ce_{0.15}CuO_4$ single crystal to be studied was prepared by crucibleless floating-zone melting with radiative heating [7]. A four-mirror furnace (Crystal System Inc., Japan) with 300-W lamps was employed. The starting materials for the feeding rod and solvent were Nd_2O_3, CuO, and CeO_2 powders of 99.9–99.99% purity. The crystal was grown at an oxygen pressure of 0.08 atm and a growth rate of 0.4–0.8 mm/h along the *a* axis of the $(NdCe)_2CuO_4$ seed crystal. During the growth, the feeding rod and the growing crystal were rotated in opposite senses at a rate of 20–30 rpm to ensure efficient mixing and uniformity of the temperature distribution in the melt zone. The melt zone temperature was controlled with high precision by properly adjusting the lamp current.

The sample thus grown was checked for composition and uniformity by ICP-OES spectroscopy (inductively coupled plasma), electron probe microanalysis (EPMA, Cameca SX100), and x-ray powder diffraction (XRD, Philips PW-3710).

The $Nd_{1.85}Ce_{0.15}CuO_4$ single crystal obtained was 30–40 mm long and 5 mm in diameter and was nonsuperconducting. X-ray powder diffraction did not reveal any foreign inclusions. Optical polarization microscopy confirmed the absence of any other crystallites in the 10- to 20-mm-long end part of the crystal. EPMA measurements likewise showed Ce to be distributed uniformly both along and perpendicular to the growth axis.

The $Nd_{1.85}Ce_{0.15}CuO_4$ single crystal was found to be superconducting after annealing in a flow of pure argon (99.99% purity) at 1030°C for 10–20 h. This heat treatment produced a superconducting single crystal with T_c = 21–22 K and a transition width $\Delta T_c \sim 0.3$ K.

The sample heat capacity in a magnetic field of 8 T was measured in an adiabatic calorimeter with pulsed heating [8]. The experimental error in determining the heat capacity was 2% in the temperature interval 2–4 K, 1% in the range from 4 to 10 K, and 0.2–0.5% in the 10- to 40-K region. The superconducting transition temperature was determined from a jump in the heat capacity. The transitions were sharp, which attests to a high quality of the single crystal.

3. EXPERIMENTAL RESULTS AND DISCUSSION

Figure 1 presents the temperature dependence of the specific heat of the $Nd_{1.85}Ce_{0.15}CuO_4$ single crystal in the range 2–40 K measured without a magnetic field and at 8 T for two field application directions: in the *a*–*b* plane along the *b* axis and perpendicular to it, along the *c* axis. $Nd_{1.85}Ce_{0.15}CuO_4$ is a magnetic superconductor in which the superconductivity and antiferromagnetic order of Nd^{3+} magnetic moments coexist. At low temperatures, the specific heat is observed to increase strongly, which is assigned to a Schottky anomaly asso-

ciated with the Nd^{3+} ground-state doublet being split by the molecular field. Although the electronic system and the lattice contribute to the specific heat in the low-temperature region, they are substantially smaller than the magnetic contribution. A magnetic field gives rise to a highly anisotropic behavior of the specific heat; indeed, the specific heat was found to be least affected by a field applied parallel to the *c* axis, whereas application of a field along the *b* axis produced a strong growth of the specific heat associated with the shift of the Schottky anomaly toward higher temperatures. These heat capacity measurements in magnetic fields confirm the complex magnetic properties of the electron-doped $Nd_{1.85}Ce_{0.15}CuO_4$ compound, which originate from the influence of the magnetic field on the ground-state doublet splitting of the Nd^{3+} ion and provide additional information on the effect of magnetic order, as well as on magnetic coupling, in this compound. The observed strong anisotropy of the specific heat in a magnetic field for **H** ∥ *b* and **H** ∥ *c* is intimately connected with the antiferromagnetic order in the CuO_2 plane and ferromagnetic order along the *c* axis.

Figure 2 displays the temperature behavior of the specific heat of the $Nd_{1.85}Ce_{0.15}CuO_4$ single crystal near T_c obtained in zero magnetic field and at 8 T for four magnetic field directions, namely, along the *a*, *b*, and *c* axes and at a canting angle of 29° to the *a* axis. The latter orientation defines the zero energy gap direction, which was derived by us earlier from resistivity measurements made on $Nd_{1.85}Ce_{0.15}CuO_4$ [3]. To reveal a jump in the specific-heat $C(T)$ temperature dependence, which varies in curvature, the experimental data obtained in the region of the superconducting transition were constructed in various coordinate frames linearizing the original dependence. Despite the low electronic density of states combined with a large magnetic contribution to the specific heat, the temperature dependence of the specific heat exhibited jumps corresponding to the superconducting transition. A magnetic field affects the specific heat by reducing the amplitude of the jump and by shifting it toward lower temperatures. Our results show that the specific-heat jumps and their shift corresponding to the superconducting transition differ strongly in a magnetic field. The smallest shift of T_c is observed with the field directed along the *b* axis, and the largest shift, when the field is canted at 29° to the *a* axis.

The magnitude of the specific-heat jump $\Delta C/T_c$ at the superconducting transition is known to be related to renormalization of the electronic density of states $N(E)$ at the Fermi surface. Estimation of the Sommerfeld coefficient γ_n for $Nd_{1.85}Ce_{0.15}CuO_4$ made using the BCS expression $\Delta C/T_c = 1.43\gamma_n$ yields $\gamma_n = 2.3$ mJ/mol K² in the absence of a magnetic field; in a magnetic field of 8 T, we obtained $\gamma_n = 1.9$ mJ/mol K² for **H** ∥ *a*, $\gamma_n = 2.0$ mJ/mol K² for **H** ∥ *b*, $\gamma_n = 0.9$ mJ/mol K² for the field canted at 29° to the *a* axis, and $\gamma_n = 1.7$ mJ/mol K² for **H** ∥ *c*. The Sommerfeld coefficient γ_n for the $La_{1.85}Sr_{0.15}CuO_4$ single crystal is substantially larger:

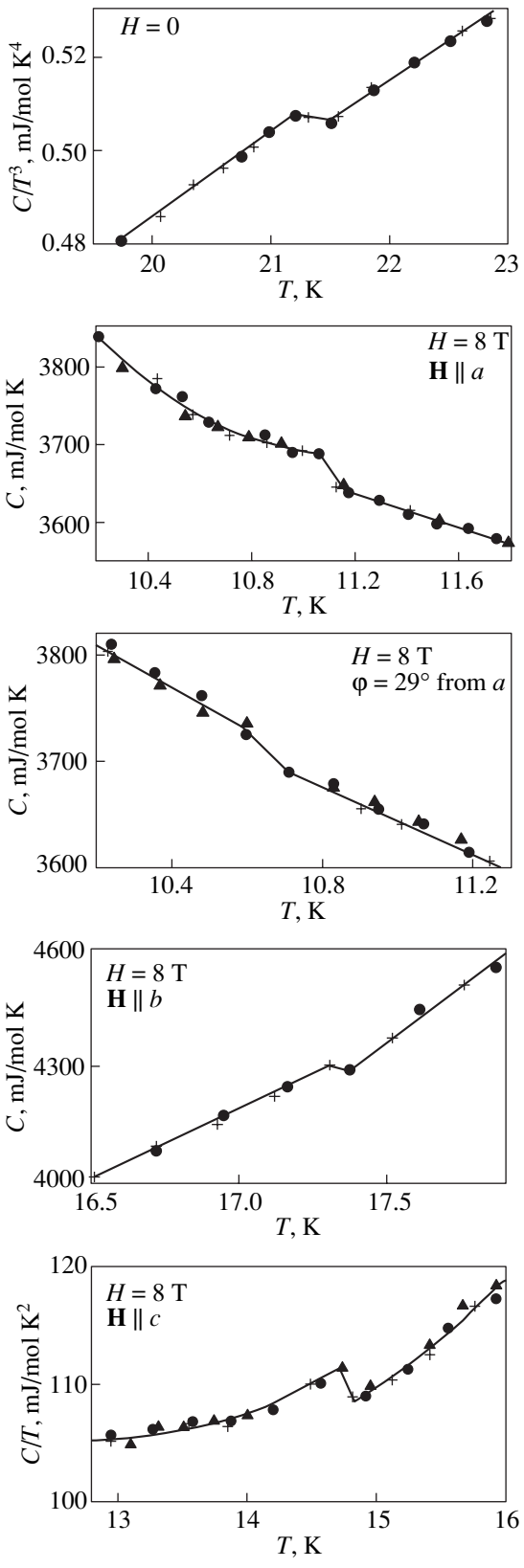

Fig. 2. Temperature dependence of the specific heat obtained near T_c measured in zero field and in a field of 8 T for four magnetic field directions, more specifically, along the *a*, *b*, *c* axes, and at 29° to the *a* axis.

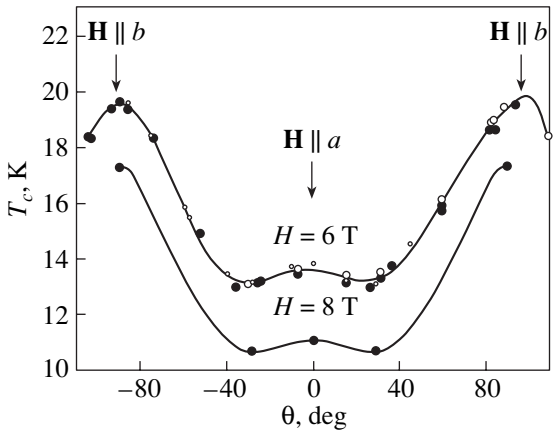

Fig. 3. Angular dependences of the superconducting transition temperature $T_c(\theta)$ in the *a*–*b* plane in a magnetic field of 8 T derived from heat capacity measurements and, for comparison, from our electrical-resistivity measurements [3] made in a magnetic field of 6 T.

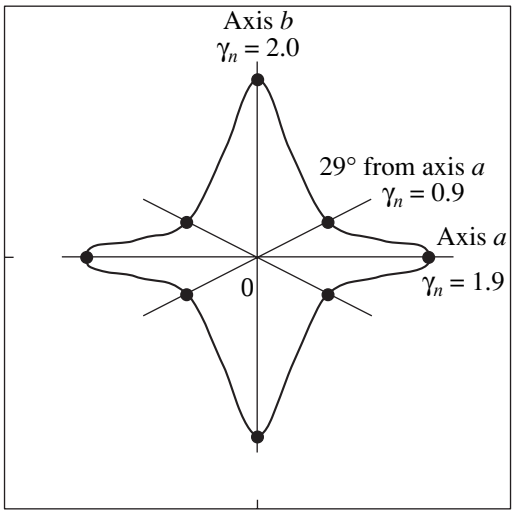

Fig. 4. Angular dependence of the Sommerfeld coefficient γ_n (mJ/mol K^2) measured in the *a*–*b* plane in a magnetic field of 8 T.

γ_n = 9 mJ/mol K^2 [9]. A comparison of these data shows that the specific-heat jumps $\Delta C/T_c$ at the superconducting transition and, hence, γ_n for $Nd_{1.85}Ce_{0.15}CuO_4$ are substantially smaller than those for $La_{1.85}Sr_{0.15}CuO_4$. This implies that the effective mass of carriers in an electron-doped system is far smaller than that in a hole-doped one.

Figure 3 shows the angular dependence of the superconducting temperature $T_c(\theta)$ obtained in the *a*–*b* plane in a magnetic field 8 T, together with the results derived by us earlier from measurements of the resistivity of $Nd_{1.85}Ce_{0.15}CuO_4$ made at 6 T and reported in [2]. The $T_c(\theta)$ curve passes through a maximum at $\theta = 90°$ (**H** || *b*) and then drops with decreasing θ; for $\theta = 0°$ (**H** || *a*), we have $T_c(90°)/T_c(0°) = 1.6$. $T_c(\theta)$ has a minimum at $\theta = 29°$ to the *a* axis; this angle identifies the zero energy gap direction. The results obtained provide supportive evidence for a strong angular dependence of the superconducting transition temperature $T_c(\theta)$ in the *a*–*b* plane in a magnetic field of 8 T, which was observed by us earlier when measuring the resistivity of $Nd_{1.85}Ce_{0.15}CuO_4$, and for the zero energy gap direction.

By estimating the Sommerfeld coefficient γ_n using BCS theory for $Nd_{1.85}Ce_{0.15}CuO_4$ from the specific-heat jump $\Delta C/T_c$ at the superconducting transition, which was measured in a magnetic field of 8 T for various magnetic field orientations in the *a*–*b* plane with respect to the crystallographic axes, we constructed the map of the angular dependence of γ_n displayed in Fig. 4. We readily see that the electronic density of states in the *a*–*b* plane is highly anisotropic, with a minimum reached at a magnetic field direction canted at 29° to the *a* axis and with a maximum at a field directed along the *b* axis. The observed difference in the magnitude of γ_n between the field orientations along the *a* and *b* axes confirms the lattice orthorhombicity associated with the change in the local symmetry of the copper atom environment, which brings about its lowering from tetragonal to orthorhombic in the low-temperature region. The strong anisotropy of γ_n observed for various magnetic field orientations in the *a*–*b* plane is characterized by a four-lobe symmetry of γ_n, in which the lowest electronic density of states for the magnetic field canted at 29° to the *a* axis determines the zero energy gap direction in the order parameter. This behavior of γ_n gives us grounds to maintain that the $Nd_{1.85}Ce_{0.15}CuO_4$ superconducting single crystal has d^{22}_{x-y} symmetry.

A comparison of these data with our earlier results obtained on a $La_{1.85}Sr_{0.15}CuO_4$ single crystal [9] reveals a similar pattern of the superconducting order parameter symmetry in the electronic superconductors. The observed difference between the zero superconducting gap directions should be assigned to specific structural features, and the four-lobe pattern of symmetry in the electronic density of states in the *a*–*b* plane may be considered a direct indication of the order parameter in the two superconductors having d^{22}_{x-y} symmetry.

4. CONCLUSIONS

Thus, our studies of the heat capacity of an $Nd_{1.85}Ce_{0.15}CuO_4$ single crystal made in the range 2–40 K, both in a magnetic field of 8 T and without it, with the field oriented along various crystallographic directions permit the following conclusions.

(1) Measurements of the temperature dependence of the heat capacity in a magnetic field has revealed (despite the low electronic densities of states and large magnetic contribution to the heat capacity) heat capac-

ity jumps corresponding to the superconducting transition.

(2) A strong anisotropy of the magnetic contribution to the heat capacity was observed to exist with the magnetic field oriented in the *a–b* plane along the *b* axis and perpendicular to it, along the *c* axis, which should be assigned to antiferromagnetic order in the CuO_2 plane and ferromagnetic ordering along the *c* axis.

(3) Measurements performed for various magnetic field orientations in the *a–b* plane revealed a strong anisotropy in the Sommerfeld coefficient $\gamma_n(H)$ characterized by a four-lobe γ_n symmetry of and a zero order-parameter gap direction. This behavior gives us grounds to conclude that superconducting single-crystal $Nd_{1.85}Ce_{0.15}CuO_4$ has d^{22}_{x-y} symmetry.

(4) A comparison of the results obtained on $Nd_{1.85}Ce_{0.15}CuO_4$ with the earlier measurements performed on single-crystal $La_{1.85}Sr_{0.15}CuO_4$ suggests that superconductivity in electron- and hole-doped superconductors operates through similar mechanisms.

(5) Our studies yielded qualitative estimates for a number of parameters of importance for the development of theory and relevant concepts concerning the order-parameter symmetry in HTSCs and the mechanism of superconductivity.

ACKNOWLEDGMENTS

This study was supported by the Ministry of Industry, Science, and Technology of the Russian Federation within the federal program “Research in Topical Areas of Science and Technology” (subprogram “Fundamental Studies in Physical Sciences”).

REFERENCES

1. Yu. A. Izyumov, Usp. Fiz. Nauk **169** (3), 225 (1999) [Phys. Usp. **42**, 215 (1999)].
2. S. Haraguchi, T. Naito, H. Iwasaki, *et al.*, Physica C (Amsterdam) **378–381**, 265 (2002).
3. G. Kh. Panova, A. A. Shikov, N. A. Chernoplekov, *et al.*, Pis’ma Zh. Éksp. Teor. Fiz. **75** (11), 699 (2002) [JETP Lett. **75**, 579 (2002)].
4. V. I. Voronin, A. E. Kar’kin, B. N. Goshchitskiĭ, *et al.*, Fiz. Tverd. Tela (St. Petersburg) **40** (2), 177 (1998) [Phys. Solid State **40**, 157 (1998)].
5. S. J. L. Billinge and T. Egami, Phys. Rev. B **47**, 14386 (1993).
6. K. Kurahashi, H. Matsushita, M. Fujita, and K. Yamada, J. Phys. Soc. Jpn. **71** (3), 910 (2002).
7. C. T. Lin, A. Maljuk, and B. Liang, Supercond. Sci. Technol. **15**, 1736 (2002).
8. M. N. Khlopkin, N. A. Chernoplekov, and P. A. Cheremnykh, Preprint No. IAÉ-3549/10, IAÉ (Inst. of Atomic Energy, Moscow, 1982).
9. G. Kh. Panova, A. A. Shikov, M. N. Khlopkin, *et al.*, Physica C (Amsterdam) **334**, 25 (2000).

Translated by G. Skrebtsov

Physics of the Solid State, Vol. 45, No. 12, 2003, pp. 2242–2248. Translated from Fizika Tverdogo Tela, Vol. 45, No. 12, 2003, pp. 2141–2146.

SEMICONDUCTORS AND DIELECTRICS

Effect of Lattice Deformation and Phase Transitions on the Electronic Spectra of $TlGaS_2$, $TlGaSe_2$, and $TlInS_2$ Layered Semiconductors

T. G. Mamedov[1] and R. A. Suleĭmanov[1, 2]

[1]*Institute of Physics, National Academy of Sciences of Azerbaijan, pr. Dzhavida 33, Baku, 370143 Azerbaijan*
e-mail: mamedov-tofig@azdata.net
[2]*Rasul-Zade State University, ul. Khalilova 23, Baku, 370148 Azerbaijan*
e-mail: rauf_suleymanov@aznetmail.com
Received November 11, 2002

Abstract—The effect of the lattice deformation on the electronic spectra of $TlGaS_2$, $TlGaSe_2$, and $TlInS_2$ layered semiconductor crystals is analyzed. It is shown that changes in the band gap of these semiconductors due to thermal expansion and a change in the composition under hydrostatic or uniaxial pressure can be described within a unified model of the deformation potential. The main feature of this model is the inclusion of deformation potentials with different signs, which is characteristic of other semiconductors with a layered structure. An analysis of the lattice deformation of the studied semiconductors in terms of the proposed model of the deformation potential has revealed that, in the immediate vicinity of the phase transitions, the crystal lattice under pressure undergo an unusual deformation. © *2003 MAIK "Nauka/Interperiodica"*.

1. INTRODUCTION

Semiconductors $TlGaS_2$, $TlGaSe_2$, and $TlInS_2$ crystallize in a layered structure and, according to the data available in the literature, have a monoclinic lattice at room temperature and atmospheric pressure [1–5]. The unit cell parameters of these crystals are such that they can be treated as crystals belonging to the quasi-tetragonal crystal system. Moreover, since anisotropy is absent in the plane of layers, the elastic and thermal properties of these materials can be described in terms of the relationships used in elasticity theory that are valid for hexagonal symmetry [6, 7]. For crystals of this family, most attention has been concentrated on the study of the phase transitions. At present, it has been reliably established that, as the temperature decreases from room temperature, $TlInS_2$ and $TlGaSe_2$ crystals transform initially into an incommensurate phase ($T_i \approx$ 216 K for $TlInS_2$ and $T_i \approx 120$ K for $TlGaSe_2$) and then into a commensurate ferroelectric phase ($T_c \approx 202$ K for $TlInS_2$ and $T_c \approx 107$ K for $TlGaSe_2$) with quadrupling of the unit cell along the C axis [8, 9]. An analysis of the influence of hydrostatic pressure on different physical properties of the studied crystals has demonstrated that phase transitions can occur under pressure [10–15]. The behavior of physical parameters upon phase transitions with a change in the pressure and temperature has been investigated in many works (see, for example, [3, 5–17]). However, despite the large amount of available data on the optical properties near the fundamental absorption edge and the results of band-structure calculations [11, 14, 16–18], the effect of external factors on the electronic band structure of the above semiconductors is not clearly understood. In this respect, the main objective of the present work was to construct a model of deformation phenomena in $TlGaS_2$, $TlGaSe_2$, and $TlInS_2$ layered crystals. This model made it possible not only to obtain new data on the specific features of the electronic structure but also to gain better insight into the mechanisms of the deformation observed in $TlInS_2$ and $TlGaSe_2$ crystals with a change in the temperature and pressure.

2. MODEL OF THE DEFORMATION POTENTIAL IN $TlGaS_2$, $TlGaSe_2$, AND $TlInS_2$ LAYERED SEMICONDUCTORS

First and foremost, we summarize the results of earlier investigations into the influence of the lattice deformation on the electronic spectra of $TlGaS_2$, $TlGaSe_2$, and $TlInS_2$ layered semiconductor crystals (for brevity, hereafter, they will be referred to as $Tl\mathit{MeX}_2$ layered crystals).

2.1. Abdullaeva *et al.* [19] revealed that the temperature dependence of the exciton energy of $TlGaS_2$ exhibits unusual behavior. In particular, it was found that the peak observed in the exciton energy shifts toward the high-energy range with an increase in the temperature over a wide range (from 4.2 to 200 K, i.e., until the peak of the exciton energy is recorded in the absorption spectra). In this temperature range, the shift in the exciton energy was approximately equal to 50 meV (Fig. 1).

It was assumed that the above behavior of the exciton energy is associated with the contribution of the lat-

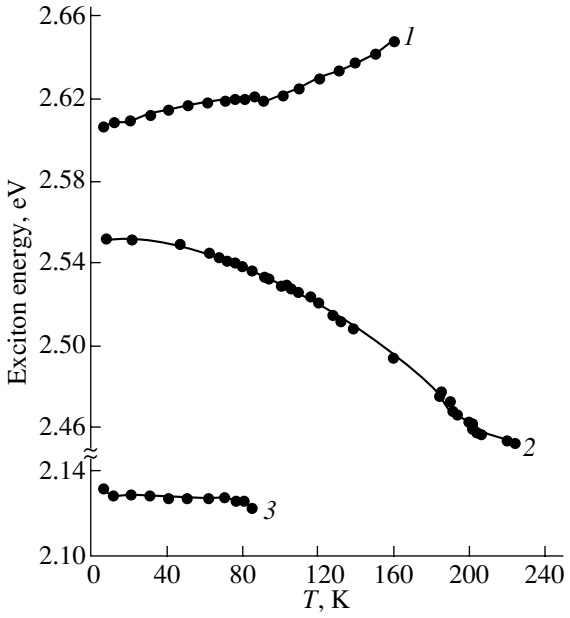

Fig. 1. Temperature dependences of the exciton energy for (*1*) $TlGaS_2$ [19], (*2*) $TlInS_2$ [16], and (*3*) $TlGaSe_2$ [19] crystals.

tice deformation to the change in the band gap E_g. Hence, the inference was drawn that the thermal expansion of $TlGaS_2$ makes a dominant contribution to the change in the band gap E_g with a variation in the temperature. Figure 2 depicts the temperature dependences of the linear thermal expansion coefficient along the directions parallel ($\alpha_\parallel$) and perpendicular ($\alpha_\perp$) to the plane of layers in $TlGaS_2$, $TlGaSe_2$, and $TlInS_2$ layered crystals [20–22]. As can be seen from Fig. 2, all three crystals are characterized by a considerable thermal expansion, especially along the direction perpendicular to the layer plane. The temperature dependence of the thermal expansion coefficient $\alpha_\parallel(T)$ along the layer plane of the $TlGaSe_2$ crystal at low temperatures ($T <$ 100 K) differs significantly from those of the $TlGaS_2$ and $TlInS_2$ crystals. The peaks observed in the curves $\alpha_\perp(T)$ and $\alpha_\parallel(T)$ correspond to the temperatures of the aforementioned phase transitions.

It is worth noting that the contribution of the thermal expansion to the change in the band gap E_g with variations in the temperature of $TlGaS_2$ differs substantially from those of $TlGaSe_2$ and $TlInS_2$. Even with allowance made for the fact that the dependence $\alpha_\parallel(T)$ of $TlGaSe_2$ exhibit a different behavior, the temperature dependences of the band gap E_g for $TlGaSe_2$ and $TlInS_2$ differ radically from that for $TlGaS_2$ (Fig. 1). At first glance, this difference casts some doubt on the similarity between the band structures of $Tl\mathit{MeX}_2$ layered crystals or, at least, the similarity between the deformation effects in them. However, as will be shown below, this assumption is erroneous: at temperatures at which all three crystals have an identical crystal structure, their band structures are similar to each other and can be

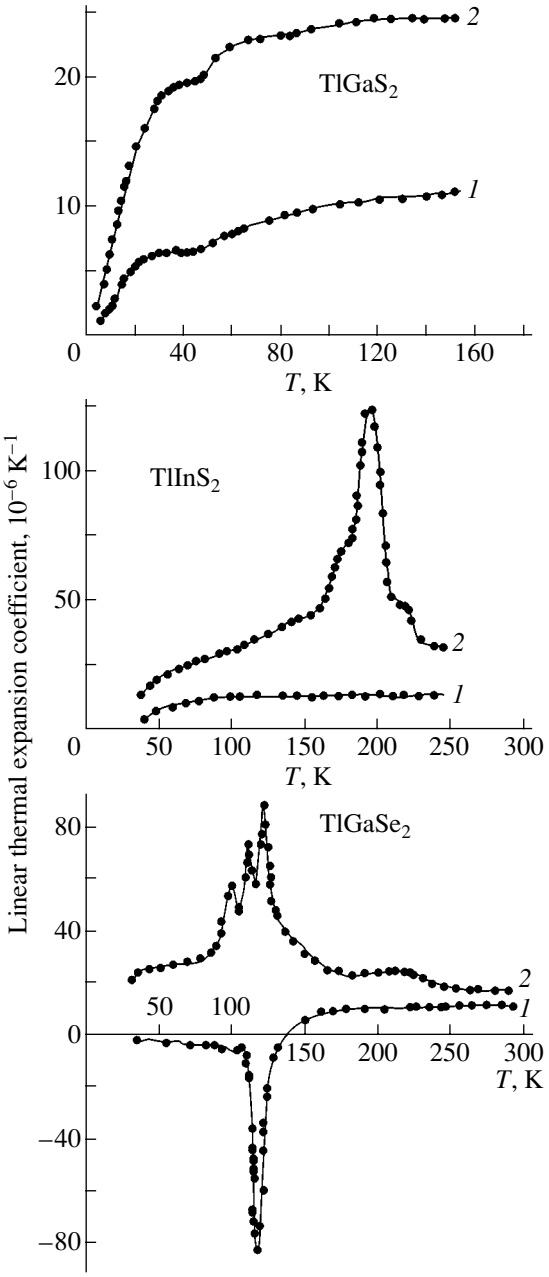

Fig. 2. Temperature dependences of the linear thermal expansion coefficient along the directions (*1*) parallel and (*2*) perpendicular to the layer plane of $TlGaS_2$, $TlInS_2$, and $TlGaSe_2$ crystals [20–22].

described by similar deformation potentials. The difference in the behavior of the dependence $E_g(T)$ in the low-temperature range is explained by the fact that, unlike the $TlGaS_2$ crystal, the $TlGaSe_2$ and $TlInS_2$ crystals undergo phase transitions with a decrease in the temperature.

2.2. Allakhverdiyev *et al.* [11] investigated the influence of hydrostatic pressure on the optical absorption edge for all three crystals at room temperature. The behavior of the pressure coefficient of the band gap

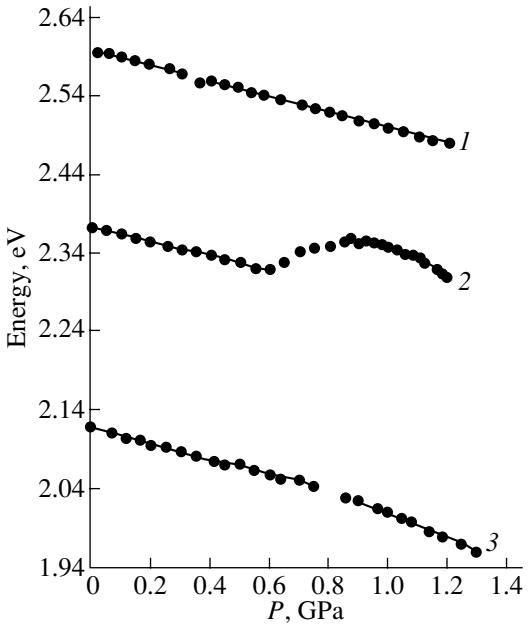

Fig. 3. Dependences $E(P)_{\alpha = \text{const}}$ for (*1*) $TlGaS_2$, (*2*) $TlInS_2$, and (*3*) $TlGaSe_2$ crystals at T = 300 K for absorption coefficients α = (*1*) 600, (*2*) 180, and (*3*) 270 cm^{-1} [11].

dE_g/dP was examined by considering the dependence $E(P)_{\alpha = \text{const}}$ constructed from the absorption edge spectra at different absorption coefficients α. It was demonstrated that, at low pressures ($P < 0.5$ GPa), the pressure coefficients dE_g/dP for all three crystals are negative in sign (Fig. 3), which is typical of all crystals with a layered structure [23]. However, as the pressure increases, the behavior of the pressure coefficient dE_g/dP becomes different. With an increase in the pressure, the pressure coefficient dE_g/dP for the $TlInS_2$ crystal changes sign from negative to positive in the range close to $P \approx 0.59$ GPa (Fig. 3), remains positive to $P \approx$ 0.9 GPa, and again changes sign from positive to negative but considerably increases in magnitude: $dE_g/dP \approx -22.0 \times 10^{-11}$ eV Pa^{-1} at $P > 0.9$ GPa and $dE_g/dP \approx -8.5 \times 10^{-11}$ eV Pa^{-1} at $P < 0.5$ GPa.

For the $TlGaSe_2$ crystal, the pressure coefficient $dE_g/dP \approx -12.5 \times 10^{-11}$ eV Pa^{-1} remains constant to $P \approx$ 0.92 GPa and then drastically increases in magnitude ($dE_g/dP \approx -20.0 \times 10^{-11}$ eV Pa^{-1}) without changing sign. For the $TlGaS_2$ crystal, the pressure coefficient $dE_g/dP \approx -7.26 \times 10^{-11}$ eV Pa^{-1} remains virtually unchanged over the entire pressure range under investigation.

According to [14, 15], the drastic changes in the pressure coefficient of the $TlInS_2$ and $TlGaSe_2$ crystals are accompanied by thermal effects. This indicates that phase transitions can occur in these crystals under pressure.

Attempts to interpret the experimental data on the effect of pressure on the band structure and to explain such different pressure dependences of the pressure coefficient for the $TlGaS_2$, $TlInS_2$, and $TlGaSe_2$ crystals have failed because of the lack of information on the deformation potentials for $TlGaSe_2$-type layered crystals.

2.3. Guseynov *et al.* [24] studied the effect of uniaxial pressure applied perpendicularly to the layer plane on the exciton spectra of $TlGaS_2$ and $TlGaSe_2$ semiconductors at low temperatures (4.2–100 K). It was shown that, for both semiconductor crystals, the pressure coefficient $dE_g/dP \approx -3 \times 10^{-11}$ eV Pa^{-1} does not depend on the temperature, as is the case with III–VI semiconductors with a layered structure (GaSe, GaS, InSe) [23].

The above results demonstrate that the deformation effects revealed in $Tl\mathit{MeX}_2$ layered crystals have both common and specific features. In this paper, we propose a model of the deformation potential that makes it possible, within a unified approach, to describe the deformation effects in all the three crystals under consideration and to elucidate the reasons for the observed differences.

In order to describe the change in the band gap E_g under deformation, we introduce two deformation potentials, namely, $D_\parallel$ and $D_\perp$. In this case, the change in the band gap E_g under deformation can be represented in the form

$$\Delta E_g = D_\perp U_\perp + 2D_\parallel U_\parallel, \quad (1)$$

where $U_\perp$ and $U_\parallel$ are the strains along the directions perpendicular and parallel to the crystal layers, respectively. In the framework of this simple model, Belen'kiĭ *et al.* [23] described the entire set of deformation effects in III–VI semiconductors with a layered structure and revealed the specific features of the effects associated with the layered structure.

The deformation potentials $D_\parallel$ and $D_\perp$ can be determined from the results of at least two deformation experiments. In the first experiment, we examined how the hydrostatic pressure affects the band gap E_g. It is important to keep in mind that the available data on the effect of uniaxial pressure on the band gap E_g at low temperatures cannot be used in this case because the pressure coefficients of the band gap for layered crystals strongly depend on the temperature [23]. Furthermore, even the change in sign of the pressure coefficient dE_g/dP with a variation in the temperature is observed for GaSe, GaS, and InSe layered crystals. As will be shown below, these features are also typical of $Tl\mathit{MeX}_2$ crystals. Consequently, the low-temperature (T = 4.2 K) deformation potentials can substantially differ from the high-temperature (T = 300 K) deformation potentials.

As was already mentioned, the main objective of the present work was to construct a unified model of the deformation potential for all three crystals. For this purpose, we estimated the deformation potentials $D_\parallel$ and $D_\perp$ from the experimental data on the effect of hydrostatic pressure on the optical absorption edge for $TlInS_2$

Lattice parameters and elastic constants of $TlGaS_2$, $TlGaSe_2$, and $TlInS_2$ crystals

Crystal	Lattice parameters, Å [1–3]			Elastic constants, 10^{10} Pa [6]			
	a	b	c	C_{11}	C_{12}	C_{33}	C_{44}
$TlGaS_2$	10.29	10.29	15.28	–	–	–	–
$TlGaSe_2$	10.77	10.77	15.64	6.42	3.88	4.37	0.5
$TlInS_2$	10.95	10.95	15.14	4.49	3.05	3.99	0.5

and $TlGaSe_2$ layered semiconductor crystals under the assumption that the values of $D_\parallel$ and $D_\perp$ for these crystals are equal to each other, respectively. In this case, we took into account that the elastic constants C_{ij} (see table) and their temperature dependences [6] are known for these two crystals.

It should be noted, for the $TlInS_2$ crystal, the absorption edge is governed by direct transitions. For the $TlGaSe_2$ crystal, according to the data obtained in a number of works, indirect transitions also contribute to the absorption edge. However, as was shown in [19], no indirect transitions are observed in the geometry used in the experiment on the influence of hydrostatic pressure on the absorption edge for the $TlGaSe_2$ crystal. Therefore, the pressure coefficients chosen in our case for the $TlInS_2$ and $TlGaSe_2$ crystals correspond to direct transitions. After simple calculations, we obtained the following deformation potentials: $D_\parallel = -7.3$ eV and $D_\perp = 11.9$ eV. As was noted above, the strains $U_\parallel$ and $U_\perp$ can be determined from the relationships used in elasticity theory that are valid for crystals of hexagonal symmetry; that is,

$$U_\perp = -\frac{C_{11} + C_{12} - 2C_{13}}{(C_{11} + C_{12})C_{33} - 2C_{13}^2}P,$$
$$U_\parallel = -\frac{C_{33} - C_{13}}{(C_{11} + C_{12})C_{33} - 2C_{13}^2}P. \quad (2)$$

For our calculations, it is necessary to know the elastic constants C_{13} of the $TlInS_2$ and $TlGaSe_2$ crystals, which are not available in the literature, because the experimental determination of these constants for layered crystals presents considerable difficulties. The influence of the elastic constant C_{13} on the physical properties of the $TlInS_2$ and $TlGaSe_2$ crystals will be discussed below. Here, we only note that, at low pressures and room temperature, the value of C_{13} is nearly identical for all layered crystals [23]. In our calculations, this constant was taken to be $C_{13} = 1.5 \times 10^{10}$ Pa.

Let us now attempt to describe the results of other deformation experiments in terms of the deformation potentials derived above. First, we evaluate the contribution of the thermal expansion to the change in the band gap E_g with a variation in the temperature. We will restrict our consideration to the temperature range 4.2–100 K by assuming that the contribution of the electron–phonon interaction in this range is insignificant. According to the estimates, the thermal expansion of the $TlGaS_2$ crystal due to an increase in the temperature should lead to an increase in the band gap E_g by $\approx$20 meV, which is in good agreement with the experimental data. For the $TlGaSe_2$ crystal, the shift in the band gap E_g should be approximately equal to +25 meV, because the thermal expansion in the layer plane is not very large in the temperature range covered. For the $TlInS_2$ crystal, the calculation gives $\Delta E_g \approx$ +25 meV. Thus, the calculated changes in the band gap E_g for the last two crystals differ significantly from the experimental values. However, it can be shown that this disagreement is unrelated to the error in determining the deformation potentials $D_\parallel$ and $D_\perp$. Indeed, as the temperature decreases, the $TlGaSe_2$ and $TlInS_2$ crystals undergo a transformation into the ferroelectric phase at temperatures of 107 and 202 K, respectively. As a result, these crystals, unlike the $TlGaS_2$ crystal, are in the ferroelectric phase in the temperature range 4.2–100 K. Abdullaeva *et al.* [19] demonstrated that, upon substitution of S for only 10% Se in $TlGaSe_2$, the temperature behavior of the band gap E_g changes and becomes similar to that of $TlGaS_2$. Moreover, Volkov *et al.* [25] revealed that the substitution of sulfur for selenium in $TlGaSe_2$ leads to a decrease in the temperature of the ferroelectric phase transition and to the complete disappearance of the features attributed to the phase transition at sulfur concentrations $\geq$25%. The way in which the band structure of the $TlGaSe_2$ and $TlInS_2$ crystals changes upon phase transition is unknown. However, we can argue that the phase transition is responsible for the change in the behavior of the dependence $E_g(T)$ at low temperatures.

Now, we consider one more deformation effect and estimate the change in the band gap E_g for $TlGaS_{2(1-x)}Se_{2x}$ solid solutions. In this case, the change in the quantity x in the system is considered an effective "strain." According to the estimates obtained from the deformation potentials derived above and the unit cell parameters of these crystals, the "contraction" of the crystal lattice upon the transition from $TlGaSe_2$ to $TlGaS_2$ (see table) should result in an increase in the band gap E_g by 0.4 eV, which is very close to the data obtained in [19].

Therefore, we can draw the inference that the model based on the deformation potentials $D_\parallel$ and $D_\perp$ offers an adequate description of the results of at least four independent experiments on (i) the influence of hydrostatic

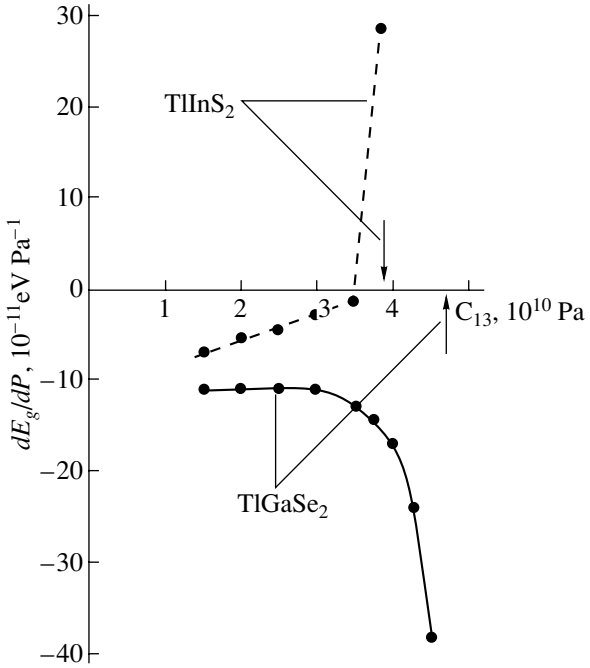

Fig. 4. Dependences of the pressure coefficient of the band gap on the elastic constant C_{13} for $TlInS_2$ and $TlGaSe_2$ crystals. Arrows indicate the elastic constants C_{13} at which the crystals can undergo phase transitions.

pressure on the band gap E_g for the $TlInS_2$ crystal, (ii) the influence of hydrostatic pressure on the band gap E_g for the $TlGaSe_2$ crystal, (iii) the increase in the band gap E_g for the $TlGaS_2$ crystal with an increase in the temperature, and (iv) the concentration dependence of the band gap E_g for $TlGaS_{2(1-x)}Se_{2x}$ solid solutions.

Up to this point, we have not been concerned with the unusual pressure dependences of the band gap and the difference between these dependences for the $TlGaSe_2$ and $TlInS_2$ crystals (Fig. 3). Now, we focus our attention on the behavior of the pressure coefficient dE_g/dP in the range close to $P \approx 0.59$ GPa for the $TlInS_2$ crystal and in the vicinity of $P \approx 0.92$ GPa for the $TlGaSe_2$ crystal. We will not consider the behavior of the pressure coefficient dE_g/dP in the immediate vicinity of $P \approx 0.9$ GPa for the $TlInS_2$ crystal (Fig. 3), because the absorption edge for this crystal changes at $P \approx 0.9$ GPa [11, 14]. According to [11, 14], the change in the absorption edge is associated with the fact that, at pressures above 0.9 GPa, the role of the valence band top or the conduction band bottom is played by a new band. As the pressure increases, this band undergoes a more significant shift as compared to one of the aforementioned extrema. It should be emphasized that, in the pressure range under investigation, the absorption edges for the $TlInS_2$ and $TlGaSe_2$ crystals are governed by transitions between the same extrema. In order to evaluate the change in the quantity dE_g/dP under pressure, it is necessary to know the pressure dependences of the elastic constants. However, these constants for $Tl\mathit{MeX}_2$ layered crystals are not available in the literature. Nonetheless, we will attempt to construct a qualitative pressure dependence of the pressure coefficient with the use of the data available for other layered crystals. As was noted above, the pressure coefficients of layered semiconductors strongly depend on the pressure and temperature [23]. This can be explained by the high pressure and temperature sensitivities of the elastic constants characterizing the weak interlayer interaction (for layered crystals of hexagonal symmetry, these are the elastic constants C_{33}, C_{13}, and C_{44}).

It should also be noted that, as in the case of III–VI semiconductors with a layered structure, the deformation potentials $D_\parallel$ and $D_\perp$ for $Tl\mathit{MeX}_2$ layered crystals are opposite in sign: a decrease in the interlayer spacing under compression of the crystal leads to a decrease in the band gap E_g, whereas the compression of the layers themselves results in an increase in the band gap E_g. As a consequence, with an increase in the pressure and a relatively faster increase in the "interlayer" elastic constants, the negative contribution to the change in the band gap E_g decreases and the resultant pressure coefficient increases. Furthermore, the pressure coefficients dE_g/dP for GaSe and GaS crystals even change sign from negative to positive [23]. For the same reason, the pressure coefficients for III–VI semiconductors change sign with a decrease in the temperature.

Preparatory to constructing a qualitative pressure dependence of the pressure coefficient of the band gap, we will make the assumption that, among all the elastic constants describing the deformation of $Tl\mathit{MeX}_2$ layered crystals, the constant C_{13} is the most sensitive to pressure, even though the constant C_{33} can also change with a variation in the pressure. The dependences of the pressure coefficient of the band gap on the elastic constant C_{13} of the $TlInS_2$ and $TlGaSe_2$ crystals (Fig. 4) were constructed using the deformation potentials $D_\parallel$ and $D_\perp$. As can be seen from Fig. 4, even this crude model offers an adequate qualitative (and even quantitative) description of the behavior of the pressure coefficient dE_g/dP with a variation in the pressure. In actual fact, it can be seen from this figure that, as the elastic constant C_{13} increases (i.e., as the pressure rises), the pressure coefficient dE_g/dP for the $TlInS_2$ crystal changes sign at pressures where the elastic constant C_{13} approaches a value of $\approx 3.75 \times 10^{10}$ Pa. A different situation occurs with the $TlGaSe_2$ crystal: as the elastic constant C_{13} increases, the pressure coefficient of the band gap dE_g/dP first changes only slightly and then increases drastically in magnitude when the constant C_{13} approaches a value of $\approx 4.3 \times 10^{10}$ Pa. The reason for this difference between the pressure dependences of the pressure coefficient dE_g/dP for the $TlInS_2$ and $TlGaSe_2$ crystals is obvious. Indeed, it follows from relationships (2) for the strains $U_\parallel$ and $U_\perp$ that, as the elastic constant C_{13} of the $TlInS_2$ crystal increases and approaches the quantity $(C_{11} + C_{12})/2$, the strain $U_\perp$ tends to zero, whereas the strain $U_\parallel$ remains nonzero. Compared to the $TlInS_2$ crystal, the $TlGaSe_2$ crystal

exhibits a stronger anisotropy; hence, the elastic constants for the $TlGaSe_2$ crystal satisfy the inequality $(C_{11} + C_{12})/2 > C_{33}$. Therefore, with an increase in the elastic constant C_{13} in the latter case ($TlGaSe_2$), the strain $U_\parallel$ tends to zero and $U_\perp \neq 0$. In the former case ($TlInS_2$), as the elastic constant C_{13} approaches the quantity $(C_{11} + C_{12})/2$, the contribution of the layer strain to the change in the band gap E_g under pressure appears to be dominant and the pressure coefficient dE_g/dP changes sign from negative to positive. By contrast, with an increase in the pressure for the $TlGaSe_2$ crystal, the strain $U_\parallel$ tends to zero; hence, the pressure coefficient dE_g/dP remains negative but drastically increases in magnitude. The elastic constants of the $TlGaS_2$ crystal are unknown. However, judging from the unit cell parameters, the elastic constants of this crystal are even larger in magnitude than those of the $TlGaSe_2$ crystal. This implies that the pressure-induced change in the pressure coefficient dE_g/dP for the $TlGaS_2$ crystal can be achieved at a higher pressure as compared to that for the $TlGaSe_2$ crystal (and, especially, for the $TlInS_2$ crystal). This inference is in agreement with the experimental data.

Another important inference is the fact that the specific features in the behavior of the pressure coefficient for the $TlInS_2$ and $TlGaSe_2$ crystals are observed in the case where the elastic constants C_{13} are close to values corresponding to the stability threshold, which can be determined from the condition

$$(C_{11} + C_{12})C_{33} - 2C_{13}^2 \geq 0. \quad (3)$$

Thus, the above estimates allow us to draw the conclusion that the drastic changes in the behavior of the pressure coefficients for the $TlInS_2$ and $TlGaSe_2$ crystals can be accompanied by loss of stability or, in other words, by phase transitions, which also agrees with the experimental data.

Despite its simplicity, the proposed model of the deformation potential provides a satisfactory explanation of the results of many experiments on the evolution of the electronic spectra of $TlMeX_2$ layered crystals under deformation of different types.

The main feature of this model is the inclusion of deformation potentials with different signs and the possibility of changing the relative contributions of the strains $U_\parallel$ and $U_\perp$ with variations in the pressure and temperature. The effect of pressure on the pressure coefficients was considered above. It can easily be shown that, although the sign of the pressure coefficients dE_g/dP for $TlMeX_2$ layered crystals remains unchanged, the effect of uniaxial compression (in a direction perpendicular to the crystal layers) on these coefficients strongly depends on the temperature. Indeed, it is easy to verify with the use of the deformation potentials $D_\parallel$ and $D_\perp$ that, under uniaxial compression in a direction perpendicular to the layers, the $TlGaSe_2$ and $TlInS_2$ crystals have the pressure coefficients $dE_g/dP = -34 \times 10^{-11}$ and -41×10^{-11} eV Pa^{-1}, respectively. These coefficients are more than one order of magnitude larger than those obtained in the experiment at low temperatures [24]. As in the case of III–VI semiconductors, we can assume that, with a decrease in the temperature, the change in the interlayer spacing under deformation of the crystals is of little importance. For III–VI semiconductors under compression, the pressure coefficients of the band gap change sign from negative to positive. For $TlMeX_2$ crystals, the sign of the pressure coefficient dE_g/dP does not change, but the coefficients themselves appreciably decrease in magnitude.

Therefore, we can state that the deformation effects observed in $TlMeX_2$ and III–VI semiconductor crystals have much in common. This can be explained by the fact that the main feature of the band structure of III–VI semiconductor crystals is also inherent in the $TlMeX_2$ crystals. This feature is that the valence band top and the conduction band bottom in the band structure of layered semiconductors are split as a result of the interaction between the layers [23]. As a consequence, a decrease in the interlayer spacing leads to an increase in the splitting and, hence, to a decrease in the band gap E_g; i.e., the deformation potential $D_\perp$ becomes positive in sign. Making allowance for the negative sign of the deformation potential $D_\parallel$, this accounts for many specific features of the deformation effects in layered crystals (the negative sign of the pressure coefficients of the band gap at low pressures and room temperature, the relatively small magnitudes of the pressure coefficients dE_g/dP, and their strong dependences on the temperature and pressure). It is evident that the band structure of $TlMeX_2$ crystals has many specific features inherent in layered semiconductors.

Note once again that the dependences of the pressure coefficient of the band gap on the pressure for the $TlGaSe_2$ and $TlInS_2$ crystals differ from each other. It is not surprising that the pressure coefficient dE_g/dP for the $TlInS_2$ crystal changes sign with a variation in the pressure. This situation is typical of III–VI semiconductors with a layered structure and stems from the fact that, with an increase in the pressure, the contribution from the layer strain to the change in the band gap E_g increases more rapidly as compared to the contribution from the decrease in the interlayer spacing. The behavior of the pressure coefficient of the band gap dE_g/dP for the $TlGaSe_2$ crystal is more surprising: the pressure coefficient drastically increases in magnitude and retains negative sign. It should be emphasized that this behavior of the pressure coefficient for the $TlGaSe_2$ crystal can be explained only under the assumption that, with an increase in the pressure, the elastic constant C_{13} increases and becomes approximately equal to the elastic constant C_{33}. In [6], it was observed that the elastic constant C_{13} for the $TlGaSe_2$ crystal increases significantly and approaches the elastic constant C_{33} with a decrease in the temperature. In particular, this accounts for the specific features in the temperature dependence of the linear thermal expansion coefficient

along the direction parallel to the layer plane of the $TlGaSe_2$ crystal (see Fig. 2). In our recent work [7], we showed that the sharp negative peak observed in the dependence $\alpha_{\parallel}(T)$ for the $TlGaSe_2$ crystal upon the phase transition and the negative thermal expansion coefficient over a wide range of temperatures are associated with the drastic increase in the elastic constant C_{13}, which approaches the elastic constant C_{33} with a decrease in the temperature. Thus, the unusual increase in the elastic constant C_{13} with a variation in the temperature is characteristic of $TlGaSe_2$ crystals and the above assumption that this elastic constant can exhibit a similar behavior with a change in the pressure is justified.

ACKNOWLEDGMENTS

This work was supported by the Institute of Physics, National Academy of Sciences of Azerbaijan.

REFERENCES

1. D. Muller, F. E. Poltman, and H. Z. Hahn, Naturforscher B **29** (1), 117 (1974).
2. D. Muller and H. Z. Hahn, Z. Anorg. Allg. Chem. **438** (1), 258 (1978).
3. K. R. Allakhverdiyev, T. G. Mamedov, B. G. Akinoglu, and Sh. S. Ellialtioglu, Turk. J. Phys. **18** (1), 1 (1994).
4. W. Henkel, H. D. Hochheimer, C. Carlone, *et al.*, Phys. Rev. B **26** (6), 3211 (1982).
5. K. A. Yee and T. A. Albright, J. Am. Chem. Soc. **113** (17), 6474 (1991).
6. R. A. Suleĭmanov, M. Yu. Seidov, and F. M. Salaev, Fiz. Tverd. Tela (Leningrad) **33** (6), 1797 (1991) [Sov. Phys. Solid State **33**, 1010 (1991)].
7. N. A. Abdullaev, T. G. Mamedov, and R. A. Suleĭmanov, Fiz. Nizk. Temp. **27** (8), 915 (2001) [Low Temp. Phys. **27**, 676 (2001)].
8. S. B. Vakhrushev, V. V. Zhdanova, G. E. Kvyatkovskiĭ, *et al.*, Pis'ma Zh. Éksp. Teor. Fiz. **39** (6), 245 (1984) [JETP Lett. **39**, 291 (1984)].
9. D. F. Mc. Morrow, R. A. Cowley, P. O. Hatton, and J. Banys, J. Phys.: Condens. Matter **2** (16), 3699 (1990).
10. E. A. Vinogradov, G. N. Zhizhin, N. N. Melnik, *et al.*, Phys. Status Solidi B **95** (1), 383 (1979).
11. K. R. Allakhverdiyev, T. G. Mamedov, V. V. Panfilov, *et al.*, Phys. Status Solidi B **131** (1), k23 (1985).
12. K. R. Allakhverdiev, A. I. Baranov, T. G. Mamedov, *et al.*, Fiz. Tverd. Tela (Leningrad) **30** (6), 1751 (1988) [Sov. Phys. Solid State **30**, 1007 (1988)].
13. E. Bairamova, K. R. Allakhverdiyev, B. G. Akinoglu, *et al.*, Turk. J. Phys. **18** (4), 497 (1994).
14. K. R. Allakhverdiev, T. G. Mamedov, and M. M. Tagiev, in *Physics and Engineering of High Pressures* (Naukova Dumka, Kiev, 1988), No. 28, p. 1.
15. K. R. Allakhverdiev, T. G. Mamedov, G. I. Peresada, *et al.*, Fiz. Tverd. Tela (Leningrad) **27** (3), 927 (1985) [Sov. Phys. Solid State **27**, 568 (1985)].
16. K. R. Allakhverdiev, S. S. Babaev, N. A. Bakhyshov, *et al.*, Fiz. Tekh. Poluprovodn. (Leningrad) **18** (7), 1307 (1984) [Sov. Phys. Semicond. **18**, 817 (1984)].
17. K. R. Allakhverdiyev, M. A. Aldzanov, T. G. Mamedov, and E. Yu. Salaev, Solid State Commun. **58** (5), 295 (1986).
18. S. G. Abdullaeva, N. T. Mamedov, and S. S. Orudzhev, Phys. Status Solidi B **119** (1), 41 (1983).
19. S. G. Abdullaeva, G. L. Belenkii, and N. T. Mamedov, Phys. Status Solidi B **102** (1), 19 (1980).
20. N. A. Abdullaev, K. R. Allakhverdiev, G. L. Belen'kiĭ, *et al.*, Dokl. Akad. Nauk AzSSR **41** (12), 21 (1985).
21. G. L. Belenkii, S. G. Abdullaeva, A. B. Solodukhin, and R. A. Suleymanov, Solid State Commun. **44** (12), 1613 (1982).
22. G. L. Belenkii, T. G. Mamedov, N. D. Abdullaev, *et al.*, Solid State Commun. **53** (7), 601 (1985).
23. G. A. Belen'kiĭ, É. Yu. Salaev, and R. A. Suleĭmanov, Usp. Fiz. Nauk **155** (1), 89 (1988) [Sov. Phys. Usp. **31**, 434 (1988)].
24. S. G. Guseynov, G. D. Guseynov, N. Z. Gasanov, and S. B. Kyazimov, Phys. Status Solidi B **133** (1), k25 (1986).
25. A. A. Volkov, Yu. V. Goncharov, G. V. Kozlov, *et al.*, Fiz. Tverd. Tela (Leningrad) **26** (9), 2754 (1984) [Sov. Phys. Solid State **26**, 1668 (1984)].

Translated by O. Borovik-Romanova

Physics of the Solid State, Vol. 45, No. 12, 2003, pp. 2249–2254. Translated from Fizika Tverdogo Tela, Vol. 45, No. 12, 2003, pp. 2147–2152.

SEMICONDUCTORS AND DIELECTRICS

Effect of Electron Irradiation on the Galvanomagnetic Properties of $In_xBi_{2-x}Te_3$ Semiconductor Single Crystals

A. E. Kar'kin*, V. V. Shchennikov*, B. N. Goshchitskiĭ*, S. E. Danilov*, V. L. Arbuzov*, and V. A. Kul'bachinskiĭ**

**Institute of Metal Physics, Ural Division, Russian Academy of Sciences, ul. S. Kovalevskoĭ 18, Yekaterinburg, 620219 Russia*

***Moscow State University, Vorob'evy gory, Moscow, 119992 Russia*

e-mail: kulb@mig.phys.msu.ru

Received December 3, 2002; in final form, May 15, 2003

Abstract—The effect of 5-MeV electron irradiation of p-$In_xBi_{2-x}Te_3$ single crystals (x = 0, 0.04, 0.07), performed at 250 K, on the galvanomagnetic properties of the crystals was studied. The irradiation was shown to change the conduction from the p to the n type. Annealing at temperatures of 310–390 K restores the conduction to the p type. The reversal of the conduction type and variation of the carrier concentration can be accounted for by an increase in the concentration of charged point radiation defects produced in $In_xBi_{2-x}Te_3$ by irradiation. Electron irradiation of p-type Te single crystals reduces the electrical resistivity without reversing the conduction type. Annealing restores the original properties almost completely. © *2003 MAIK "Nauka/Interperiodica".*

1. INTRODUCTION

Bismuth telluride Bi_2Te_3 belongs to the class of layered semiconductors with rhombohedral structure and space symmetry group R_{3m} (D_{3d}^5). The crystal lattice is made up of periodically stacked layers, each consisting of five atomic planes (quintets) alternating as Te^1–Bi–Te^2–Bi–Te^1. Here, Te^2 and Te^1 stand for Te atoms occupying two different positions. The chemical bonding in each quintet is partially covalent and partially ionic, and the quintets are coupled by van der Waals bonds. This structure accounts for anisotropy in the electrophysical properties of Bi_2Te_3 single crystals [1]. A characteristic feature of Bi_2Te_3 single crystals is the existence of native point structural defects associated with Bi atoms substitutionally entering Te sites in the lattice [2]. Because such antisite defects are negatively charged, bismuth telluride crystals usually have a high initial hole concentration, $p \approx 10^{18}$ cm^{-3}. The relatively weak bond polarity favors the formation of such native defects. As a result of such specific features, for example, atoms of Sn (Group IV of the Periodic table) carry a negative charge and bring about an increase in the hole concentration [3]. The hole concentration in Bi_2Te_3 can be reduced by suppressing the cause of the native defect formation, for instance, by incorporating In atoms into the lattice [4–6]. A study of the influence of In on the galvanomagnetic effects in $In_xBi_{2-x}Te_3$ single crystals, including measurements carried out under pressure, revealed that indium not only reduces the hole concentration but also forms an impurity band [4, 5]. Doping with indium exerts the same donor action in Sb_2Te_3 [7, 8].

Irradiation of crystals by electrons of an appropriate energy is known to produce point defects [9]. The effect of electron irradiation on bismuth telluride was studied earlier at an electron energy of 2 MeV [10, 11]. Because of the low electron energy, no residual effects were observed in the samples. Irradiation by other agents, for instance, by neutrons, was found to reverse the sign of the Hall coefficient R_H, but the mechanism underlying this effect involved the formation of donor impurities (iodine) as a result of a tellurium isotope capturing a neutron. The R_H sign reversal under proton irradiation can be assigned to the formation of charged donor impurities which compensate the acceptors (see the review in monograph [1]).

In the present communication, we report on a study of the effect of 5-MeV electron irradiation to a dose of 10^{19} cm^{-2} performed at a temperature of 250 K on the Hall coefficient and temperature dependences of the resistivity of single-crystal p-$In_xBi_{2-x}Te_3$ samples (x = 0, 0.04, 0.07) and compare the irradiation effects produced in this compound and in Te single crystals.

2. SAMPLES AND MEASUREMENT TECHNIQUES

The p-$In_xBi_{2-x}Te_3$ single crystals used in the measurements were cut from the same ingots as the ones employed in [5]. The Hall coefficient measured at 4.2 K in a magnetic field of 7 T was 0.7 cm^3/C for Bi_2Te_3,

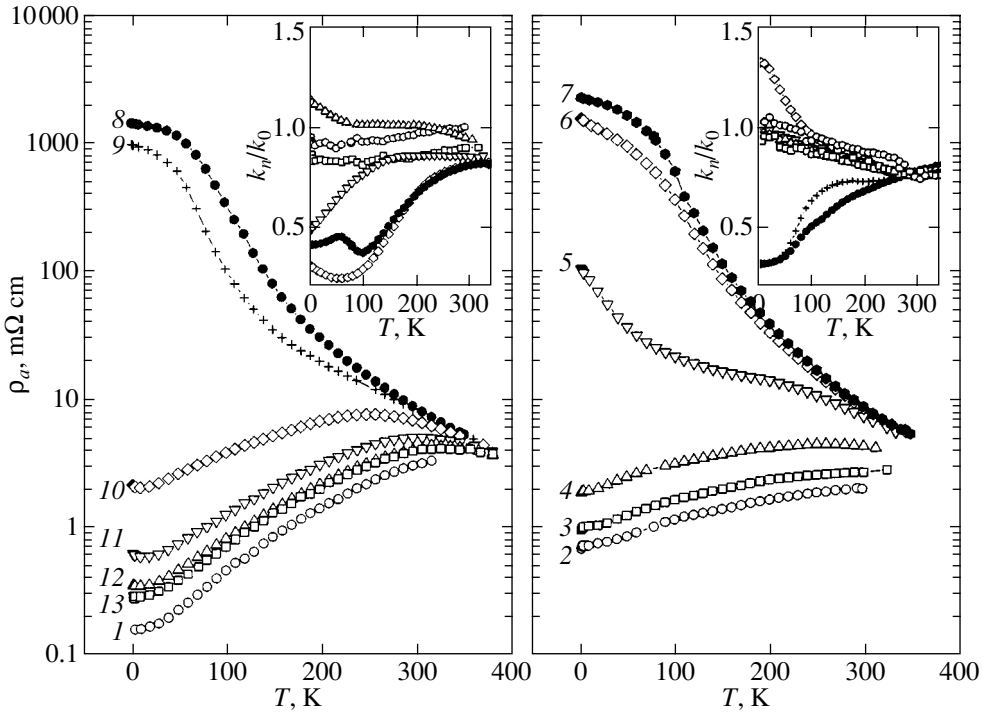

Fig. 1. Temperature behavior of the basal-plane electrical resistivity ρ_a (*1*) of the original *p*-$In_xBi_{2-x}Te_3$ sample with $x = 0.04$ and (*2*) of the same sample after electron irradiation to a dose of 10^{19} cm^{-2}. Curves *3–13* were obtained on annealed samples. Annealing temperatures (K): (*3*) 310 (60 min), (*4*) 320 (60 min), (*5*) 330 (60 min), (*6*) 335 (30 min), (*7*) 340 (30 min), (*8*) 345 (30 min), (*9*) 350 (30 min), (*10*) 360 (60 min), (*11*) 370 (60 min), (*12*) 380 (60 min), and (*13*) 390 (60 min). Insets plot the corresponding temperature dependences of the relative resistivity anisotropy $k_n(T)/k_0$ (k_0 is the anisotropy of an unirradiated sample at 300 K).

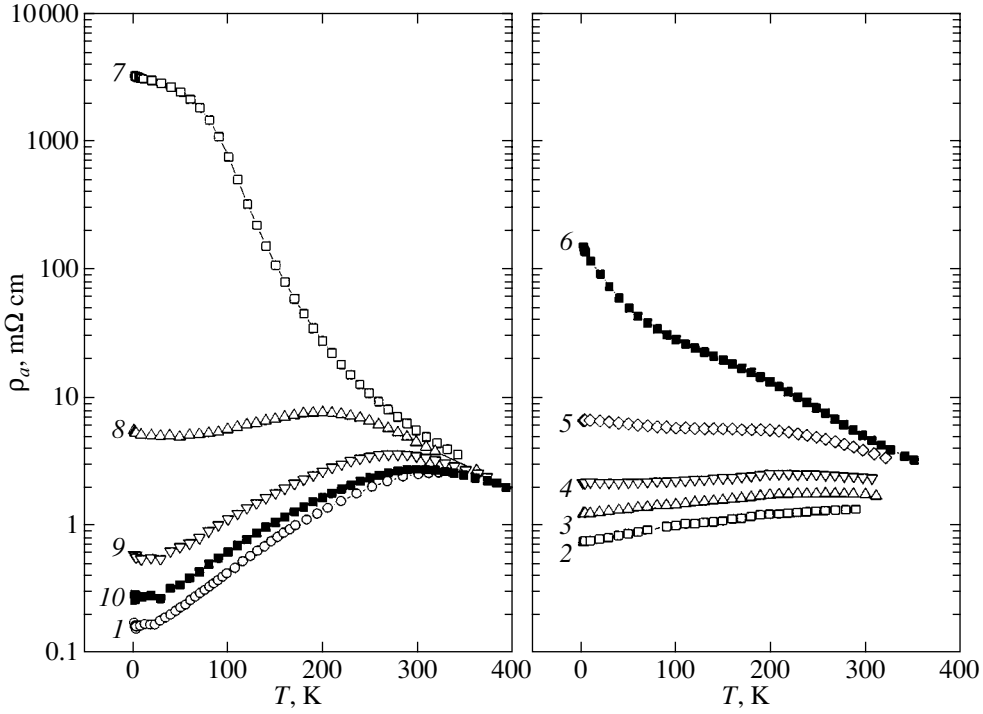

Fig. 2. Temperature behavior of the basal-plane electrical resistivity ρ_a (*1*) of the original *p*-$In_xBi_{2-x}Te_3$ sample with $x = 0.07$ and (*2*) of the same sample after electron irradiation to a dose of 10^{19} cm^{-2}. Curves *3–10* were obtained on samples annealed for 60 min. Annealing temperatures (K): (*3*) 310, (*4*) 320, (*5*) 330, (*6*) 340, (*7*) 350, (*8*) 360, (*9*) 370, and (*10*) 380.

2.3 cm^3/C for $In_{0.04}Bi_{1.96}Te_3$, and 2.7 cm^3/C for $In_{0.07}Bi_{1.93}Te_3$. To compare the effects of equal doses, tellurium single crystals were also used. The samples typically measured $1 \times 0.5 \times 0.2$ mm. The samples were chosen to be this small on purpose, to ensure uniform irradiation.

The samples were irradiated in a channel of a 5-MeV-electron accelerator to a dose of 10^{19} cm^{-2} under cooling by purified gaseous helium to a temperature of about 250 K. The sample irradiation was followed by annealing at temperatures of 310–390 K directly in the measuring cryostat, exactly as performed in [12]. X-ray diffraction studies showed that the irradiation chosen did not bring about amorphization of the samples.

The galvanomagnetic properties were investigated in the temperature region 1.7–380 K in magnetic fields B of up to 13.6 T generated by a superconducting solenoid. The electrical resistivity in the basal plane and the Hall effect were measured using the Montgomery method [13]. We also measured the resistivity along the C_3 axis and the resistivity anisotropy.

3. RESULTS OF THE MEASUREMENTS AND DISCUSSION

Figure 1 displays temperature dependences of the electrical resistivity in the basal plane for the starting p-$In_xBi_{2-x}Te_3$ sample with $x = 0.04$ (curve *1*), irradiated to an electron dose of 10^{19} cm^{-2} (curve *2*), and annealed at various temperatures after irradiation (curves *3–13*). Figure 2 presents similar plots obtained for an $In_xBi_{2-x}Te_3$ sample with $x = 0.07$. As seen from Figs. 1 and 2, the resistivity of the irradiated samples increases only slightly. The most interesting observation is the variation of the resistivity during the course of annealing. As the annealing temperature was increased to T_{ann} = 340–345 K, the electrical resistivity of the samples increased by several orders of magnitude. We believe this to be due to specific features of defect generation by high-energy electrons [9, 14]. For the chosen dimensions of the samples, the irradiation dose (10^{19} cm^{-2}) used ensures defect formation over the entire volume of a sample, because the electron penetration depth greatly exceeds the sample size. 5-MeV electrons knock the atoms out of the lattice sites to form positively charged point defects (bismuth and tellurium vacancies, interstitial atoms), which are electrically active and compensate the initial hole concentration. At irradiation doses of 10^{19} cm^{-2}, the number of charged point defects thus formed exceeds the original hole concentration and the Hall effect reverses sign. The level of compensation depends on the temperature of the subsequent annealing and its duration. Part of the defects heal, and the electrons and holes can attain complete compensation; indeed, for T_{ann} = 340–345 K, the temperature dependences of the resistivity acquire a

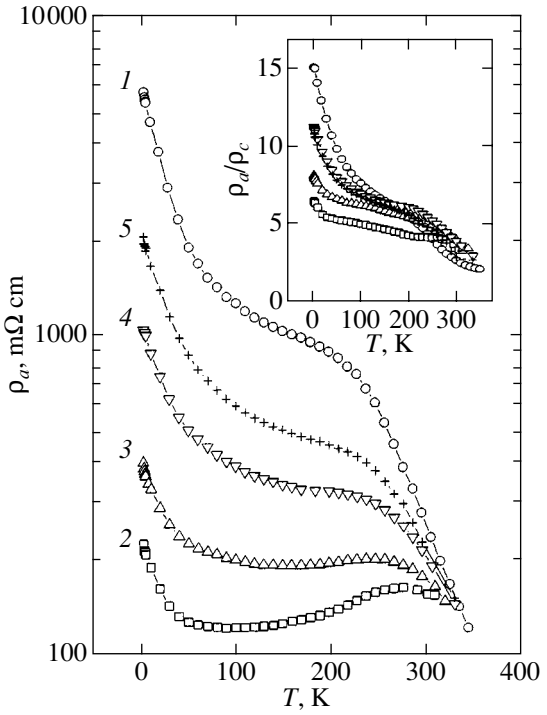

Fig. 3. Temperature behavior of the electrical resistivity ρ_c (*1*) of a Te sample and (*2*) of the same sample after electron irradiation to a dose of 10^{19} cm^{-2}. Curves *3–5* were obtained on a sample subjected to consecutive 30-min anneals. Annealing temperatures (K): (*3*) 310, (*4*) 320, and (*5*) 330. Inset shows the temperature dependences of the resistivity anisotropy ρ_a/ρ_c of the irradiated sample subjected to various anneals.

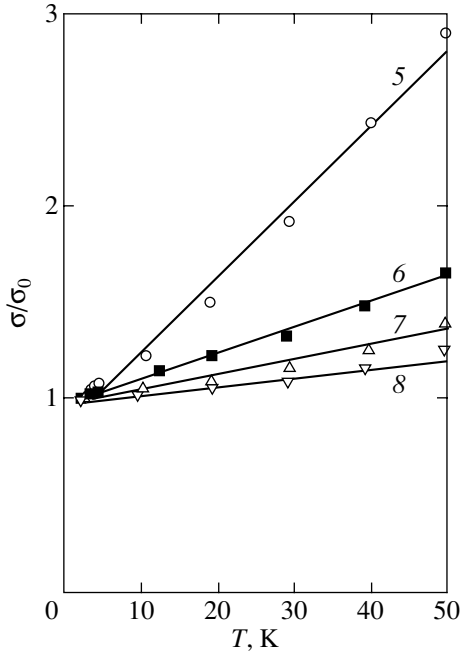

Fig. 4. Temperature behavior of reduced conductivity σ/σ_0 (σ_0 is the conductivity of a given sample reduced to zero temperature) measured on a $In_xBi_{2-x}Te_3$ sample ($x = 0.04$). The notation in the curve is the same as that in Fig. 1.

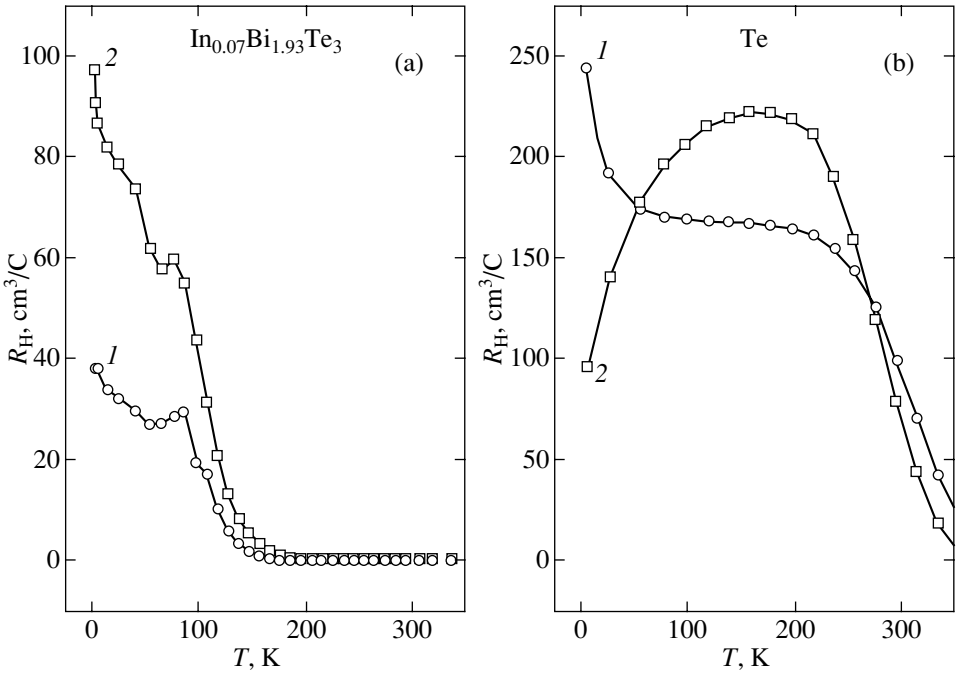

Fig. 5. Temperature behavior of the Hall coefficient R_H in a magnetic field B = 13.6 T measured (*1*) in the basal plane (**B** perpendicular to the layers) and (*2*) perpendicular to the layers (**B** in the basal plane) for (a) $In_{0.07}Bi_{1.93}Te_3$ and (b) Te samples annealed at T_{ann} = 350 K after irradiation.

semiconducting pattern (see Fig. 1, curves *5*–*9*, and Fig. 2, curves *6*, *7*). The electrical resistivity of the samples may become as high as a few Ω cm. Reaching such a high resistivity in semiconductors of the bismuth telluride type using standard methods would meet with staggering difficulties.

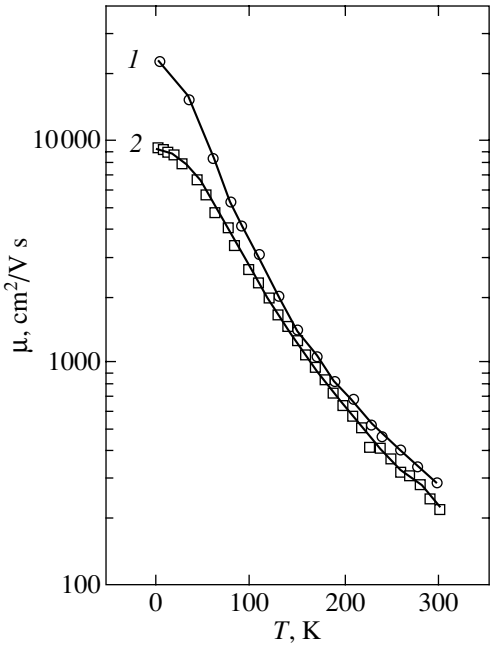

Fig. 6. Hall mobilities μ plotted vs. temperature for (*1*) the original and (*2*) irradiated *p*-Bi_2Te_3 samples.

Due to the layered structure, the electrical resistivity of $In_xBi_{2-x}Te_3$ single crystals is anisotropic along the layers (R_a) and perpendicular to them (R_c) [15] and that of single-crystal Te is anisotropic along the trigonal axis and perpendicular to it. Under irradiation, part of the atoms are knocked out of the lattice to become interstitials and into the interlayer space (self-intercalation of samples). This results in a change of the resistivity anisotropy under irradiation, an effect observed experimentally from the relative change of the anisotropy on the same sample. The inset to Fig. 1 plots the temperature dependences of the relative variation of the sample anisotropy k_n/k_0, where $k_n(T) = R_c/R_a(T)$, which is equal to $k_0 = R_c/R_a$ at 300 K. Edge effects preclude precise measurement of the absolute values of the anisotropy on small samples. Annealing likewise changes the resistivity anisotropy, which is associated with defect healing. We did not succeed, however, in completely restoring the original hole concentration and the electrical resistivity (see Figs. 1, 2). The resistivity anisotropy in Te irradiated to the same dose decreases in the same way (inset to Fig. 3). Annealing restores the resistivity anisotropy.

Electron irradiation of high-resistivity *p*-Te samples also produces charged defects, which increase the hole concentration. Figure 3 plots the electrical resistivity ρ_c along the direction perpendicular to the basal plane as a function of temperature for the starting sample (curve *1*)

and after irradiation by electrons to a dose of 10^{19} cm^{-2} (curve *2*) and subsequent annealing (curves *3*–*5*). In this case, irradiation brings about a decrease in the electrical resistivity, which implies an increase in the hole concentration. This conclusion is borne out by Hall effect studies.

The specific features in galvanomagnetic effects observed in In-doped Bi_2Te_3 samples under pressure indicate the existence of an impurity band [5]. After annealing, irradiated samples exhibit a linear dependence of the conductivity on temperature in the low-temperature region (Fig. 4), which does not allow interpretation in terms of a simple model developed for heavily doped semiconductors. However, the presence of a peak in the density of states near the Fermi energy, which is associated with the existence of an impurity band with a low carrier mobility, provides a plausible explanation for this dependence. Irradiation is apparently capable of varying the density of states in this band. The majority of defects in the starting sample are antisites; i.e., Bi atoms sit at the Te sites. This is what accounts for the high initial hole concentration. As already pointed out, the formation of antisite defects is hindered by In doping and, therefore, In acts here as a donor. The 5-MeV electrons create, most probably, not antisite point defects but rather vacancies and interstitial atoms, which become annealed not at the temperature of irradiation but at a higher temperature. Special structural studies would, however, be needed to provide an accurate answer to the question regarding the type of defects generated under irradiation.

Irradiation of *p*-Bi_2Te_3 by electrons to a dose of 10^{19} cm^{-2} reverses the sign of the Hall coefficient R_H both in the basal plane (with the magnetic field **B** oriented perpendicular to it) and in the direction perpendicular to it. Annealing restores the original sign of the Hall coefficient. A similar effect is also observed to occur in *p*-$In_xBi_{2-x}Te_3$ samples. For illustration, Fig. 5 presents temperature dependences of the Hall coefficient measured in the basal plane of $In_{0.07}Bi_{1.93}Te_3$ (Fig. 5a) and Te (Fig. 5b) samples that were annealed following irradiation. Note that, unlike *p*-Bi_2Te_3 and *p*-$In_xBi_{2-x}Te_3$, Te single crystals do not reverse their conduction type after the used electron irradiation.

As already mentioned, doping bismuth telluride with indium lowers the hole concentration, so that in $In_xBi_{2-x}Te_3$ samples the Hall coefficient in the basal plane becomes as large as $R_H = 2.3$ cm^3/C for $x = 0.04$ and 2.7 cm^3/C for $x = 0.07$, whereas the Bi_2Te_3 sample exhibits $R_H = 0.7$ cm^3/C [5]. The temperature and magnetic-field dependences of the Hall coefficient in bismuth telluride can be traced to the complexity of the energy spectrum; indeed, the top of the valence band consists of two bands, each sixfold degenerate. This feature entails anomalous dependences of the Hall coefficient on magnetic field and temperature, which, however, allow interpretation, quantitative as well as qualitative, in terms of the two-band model, as shown in [16].

Note that *p*-Bi_2Te_3 and *p*-$In_xBi_{2-x}Te_3$ are basically heavily defected crystals characterized by a relatively low carrier Hall mobility; therefore, while irradiation by fast electrons does produce additional defects, it does not reduce the carrier mobility noticeably. This is illustrated in Fig. 6, which shows the temperature dependences of mobility for the starting and irradiated bismuth telluride single crystal.

The influence of irradiation on thermal conductivity is apparently not very significant. The additional thermal resistivity increases because of antisite defects [1], but this effect may constitute a few percentage points at the most (less than 5%). Because the mobility remains high, the thermoelectric efficiency should not deteriorate. For instance, the thermal conductivity of *n*-type samples decreased by 20% under irradiation by neutrons, while at doses below 10^{18} neutrons per cm^2 it did not change at all [1]. Irradiation by gamma rays up to 2 MeV in energy likewise did not produce noticeable changes in the thermal conductivity. In monograph [1], it was concluded that all kinds of radiation degrade the thermoelectric efficiency of bismuth telluride. However, our present results suggest that the electron irradiation used here at least does not degrade it.

4. CONCLUSION

Thus, irradiation of *p*-$In_xBi_{2-x}Te_3$ by 5-MeV electrons to a dose of 10^{19} cm^{-2} brings about a substantial change in the carrier concentration and a reversal of the sign of the Hall coefficient from positive to negative, which indicates compensation of positively charged native structural defects by defects of another type. At the same time, the carrier Hall mobility varies insignificantly because of the starting samples already having a large point defect density; as a result, the original carrier mobility is low and does not decrease noticeably under irradiation. Annealing restores the conduction character of the samples.

ACKNOWLEDGMENTS

This study was supported by the Ministry of Industry, Science, and Technology of the Russian Federation (State contract 40.020.1.1.1166, project no. 10/20), the federal basic research program of the Russian Academy of Sciences "Quantum Macrophysics" (project no. 25/02), and the Russian Foundation for Basic Research (project nos. 01-02-16877, 01-02-17203).

REFERENCES

1. B. M. Gol'tsman, V. A. Kudinov, and I. A. Smirnov, *Semiconducting Thermoelectric Materials Based on Bi_2Te_3* (Nauka, Moscow, 1972).
2. G. R. Muller and Y. L. Che, J. Phys. Chem. Solids **26**, 173 (1965).

3. V. A. Kul'bachinskiĭ, N. E. Klokova, Ya. Khorak, and P. Loshtak, Fiz. Tverd. Tela (Leningrad) **31** (1), 205 (1989) [Sov. Phys. Solid State **31**, 112 (1989)].
4. S. A. Azou, V. A. Kul'bachinskiĭ, G. A. Mironova, and S. Ya. Skipidarov, Fiz. Tekh. Poluprovodn. (Leningrad) **24**, 283 (1990) [Sov. Phys. Semicond. **24**, 173 (1990)].
5. N. B. Brandt and V. A. Kulbachinskii, Semicond. Sci. Technol. **7**, 907 (1992).
6. S. Karamazov, P. Lostak, J. Horak, and R. Kuzel, Phys. Status Solidi A **148**, 229 (1995).
7. V. A. Kul'bachinskiĭ, A. N. Chaĭka, Z. M. Dashevskiĭ, *et al.*, Fiz. Tverd. Tela (St. Petersburg) **37**, 1997 (1995) [Phys. Solid State **37**, 1088 (1995)].
8. V. A. Kulbachinskii, Z. M. Dashevskii, M. Inoue, *et al.*, Phys. Rev. B **52**, 10915 (1995).
9. V. S. Vavilov, A. E. Kiv, and O. R. Niyazova, *The Mechanisms of Defect Formation and Migration in Semiconductors* (Nauka, Moscow, 1981).
10. R. Levy, Bull. Am. Phys. Soc. **5**, 168 (1960).
11. W. Parker and R. Jenkins, Adv. Energy Convers. **2**, 87 (1962).
12. A. E. Kar'kin, V. V. Shchennikov, B. N. Goshchitskiĭ, *et al.*, Zh. Éksp. Teor. Fiz. **113**, 1787 (1998) [JETP **86**, 976 (1998)].
13. H. C. Montgomery, J. Appl. Phys. **42**, 2971 (1971).
14. N. B. Brandt and E. P. Skipetrov, Fiz. Nizk. Temp. **22**, 870 (1996) [Low Temp. Phys. **22**, 665 (1996)].
15. V. A. Kutasov and L. N. Luk'yanova, Fiz. Tverd. Tela (Leningrad) **32**, 488 (1990) [Sov. Phys. Solid State **32**, 282 (1990)].
16. V. A. Kulbachinskii, A. Yu. Kaminskii, K. Kindo, *et al.*, Phys. Status Solidi B **229**, 1467 (2002).

Translated by G. Skrebtsov

Physics of the Solid State, Vol. 45, No. 12, 2003, pp. 2255–2263. Translated from Fizika Tverdogo Tela, Vol. 45, No. 12, 2003, pp. 2153–2160.

SEMICONDUCTORS AND DIELECTRICS

The Hanle Effect in Nonuniformly Doped GaAs

R. I. Dzhioev, B. P. Zakharchenya, K. V. Kavokin, and M. V. Lazarev

Ioffe Physicotechnical Institute, Russian Academy of Sciences, Politekhnicheskaya ul. 26, St. Petersburg, 194021 Russia

e-mail: dzhioev@orient.ioffe.ru

Received June 2, 2003

Abstract—Spin density distribution in the GaAs/AlGaAs heterostructure was studied under steady-state optical orientation conditions. A comprehensive analysis of the dynamics and relaxation processes responsible for the steady-state nonuniformity of spin orientation was made. The acceptor impurity concentrations in various regions of nonuniformly doped gallium arsenide were determined. The concentrations were derived from the spin relaxation times measured using the optical orientation method. © *2003 MAIK "Nauka/Interperiodica".*

1. High hopes were pinned on the spin orientation in semiconductors as a phenomenon which could be potentially applied in the area of information recording, processing, and storage [1]. Recently, studies of spin phenomena in various materials, including semiconductors, have been attracting considerable interest. Record-long spin memory times of electrons in *n*-GaAs have been detected [2]. It has been shown that the spin relaxation time in *p*-GaAs exceeds the lifetime of photoexcited electrons [3] and that the decrease in orientation can be assigned to luminescence photon recycling. In gallium arsenide and the related heterostructures, the spin relaxation time can be controlled by properly varying the external magnetic field [4], doping level [2], electric field [5], and pump photon energy [6].

Controlling the electron spin as an information carrier is intimately connected with the nonuniform spin density distribution and spin transport. The nonuniformity in spin distribution also makes it possible to determine the kinetic recombination parameters and the mechanisms responsible for the transport of carriers and of their average spin [3]. It is appropriate to note here that the first observation of motion of nonequilibrium spins of optically oriented electrons was made in an experiment involving a heterogeneous structure. It was demonstrated that the spin orientation of electrons crossing the interface between a comparatively broad- to a narrow-band-gap semiconductor is preserved [7]. Later studies revealed a drift of spin-polarized electrons in variable band-gap structures [8].

The effects of the recombination conditions at the crystal surface and in the bulk on optical orientation in doped gallium arsenide were found to be inequivalent earlier in [9]. A study was made of the edge luminescence depolarization in a transverse magnetic field (the Hanle effect) and of the dependence of the depolarization rate on pump photon energy. The idea underlying the experiment was as follows. In GaAs, we deal with direct optical transitions and, hence, a high absorption coefficient α. Optical orientation is produced in a thin surface crystal layer whose effective thickness $d \sim \alpha^{-1}$ varies strongly with variation of the pump photon energy $E_{h\nu}$. If the surface recombination velocity of electrons η is large enough (the η/d ratio is of the order of the reciprocal spin orientation lifetime T_s^{-1}), it can be measured using the spin orientation effect. The half-width of the $\rho(H)$ dependence was found to vary with pump photon energy at 77 K (ρ is the degree of luminescence circular polarization, H is a transverse magnetic field), and this was assigned to the effect of the spin relaxation rate and recombination velocity on the free GaAs surface [9, 10].

However, comprehensive studies of the kinetic parameters performed later on GaAs samples with the same doping level using various methods [3, 11] led to results that are in contradiction to the conclusion drawn in [9]; namely, it was found that surface recombination in *p*-GaAs at 77 K is very weak and should not affect the optical orientation noticeably.

This communication reports on additional experiments carried out on *p*-GaAs/AlGaAs heterostructures, including samples studied in [9], and reveals the reasons for the contradictory interpretation of the results of optical orientation experiments reported in [3, 11] and [9]. It is shown that the variation of the magnetic luminescence depolarization rate with pump photon energy is caused by the nonuniform distribution of the acceptor concentration across the *p*-GaAs layer in the structure studied in the first experiments [9].

The measurements reported in [11] were conducted in stationary conditions at room temperature and under high-frequency (26.6 kHz) modulation of the polarization and intensity of luminescence. This method of measuring the nonequilibrium-carrier diffusion length is based on the use of self-absorption, i.e., the absorp-

tion of the recombination radiation in the sample itself, which is a GaAs crystal in our case [12]. If the dependence of the absorption coefficient α on the wavelength of light λ is known, the distribution of the nonequilibrium carrier concentration can be derived from the variation of the luminescence line shape.

When the crystal surface is illuminated by photons of energy $E_{h\nu} \geq E_g$, the spatial distribution of photoexcited carriers is determined primarily by their diffusion into the crystal bulk and recombination. The distribution of nonequilibrium carrier concentration in thin crystals (with thickness of the order of the electron diffusion length) depends on the recombination velocity at the surface opposite the illuminated side. The surface recombination velocity at the free *p*-GaAs surface ($p \sim 10^{18}$ cm^{-3}) is fairly high ($\eta_0 = 8 \times 10^5$ cm/s at $T = 300$ K [13]). It is known, however, that crystallization of the solid solution on the GaAs surface gives rise to passivation, a process in which the number of defects and states characteristic of the free GaAs surface decreases substantially [14], thus resulting in a decrease in the surface recombination velocity.

These effects in thin layers can be studied most conveniently from the spectral dependence of the intensity ratio of the luminescence leaving opposite sides of a plane-parallel sample, $I_1(\lambda)/I_2(\lambda)$. This ratio does not contain parameters capable of affecting the luminescence line shape, which facilitates analysis of the experimental data. The behavior of the $I_1(\lambda)/I_2(\lambda)$ dependence is governed by the $\alpha(\lambda)$ relation at the absorption edge and by the carrier spatial distribution in the crystal.

The study of the effect of the nonuniform distributions of electron concentration and spin density on optical orientation was carried out in three stages. In the first stage, measurements of the wavelength dependence of the absorption coefficient α for the GaAs layers of interest were performed in the edge luminescence region. In the second stage, the $I_1(\lambda)/I_2(\lambda)$ dependence was obtained and the $\alpha(\lambda)$ relation was used to determine the room-temperature recombination velocity at the free GaAs surface. It was also shown experimentally that the electron recombination at the free GaAs surface at 77 K is very small and cannot affect the electron concentration distribution away from the light-illuminated heterointerface into the bulk of the gallium arsenide crystal. In the third stage, experiments were carried out on the samples employed in [9]. We studied luminescence spectra and electron spin orientation in the reflection geometry. The results obtained in these experiments indicate that the doping is substantially nonuniform in the region close to the free GaAs surface.

2. Samples of the first group were inverted structures [15] similar to those used in the production of GaAs-based photocathodes. A 0.5-mm-thick layered structure (n-$Al_{0.6}Ga_{0.4}As$)/(p-GaAs)/(p-$Al_{0.6}Ga_{0.4}As$) was grown through molecular beam epitaxy on a GaAs substrate. An 8-μm-thick *p*-GaAs active layer was doped by germanium to a level of $(3–5) \times 10^{18}$ cm^{-3}. A p-$Al_{0.6}Ga_{0.4}As$ buffer layer 1–2 μm thick, doped by germanium to $(5–8) \times 10^{17}$ cm^{-3}, was capped by a 150- to 200-nm-thick SiO_2 layer. Next, this structure was welded through thermal compression with a glass having a thermal expansion coefficient close to that of gallium arsenide. After this, the substrate and the n-$Al_{0.6}Ga_{0.4}As$ stopper layer were etched off chemically. Below, we present experimental data on two samples that differ only in the thickness of the *p*-GaAs layer (2.5 and 5 μm).

The parameters characterizing the spatial distribution of electrons in the GaAs layer were derived from the spectral dependence of the intensity ratio $I_{tr}/I_{ref}(\lambda)$ of the luminescence emerging from the GaAs layer through the opposite surfaces, i.e., in the transmission and reflection geometries. It is known that the absorption coefficient in GaAs can vary by three to four orders of magnitude within the edge luminescence band and can reach levels of the order of 10^4 at its short-wavelength edge [16]. As already mentioned, the radiation that is emitted in electron recombination in the bulk of the layer and exits through the two layer faces is weakened through self-absorption. Due to the nonuniform spatial distribution of electrons generated by stationary pumping near one of the layer faces, which is obtained by diffusion and recombination, the transmitted luminescence travels, on average, a longer path in the absorbing medium than the reflected one. The value of I_{tr}/I_{ref} is close to unity in the long-wavelength part of the spectrum (where the absorption coefficient α is small) and decreases with decreasing luminescence wavelength (i.e., with increasing α). Thus, the $I_{tr}/I_{ref}(\lambda)$ dependence carries information on the spatial distribution of nonequilibrium electrons in the crystal, which can be extracted by comparing the measured values of $I_{tr}/I_{ref}(\lambda)$ with calculated ones. The sensitivity of this method is highest when the layer thickness is of the order of the electron diffusion length.

The $I_{tr}/I_{ref}(\lambda)$ dependence can be expressed analytically as

$$\frac{I_{tr}}{I_{ref}} = \frac{\int_0^d n(Z)e^{-\alpha(\lambda)(d-Z)}dZ}{\int_0^d n(Z)e^{-\alpha(\lambda)Z}dZ}, \quad (1)$$

where n is the electron concentration, Z is the spatial coordinate along the crystal surface normal, and d is the layer thickness.

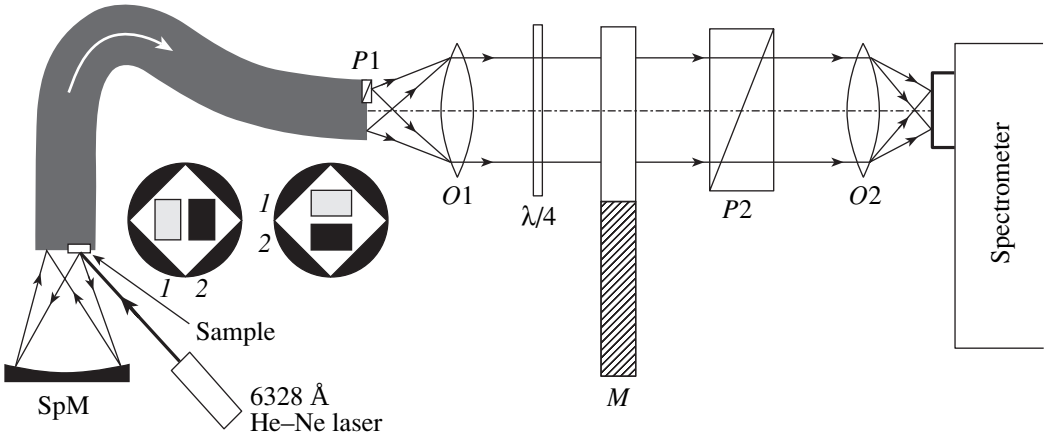

Fig. 1. Setup for measurement of the photoluminescence intensity ratio in the transmission and reflection geometries (I_{tr}/I_{ref}).

To find $n(Z)$, one has to solve the diffusion equation for nonequilibrium electrons with the corresponding boundary conditions:

$$\begin{aligned} Dn''(Z) - \frac{n(Z)}{\tau} &= 0, \\ Dn'(0) &= -I + \eta_0 n(0), \\ Dn'(d) &= -\eta_d n(d), \end{aligned} \tag{2}$$

where D is the diffusion coefficient, τ is the lifetime, I is the pump intensity, and η_0 and η_d are the recombination velocities on the excited surface and the opposite side, respectively.

Equation (2) was derived with allowance for the fact that the width of the pump beam is much larger and the depth of its penetration into the crystal is much lower than the layer thickness and the electron diffusion length. Substituting the solution to Eq. (2) into Eq. (1) yields

$$\frac{I_{tr}}{I_{ref}} = e^{-\alpha d}\frac{(1-\xi)\dfrac{e^{\alpha d}-e^{-d/L}}{1+\alpha L} - (1+\xi)\dfrac{e^{\alpha d}-e^{d/L}}{1-\alpha L}}{(1-\xi)\dfrac{e^{-\alpha d}-e^{-d/L}}{1-\alpha L} - (1+\xi)\dfrac{e^{-\alpha d}-e^{d/L}}{1+\alpha L}}, \tag{3}$$

where $L = \sqrt{D\tau}$ is the electron diffusion length and $\xi = \eta_d\tau/L$ is a dimensionless parameter characterizing the relative contribution from the recombination on the surface opposite the excited surface (note that surface recombination at the pumped surface does not affect the I_{tr}/I_{ref} ratio). We subsequently denote this parameter for the free surface by ξ_f and for the interface by ξ_i.

Figure 1 gives a schematic representation of the optical setup used to measure I_{tr}/I_{ref}. The sample fixed at an end face of a regular fiber bunch (that does not distort the image) is pumped by a He–Ne laser beam (λ = 6328 Å). A spherical concave mirror (SpM) fixed at a distance that is twice the focal length from the sample focuses the luminescence, studied in the reflection geometry, onto the fiber bunch end face near the sample. The luminescence propagates to the other fiber bunch end together with the luminescence leaving the other side of the sample (i.e., as studied in the transmission geometry). In this way, one can obtain two images, *1* and *2*, arranged one under the other. The light emerging from the fiber bunch is unpolarized. Next, one of the beams is passed through polaroid *P*1. After this, the two diverging luminescence beams are made parallel by objective lens *O*1. The beam of linearly polarized luminescence is transformed into circularly polarized light by passing it through a $\lambda/4$ phase plate (the quarter-wavelength phase plates designed to operate in the spectral scanning range were selected from mica chips of different thickness). Next, the two light beams traverse photoelastic polarization modulator *M*, which represents a rectangular fused quartz parallelepiped subjected to uniaxial strain at the natural mechanical-resonance frequency [17]. On passing through linear polarizer *P*2 with the transmission axis set at 45° to the quartz strain axis [17], the intensity of the reflection luminescence is modulated at the same frequency. The intensity of the unpolarized (transmission) luminescence remains constant. Objective *O*2 focuses both beams onto the spectrometer entrance slit. The light that passed through the spectrometer is recorded with a PM tube. The PM tube output pulses are fed into the intensity ratio measurement circuit. The reference oscillator frequency of quartz modulator *M* is used to generate a train of pulses of equal length, which alternately activate two photon-counting channels. The number of pulses N_1 accumulated in the first channel during the exposure time needed to reach the given accuracy is proportional to $I_{tr} + I_{ref}$, and the number of pulses N_2 in the second channel is proportional to I_{tr}. Thus,

$$\frac{I_{tr}}{I_{ref}} = \left(\frac{N_1}{N_2} - 1\right)^{-1}.$$

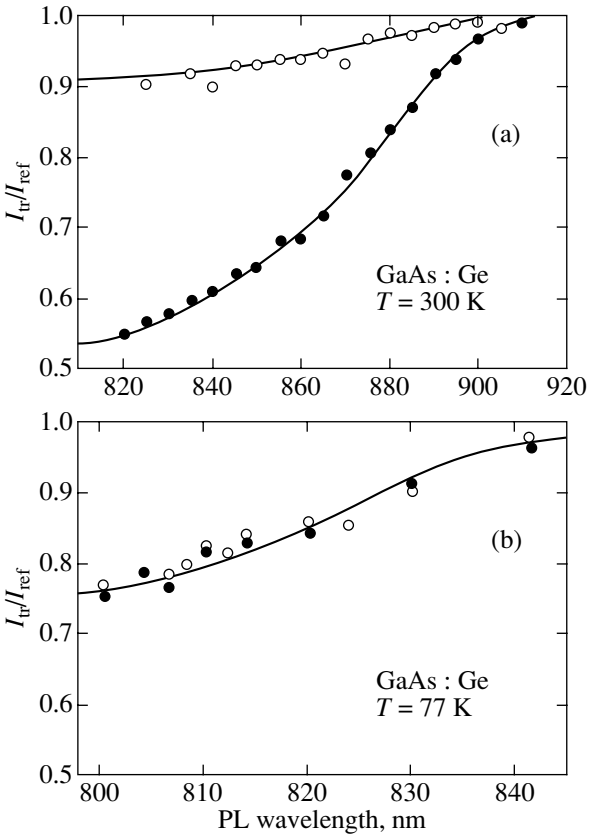

Fig. 2. Spectral dependence of the photoluminescence intensity ratio in the transmission and reflection geometries (I_{tr}/I_{ref}) measured on a GaAs : Ge sample (d = 2.5 μm) at (a) T = 300 and (b) 77 K. The open circles relate to excitation through the free surface, and the filled ones, to that through the heterointerface.

The measured ratio I_{tr}/I_{ref} is corrected for the intensity modulation depth of the polarized light beam. Figure 2 is a graphical representation of the spectral dependence of this ratio (circles) obtained at T = 300 K (Fig. 2a) and 77 K (Fig. 2b).

Recall that the quantity I_{tr}/I_{ref} was measured throughout the spectral region of the edge luminescence. To extract the kinetic parameters from Eq. (3), one has to know the values of the absorption coefficient $\alpha(\lambda)$ for the same spectral intervals.

The use of data obtained by different authors on the spectral dependence of the absorption coefficient should not produce large errors. However, precise determination of the electron diffusion length and of the surface recombination velocity for these samples was of fundamental importance, because this determination served as a check on the method of measuring the dynamic parameters based on electron spin transport [3]. Therefore, it was the samples used in the study that were chosen to measure the spectral response of the absorption coefficient $\alpha(\lambda)$. We measured the intensity ratio of two light beams that passed through samples of the photocathode structure with different GaAs layer thicknesses. The samples employed in this experiment were obtained from the same structure with an active GaAs layer 8 μm thick. This layer was subsequently etched off to a thickness of 2.5 and 5 μm, respectively.

Prior to determining the electron diffusion length and other parameters influencing the steady-state electron concentration distribution away from the surface excited by light into the bulk of the sample, we consider the results of $\alpha(\lambda)$ measurements.

3. The absorption coefficient measurements were performed on these same samples with different GaAs layer thicknesses (2.5 and 5 μm). The intensity of the light transmitted through the crystal can be written as

$$I_{tr} = I_0 R_1 R_2 e^{-\alpha d}, \quad (4)$$

where R_1 and R_2 are the coefficients of reflection from the two opposite crystal faces and I_0 is the incident light intensity. By measuring the ratio

$$\frac{I_{tr1}}{I_{tr2}} = \frac{I_{01}}{I_{02}} e^{-\alpha(d_1 - d_2)} \quad (5)$$

(where I_{01} and I_{02} are the light intensities incident on samples 1 and 2), one can eliminate the reflection coefficients and determine the quantity $e^{-\alpha(d_1 - d_2)}$ to within a constant factor I_{01}/I_{02}. The constant factor can be determined through normalization to the long-wavelength region, where the value of $e^{-\alpha(d_1 - d_2)}$ can be assumed equal to unity (weak absorption).

The I_{tr1}/I_{tr2} ratio was measured using a modulation technique similar to the one employed to determine the ratio of the luminescence intensities in the transmission and reflection geometries. The light striking the sample was previously passed through a monochromator having a wavelength matching that of the recording spectrometer (Fig. 1). This permitted us to exclude the effect of luminescence on the magnitude of the measured signal. Because the intensities of the two light beams were compared using an optical arrangement, both samples should have equal distributions of the intensity and of the spectral composition over the area of the light spot (to exclude the effect of possible mismatch between the monochromator and spectrometer). The light beam was split into two beams differing only in polarization. This was achieved by means of a natural Iceland spar crystal ($CaCO_3 \cdot H_2O$), which was placed between the monochromator slit and the condenser (Fig. 3). In the focal plane, the condenser produced two slit images due to the two light beams linearly polarized in mutually perpendicular directions. By properly varying the thickness of the Iceland spar crystal, we could change the distance between the two slit images. They were projected by the condenser onto two GaAs samples of different thickness. The distance between the images in the focal plane was 3 mm. The samples were placed the same distance apart on the end face of the regular

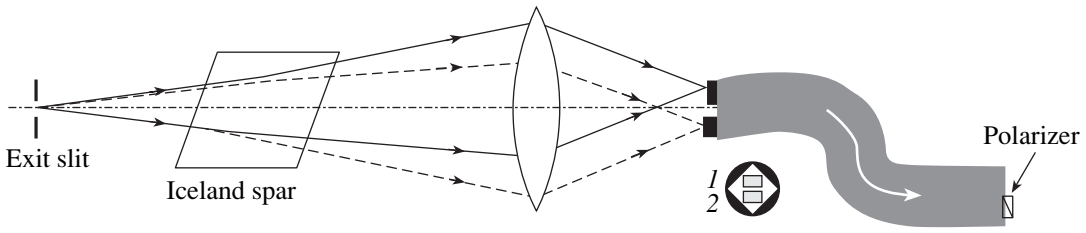

Fig. 3. Light beam splitting used to measure the absorption coefficient.

waveguide. The luminescence leaving the waveguide was completely depolarized. The other (output) end face of the fiber bunch could be turned so as to arrange the images of the crystals vertically, one under the other. This permitted us to translate them onto the entrance slit of the recording spectral instrument, as shown in Fig. 1. The modulation of one of the beams in intensity and the measurement of the beam intensity ratio were subsequently performed following the above technique (Fig. 1).

Figures 4 and 5 plot the absorption coefficient of the active *p*-GaAs layer [Ge concentration $(3–5)\times 10^{18}$ cm^{-3}] of the samples of the photocathode structure measured at the nitrogen boiling point and room temperature. At 77 K, the shape of the $\alpha(\lambda)$ dependence is affected by the splitting into light and heavy holes caused by the residual strains that originate from welding the structure with glass (the effect of strain-induced subband splitting is still more pronounced at lower temperatures [18]).

4. Figure 2a plots the values of I_{tr}/I_{ref} measured at room temperature (filled circles relate to excitation carried out through the solid-solution layer, and open ones, to pumping across the free GaAs surface). The solid curves are plots of Eq. (3). The calculation was performed using the values of the absorption coefficient measured earlier (Fig. 4). The best fit of the experimental to calculated relations is reached for $L = 4$ μm, $\xi_f = \eta_f\tau/L = 4$, and $\xi_i < 0.1$.

The optical orientation experiments carried out at liquid nitrogen temperature revealed a substantial effect of luminescence photon recycling on the distribution of the nonequilibrium carrier concentration away from the pumped surface into the bulk of the crystal [3]. In this case, determination of the kinetic parameters is no longer a simple problem, as it was at 300 K. The coincidence (to within the accuracy of measurement) of the experimental values of I_{tr}/I_{ref} obtained under pumping through the interface and the free surface (Fig. 2b) suggests, however, that recombination at the free surface has practically no effect on the stationary electron concentration distribution in terms of layer depth (the recombination velocity at the interface can be neglected). Thus, surface recombination does not influence the spatial distribution of the electrons and their effective lifetime at $T = 77$ K.

To determine the lifetime of photoexcited electrons, we carried out measurements of the degree of circular polarization of the recombination radiation involving optically oriented electrons in a transverse magnetic field (see [4, Chapter 1]). The luminescence was excited from the side of the heterointerface by circularly polarized light with photon energy $E_{h\nu} = 1.55$ eV ($\lambda = 800$ nm). To reduce the effect of recombination at the other (free of AlGaAs) surface, the measurements

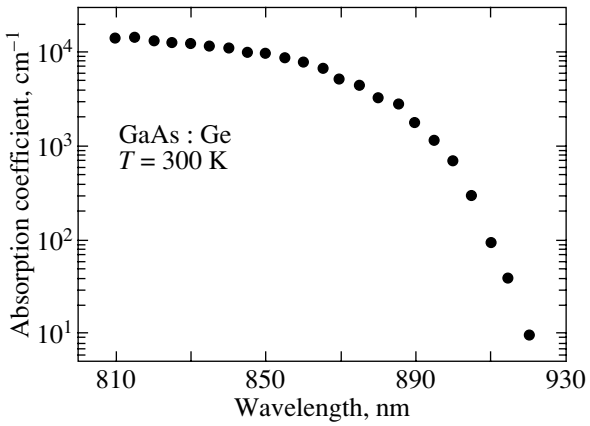

Fig. 4. Absorption coefficient of the GaAs : Ge sample plotted vs. wavelength at 300 K.

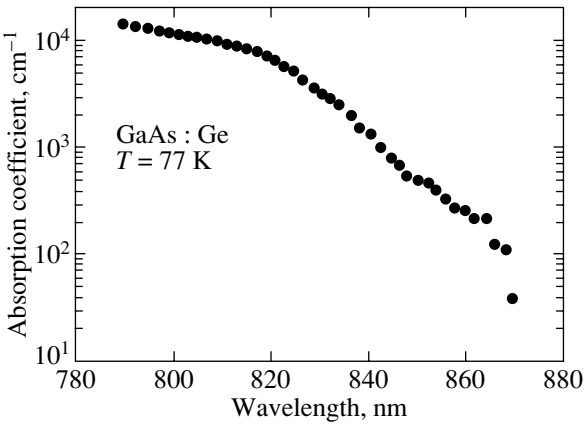

Fig. 5. Same as Fig. 4 but measured at $T = 77$ K.

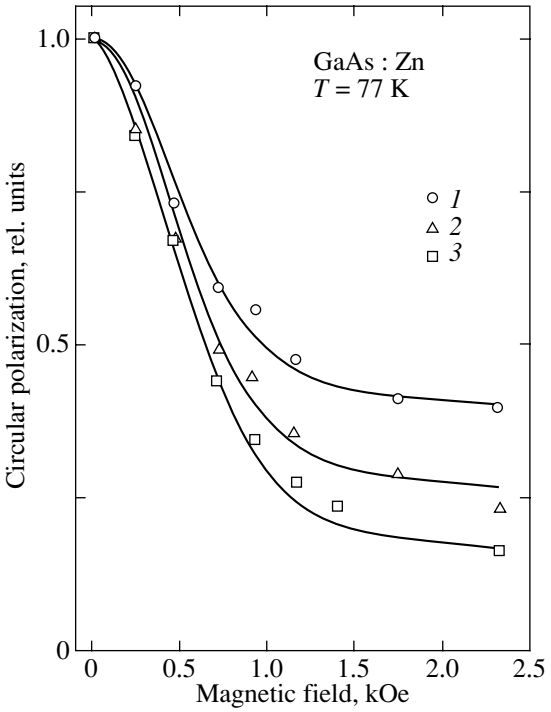

Fig. 6. Hanle effect measured in the transmission geometry under excitation through the free surface for different values of $E_{h\nu}$: (*1*) 1.85, (*2*) 1.74, and (*3*) 1.54 eV.

were conducted on the starting structure with GaAs layer thickness $d = 8$ μm. Assuming the g factor to be $g = -0.44$ [19], the lifetime was found to be $\tau = 2.3 \times 10^{-9}$ s.

The known values of L, τ, and ξ_f were used to calculate the diffusion coefficient $D = L^2/\tau = 70$ cm^2/s and the recombination velocity at the free surface $\eta_f = L\xi_f/\tau \approx 7 \times 10^5$ cm/s. The recombination velocity at the interface was estimated as $\eta_i < 10^4$ cm/s.

It should be noted that important parameters of the gallium arsenide layers, such as the absorption coefficient, the lifetime of photoexcited electrons, their diffusion length, and the surface recombination velocity, were measured under stationary conditions using the same setup (based on the light polarization modulation). The values of the parameters obtained by us agree with the data quoted by other authors [15, 20].

5. The results presented above were obtained on the uniformly doped samples described in the beginning of Section 2. The results described below were obtained on sample 1224 studied in [9]. This sample was a 0.4-mm-thick plane-parallel plate of Czochralski-grown gallium arsenide. Zinc was doped by diffusion through opposite sides of the plate [21]. The Zn dopant concentration was measured on both crystal surfaces to be 3×10^{18} cm^{-3}. After this, a layer of the $Al_xGa_{1-x}As$ solid solution ($x \approx 0.6$) was deposited through liquid phase epitaxy on one of the surfaces. This layer was optically transparent to the light used to excite the GaAs: 2.1 eV = E_g(AlGaAs) ≥ $E_{h\nu} \geq E_g$(GaAs) = 1.52 eV.

In [9], measurement of the luminescence depolarization was performed on optically oriented electrons in a transverse magnetic field at different pump photon energies. Samples were excited from the side of the free GaAs surface. The luminescence polarization was measured at the wavelength $\lambda = 850$ nm in the transmission geometry. Figure 6 plots normalized $\rho(H)$ dependences for photon energies of 1.85, 1.74, and 1.54 eV. We observe that the depolarization curves differ noticeably in width. The luminescence detected at different pump photon energies $E_{h\nu}$ emerged from regions of different depth (the electron diffusion length under such doping is small, $L_e \sim 1$ μm [3]). Thus, the spin orientation lifetime in the GaAs surface layer of thickness $\alpha^{-1} \sim 0.3$ μm ($E_{h\nu} = 1.85$ eV) is substantially shorter than that measured in the surface layer with thickness $\alpha^{-1} \sim 1$ μm ($E_{h\nu} = 1.54$ eV). This implies that the doping profile near the free GaAs surface is nonuniform.

The resultant doping profile obtained after Zn diffusion into GaAs was studied in [21]. It was shown that, at the doping temperature 850°C, zinc diffuses to produce a concentration $p \sim 10^{18}$ cm^{-3} not farther than 0.5–1 μm from the surface; directly at the surface, the doping level is two orders of magnitude higher. It is difficult to attain a more uniform doping; indeed, the zinc concentrations at the surface and in the bulk differ by a few times even when special measures are taken to counter this effect [22]. No efforts were made to level the doping profile in sample 1224. An epitaxially grown $Al_xGa_{1-x}As$ layer on one of the surfaces could, however, substantially lower the zinc concentration in the GaAs layer near the heterointerface.

Below, we present the results of the optical orientation experiments additionally performed on sample 1224. The experiments were conducted at 77 K in the reflection geometry [23].

We measured the spectra of luminescence and of the degree of its circular polarization under excitation from both sides of the sample at different pump energies. A tunable titanium–sapphire laser and a He–Ne laser ($E_{h\nu} = 1.96$ eV) were used as excitation sources. The electron spin relaxation times were determined in various experimental conditions.

When excited by circularly polarized light, the degree of circular polarization of photoluminescence (PL) as a function of transverse magnetic field can be fitted by a Lorentzian,

$$\rho(H) = \frac{\rho(0)}{1 + (H/H_{1/2})^2}.$$

The PL polarization in a zero magnetic field, $\rho(0)$, and the half-width $H_{1/2}$ are found from fitting the theoretical relation to the experimental data. Knowing $H_{1/2}$, one can derive the lifetime of the nonequilibrium spin ori-

entation T_s ($T_s^{-1} = \tau_s^{-1} + \tau^{-1}$; τ and τ_s are the electron lifetime and the spin relaxation time, respectively):

$$T_s = \hbar/(\mu_B g H_{1/2}). \quad (6)$$

The polarization in a zero magnetic field is $\rho(0) = \rho_{max}(T_s/\tau)$. Here, ρ_{max} is the PL polarization in the absence of spin relaxation. When excited near the fundamental absorption edge, $\rho_{max} = 25\%$; ρ_{max} decreases with increasing pumping energy and can become negative at a certain concentration of the acceptor impurity. Knowing $\rho(0)$ and T_s, we can determine the electron lifetime and spin relaxation time

$$\tau = \frac{\rho_{max}}{\rho(0)} T_s, \quad \tau_s = (1/T_s - 1/\tau)^{-1}. \quad (7)$$

Figure 7 presents the results of the Hanle effect experiments obtained under excitation from the side of the interface (Fig. 7a) and the free surface (Fig. 7b) at (*1*) $E_{h\nu} = 1.55$ and (*2*) 1.96 eV. The $\rho(H)$ relations are normalized, and the values of the PL polarization in a zero magnetic field are listed in the table.

The table also presents the values of the times calculated from Eqs. (6) and (7) using the experimental data. At $E_{h\nu} = 1.55$ eV, the excitation is quasi-resonant and, hence, $\rho_{max} = 25\%$ [4] (for both surfaces). The spin relaxation time determined for $\alpha^{-1} \sim 0.3$ μm ($E_{h\nu} = 1.85$ eV) is 0.6 ns for the region near the heterointerface and 0.4 ns for the free surface. When pumped from the side of the free surface with $E_{h\nu} = 1.96$ eV (nonresonant excitation), ρ_{max} was assumed equal to 7%, in accordance with [4, Chapter 2, item 4.1]. In this case, $\tau_s = 0.3$ ns.

Let us use known values of the spin relaxation time to estimate the acceptor concentration on both sides of the gallium arsenide layer. Because the doping level near the heterointerface is small, the D'yakonov–Perel' mechanism of electron spin relaxation should be dominant [24]. In this mechanism, the spin relaxation time is related to the momentum relaxation time of electrons τ_p. Accepting $\tau_s = 0.6$ ns for the spin relaxation time, we obtain $\tau_p = 0.7$ ps and the electron mobility $\mu_e = e\tau_p/m_e = 19\,500$ cm^2/Vs for gallium arsenide at 77 K. Such values of the electron mobility are characteristic of *p*-GaAs samples with doping levels on the order of 10^{16} cm^{-3} [25], i.e., for fairly pure samples.

Note that the experimental relations plotted in Fig. 7a coincide with one another; in other words, the

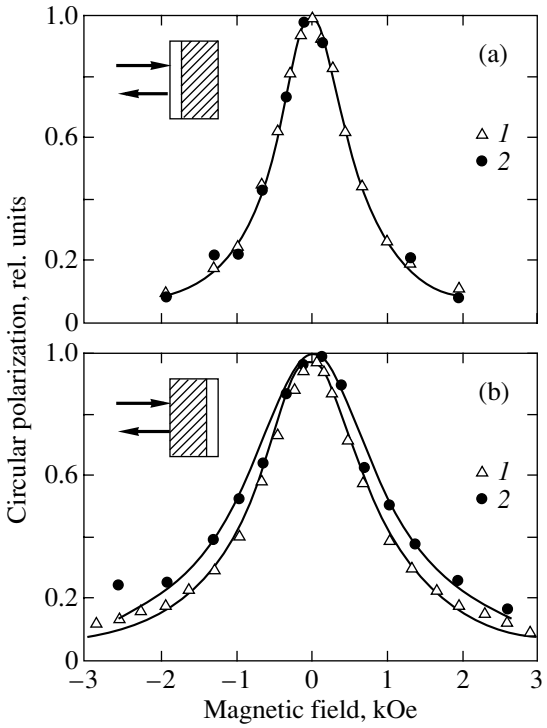

Fig. 7. Hanle effect measured in the reflection geometry under excitation (a) of the heterointerface and (b) of the free surface for $E_{h\nu}$ equal to (*1*) 1.55 and (*2*) 1.96 eV.

electron spin orientation lifetime T_s is the same in both cases. This means that the corresponding spin relaxation times are also equal. The latter implies, in turn, that the doping near the heterointerface is practically uniform, because these two experiments differ only in excitation energy (i.e., in the depth of the pumped layer).

The doping level in the immediate vicinity of the free surface should be estimated from the experimental data corresponding to excitation to high energy levels in the conduction band ($E_{h\nu} = 1.96$ eV). In this case, the absorption coefficient is fairly large and electrons will be created in a thin surface layer. Because the spin relaxation time in these conditions (0.4 ns; see table) is not very different from the value determined near the heterointerface (0.6 ns), it may be assumed that the spin relaxation of electrons near the free surface likewise occurs through the D'yakonov–Perel' mechanism. However, the spin relaxation time τ_s of electrons at the

Electron parameters in the conduction band of *p*-GaAs

	$E_{h\nu}$, eV	$H_{1/2}$, kOe	$\rho(0)$, %	T_s, ns	τ_s, ns	μ_e, cm^2/V s	D, cm^2/s	L, μm	L_s, μm
Heterointerface	1.55	0.60	7.5	0.4	0.6	19500	130	4.3	2.4
	1.96	0.58	−0.81	0.4					
Free surface	1.55	0.87	7.15	0.3	0.4				
	1.96	1.1	1.32	0.24	0.3				

free surface is shorter than that at the interface. Also, the momentum relaxation time of electrons τ_p is, by contrast, longer (in the D'yakonov–Perel' mechanism, τ_s is inversely proportional to τ_p). This situation corresponds to lower impurity concentrations, which is in contradiction to [21]. It seems reasonable to conclude that the electron spin relaxation near a free surface occurs through a mechanism other than the D'yakonov–Perel' mechanism.

Indeed, the impurity concentration near a free surface is high [21]; hence, the electron spin relaxation can proceed through the Bir–Aronov–Pikus mechanism, in which the electron spin relaxes during exchange interaction with holes. Here, the spin relaxation time is governed, in the end, by the concentration of acceptors (see [4, Chapter 3, items 5, 8.3.4]), which makes it possible to determine this concentration from the known spin relaxation time. For $\tau_s = 0.3$ ns, we obtain an estimate of the order of 10^{20} cm^{-3}. This value is in good agreement with the data reported in [21].

The nonuniformity of doping near the free surface becomes manifest in the experiment with quasi-resonant excitation on this surface ($E_{h\nu} = 1.55$ eV). In this case, electrons are generated in a thicker surface layer ($\alpha^{-1} \sim 1$ μm), which also includes, in addition to a heavily doped region, a lightly doped one [21], which should affect the measured spin relaxation velocity. Here the spin relaxation time (0.4 ns) is shorter than that calculated for the lightly doped region near the heterointerface but longer than the value of τ_s calculated for the heavily doped crystal region.

It should be pointed out that a straightforward comparison of edge luminescence spectra obtained under quasi-resonant and high-energy excitation from the side of the free surface also provides a convincing argument for the doping in sample 1224 being nonuniform. At room temperature, edge luminescence at $E_{h\nu} = 1.96$ eV produces one broad line (half-width 90 meV), whereas for $E_{h\nu} = 1.55$ eV its spectrum consists of two lines. The luminescence originating from the surface layer is complemented by recombination radiation emerging from deeper regions, which has a smaller half-width (20 meV) and a maximum shifted toward shorter wavelengths.

6. Thus, we have reported on the results obtained in an experimental study of gallium arsenide structures doped by germanium (samples 2.5 and 5 μm thick) and by zinc (0.4-mm-thick sample). The study was carried out using the optical orientation method. We have determined the kinetic parameters of electrons in the GaAs conduction band, namely, the lifetime, spin relaxation time, mobility, diffusion coefficient, and diffusion lengths of electrons and of their average spin (see table).

Eliminating the controversy between the conclusions drawn in [9] and [3, 11] is the main point of this work. While the Hanle effect was found in [9] to depend on the pump light wavelength, which was assigned to the effect of electron recombination at the gallium arsenide surface, the experiment conducted in [11] showed surface recombination to be insignificant. Our study revealed that the dependence of the Hanle effect on pump wavelength is due not to the electron surface recombination but rather to the nonuniformity of the acceptor impurity over the *p*-GaAs thickness. This conclusion finds support in studies on impurity diffusion during the growth of a structure [21].

The optical orientation measurements yielded the spin relaxation times (see table). It was found that the impurity concentrations near two opposite surfaces are different; more specifically, at the surface on which AlGaAs was grown (the heterointerface), the impurity concentration is small ($N_a = 10^{16}$ cm^{-3}), while near the free surface the doping level is high ($N_a = 10^{20}$ cm^{-3}) and then drops to 10^{18} cm^{-3} at distances of the order of one micron from the surface.

Thus, although determination of the kinetic parameters of recombination, electron transport, and electron average spin is more difficult under nonuniform doping, experimental data on the carrier optical orientation nevertheless make it possible to estimate the electron spin relaxation time and, in the end, to determine the impurity concentration in various regions of the GaAs/AlGaAs heterostructure.

ACKNOWLEDGMENTS

This study was supported by the Russian Foundation of Basic Research.

REFERENCES

1. G. A. Prinz, Science **282**, 1660 (1998).
2. R. I. Dzhioev, K. V. Kavokin, V. L. Korenev, *et al.*, Phys. Rev. B **66**, 245204 (2002); R. I. Dzhioev, B. P. Zakharchenya, V. L. Korenev, *et al.*, Pis'ma Zh. Éksp. Teor. Fiz. **74**, 200 (2001) [JETP Lett. **74**, 182 (2001)].
3. R. I. Dzhioev, B. P. Zakharchenya, K. V. Kavokin, and P. E. Pak, Fiz. Tverd. Tela (St. Petersburg) **36**, 2752 (1994) [Phys. Solid State **36**, 1501 (1994)].
4. *Optical Orientation, Modern Problems in Condensed Matter Science*, Ed. by F. Meier and B. P. Zakharchenya (North-Holland, Amsterdam, 1984; Nauka, Leningrad, 1989).
5. J. S. Sandhu, A. P. Heberle, J. J. Baumberg, and J. R. A. Cleaver, Phys. Rev. Lett. **86**, 2150 (2001).
6. R. I. Dzhioev, V. L. Korenev, I. A. Merkulov, *et al.*, Phys. Rev. Lett. **88**, 256801 (2002).
7. D. Z. Garbuzov, I. A. Merkulov, V. A. Novikov, and V. G. Fleĭsher, Fiz. Tekh. Poluprovodn. (Leningrad) **10**, 354 (1976) [Sov. Phys. Semicond. **10**, 552 (1976)].
8. A. S. Volkov, I. K. Volkova, A. L. Lipko, *et al.*, Fiz. Tekh. Poluprovodn. (Leningrad) **21**, 1893 (1987) [Sov. Phys. Semicond. **21**, 1146 (1987)].

9. D. Z. Garbuzov, R. I. Dzhioev, L. M. Kanskaya, and V. G. Fleĭsher, Fiz. Tverd. Tela (Leningrad) **14**, 1720 (1972) [Sov. Phys. Solid State **14**, 1481 (1972)].
10. R. I. Dzhioev, I. A. Merkulov, and V. A. Novikov, Fiz. Tekh. Poluprovodn. (Leningrad) **12**, 748 (1978) [Sov. Phys. Semicond. **12**, 437 (1978)].
11. R. I. Dzhioev and K. V. Kavokin, Fiz. Tverd. Tela (Leningrad) **33**, 2928 (1991) [Sov. Phys. Solid State **33**, 1654 (1991)].
12. P. Asbeck, J. Appl. Phys. **48**, 820 (1977).
13. A. Gavalini, B. Fraboni, and D. Cavalcoli, J. Appl. Phys. **71**, 5964 (1992).
14. J. Hayashi and M. B. Panish, J. Appl. Phys. **41**, 150 (1970).
15. J. P. Andre, P. Guittard, J. Hallais, and C. Piaget, J. Cryst. Growth **55**, 235 (1981).
16. H. C. Casey, Jr., D. D. Sell, and K. W. Wecht, J. Appl. Phys. **46**, 250 (1975).
17. S. N. Jasperson and S. E. Shnaterly, Rev. Sci. Instrum. **40**, 761 (1969).
18. D. D. Sell and H. C. Casey, Jr., J. Appl. Phys. **45**, 800 (1974).
19. C. Weisbuch and C. Hermann, Phys. Rev. B **15**, 816 (1977).
20. D. R. Wight, P. E. Oliver, T. Prentice, and V. W. Steward, J. Cryst. Growth **55**, 183 (1981).
21. S. Tiwari, J. Hintzman, and A. Callegari, Appl. Phys. Lett. **51**, 2118 (1987); K. B. Kahen, Appl. Phys. Lett. **55**, 2117 (1990).
22. T. Wada, A. Takeda, M. Ichimura, *et al.*, in *Proceedings of the 3rd International Conference on Shallow Impurities in Semiconductors, Linkoping, Sweden* (1988).
23. R. I. Dzhioev, B. P. Zakharchenya, R. R. Ichkitidze, *et al.*, Fiz. Tverd. Tela (St. Petersburg) **35**, 2821 (1993) [Phys. Solid State **35**, 1396 (1993)].
24. M. I. D'yakonov and V. I. Perel', Fiz. Tverd. Tela (Leningrad) **13**, 3581 (1971) [Sov. Phys. Solid State **13**, 3023 (1971)].
25. W. Walukievicz, J. Lagowski, L. Jastrzebski, and M. C. Gatos, J. Appl. Phys. **50**, 5040 (1979).

Translated by G. Skrebtsov

Physics of the Solid State, Vol. 45, No. 12, 2003, pp. 2264–2270. Translated from Fizika Tverdogo Tela, Vol. 45, No. 12, 2003, pp. 2161–2167.

SEMICONDUCTORS AND DIELECTRICS

Shubnikov–de Haas Effect and Energy Spectra of Graphite–Nitric Acid Intercalation Compounds

V. A. Kulbachinskiĭ, N. E. Sorokina, S. V. Kuvshinnikov, and S. G. Ionov

Moscow State University, Vorob'evy gory, Moscow, 119992 Russia

Received May 22, 2003

Abstract—Single crystals of first- to fourth-stage graphite–nitric acid intercalation compounds are synthesized. The Hall and Shubnikov–de Haas effects are investigated in magnetic fields up to 6 T at low temperatures (≈4.2 K). The temperature dependence of the resistance is measured in the basal plane. The parameters of the crystal structure and the characteristics of the energy spectra of charge carriers are determined for all the compounds prepared. © *2003 MAIK "Nauka/Interperiodica".*

1. INTRODUCTION

For compounds with a layered structure, such as graphite, sulfides, selenides, iodides, and their intercalation compounds, the large difference between the interaction energy of atoms located in the same layer and the interaction energy of atoms located in adjacent layers leads to strong anisotropy of their physical properties. The graphite structure is formed by perfectly planar hexagonal layers. In a layer, carbon atoms are linked by strong covalent bonds. The distance between carbon atoms in the layer is found to be $b_0 = 0.1415$ nm. The interlayer spacing at room temperature is $d_0 = 0.33538$ nm [1], and the interlayer interaction is governed by weak van der Waals forces. Owing to this structure, atoms and molecules can be intercalated between layers, thus forming a new class of graphite intercalation compounds. In their lattice, planar layers of carbon alternate with layers formed by an intercalated material (intercalant). Graphite intercalation compounds exhibit metallic properties and high electrical conductivity, and some of these compounds are superconductors [2].

A large number of graphite intercalation compounds have been synthesized to date. These compounds have been intensively studied for the following reasons. First, owing to their specific physical and chemical properties, these materials have found wide practical application in the manufacturing of IR polarizers, low-energy neutron monochromators, light filters tuned to a particular wavelength, electrochemical devices used in optical displays, and heat-shield systems. Second, graphite intercalation compounds are of considerable interest as model objects for studying physical and chemical processes occurring in low-dimensional systems.

Graphite intercalation compounds are divided into two large classes, namely, donor and acceptor compounds. The redistribution of the electron density among intercalant molecules and carbon atoms in acceptor graphite intercalation compounds gives rise to additional delocalized holes in graphite layers. In donor compounds, intercalated molecules donate valence electrons and the conduction is provided by excess electrons in carbon layers. Acceptor compounds are formed upon intercalation of halogens, metal halides, and acids. Donor compounds are formed upon intercalation of alkali and alkaline-earth metals into the graphite matrix. Examples of donor compounds are C_4K, C_8Li, C_8Ca, C_4Hg, etc. Acceptor compounds have more complex compositions, such as $C_{16}Br_2$, $C_{20}FeCl_3$, $C_{16}ICl$, $C_{24}^+HSO_4^-2H_2SO_4$, and $C_{24}^+NO_3^-3HNO_3$ [3–5].

Moreover, there exist graphite intercalation compounds in which two intercalating agents are alternately located between layers. These are the so-called heterocompounds, for example, graphite intercalation compounds with $CuCl_2$ and ICl [5]. The heterocompounds have opened up fresh opportunities for synthesizing new materials with a unique combination of physicochemical properties.

The intercalation always leads to a considerable (twofold or threefold) increase in the spacing between graphite layers and can disturb the order of layer alternation typical of single-crystal graphite. The distinctive feature of graphite intercalation compounds is that the same intercalant can form a large variety of compounds with different compositions and structures. These compounds are referred to as stages. The stage number N is equal to the number of graphite layers between the nearest neighbor layers of an intercalated material. For graphite intercalation compounds, the intercalant layer thickness d_i and the identity periods I_c, that is,

$$I_c = d_i + (N-1)d_0, \tag{1}$$

have been determined with the use of the (001) reflections [3].

Graphite intercalation compounds are characterized by a strong anisotropy of the electrical conductivity $\eta =$

σ_a/σ_c, which is equal to 10^3–10^4 for pure graphite and increases to 10^5–10^6 in acceptor graphite intercalation compounds [4]. High conductivity σ_a of graphite intercalation compounds in the basal plane is determined by the composition of the intercalated material, the graphite type, and the stage number. As the intercalant content increases, the conductivity increases and reaches a maximum for second- or third-stage graphite intercalation compounds, predominantly for metal halide intercalation compounds [5].

The HNO_3-intercalated graphite is a representative of acceptor graphite intercalation compounds. There exist two modifications of graphite intercalation compounds with nitric acid, namely, the α and β modifications, which differ in the orientation and position of NO_3^- anions in the graphite matrix [6–12]. In the α-HNO_3-intercalated graphite modification of chemical formula $C_{5.5N}HNO_3$, nitric acid anions, whose structure can be represented in the form of triangles with nitrogen atoms situated at the centers and oxygen atoms occupying the vertices, are located perpendicularly to graphite planes between layers. In the β-HNO_3-intercalated graphite modification, the triangle planes are aligned parallel to the graphite layers. As a consequence, the amount of intercalant and the identity period of these graphite intercalation compounds are less than those of other intercalation compounds and the chemical formula can be written as $C_{8N}HNO_3$.

Upon cooling from room temperature, at which graphite intercalation compounds with nitric acid are synthesized, the intercalated acid transforms from the two-dimensional liquid phase into the solid phase. A superlattice that is commensurate to the graphite lattice along one direction and incommensurate along another direction is formed at $T = 250$ K. A decrease in the temperature to $T = 210$ K leads to the formation of a superlattice commensurate to the graphite structure along both directions. A similar superlattice was found, for example, in graphite–sulfuric acid intercalation compounds [13]. Takahashi *et al.* [14] investigated the de Haas–van Alphen effect in the third-stage graphite–nitric acid intercalation compound. These authors revealed seven different oscillation frequencies, which are most likely associated with the formation of an intercalant superlattice.

In this work, we studied samples of the α-HNO_3-intercalated graphite modification. The β modification was prepared from the α modification after holding in air for several days. In this case, we did not observe a superlattice, because it can only be formed upon slow cooling (for approximately 24 h), whereas the samples in our experiments were rapidly cooled (for a few minutes) in order to prevent degradation of the contacts.

The physical properties (electrical conductivity, temperature dependence of the resistance, phase transitions) of graphite intercalation compounds with nitric acid have been investigated in sufficient detail. In particular, Ubbelohde [15] examined the temperature dependence of the resistance R_c along the c axis for first- and second-stage graphite–nitric acid intercalation compounds. The anomalies revealed in the dependence $R_c(T)$ at a temperature of 253 K were attributed to an order–disorder phase transition (two-dimensional melting) in intercalant layers. Furthermore, the dependence $R_c(T)$ in the phase transition range exhibits a hysteresis characteristic of first-order phase transitions. Anomalies in the temperature dependences of the thermal expansion coefficient and the thermopower have also been observed at a temperature of 253 K.

Table 1. Synthesis times, HNO_3 concentrations, identity periods, and gains in the weight for graphite–nitric acid intercalation compounds of different stages

Stage number N	HNO_3 concentration, %	Synthesis time, h	Identity period I_c, nm	Gain in weight, %
1	98	1	0.798	100
2	98	0.5	1.121	53
3	85	1	1.456	38
4	83	1.5	1.807	31

Fisher *et al.* [16] investigated the optical and electrical properties of first- to third-stage graphite–nitric acid intercalation compounds. It was shown that these materials possess metallic properties. However, attempts of these authors to use the Drude theory demonstrated that this simple model is inapplicable.

The properties and synthesis of HNO_3- and H_2SO_4-intercalated graphites, which are the initial materials for preparing cellular graphite, have been investigated in a large number of works. Nitric acid is a strong oxidizing agent. Consequently, the synthesis of graphite intercalation compounds in the HNO_3–graphite system, unlike the H_2SO_4–graphite system, can be performed without additional chemical or electrochemical oxidation [17].

The purpose of this work was to investigate the Shubnikov–de Haas and Hall effects in first- to fourth-stage graphite–nitric acid intercalation compounds and to calculate the parameters of the energy spectra according to the Blinowski–Rigaux model.

2. SAMPLE PREPARATION AND EXPERIMENTAL TECHNIQUE

Graphite and 98 ($d = 1.51$ g/cm^3), 85, and 83% nitric acids (reagent grade) served as initial compounds for synthesizing graphite nitrate. We used an oriented UPV-1-TMO pyrolytic graphite prepared by thermomechanical treatment at a temperature above 3000°C. The misorientation angle of the crystals with respect to the c axis was equal to 71′, and the carbon content was 99.999%. Graphite samples were prepared in the form of plates 2×5 mm in size, 0.1–0.25 mm in thickness,

Table 2. Extremal cross sections of the Fermi surface, charge carrier densities P_{osc}, Hall coefficients R_H, and Hall densities P_{Hall} of holes in graphite–nitric acid intercalation compounds

Stage number N	S_{extr1}, 10^{13} cm^{-2}	S_{extr2}, 10^{13} cm^{-2}	S_{extr3}, 10^{13} cm^{-2}	P_{osc}, 10^{21} cm^{-3}	R_H, cm^3/C	P_{Hall}, 10^{21} cm^{-3}
1	2.99	–	–	0.04	0.06	0.10
2	3.40	14.30	–	0.16	0.05	0.13
3	2.40	4.30	23.80	0.21	0.01	0.60
4	0.57	14.30	–	0.08	0.15	0.04

and 10–15 mg in weight. For single-crystal samples, the interplanar distance was equal to 0.3354–0.3359 nm.

The second- to fourth-stage graphite intercalation compounds were synthesized by the liquid-phase method. The graphite plates were immersed in a hermetically sealed vessel containing 2–3 ml of an HNO_3 solution for a time. The first-stage graphite intercalation compound was prepared by anodic oxidation of graphite in HNO_3 in a three-electrode cell under galvanostatic conditions (I = 1.5 mA) according to the procedure described in [18]. The synthesis times and HNO_3 concentrations necessary for preparing particular stages are presented in Table 1.

All the graphite–nitric acid intercalation compounds synthesized were investigated using x-ray diffraction on a DRON-2 diffractometer. The identity periods I_c were in good agreement with those available in the literature for the α modification (Table 1). Another important characteristic of graphite intercalation compounds is the gain in weight (Δm) of the sample upon intercalation. According to the gravimetric data (Table 1), the graphite–nitric acid intercalation compounds have the formula $C_{5.5N}HNO_3$. This corresponds to the compositions of stages N for the given graphite intercalation compounds, which, like all compounds of this type, are characterized by an extended homogeneity region. The measurements were carried out using only perfect single-phase samples of first- to fourth-stage α-HNO_3-intercalated graphite modifications.

The temperature dependences of the electrical resistance, galvanomagnetic properties (the longitudinal and transverse magnetoresistances, the Hall effect), and the Shubnikov–de Haas effect were measured by the standard dc four-point probe method. Contacts were produced with a silver paste. Stationary magnetic fields with a strength up to 6 T were generated by a superconducting solenoid placed in liquid helium. When studying the quantum oscillation effects, the monotonic part of the magnetoresistance was compensated. In order to exclude thermoelectric and thermomagnetic effects, all measurements were performed four times in two opposite directions of the field and current flowing through the samples. The samples were cooled to the liquid-helium temperature in a matter of minutes, which did not result in the formation of an ordered structure in layers of intercalated nitric acid.

3. THE SHUBNIKOV–DE HAAS EFFECT IN GRAPHITE–NITRIC ACID INTERCALATION COMPOUNDS

The Shubnikov–de Haas effect was observed in the graphite–nitric acid intercalation compounds of all stages at the liquid-helium temperature. Figure 1 shows the oscillating parts of the transverse magnetoresistance and their Fourier spectra of the first- to fourth-stage graphite–nitric acid intercalation compounds. The observed oscillation frequencies are designated by F_i.

The extremal cross sections S_{extr} of the Fermi surface and the charge carrier densities P_{osc} (Table 2) were determined from the frequencies of quantum oscillations of the transverse magnetoresistance. The Hall densities P_{Hall} of holes in the graphite intercalation compounds under investigation are also listed in Table 2. The charge carrier densities P_{osc} were calculated from the relationship

$$P_{osc} = \frac{4\sum_i S_{extri}}{(2\pi\hbar)^2[d_i + (N-1)d_0]} \qquad (2)$$

under the assumption that the Fermi surface consists of smooth cylinders. In relationship (2), factor 4 accounts for the Pauli exclusion principle and the fact that, in the case of graphite intercalation compounds, there are two cylinders of the Fermi surface with the extremal cross section S_{extri} for every band with index i (the summation is performed over different occupied bands).

The Hall effect was measured with the aim of determining the densities of free charge carriers in the graphite intercalation compounds. For single-phase samples of the same stage, the Shubnikov–de Haas oscillation frequencies and, hence, the densities of delocalized charge carriers can differ by 10%.

4. THE HALL EFFECT AND THE TEMPERATURE DEPENDENCE OF THE RESISTANCE

For a number of samples, we measured the temperature dependences of the resistance. These measurements were complicated at temperatures above the phase transition point T_c (T_c = 210 K is the solidification temperature of nitric acid in graphite intercalation compounds), because nitric acid in the layers becomes liq-

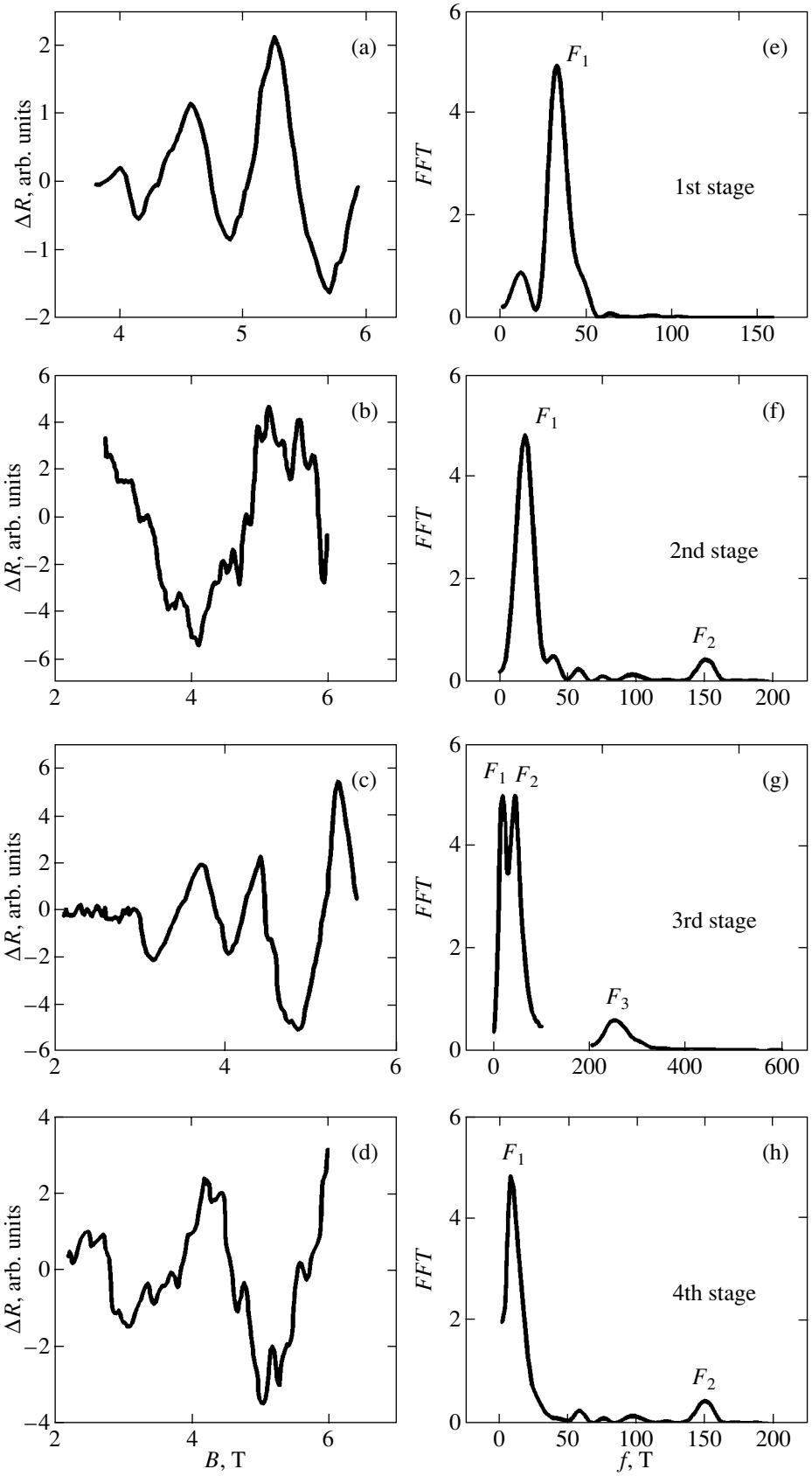

Fig. 1. (a–d) Shubnikov–de Haas oscillations and (e–h) Fourier spectra of first- to fourth-stage graphite–nitric acid intercalation compounds.

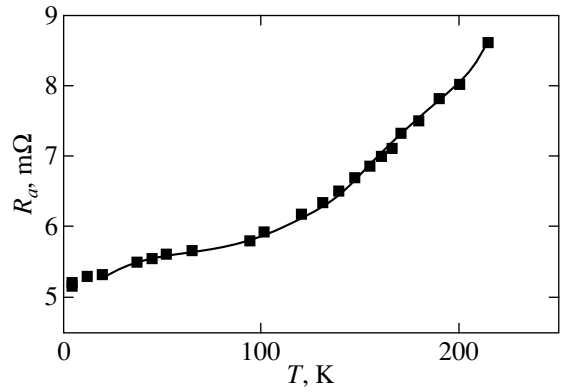

Fig. 2. Temperature dependence of the resistance R_a of the second stage graphite–nitric acid intercalation compound.

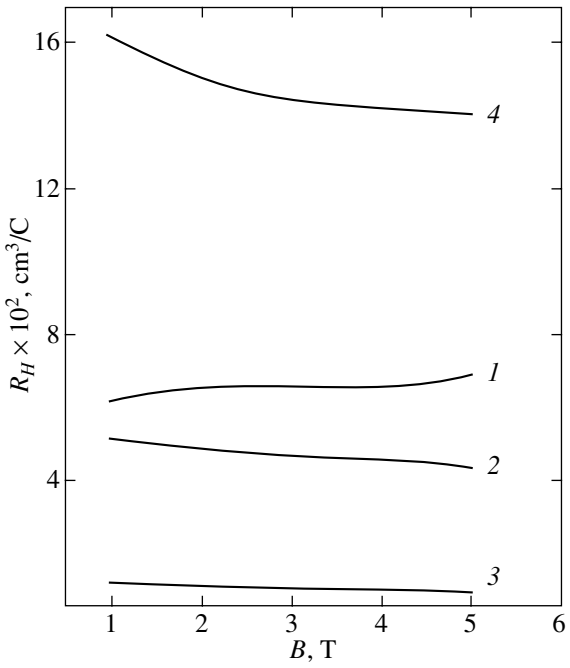

Fig. 3. Dependences of the Hall coefficient R_H on the magnetic field strength for the first- to fourth-stage graphite–nitric acid intercalation compounds (numerals near the curves correspond to the stage numbers).

uid and attacks the contacts. The temperature dependence of the resistance R_a in the basal plane for the second-stage graphite intercalation compound is plotted in Fig. 2. It can be seen from this figure that the dependence of the resistance exhibits a metallic behavior, which is in agreement with the available data on the metallic properties of graphite–nitric acid intercalation compounds [16].

The Hall effect in HNO_3-intercalated graphite samples was measured at a temperature of 4.2 K. The dependences of the Hall coefficient R_H on the magnetic field strength for the first- to fourth-stage graphite–nitric acid intercalation compounds are depicted in Fig. 3. As can be seen from this figure, the Hall coefficient for the first- to third-stage samples is virtually independent of the magnetic field strength, whereas the Hall coefficient for the fourth-stage sample decreases with an increase in the magnetic field strength. This is explained by the fact that the fourth-stage sample has a sandwich structure in which four graphite layers are located between two intercalant layers. Two inner graphite layers are not in contact with the intercalant and possess the properties of pure graphite if the screening length does not exceed the interlayer spacing. In our case, this condition is satisfied, because the Shubnikov–de Haas oscillations at the frequency corresponding to graphite are observed for the fourth-stage sample (Fig. 1d). Graphite is a semimetal in which electrons and holes are charge carriers. At the same time, it is known that, for materials with several types of charge carriers, the Hall coefficient always decreases in a magnetic field, which is observed for the fourth-stage graphite intercalation compound. Seemingly, a similar behavior of the Hall coefficient should also be observed for the third-stage graphite intercalation compound. However, this material is characterized by a very high hole density and, hence, a small Hall coefficient, which is determined with a considerably lower accuracy as compared to that for the fourth-stage graphite intercalation compound. Moreover, only one inner graphite layer is not in contact with the intercalant in the structure of the third-stage sample. When the charge transfer to this layer is absent upon intercalation and the hole density is very high, electrons of the layer make only a small additional contribution.

The Hall coefficients were used to calculate the charge carrier densities from the formula $P_{\text{Hall}} = 1/eR_{\text{H}}$ (Table 2). The charge carrier densities determined from the Hall effect are in reasonable agreement with those obtained from the experimental data on the quantum oscillations. The differences are primarily associated with the fact that the Hall density was evaluated from the formula valid for one type of charge carriers, whereas the third-stage and fourth-stage graphite intercalation compounds involve several types of charge carriers. The data presented in Table 2 indicate that the third-stage sample has the highest density of charge carriers.

5. ENERGY SPECTRA OF GRAPHITE–NITRIC ACID INTERCALATION COMPOUNDS

In 1980, Blinowski and Rigaux [19–21] proposed a model for the energy spectrum of low-stage acceptor graphite intercalation compounds. Within this model, first-stage graphite intercalation compounds are treated as systems of equivalent noninteracting graphite layers. The dispersion law for first-stage acceptor graphite intercalation compounds can be written in the form

$$E_{c,v} = \pm\frac{3}{2}\gamma_0 b_0 k, \qquad (3)$$

where γ_0 is the parameter describing the interaction of the nearest neighbor carbon atoms in the layer.

For second-stage graphite intercalation compounds, only the interactions of adjacent carbon atoms in the basal plane (described by the parameter γ_0) and the nearest neighbor atoms in adjacent layers (described by the parameter γ_1) are considered in a subsystem of two graphite layers. The dispersion laws for the valence and conduction bands have the form

$$E_1 \equiv -E_{v_1} = E_{c_1} = \frac{1}{2}\{-\gamma_1 + [\gamma_1^2 + 9\gamma_0^2 b_0^2 k^2]^{1/2}\}, \quad (4)$$

$$E_2 \equiv -E_{v_2} = E_{c_2} = \frac{1}{2}\{\gamma_1 + [\gamma_1^2 + 9\gamma_0^2 b_0^2 k^2]^{1/2}\}. \quad (5)$$

In third-stage graphite intercalation compounds, graphite layers are not equivalent with respect to the intercalant and the parameter δ, which characterizes the difference between the potential energies of carbon atoms in outer and inner layers, appears in calculations. The energy spectrum of third-stage graphite intercalation compounds consists of six branches:

$$E_1^{c,v} = \delta \pm |x|, \quad (6)$$

$$E_2^{c,v} = \pm\{\delta^2 + \gamma_1^2 + |x|^2 - [\gamma_1^4 + (4\delta^2 + 2\gamma_1^2)|x|^2]^{1/2}\}^{1/2}, \quad (7)$$

$$E_3^{c,v} = \pm\{\delta^2 + \gamma_1^2 + |x|^2 + [\gamma_1^4 + (4\delta^2 + 2\gamma_1^2)|x|^2]^{1/2}\}^{1/2}, \quad (8)$$

where $|x| = 3\gamma_0 b_0 k$ and δ is the parameter dependent on the distribution of excess charge over the inner and outer graphite layers. Therefore, the energy spectrum of both the conduction and valence bands involves three branches. From a comparison of experimental data on the optical reflection in graphite intercalation compounds with the results of theoretical calculations, the above parameter was estimated as $\delta \approx 0.2$ eV. For this parameter δ, the fraction of the excess charge redistributed into the inner graphite layer was evaluated to be $z = 0.15$. The uniform charge distribution over three graphite layers is characterized by $z = 1/3$. It should be noted that, in the case when the inner graphite layer is completely screened, the Shubnikov–de Haas oscillations in third-stage graphite intercalation compounds should be observed at a frequency corresponding to pure graphite.

Undeniably, the Blinowski–Rigaux model can only be considered a simplified approach. However, this model adequately describes the data on the optical reflection in a number of low-stage acceptor graphite intercalation compounds. Within this model, the Fermi surface of first-stage acceptor graphite intercalation compounds ($N = 1$) consists of two cylinders located along the edges of the hexagonal Brillouin zone (as a rule, it is depicted as six cylinders located along all edges, so that the total volume of the Fermi surface per band is equal to 6/3 = 2). The Fermi surface of second-stage intercalation compounds with strong acceptors is composed of coaxial cylinders (two cylinders per band). For third-stage intercalation compounds, the number of coaxial cylinders can be equal to three at a high Fermi energy, i.e., when three bands are occupied (the total number of cylinders is six).

Dresselhaus *et al.* [22] proposed a model for describing the energy spectra of dilute graphite intercalation compounds with large stage numbers (beginning with at least the fourth stage). According to this model, the intercalation does not lead to a substantial change in the band structure of graphite and is only accompanied by a lowering (for acceptors) or raising (for donors) of the Fermi level (the so-called rigid-band model). If this were the case with HNO_3-intercalated graphite, Shubnikov–de Haas oscillations at a frequency slightly higher than the frequency corresponding to graphite would be observed for the fourth-stage intercalation compound. However, the experimental data demonstrate that the oscillations occur at both high frequencies and the frequency corresponding to graphite. This implies that the two inner graphite layers between the nearest intercalant layers are screened completely. The high-frequency oscillations are associated with two graphite layers adjacent to the intercalant layers. To put it differently, the system is extremely inhomogeneous and can be represented as a one-dimensional superlattice composed of alternating layers (double graphite layers alternate with graphite–intercalant–graphite layers) with high metallic conductivity. A similar heterogeneous two-phase structure of high-stage graphite–Br_2 intercalation compounds was considered earlier by Bender and Young [23].

In order to describe the energy spectra of first- to third-stage graphite–nitric acid intercalation compounds, we use relationships (3)–(8). The experimental data agree well with the theoretical predictions. Actually, for the first-stage graphite intercalation compound, there is one hole band and the oscillations are observed at one frequency F_1 (Fig. 1e). In the case of the second-stage graphite intercalation compound, two hole bands are occupied and the oscillations occur at two frequencies F_1 and F_2 (Fig. 1f). For the third-stage graphite intercalation compound, three hole bands are occupied and the oscillations are observed at three frequencies F_1, F_2, and F_3 (Fig. 1g). The Fermi energy E_F for the first-stage compound can be calculated from formula (3) and the experimental cross section of the Fermi surface (Table 2). Moreover, it is necessary to know the parameter γ_0 describing the interaction of the nearest neighbor carbon atoms in the layer. This parameter for intercalation compounds remains virtually unchanged. Hence, we performed our calculations with the parameter $\gamma_0 = 3.2$ eV, which is characteristic of graphite. The determination of the Fermi energy for graphite intercalation compounds of other stages requires knowledge of the parameter γ_1. This parameter

for graphite intercalation compounds, as a rule, is either equal to or slightly smaller than that for graphite [24–26]. For this reason, we used the approximate value $\gamma_1 = 0.3$ eV. For the first-stage compound, the Fermi energy was found to be $E_F = 0.21$ eV. From relationships (4) and (5), we obtained $E_F = 0.42$ eV for the second-stage compound. Finally, from expressions (6)–(8), we determined the Fermi energy $E_F = 0.75$ eV for the third-stage compound.

6. CONCLUSIONS

Thus, we synthesized perfect single crystals of first- to fourth-stage graphite–nitric acid intercalation compounds and investigated the Hall and Shubnikov–de Haas effects. The results obtained are consistent with the Blinowski–Rigaux two-dimensional model for graphite intercalation compounds. Within this model, we calculated the Fermi energies for the materials synthesized.

REFERENCES

1. R. E. Franclin, Acta Crystallogr. **3**, 253 (1951).
2. S. V. Shulepov, *Physics of Graphitic Carbon Materials* (Metallurgiya, Moscow, 1972).
3. A. Herold, NATO ASI Ser., Ser. B **172**, 3 (1987).
4. M. S. Dresselhaus, Proc. NATO, Ser. B **16**, 102 (1980).
5. V. V. Avdeev, V. Ya. Akim, N. B. Brandt, *et al.*, Zh. Éksp. Teor. Fiz. **94** (12), 188 (1988) [Sov. Phys. JETP **67**, 2496 (1988)].
6. R. Moreh, O. Shahal, and G. Kimmel, Phys. Rev. B **33**, 5717 (1986).
7. P. Touzain, Synth. Met. **1**, 3 (1979).
8. E. J. Samuelsen, R. Moret, and R. Comes, Synth. Met., No. 10, 13 (1984).
9. F. Batallan, I. Rosenman, A. Magerl, and H. Fuzellier, Physica B (Amsterdam) **136**, 12 (1986).
10. I. Rosenman, Ch. Simon, F. Batallan, *et al.*, Synth. Met. **23**, 339 (1988).
11. R. Moret, R. Comes, G. Furdin, *et al.*, Mater. Res. Soc. Symp. Proc. **20**, 27 (1983).
12. H. Shaked, H. Pinto, and M. Melamud, Phys. Rev. B **35**, 838 (1987).
13. N. B. Brandt, V. A. Kul'bachinskiĭ, S. A. Lapin, *et al.*, Fiz. Tverd. Tela (Leningrad) **32**, 94 (1990) [Sov. Phys. Solid State **32**, 51 (1990)].
14. O. Takahashi, Y. Iye, and S. Tanuma, Solid State Commun. **37**, 863 (1981).
15. A. R. Ubbelohde, Proc. R. Soc. London, Ser. A **304**, 72 (1968).
16. J. E. Fisher, T. E. Thompson, G. M. T. Foley, *et al.*, Phys. Rev. Lett. **37**, 769 (1976).
17. W. S. Forsman, T. Dziemianowicz, K. Leong, and D. Carl, Synth. Met. **5**, 77 (1983).
18. V. V. Avdeev, O. A. Tverezovskaya, N. E. Sorokina, *et al.*, Neorg. Mater. **36**, 276 (2000).
19. J. Blinowski, Nguyen Hy Hay, C. Rigaux, and J. P. Vieren, J. Phys. (Paris) **41**, 47 (1980).
20. J. Blinowski and C. Rigaux, J. Phys. (Paris) **41**, 667 (1980).
21. Nguyen Hy Hay, J. Blinowski, C. Rigaux, and R. Letoullec, Synth. Met. **3**, 99 (1981).
22. M. S. Dresselhaus, G. Dresselhaus, and G. E. Fisher, Phys. Rev. B **15**, 3180 (1977).
23. A. S. Bender and D. A. Young, J. Phys. Chem. **5**, 2163 (1972).
24. V. A. Kulbachinskii, S. G. Ionov, S. A. Lapin, and A. de Visser, Phys. Rev. B **51**, 10313 (1995).
25. V. A. Kulbachinskii, S. G. Ionov, S. A. Lapin, and V. V. Avdeev, J. Phys. I **2**, 1941 (1992).
26. V. A. Kulbachinskii, S. G. Ionov, S. A. Lapin, *et al.*, Mol. Cryst. Liq. Cryst. **245**, 31 (1994).

Translated by O. Borovik-Romanova

Physics of the Solid State, Vol. 45, No. 12, 2003, pp. 2271–2275. Translated from Fizika Tverdogo Tela, Vol. 45, No. 12, 2003, pp. 2168–2172.

SEMICONDUCTORS AND DIELECTRICS

Effects of Averaging of Spin Packets of Interacting Resonances in Gd^{3+} EPR Spectra of Scheelites

V. A. Vazhenin, V. B. Guseva, and M. Yu. Artemov

Research Institute of Physics and Applied Mathematics, Ural State University, pr. Lenina 51, Yekaterinburg, 620083 Russia
e-mail: vladimir.vazhenin@usu.ru

Received May 6, 2003

Abstract—The EPR spectra of Gd^{3+} tetragonal centers in crystals with a scheelite structure are analyzed. It is found that the EPR spectra exhibit additional signals in the vicinity of coincidence of the resonance lines attributed to Gd^{3+} EPR transitions. It is shown that these signals are caused by averaging (due to relaxation spin–lattice transitions between the resonance doublets) of the internal part of the quasi-symmetric system of spin packets corresponding to the inhomogeneously broadened initial EPR lines. The quasi-symmetric arrangement of the spin packets is associated with the mosaic structure of the studied crystals. © *2003 MAIK "Nauka/Interperiodica".*

1. As was shown earlier in [1–4], an additional EPR signal appears between the initial signals when the orientation of a polarizing magnetic field corresponds to the coincidence of the resonance lines associated with two EPR transitions. The initial EPR signals were attributed either to different transitions of a high-spin center in [1–3] or to hyperfine components of two off-center configurations related through thermally activated transitions of a low-spin center in [4]. It is believed that, in all cases, the transitions between the initial resonances are due to spin–spin, spin–lattice, or orientational relaxation.

In our previous works [5, 6], we demonstrated that an additional signal in the EPR spectrum of $Pb_5Ge_3O_{11}:Gd^{3+}$ is caused by averaging (due to relaxation spin–lattice transitions between the resonance doublets) of the internal part of the quasi-symmetric spin packets corresponding to the initial lines. The quasi-symmetric structure of spin packets for a pair of initial lines is associated with the spread of the spin Hamiltonian parameters b_{21} and b_{43}. This spread increases as the ferroelectric phase transition point is approached. Within the proposed model of a three-component EPR spectrum, we performed computer simulation of the temperature dependences of the spin-packet width and the rate of relaxation between the resonance doublets. It was found that these temperature dependences ($\sim T^2$) exhibit a narrow maximum in the vicinity of the ferroelectric phase transition point. In [7], we made an attempt, within this model, to explain the appearance of the additional signals revealed in [2–4] in the vicinity of accidental coincidence of the resonance lines attributed to EPR transitions.

The purpose of this work was to elucidate the mechanisms responsible for the appearance of additional signals in the range close to the intersections of the angular dependences of the positions of the EPR signals assigned to the transitions of Gd^{3+} tetragonal centers (symmetry group S_4) in crystals with a scheelite structure.

2. The experiments were performed with $SrMoO_4$ single crystals doped by gadolinium oxide (0.2 and 0.007 mol % in the batch) and compensated with sodium and also $CaWO_4$, $PbWO_4$, $CaMoO_4$, and $PbMoO_4$ crystals containing Gd^{3+} impurity tetragonal centers. The EPR spectra were recorded on a spectrometer operating in the 3-cm band.

For the majority of the samples, the EPR spectra measured at a small misorientation ($\Delta\theta = \theta - \theta_0 \approx 0.2°$) with respect to $\theta_0 \approx 50°$ (θ_0 is the polar angle at which the initial resonances coincide with each other) exhibit weak signals of two-photon transitions between the signals associated with the $3 \rightleftharpoons 4$ and $4 \rightleftharpoons 5$ transitions. The assignment of the weak signals to two-photon transitions is supported by the decrease in their relative intensity with a decrease in the microwave power. For the other samples, a decrease in the microwave power leads to an improvement of the resolution of the initial signals, which, in our opinion, can also be explained by the decrease in the intensity of unresolved lines of the two-photon transitions. No two-photon transitions are observed in the range where the angular dependences of the positions of the signals attributed to the $4 \rightleftharpoons 5$ and $5 \rightleftharpoons 6$ transitions intersect each other.

The Gd^{3+} EPR spectra of $SrMoO_4$ crystals at both impurity contents and the spectra of $CaWO_4$ and $CaMoO_4$ crystals contain three lines (Fig. 2) in the range where the positions of the signals associated with the $3 \rightleftharpoons 4$ and $5 \rightleftharpoons 6$ transitions coincide with each other (Fig. 1, $\theta_0 \approx 40°$). A variation in the azimuthal angle does not substantially affect the relative intensity of the additional signal. In the temperature range 140–

1063-7834/03/4512-2271$24.00

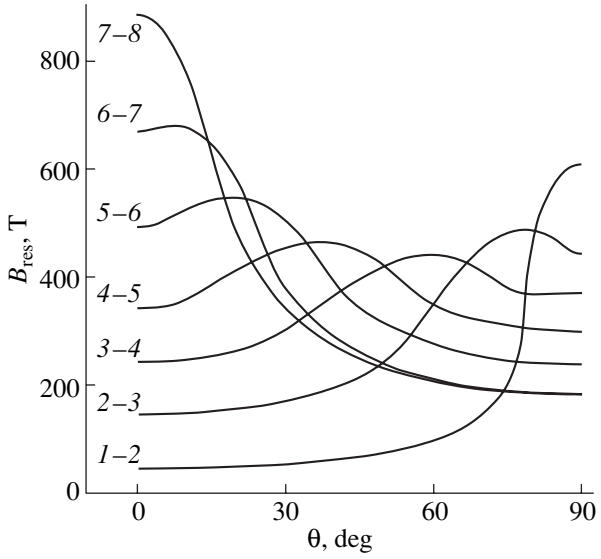

Fig. 1. Polar angular dependences of the position of the EPR signal of Gd^{3+} tetragonal centers in $SrMoO_4$ [8] at φ = 0. Variation in the azimuthal angle weakly affects the polar dependences. Numbers on the curves indicate the numbering of states involved in the transitions. Angular dependences of B_{res} for other crystals with a scheelite structure [9] are similar to those depicted in this figure.

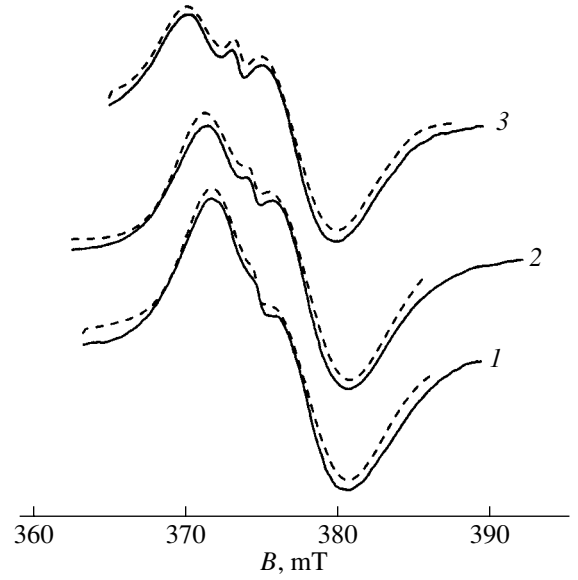

Fig. 2. EPR spectra of $SrMoO_4$ (0.2 mol % Gd^{3+}) in the vicinity of the coincidence of the signals associated with the $3 \rightleftharpoons 4$ and $5 \rightleftharpoons 6$ transitions ($\theta_0 \approx 40°$): (*1*) $\Delta\theta \approx 0.25°$, T = 225 K; (*2*) $\Delta\theta \approx 0.33°$, T = 329 K; and (*3*) $\Delta\theta \approx 0.68°$, T = 483 K. Solid lines are experimental data. Dashed lines represent the results of computer simulation.

540 K, the intensity of the additional signal at a constant misorientation angle Δθ increases only slightly with an increase in the temperature. The misorientation angles (Fig. 2) were chosen in such a way as to provide the most efficient detection of additional signals.

The EPR spectra of $CaWO_4$ and heavily doped $SrMoO_4$ crystals (Fig. 3) also exhibit an additional signal between the signals of the $3 \rightleftharpoons 4$ and $6 \rightleftharpoons 7$ transitions in the range where the angular dependences of their positions intersect each other (Fig. 1, $\theta_0 \approx 35°$). Note that no additional signals were observed in [1–4] when the positions of the signals corresponding to transitions in doublets separated by more than one energy interval coincided with each other. This brings up the question as to whether the signal of the two-photon transition observed in the vicinity of the coincidence of the signals attributed to the $3 \rightleftharpoons 4$ and $4 \rightleftharpoons 5$ transitions masks an additional signal of a different nature, as is the case with transitions in the triplet of dimeric exchange clusters [2]. A comparison of the shape of the EPR spectrum of heavily doped $SrMoO_4 : Gd^{3+}$ (measured at a microwave power of 20 dB and $\Delta\theta = 0.35°$) with the initial signals recorded at $\Delta\theta = 1.5°$ and then shifted to the position at $\Delta\theta = 0.35°$ shows that, within the limits of experimental error, the spectrum contains no additional signal.

3. In order to elucidate the mechanisms responsible for the appearance of the additional signals, we examined the broadening of the EPR spectra. In the temperature range 140–540 K, the EPR linewidth for heavily doped $SrMoO_4$ (the $5 \rightleftharpoons 6$ transition for the orientation $\mathbf{B} \perp \mathbf{S}_4$ at $\Delta B_{pp}(300\ \text{K}) = 0.5$ mT, where ΔB_{pp} is the separation between the extrema of the first-order derivative of the absorption line) changes by no more than 0.3 mT. According to estimates, the spin–spin relaxation rate does not exceed 10^6 Hz. Therefore, the width

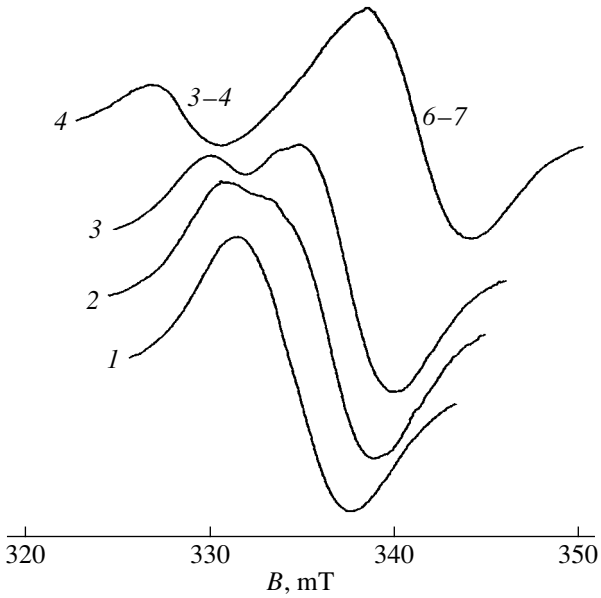

Fig. 3. EPR spectra of $SrMoO_4$ (0.2 mol % Gd^{3+}) in the vicinity of the coincidence of the signals associated with the $3 \rightleftharpoons 4$ and $6 \rightleftharpoons 7$ transitions ($\theta_0 \approx 35°$): $\Delta\theta \approx$ (*1*) 0.2°, (*2*) ≈0.3°, (*3*) ≈0.4°, and (*4*) ≈0.8°.

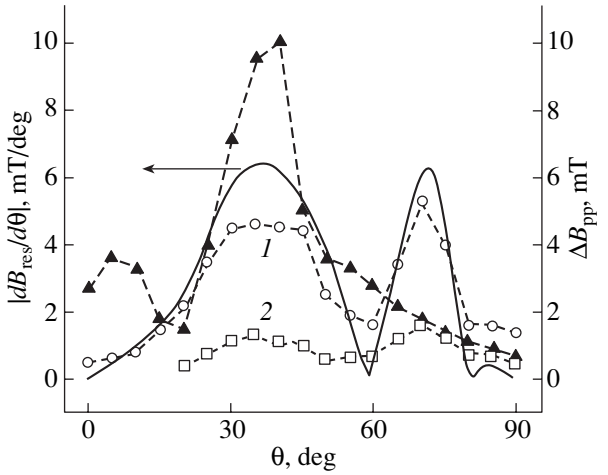

Fig. 4. Dependences of the EPR linewidth on the polar angle for (*1*) *3* ⇄ *4* (0.2 mol % Gd^{3+}), (*2*) *3* ⇄ *4* (0.007 mol % Gd^{3+}), and (*3*) *5* ⇄ *6* (0.2 mol % Gd^{3+}) transitions in $SrMoO_4$. The solid line shows the dependence of the magnitude of $\partial B_{res}/\partial\theta$ on the polar angle for the *3* ⇄ *4* transition in $SrMoO_4$.

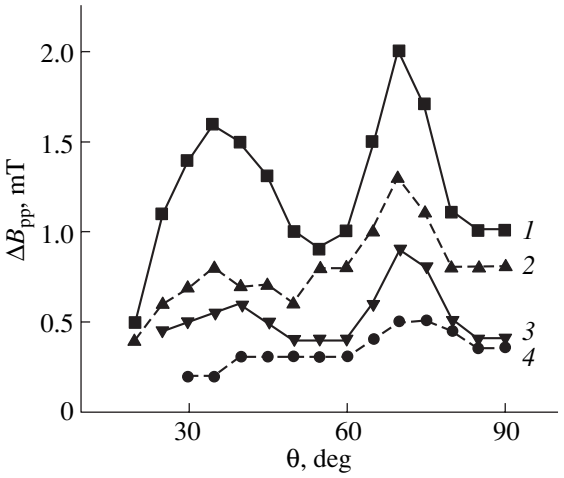

Fig. 5. Polar angular dependences of the Gd^{3+} EPR linewidth for the *3* ⇄ *4* transition in (*1*) $CaWO_4$, (*2*) $PbWO_4$, (*3*) $CaMoO_4$, and (*4*) $PbMoO_4$.

of the spin packet at room temperature should not exceed several tenths of mT.

For Gd^{3+} tetragonal centers in the majority of the studied crystals, the linewidth is characterized by strong anisotropy. The polar angular dependences of the linewidth ΔB_{pp} (Figs. 4, 5) correlate well with the orientation dependence of the magnitude of $\partial B_{res}/\partial\theta(\theta)$ (Fig. 4). A similar correlation is observed for other transitions. Hence, it follows that, in the vicinity of the maxima observed in the dependence $\Delta B_{pp}(\theta)$, the mosaic structure of the crystal makes a dominant contribution to the EPR linewidth. For heavily doped $SrMoO_4$, the mosaicity parameter was estimated from the peak-to-peak value of the angular dependence of the linewidth as follows: $\sqrt{\langle\Delta\theta^2\rangle} \approx 0.3°$.

It should be noted that additional signals are observed for crystals whose mosaic structure makes a significant contribution to the total linewidth. This finding is in agreement with our inference that the symmetric arrangement of the spin packets is a necessary condition for the appearance of a three-component spectrum [5, 6]. Since the angular dependences of the positions of the signals associated with the *3* ⇄ *4*, *5* ⇄ *6* and *3* ⇄ *4*, *6* ⇄ *7* transitions intersect in the vicinity of the maxima in the dependence $|\partial B_{res}/\partial\theta(\theta)|$ (Fig. 4) and the derivatives are opposite in sign (Fig. 1), the pair of initial signals should be characterized by a quasi-symmetric system of spin packets owing to the mosaic structure.

The aforementioned absence of the two-photon transition in the vicinity of the coincidence of the *5* ⇄ *6* and *4* ⇄ *5* transitions (see Section 2) can be associated with the asymmetric arrangement of the spin packets (as can be seen from Fig. 1, the values of $\partial B_{res}/\partial\theta$ for the *5* ⇄ *6* and *4* ⇄ *5* transitions differ significantly), which leads to a broadening of the EPR line attributed to the two-photon transition. Moreover, the EPR signal corresponding to this transition is difficult to observe because of the large difference between the intensities of the initial signals.

The contribution to the inhomogeneously broadened line, which depends only slightly on the orientation of the magnetic field and is unrelated to the mosaic structure, is most likely determined by the magnetic dipole interaction and the spread of the fine-structure parameters due to random electric and strain fields. The changes in the parameters of the second-rank spin Hamiltonian [10] in an electric field E_i [11] at a strain e_{ij} [12] can be represented by the expressions

$$\begin{aligned}
\Delta b_{20} &= 9/2[G_{33}e_{zz} + 2G_{36}(e_{xx} + e_{yy})],\\
\Delta b_{22} &= 6(G_{11} + G_{12})(e_{xx} - e_{yy}) + 3R_{31}E_z,\\
\Delta c_{22} &= 12(G_{12} - G_{11})e_{xy} + 3R_{36}E_z,\\
\Delta b_{21} &= 24G_{54}e_{xz} + 6(R_{15}E_x + R_{14}E_y),\\
\Delta c_{21} &= 24G_{54}e_{yz} + 6(R_{14}E_x - R_{15}E_y),
\end{aligned} \qquad (1)$$

where G_{ij} are the components of the fourth-rank tensor of the spin–strain interaction (according to the Voigt notation) and R_{ij} are the components of the third-rank tensor of the linear electric-field effect.

The static modulation of the parameters b_{22} and c_{22} can be judged from the strong azimuthal angular dependence (for the *3* ⇄ *4* transition, the peak-to-peak value is approximately equal to 1 mT) of the linewidth at $\mathbf{B} \perp \mathbf{S}_4$, which is governed by fluctuations in these parameters. For this transition, the shift in the position of the EPR signal depending on the azimuthal angle φ can be written as

$$\Delta B(\varphi) = Q(b_{22}\cos 2\varphi + c_{22}\sin 2\varphi), \qquad (2)$$

where Q is the peak value of $\partial B_{res}/\partial b_{22}$ and $\partial B_{res}/\partial c_{22}$. The shift in the position of the EPR signal only due to the electric field ($\mathbf{z} \parallel \mathbf{S}_4$) can be represented in the form

$$\Delta B(\varphi) = Q\left[\frac{\partial b_{22}}{\partial E_z}\cos 2\varphi + \frac{\partial c_{22}}{\partial E_z}\sin 2\varphi\right]E_z$$
$$= 3Q(R_{31}\cos 2\varphi + R_{36}\sin 2\varphi)E_z$$
$$= 3Q\sqrt{R_{31}^2 + R_{36}^2}\sin 2(\varphi + \varphi_0)E_z,$$

where $\tan 2\varphi_0 = (R_{31}/R_{36})$. By squaring and averaging this expression, we obtain the contribution to the linewidth in the form

$$\Delta B_{pp}(\varphi) \sim Q\sqrt{R_{31}^2 + R_{36}^2}\left|\sin 2(\varphi + \varphi_0)\right|\sqrt{\langle E_z^2\rangle}. \quad (3)$$

In this case, the position of the signal associated with the transitions varies as ~$\cos 4\varphi$. Indeed, the extrema in the observed dependence of the linewidth are shifted with respect to those in the dependence $B_{res}(\varphi)$ [11, 13].

The value of Q for the *3* ⟷ *4* transition is equal to 0.056 mT/MHz [the peak-to-peak value of the dependence $\Delta B_{pp}(\varphi)$ is approximately equal to 1 mT] at $\mathbf{B} \perp \mathbf{S}_4$ and to only 0.006 mT/MHz at an angle $\theta = 40°$ at which the angular dependences of the position of the signal associated with the *3* ⟷ *4* and *5* ⟷ *6* transitions intersect each other. Consequently, the contribution from this mechanism to the linewidth at $\theta = 40°$ is of the order of 0.1 mT for the *3* ⟷ *4* transition and increases by a factor of approximately four for the *5* ⟷ *6* transition due to the larger value of Q. It should be noted that the above derivatives for the transitions under consideration have the same sign, which results in the formation of an asymmetric structure of the spin packet for the pair of initial signals. The dipole interaction leads to the antisymmetric arrangement of the spin packets, whereas fluctuations of the parameters b_{20}, b_{21}, and c_{21} [defined by relationships (1)], according to the numerical calculations, are responsible for the formation of a quasi-symmetric structure of the spin packets for the pair of initial signals.

For the *3* ⟷ *4* and *5* ⟷ *6* transitions, the broadening can occur through the quasi-symmetric mechanism due to the spread of the azimuthal angles. This should lead to a dependence of the relative intensity in the three-component spectrum on the angle φ. The absence of a noticeable dependence (see Section 2) is most likely associated with the compensation for this contribution (i.e., with the broadening of the additional line) due to fluctuations of the parameters b_{22} and c_{22}, which are characterized by an asymmetric structure of the spin packets. According to [14], the mosaic structure of crystals is responsible for a Gaussian shape of the EPR line, the spread of electric fields of point charges is described by a Holtsmarkian distribution, and fields of point electric dipoles and elastic stresses are represented by a Lorentzian distribution.

4. The initial EPR signals of heavily doped $SrMoO_4$: Gd^{3+} at the misorientation angle $\Delta\theta = \theta - \theta_0 \approx 1°$ were processed under the assumption that the signal shape represents a convolution of the Lorentzian and the Gaussian. For the *3* ⟷ *4* transition, the Gaussian contribution to the linewidth was estimated as $\Delta B_{pp} \approx 3$ mT and the Lorentzian contribution was determined to be 1.2 mT. For the *5* ⟷ *6* transition, the Gaussian and Lorentzian contributions are equal to 4 and 3 mT, respectively. These results are in qualitative agreement with both the data presented in Fig. 4 at $\theta = 40°$ and the above quantities $\partial B_{res}/\partial b_{22}$. In the field range covered (Fig. 2), the parameters obtained do not depend on the temperature.

The computer simulation of the three-component spectrum in the region of the coincidence of the signals associated with the *3* ⟷ *4* and *5* ⟷ *6* transitions was performed using the modified Abragam formulas [6, 7, 15]. It was assumed that the broadening of the EPR spectrum includes the following contributions: (i) inhomogeneous broadening with a symmetric structure of the spin packets with the Gaussian distribution (ΔB_{pp}^{GS}), (ii) inhomogeneous broadening with a symmetric structure of the spin packets with the Lorentzian distribution (ΔB_{pp}^{LS}), and (iii) Lorentzian broadening with an antisymmetric structure of the spin packets (ΔB_{pp}^{LAS}). The shape of the absorption line was described by the expression

$$I(B) = \sum_k \frac{1}{1 + \frac{4}{3}(ke/\Delta B_{pp}^{LAS})^2}\left\{\sum_m \frac{1}{1 + \frac{4}{3}(mc/\Delta B_{pp}^{LS})^2}\left[\sum_n \mathrm{Re}(\mathbf{W}\cdot\mathbf{A}(B)^{-1}\cdot\mathbf{1})\exp(-2(nd/\Delta B_{pp}^{GS})^2)\right]\right\},$$
$$\mathbf{A}(B) = \hat{\mathbf{c}}(B) + \check{\mathbf{I}}, \quad \check{\mathbf{I}} = \begin{vmatrix} -V & V \\ V & -V \end{vmatrix}, \quad (4)$$
$$\Omega(B) = \begin{vmatrix} i\alpha(a + ke + nd + mc - B) - V_0 & 0 \\ 0 & i\alpha'(b + ke' - nd' - mc' - B) - V_0 \end{vmatrix},$$

where **W** is the vector with components equal to the probabilities of the initial transitions induced by a radio-frequency field; **1** is the unit vector; $\check{\mathbf{I}}$ is the matrix of the probabilities of relaxation transitions between resonance levels; $\Omega(B)$ is the matrix of the parameters of the initial spin packets (the positions and the intradoublet relaxation rate V_0); *a* and *b* are the positions of the initial signals; *e*, *c*, *d*, *e*', *c*', and *d*' are the separations between the adjacent spin packets; $\alpha = g_{\text{eff}}\beta$; g_{eff} is the effective *g* factor; β is the Bohr magneton; and the *V* is the probability of the relaxation transition between the resonance levels. Expression (4) accounts for the difference in the integrated intensities of the initial signals, the difference in the effective *g* factors, and the difference in the parameters of the inhomogeneous broadening. The first-order derivatives of the simulated spectra are shown by dashed lines in Fig. 2.

As follows from the results obtained in the computer simulation of the EPR spectra in the temperature range studied (Fig. 2), an increase in the temperature leads to an increase in the interdoublet relaxation rate from 2×10^6 to 8×10^6 1/s and in the intradoublet relaxation rate from 10^7 to 6×10^7 1/s. Similar temperature behavior of the relaxation rates V_0 and *V* counts in favor of their identical nature, namely, the spin–lattice interaction. The initial signals are characterized by the same parameter of the Lorentzian broadening with an antisymmetric structure of the spin packets: $\Delta B_{pp}^{\text{LAS}} = 0.4$ mT. For the *3* $\rightleftharpoons$ *4* transition, the values of $\Delta B_{pp}^{\text{GS}}$ and $\Delta B_{pp}^{\text{LS}}$ virtually coincide with those obtained from analyzing the shape of the initial lines. For the *5* $\rightleftharpoons$ *6* transition, the parameter $\Delta B_{pp}^{\text{GS}}$ is 30% greater than the initial Gaussian width, whereas the parameter $\Delta B_{pp}^{\text{LS}}$ is equal to half the initial Lorentzian width. These differences can be explained, among other factors, by a spurious signal in the magnetic field range covered, which primarily distorts the shape of the broader line attributed to the *5* $\rightleftharpoons$ *6* transition.

5. Thus, the additional signals observed in the Gd^{3+} EPR spectra of crystals with a scheelite structure can be qualitatively (and, to some extent, quantitatively) explained as resulting from the averaging of the internal part of the quasi-symmetric structure of spin packets corresponding to two resonance lines with a fine structure. Owing to the formation of quasi-symmetric spin packets due to the mosaic structure of the crystals, the specific features observed in the EPR spectrum closely resemble the cross-singular effects revealed long ago in the NMR spectra of polycrystals [16]. The possibility of forming a quasi-symmetric structure of spin packets due to the mosaic structure of the crystals must be taken into account in the analysis of the nature of the additional EPR signals observed in [2–4].

It should be noted that, according to [9], the walk of the principal axes of paramagnetic centers under the action of charge-compensating defects rather than a geometric imperfection of the $CaMoO_4 : Nd^{3+}$ crystals is responsible for the formation of the mosaic structure. Most likely, in our crystals, the situation is reversed because the block structure clearly manifests itself in the EPR spectra of the majority of the samples.

ACKNOWLEDGMENTS

We would like to thank A.D. Gorlov for his participation in discussions of the results and A.P. Potapov for his assistance in performing the measurements.

This work was supported by the American Foundation for Civilian Research and Development for the promotion of cooperation with scientists from the New Independent States of the former Soviet Union, grant no. REC-005.

REFERENCES

1. V. A. Vazhenin and K. M. Starichenko, Pis'ma Zh. Éksp. Teor. Fiz. **51** (8), 406 (1990) [JETP Lett. **51**, 461 (1990)].
2. V. K. Voronkova, L. V. Mosina, Yu. V. Yablokov, *et al.*, Mol. Phys. **75** (6), 1275 (1992).
3. A. A. Galeev, N. M. Khasanova, A. V. Bykov, *et al.*, Appl. Magn. Reson. **11**, 61 (1996).
4. G. V. Mamin and V. N. Efimov, Mod. Phys. Lett. B **12** (22), 929 (1998).
5. V. A. Vazhenin, K. M. Starichenko, and A. D. Gorlov, Fiz. Tverd. Tela (St. Petersburg) **35** (9), 2450 (1993) [Phys. Solid State **35**, 1214 (1993)].
6. V. A. Vazhenin, V. B. Guseva, and M. Yu. Artemov, Fiz. Tverd. Tela (St. Petersburg) **44** (6), 1096 (2002) [Phys. Solid State **44**, 1145 (2002)].
7. V. A. Vazhenin, V. B. Guseva, and M. Yu. Artemov, Fiz. Tverd. Tela (St. Petersburg) **45** (1), 46 (2003) [Phys. Solid State **45**, 46 (2003)].
8. M. L. Meĭl'man, Fiz. Tverd. Tela (Leningrad) **13** (11), 3165 (1971) [Sov. Phys. Solid State **13**, 2663 (1971)].
9. I. N. Kurkin, in *Paramagnetic Resonance* (Kazan. Gos. Univ., Kazan, 1969), No. 5, p. 31.
10. S. A. Altshuler and B. M. Kozyrev, *Electron Paramagnetic Resonance in Compounds of Transition Elements* (Nauka, Moscow, 1972; Halsted, New York, 1975).
11. V. A. Vazhenin and A. P. Potapov, Fiz. Tverd. Tela (Leningrad) **31** (10), 304 (1989) [Sov. Phys. Solid State **31**, 1831 (1989)].
12. N. G. Koloskova, in *Paramagnetic Resonance* (Kazan. Gos. Univ., Kazan, 1964), p. 115.
13. G. E. Barberis and R. Calvo, Solid State Commun. **12** (10), 963 (1973).
14. I. N. Geĭfman, in *Radiospectroscopy of the Solid State* (Naukova Dumka, Kiev, 1992), p. 417.
15. A. Abragam, *The Principles of Nuclear Magnetism* (Clarendon Press, Oxford, 1961; Inostrannaya Literatura, Moscow, 1963).
16. É. P. Zeer, V. E. Zobov, and O. V. Falaleev, *New Effects in NMR of Polycrystals* (Nauka, Novosibirsk, 1991).

Translated by O. Borovik-Romanova

Physics of the Solid State, Vol. 45, No. 12, 2003, pp. 2276–2280. Translated from Fizika Tverdogo Tela, Vol. 45, No. 12, 2003, pp. 2173–2176.

SEMICONDUCTORS AND DIELECTRICS

Linear Dependence of the Phonon Thermal Resistance of Nonmetallic Crystals on the Isobaric Thermal Strain

Zh. Kh. Murlieva, K. K. Kazbekov, D. K. Palchaev, and M. M. Maangalov

Dagestan State University, Makhachkala, 367025 Dagestan, Russia

Received February 11, 2003; in final form, May 23, 2003

Abstract—This paper reports on the results of investigations into the thermal resistance W and thermal expansion coefficient β for single-crystal samples of Si, SiO_2, Al_2O_3, and NaCl. The available experimental data on the thermal resistance and thermal expansion coefficient for materials with different types of interatomic bonding and different Landau criteria for convection are analyzed. It is demonstrated that the reduced phonon thermal resistance is equal to the isobaric thermal strain at any temperature. © *2003 MAIK "Nauka/Interperiodica".*

1. INTRODUCTION

At present, the quantum-mechanical theory of anharmonic effects in crystals has been elaborated in sufficient detail [1, 2]. However, practical application of this theory involves a number of problems. In particular, although the quantum-mechanical theory offers a detailed classification of mechanisms of phonon–phonon interactions [3, 4], the concrete contributions of these mechanisms (specifically those involved in relationships describing the thermal conductivity of real systems) remain unclear. In this respect, experimental investigations into the thermal properties inherent in crystals due to the anharmonicity of atomic vibrations are of considerable scientific importance. Accumulating experimental data on the thermal properties of materials and revealing the various correlations between these properties will make it possible to interpret them phenomenologically. In turn, a consistent analysis of these correlations, as is known [5], leads to the elucidation of the mechanisms of the processes under consideration and provides deeper insight into the nature of interparticle interactions in crystals.

This work continues our previous investigations [6, 7] and is aimed at determining the parameters characterizing the thermal resistance and its temperature dependence for nonmetallic crystals.

2. THEORETICAL BACKGROUND

Kinetic coefficients can be conveniently calculated using a variational method based on solving a kinetic equation [3]. The solution to a linearized kinetic equation, as a rule, can be obtained from a phenomenological transport equation. In the framework of traditional nonequilibrium thermodynamics, the heat flux density q is proportional to the temperature gradient:

$$q = -\lambda \operatorname{grad} T, \tag{1}$$

where λ is the thermal conductivity coefficient. In particular, the heat flux in crystal structures can be treated as a thermal diffusion of quasiparticles (phonons). At a finite temperature, an ensemble of quasiparticles can be considered a nearly ideal gas of excitations in which interactions associated with both scattering by impurities and umklapp processes prevent their spontaneous convection [3, 8]. The appropriate criterion for phonon convection in the continuum limit for a sufficiently dense gas of quasiparticles can be determined from theoretical considerations given in [9]. It is known that particles involved in a normal gas are characterized by an inhomogeneous distribution in the gravitational field in the absence of an external thermal field. For particles of a phonon gas, an inhomogeneous distribution arises at the instant an external thermal field is applied due to scattering, which is responsible for the finiteness of the conductivity. Although these differences do not affect the Landau conditions of convection for a second-quantized gas in solids, it is necessary to distinguish between the situations observed in the presence and absence of an external thermal field. According to the Landau theory, the extremality of the entropy of a phonon gas along the direction of propagation of the heat flux must be postulated for a particular system. Justification of this postulate in terms of the problem solved in [9] is based on the following considerations.

It is assumed that a volume element of a phonon gas with the center at a point x has a specific volume $V(P, S)$. After an accidental adiabatic displacement of this element over a distance ξ, the specific volume becomes equal to $V(P', S)$, where P' is the pressure of the phonon gas at a point $x + \xi$. To accomplish this, the element must displace the specific volume $V(P', S')$, where S' is the equilibrium entropy at the point $x + \xi$. The stability condition for this system in the absence of a tempera-

ture gradient is determined by the equality of the elementary volumes of the phonons:

$$V(P', S') = V(P', S). \quad (2)$$

In the case when an external thermal field $\Delta T \neq 0$ is applied along the x axis of the sample, condition (2) is violated, because there arises a difference between the temperatures at the sample ends. This must necessarily lead to a dependence of the entropy of the system on the distance x ($\Delta S/\Delta x > 0$); i.e., the entropy increases with increasing x. In turn, the phonon concentration gradient gives rise to a convective heat flux, which results in the appearance of an inverse dependence of the entropy on x ($\Delta S/\Delta x < 0$); i.e., the entropy decreases with increasing x. Therefore, according to [9], the entropy of the system in a stationary state at $\Delta T \neq 0$ should follow an extreme dependence on x satisfying the equality

$$dS(x)/dx = 0. \quad (3)$$

The entropy of the phonon gas of quasiparticles is a function of the temperature T and pressure P. Consequently, condition (3) can be represented in the form

$$\frac{dS}{dx} = \left(\frac{\partial S}{\partial T}\right)_P \frac{dT}{dx} + \left(\frac{\partial S}{\partial P}\right)_T \frac{\partial P}{\partial x} = \frac{C_P}{T}\frac{dT}{dx} - \left(\frac{\partial V}{\partial T}\right)_P \frac{dP}{dx} = 0. \quad (4)$$

Here, $C_P = T(\partial S/\partial T)_P$ and V is the volume of the system under consideration. In a linear approximation, the pressure gradient of the phonon gas is proportional to the temperature gradient $G = (dT/dx)_{sc}$ arising from phonon scattering due to the anharmonicity of atomic vibrations. According to the equation of state of an ideal gas, we can write the relationship

$$\frac{dP}{dx} = -nk_B G, \quad (5)$$

where n is the equilibrium concentration of phonons at a temperature T. Therefore, according to [9], condition (4) for the phonon gas, with due regard for relationship (5), can be represented as

$$-\frac{dT}{dx} = \frac{k_B G}{c_P}\beta T, \quad (6)$$

where c_P is the atomic heat capacity of the system. Since we are dealing here with crystals, the change in the volume of the subsystem can be caused only by a change in the atomic volume of the system. Hence, the parameter $\beta = (1/V)(\partial V/\partial T)_P$ involved in formula (6) is the thermal expansion coefficient of the crystal. By using the condition for convection (3) with the inclusion of transport equation (1), we derive the phenomenological relationship for the coefficient λ:

$$\lambda^{-1} \equiv W = \left(\frac{k_B G}{qc_P}\right)\beta T. \quad (7)$$

Specifically, when the isobaric thermal strain tends to unity ($\beta T \longrightarrow 1$), according to condition (3), the phonon thermal resistance W represents a characteristic phonon thermal resistance W^*, that is,

$$W^* = \left(\frac{k_B G}{qc_P}\right)^*. \quad (8)$$

From relationships (7) and (8), we obtain the following result:

$$\frac{W}{W^*} = \beta T. \quad (9)$$

Therefore, the reduced phonon thermal resistance of crystals is a universal function directly related to the isobaric thermal strain.

3. EXPERIMENTAL TECHNIQUE

The temperature dependences of the total thermal resistance and thermal expansion coefficient were measured for the same single-crystal samples of NaCl, Al_2O_3, Si, and SiO_2 in the temperature range from 100 to 500 K. For quartz samples, the measurements were performed in directions parallel and perpendicular to the principal crystallographic axis. Samples were prepared in the form of rods $\sim 3 \times 10^{-2}$ m long with a cross section of $\sim 15 \times 10^{-6}$ m^2. The thermal resistance was measured according to the procedure described in detail in [6]. The thermal expansion coefficient of single-crystal samples was determined using a quartz dilatometer method with photoelectric registration of the displacement. The displacement sensitivity was $\sim 10^{-2}$ μm. The limiting error in estimating the thermal expansion coefficient did not exceed ~4% for materials whose thermal expansion coefficient was of the order of 1×10^{-6} K at a sample length of $\sim 3 \times 10^{-2}$ m. The travel of the measuring instrument in the temperature range 100–500 K was estimated from the thermal expansion of an M0-type copper at $\sim 3 \times 10^{-2}$ m, and the correction for the thermal expansion coefficient of the measuring cell did not exceed $\pm 5 \times 10^{-7}$ K^{-1}.

4. RESULTS AND DISCUSSION

The experimental data were approximated using the function $W = f(\beta T)$. As a result, we obtained the following expressions:

$$W = 9.46 \times 10^{-4} + 4.7\beta T \quad \text{for} \quad Al_2O_3,$$

$$W = 2.27 \times 10^{-2} + 3.36\beta T \quad \text{for} \quad NaCl,$$

$$W = 5.0 \times 10^{-2} + 11.86\beta T \quad \text{for} \quad SiO_{2\parallel},$$

$$W = 1.8 \times 10^{-2} + 10.63\beta T \quad \text{for} \quad SiO_{2\perp},$$

$$W = 1.9 \times 10^{-3} + 2.31\beta T \quad \text{for} \quad Si \quad \text{at} \quad T > 120 \text{ K}.$$

Figure 1 shows the dependence of $\log(W/W^*)$ on $\log(\beta T)$ over a wide temperature range. This dependence was obtained using our results and reference data

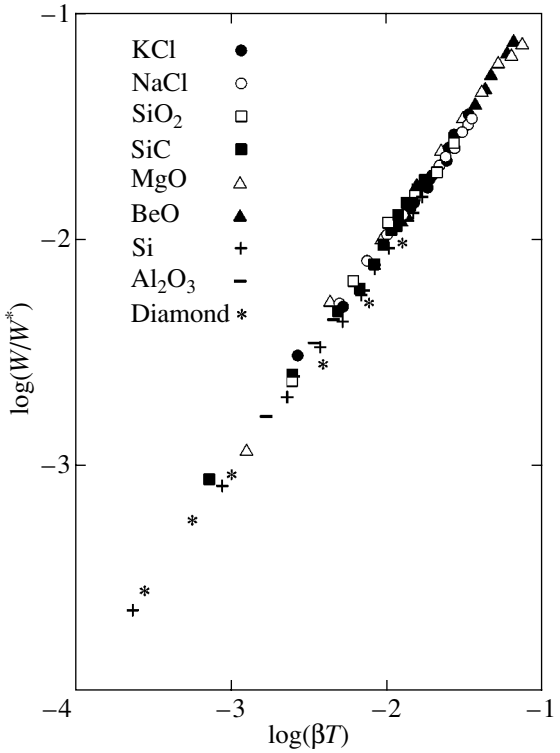

Fig. 1. Correlation between the thermal resistance W and the isobaric thermal strain βT [see expression (9)] for single-crystal samples of KCl (0.997, 60–300 K), NaCl (0.999, 80–400 K), SiO_2 (0.996, 100–500 K), SiC (0.998, 200–1200 K), MgO (0.995, 120–1600 K), BeO (0.998, 573–1673 K), Si (0.999, 150–1100 K), diamond (0.998, 150–1000 K), and Al_2O_3 (0.998, 110–600 K).

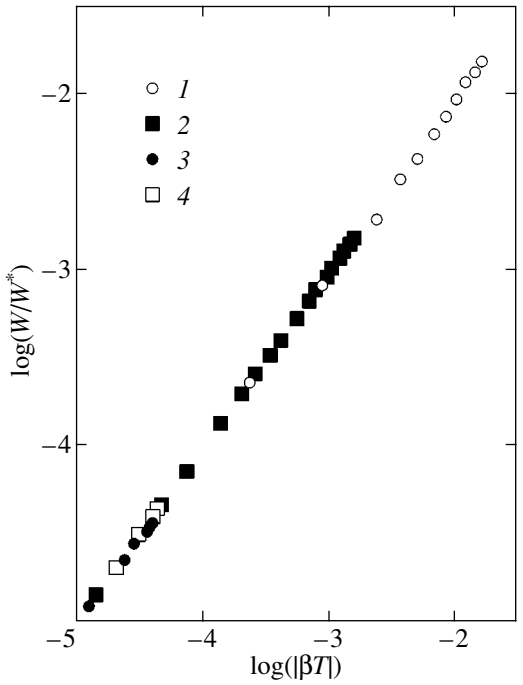

Fig. 2. Correlation between the thermal resistance W and βT [see expression (9)] for (*1*, *2*) negative and (*3*, *4*) positive isobaric thermal strains of Si and InSb single-crystal samples.

for materials with different types of interatomic bonding. The data given in parentheses in the caption to Fig. 1 are the correlation coefficients and temperature ranges for which the available data on W and β proved to be quite reliable. As can be seen from Fig. 1, the results obtained are consistent with relationship (9).

In our earlier works [6, 7], we investigated the phonon thermal resistance and thermal expansion of silicon in the temperature range 80–160 K, including the temperature at which the thermal expansion coefficient reverses sign (T_i = 121 K). As was shown in [7], the thermal resistance is a linear function of βT at positive and negative anharmonicities of atomic vibrations. Figure 2 presents the results of the correlation analysis of W^{ph}/W^* and βT for Si and InSb over a wide temperature range, including the temperature T_i. It is found that the characteristic phonon thermal resistances for the same materials at temperatures above and below T_i differ from each other. As a rule, the materials with a negative thermal strain are characterized by a higher phonon thermal resistance.

The above findings can be qualitatively interpreted as follows. In the vicinity of the temperature corresponding to sign reversal of the thermal strain, the behavior of the phonon subsystem of the crystal can be described using the semiphenomenological hydrodynamic equation of phonon transport [10]:

$$a\gamma_2 T\frac{\partial}{\partial t}\nabla T + \gamma_1\nabla T = -\nu_u a\gamma_2 T\nabla T, \qquad (10)$$

where a is the thermal diffusivity, ν_u is the kinematic viscosity of the phonon gas, and γ_1 and γ_2 are the phonon collision integrals [10]. Simultaneous solution of Eqs. (6) and (10) expressed in terms of the mean free path l of phonons leads to the expression

$$l = l^*\ln\left(\frac{1}{\beta T}\right), \qquad (11)$$

where l^* is the characteristic mean free path of phonons. The mean free path l is a real quantity for a positive value of thermal expansion coefficient β and a complex quantity for a negative value of β; that is,

$$l_{\mathrm{Re}} = l^*\ln\left(\frac{1}{|\beta|T}\right), \quad l_{\mathrm{Im}} = \pi l^*. \qquad (12)$$

The imaginary part in the mean free path is associated with the weakening of scattering of thermal phonons below the temperature of sign reversal T_i. The magnitude of this weakening is in agreement with the decrease in the phonon thermal resistance observed in the experiment.

Let us now express the characteristic phonon thermal resistance W^* in terms of microscopic parameters of the material with a positive thermal strain. The characteristic heat flux q^* can be evaluated from the following considerations. The peak acceleration imparted to an atom from the nearest neighbor atom, on average, is

Characteristic phonon thermal resistance calculated from the experimental data and relationship (17)

Material	$\bar{\mu}$, kg/kmol	γ, kg/m^3	T_D, K	W^*(17), m K/W	W^*_{exp}, m K/W
Covalent crystals					
Diamond	12.01	35.15	1860	0.412	0.41 ± 0.07
SiC	20.04	3210	1310	0.401	0.59 ± 0.10
B_4C	11.04	2520	1500	0.616	0.61 ± 0.08
BeO	12.50	3010	1280	0.740	0.83 ± 0.10
MgO	20.15	3580	900	0.900	1.26 ± 0.17
Ionic crystals					
LiF	12.97	2630	700	2.660	2.37 ± 0.13
NaF	20.98	2804	473	2.828	3.26 ± 0.50
NaCl	29.23	2161	308	4.017	4.00 ± 0.20
KCl	37.28	1988	234	4.600	4.3 ± 0.40
KBr	59.50	2780	166	5.690	5.4 ± 0.70
Loose-packed crystals					
Si	28.08	2332	674	2.51	2.16 ± 0.20
Ge	72.61	5323	377	2.80	2.9 ± 0.40
GaP	50.35	4100	445	2.82	2.8 ± 0.40
GaSb	90.75	5619	265	6.10	5.8 ± 0.80
InSb	118.3	5789	203	13.00	14.5 ± 1.50
InAs	94.85	5672	249	5.94	6.7 ± 1.10
Ionic–covalent crystals					
AlN	20.5	3200	1000	3.360	3.53 ± 0.60
Al_2O_3	20.4	3980	1020	3.62	3.86 ± 0.13
SiO_2	20.0	2650	550	10.68	10.00 ± 0.80
TiO_2	26.6	4260	712	7.90	8.60 ± 0.50

determined as the product of the peak amplitude of atomic vibrations multiplied by the Debye frequency squared $\nu_D^2(\Delta a)$. It is assumed that an atom of mass M possesses a given acceleration and, for a time $1/\nu_D$, imparts an energy to the neighbor atom located at a distance a_0. Note that, in this case, the acquired energy does not exceed the energy Q^* given by the expression

$$Q^* = M\nu_D^3(\Delta a)a_0. \quad (13)$$

Consequently, the energy flux density can be represented in the form

$$q^* = \frac{M\nu_D^3(\Delta a)}{a_0}. \quad (14)$$

According to the Pictet criterion, the peak amplitude of atomic vibrations is determined in terms of the thermal expansion coefficient and melting temperature: $(\Delta a)^* = \alpha_m T_m a_0$.

Since the difference between the temperatures of the nearest neighbor atoms does not exceed the Debye temperature and the atomic displacement in a condensed medium results in a directed elastic disturbance, the limiting temperature gradient can be expressed by the formula

$$G^* = T_D q_D, \quad (15)$$

where $q_D = (6\pi^2\rho N/\bar{\mu})^{1/3}$ is the Debye wave vector. Here, ρ and $\bar{\mu}$ are the density and the mean atomic mass of the material, respectively. Hence, the characteristic heat capacity should be equal to $c^* = k_B$; i.e., it should be equal to the heat capacity per atom. As a result, relationship (8) for the characteristic thermal resistance can be represented in terms of macroscopic parameters as

$$W^* = \frac{h^3 q_D a_0}{k_B^3 T_D^2 \bar{M}(\Delta a)^*} \quad (16)$$

or in a form more convenient for calculations as

$$W^* = K\frac{\rho^{1/3}}{T_D^2 \bar{\mu}^{3/4}}. \quad (17)$$

Here, $K = 6.6 \times 10^5/\alpha_m T_m$. All except loose-packed crystals are thermodynamically similar materials for which $\alpha_m T_m \approx 0.029$.

The above reasoning is supported by the experimental data for pure nonmetallic single crystals. The correlation analysis of our results and data available in the literature [11–14] on the total thermal resistance and thermal expansion coefficient demonstrated that the characteristic thermal resistances calculated according to relationship (17) and those found from the experiment [$W = f(\beta T)$] coincide to within the total error in determining the quantities W and β. This agreement is clearly seen from the table. For materials with a predominantly ionic or covalent type of bonding, the Pictet criterion holds true and the constant $K_{i,c}$ is estimated at 7.59×10^6. The Pictet criterion is also valid for materials characterized by almost equal contributions of ionic and covalent types of bonding, but, in this case, the constant $K_{i-c} = 37.95 \times 10^6$ is approximately five times greater than that in the former case, which is associated with the phonon scattering by electron-density fluctuations upon crossover from one type of bonding to another [15]. For thermodynamically dissimilar (loose-packed) materials, we have $K_{f-p} = 6.6 \times 10^5/\alpha_m T_m$.

5. CONCLUSIONS

The results obtained in the above investigations of the thermal resistance and thermal expansion coefficients for nonmetallic single crystals can be summarized as follows.

(i) The total thermal resistance of nonmetallic crystals is a linear function of the isobaric thermal strain.

(ii) The generalized Landau model of convective transport is applicable to a phonon gas in solids.

(iii) The reduced phonon thermal resistance of nonmetallic crystals at any temperature is equal to the isobaric thermal strain, irrespective both of the structure and type of chemical bonding in the material and of whether the thermal expansion coefficient is positive or negative.

(iv) The jump observed in the characteristic phonon thermal resistance at the point where the isobaric thermal strain reverses sign can be explained by the fact that, at a negative coefficient of thermal expansion, the mean free path of phonons appears to be a complex quantity.

REFERENCES

1. G. Leibfried and W. Ludwig, Solid State Phys. **12**, 276 (1961); Inostrannaya Literatura, Moscow, 1963.
2. M. I. Katsnel'son and A. V. Trefilov, *Dynamics and Thermodynamics of the Crystal Lattice* (IzdAT, Moscow, 2002).
3. B. M. Mogilevskiĭ and A. F. Chudnovskiĭ, *Thermal Conductivity of Semiconductors* (Nauka, Moscow, 1972).
4. J. A. Reissland, *The Physics of Phonons* (Wiley, New York, 1973; Mir, Moscow, 1975).
5. V. M. Zverev and V. P. Silin, Pis'ma Zh. Éksp. Teor. Fiz. **64** (1), 33 (1996) [JETP Lett. **64**, 37 (1996)].
6. D. K. Palchaev, Zh. Kh. Murlieva, A. B. Batdalov, *et al.*, Fiz. Tverd. Tela (St. Petersburg) **38** (3), 684 (1996) [Phys. Solid State **38**, 379 (1996)].
7. D. K. Palchaev, A. B. Batdalov, Zh. Kh. Murlieva, *et al.*, Fiz. Tverd. Tela (St. Petersburg) **43** (3), 442 (2001) [Phys. Solid State **43**, 458 (2001)].
8. J. M. Ziman, *Elements of Advanced Quantum Theory* (Cambridge Univ. Press, London, 1969; Mir, Moscow, 1971).
9. L. D. Landau and E. M. Lifshitz, *Course of Theoretical Physics*, Vol. 6: *Fluid Mechanics*, 3rd ed. (Nauka, Moscow, 1986; Pergamon, New York, 1987).
10. E. M. Lifshitz and L. P. Pitaevskiĭ, *Physical Kinetics* (Nauka, Moscow, 1979; Pergamon, Oxford, 1981), Vol. 10.
11. I. G. Kozhevnikov and L. A. Novitskiĭ, *Thermal Properties of Materials at Low Temperatures* (Mashinostroenie, Moscow, 1982).
12. *Acoustic Crystals*, Ed. by M. P. Shaskol'skaya (Nauka, Moscow, 1982).
13. *Handbook on Thermal Conductivity of Solids*, Ed. by A. S. Okhotin (Énergoatomizdat, Moscow, 1984).
14. S. I. Novikova, *Thermal Expansion of Solids* (Nauka, Moscow, 1974).
15. G. B. Bokiĭ, *Crystal Chemistry* (Nauka, Moscow, 1971).

Translated by O. Borovik-Romanova

Physics of the Solid State, Vol. 45, No. 12, 2003, pp. 2281–2286. Translated from Fizika Tverdogo Tela, Vol. 45, No. 12, 2003, pp. 2177–21181.

DEFECTS, DISLOCATIONS, AND PHYSICS OF STRENGTH

Analysis of the Structure of Tetragonal Oxygen Centers Associated with Yb^{3+} Ions in the $KMgF_3$ Crystal

A. M. Leushin

Kazan State University, ul. Kremlevskaya 18, Kazan, Tatarstan 420008, Russia

e-mail: Anatoly.Leushin@ksu.ru

Received April 21, 2003

Abstract—The parameters of the crystal field of the tetragonal oxygen center associated with a Yb^{3+} ion in the $KMgF_3$ crystal found previously in a study of optical and ESR spectra are applied to analyze lattice distortions in the vicinity of the impurity ion and the O^{2-} ion compensating for the excess positive charge. Within the superposition model, it was ascertained that the Yb^{3+} ion and the neighboring ions of fluorine and oxygen on the axis of the center shift significantly along the direction from the O^{2-} ion to the Yb^{3+} ion during the formation of the tetragonal oxygen center. As this takes place, the distances of both (fluorine and oxygen) ions from the impurity ion increase. The four F^- ions of the nearest octahedral neighborhood of Yb^{3+} that are arranged symmetrically in the plane perpendicular to the axis of the center slightly recede from the axis. *© 2003 MAIK "Nauka/Interperiodica".*

1. INTRODUCTION

The results of detailed electron spin resonance, double electron–nuclear resonance, and optical spectroscopic studies of tetragonal paramagnetic centers (PCs) associated with Yb^{3+} ions in the $KMgF_3$ crystal have shown convincingly that the observed tetragonal centers (Fig. 1) arise during the introduction of Yb^{3+} into octahedral sites of Mg^{2+} ions rather than due to the substitution of monovalent K^+ ions (surrounded by twelve fluorine ions) by Yb^{3+} ions, as expected previously [2, 3]. The excess positive charge is compensated by a nonmagnetic oxygen O^{2-} ion, which substitutes for one of the fluorine ions in the octahedron of the nearest neighborhood of a Yb^{3+} ion. The compensating ion is close to the paramagnetic ion (PI) and possibly causes a significant rearrangement in its neighborhood, which is suggested by the parameters of the crystal field (CF) acting on the Yb^{3+} ion, by the strong anisotropy of the measured g factors, and by the significant difference between the ligand hyperfine structure constants characterizing the interaction of the Yb^{3+} ion with axial (F_5^-) and planar (F_{1-4}^-) fluorine ions. The structure of the observed center was discussed in [1] only in the context of explaining the ligand hyperfine interaction (LHFI); it was assumed that the Yb^{3+} ion shifts to the O^{2-} ion during the formation of the tetragonal oxygen center (TOC), thereby increasing the distance between the PI and F_{1-5}^- ions. An adequate theoretical interpretation of the observed LHFI parameters was attained only when the least of these distances was set equal to the sum of the F^- and Yb^{3+} ion radii (≅2.2 Å [4]), which significantly exceeds the distance between Mg^{2+} and F^- ions in the undistorted $KMgF_3$ host lattice.

In this paper, we analyze the TOC structure in more detail, basing our study mainly on its CF parameters and on the superposition model (SM), which is more or less usefully applied for solving such structural problems [5–9].

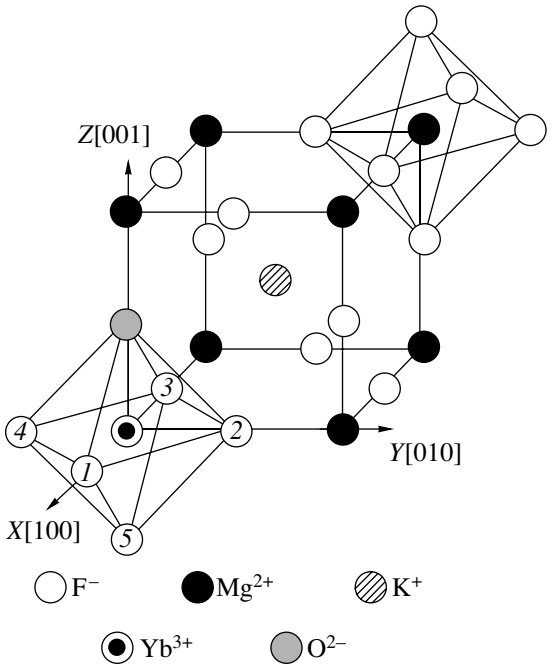

Fig. 1. Fragment of the $KMgF_3$ structure containing a tetragonal oxygen center.

1063-7834/03/4512-2281$24.00 © 2003 MAIK "Nauka/Interperiodica"

Table 1. Crystal-field parameters (cm^{-1}) of tetragonal oxygen and cubic centers associated with the Yb^{3+} ion in $KMgF_3$

	B_2^0	B_4^0	B_4^4	B_6^0	B_6^4
B_k^q (tetr.exp.)	850	39	1274	–1	137
Model A		146	1245	0	–24
Model B		37	1275	26	132
B_k^q (cub.exp.)	0	334	1671	4	–86
ΔB_k^q	850	–295	–397	–5	223

Note: $\Delta B_k^q = B_k^q$ (tetr.exp.) – B_k^q (cub.exp.) are the changes in the parameters due to the formation of tetragonal oxygen centers.

2. SUPERPOSITION MODEL PARAMETERS FOR FLUORINE IONS

Using the energy-level diagram obtained in [1] and the g factors of the ground-state Kramers doublet, we determined the parameters B_k^q of the Hamiltonian of the Yb^{3+} ion interaction with the TOC crystal field:

$$H_{cr}(\mathbf{C}_{4v}) = B_2^0V_2^0 + B_4^0V_4^0 + B_4^4V_4^4 + B_6^0V_6^0 + B_6^4V_6^4. \quad (1)$$

The values of these parameters B_k^q (tetr.exp.), as well as the values of the CF parameters of the cubic center (in tetragonal notation) B_k^q (cub.exp.) taken from [10], are shown in Table 1. The quantities V_k^q in Hamiltonian (1) are harmonic Stevens polynomials [11] in which the Cartesian coordinates of 4*f* electrons are related to the cubic crystal axes, with the *z* axis taken to be the *Z* axis of the TOC symmetry (Fig. 1).

The CF parameters suggest that the CF of the TOC in the $KMgF_3$ crystal is strong. A comparison of the CF parameters with those of cubic centers shows that the cubic crystal field is rather strongly distorted during the formation of the tetragonal PC.

Since the CF acting on the PI is mainly determined by the electrostatic and contact interaction between the Yb^{3+} and the nearest neighbor F^- ions, it can be assumed that the ligand sites change significantly during the TOC formation in comparison with those in the case of cubic symmetry.

To quantitatively estimate the lattice distortions near the impurity ion, we invoke the SM proposed by Newman [6, 9, 12]. This model postulates that the total CF is a linear superposition of fields induced by each ion of the crystal. In this case, the resulting CF parameters are written as

$$B_k^q = \sum_i K_k^q(\vartheta_i, \phi_i)\bar{B}_k(R_i), \quad (2)$$

where $K_k^q(\vartheta_i, \phi_i)$ are structural factors depending on the angular positions (defined by the spherical angles ϑ_i and ϕ_i) of all ions being at a distance R_i from the PI (the most complete table of their expressions can be found in [13]) and $\bar{B}_k(R_i)$ are the "intrinsic" parameters depending on the ligand type. In practice, it is generally assumed that the dependence of the parameters $\bar{B}_k$ on R_i in a limited range of distances is given by

$$\bar{B}_k(R_i) = \bar{B}_k(R_0)(R_0/R_i)^{t_k}, \quad (3)$$

where t_k is the exponent and $\bar{B}_k(R_0)$ is a model parameter related to a certain average distance R_0, which is, in general, taken equal to the sum of the ion radii of the magnetic ion and a ligand.

The values of t_k and $\bar{B}_k(R_0^F)$ characterizing the field produced by F^- ions can be determined from the CF parameters of the cubic Yb^{3+} centers in isomorphous $KMgF_3$ and $KZnF_3$ crystals if the equilibrium distances R from the F^- ligands to the paramagnetic Yb^{3+} center are known. This is precisely the way we chose to analyze the structure of trigonal fluorine centers associated with the Yb^{3+} ion in SrF_2 and BaF_2 crystals [14]. Unfortunately, there are no reliable data on the distance from an impurity ion to its nearest neighbors for fluorine perovskite crystals with impurities; therefore, we determined the parameters t_k and $\bar{B}_k(R_0^F)$ in a somewhat different way. The authors of [15], when considering the LHFI in trigonal vacancy centers associated with the Yb^{3+} ion, calculated lattice distortions by minimizing the energy of the complex consisting of an Yb^{3+} ion and its five surrounding coordination shells formed by F^-, K^+ and Mg^{2+} ions in the crystal $KMgF_3$. We took the coordinates of the nearest six F^- ions to the Yb^{3+} ion from [15] and assumed that they determine (within the SM) the CF of the trigonal vacancy center of the Yb^{3+} ion in the $KMgF_3$ crystal found in [10] from the optical spectra. With these coordinates, by closely fitting the CF parameters to the experimental ones, we obtained the following values of the SM parameters: $t_4 = 7.95$, $\bar{B}_4(R_0^F) = 105.72$ cm^{-1}, $t_6 = 49.83$, and $\bar{B}_6(R_0^F) = 18.48$ cm^{-1}. In this case, the distance $R_0^F = 2.19$ Å appeared to be somewhat less than the equilibrium value used in [1]. For the cubic centers, we obtained the value $R = 2.22$ Å. Details of the calculations carried out

will be given in a separate paper devoted to trigonal vacancy centers in double-fluoride crystals. It is also worth noting that the values of the SM parameters differ appreciably from the values 6.43, 67.68 cm^{-1}, 9.93, and 18.79 cm^{-1}, respectively, which we obtained in [14] for the Yb^{3+} ion in SrF_2 and BaF_2 crystals at $R_0^F = 2.295$ Å. This is especially true for the exponent t_6. However, this difference can be expected if we taken into account that a pair of interacting Yb^{3+} and F^- ions in double fluoride crystals differs greatly (in terms of the SM) from the pairs in alkaline-earth fluoride crystals. These pairs differ distinctly in the distance between ions, and introduction of Yb^{3+} ions into the fluorite lattice is accompanied by crystal compression near the PIs, whereas Yb^{3+} ions in the double-fluoride lattice, on the contrary, cause the crystal to expand.

3. THE STRUCTURE OF TETRAGONAL OXYGEN CENTERS

Fluorine ions F^-_{1-6}, composing the octahedron of the nearest neighborhood of the Yb^{3+} ion, occupy sites with coordinates $R_1 = R_2 = R_3 = R_4 = R_5 = R_6 = R$, $\vartheta_1 = \vartheta_2 = \vartheta_3 = \vartheta_4 = \pi/2$, $\vartheta_5 = \pi$, $\vartheta_6 = 0$, $\phi_1 = 0$, $\phi_2 = \pi/2$, $\phi_3 = \pi$, and $\phi_4 = 3\pi/2$ in the coordinate system of the cubic center (Fig. 1).

First, let us assume that the Yb^{3+} ion and four F^-_{1-4} ions remain in the same plane perpendicular to the center axis during the formation of a TOC in which the F^-_6 ion is replaced by O^{2-}; hence, the angular coordinates of these ions remain unchanged and only the coordinates R_{1-5} are changed, with the distances R_{1-4} remaining equal due to tetragonal symmetry of the center. According to the SM, one more term should be added to expression (2) in the sum over *i*; this term is caused by the compensating ion O^{2-} located at the distance R_k from the Yb^{3+} ion. Within this model, the changes in the crystal-field parameters $\Delta B_k^q = B_k^q(\text{tetr.exp.}) - B_k^q(\text{cub.exp.})$ are described by the equations

$$\begin{aligned}
\Delta B_4^0 &= \bar{B}_4(R_k) + \bar{B}_4(R_5) + \frac{3}{2}\bar{B}_4(R_1) - \frac{7}{2}\bar{B}_4(R),\\
\Delta B_4^4 &= \frac{35}{2}\bar{B}_4(R_1) - \frac{35}{2}\bar{B}_4(R),\\
\Delta B_6^0 &= \bar{B}_6(R_k) + \bar{B}_6(R_5) - \frac{5}{4}\bar{B}_6(R_1) - \frac{3}{4}\bar{B}_6(R),\\
\Delta B_6^4 &= -\frac{63}{4}\bar{B}_6(R_1) + \frac{63}{4}\bar{B}_6(R),
\end{aligned} \qquad (4)$$

Table 2. Structural parameters of the tetragonal oxygen center associated with the Yb^{3+} ion in $KMgF_3$

	R_k, Å	R_5, Å	R_1, Å	ϑ_1, deg
Model A	2.67	2.55	2.30	90.0
Model B	2.53	2.33	2.20	66.5

Note: In the cubic center, $R = 2.22$ Å for all fluorine ions, the impurity-free crystal, $R = R_0 = 1.987$ Å [2].

which, in combination with the values of ΔB_k^q listed in Table 1, make it possible to determine the distances R_1, R_5, and R_k characterizing the TOC structure. A term involving the parameter B_2^0 (which is absent in the case of cubic centers) also arises in potential (1) for tetragonal centers. However, the use of the equation for this parameter is beyond the framework of the ligand SM, since the electrostatic interactions of the PI with more distant (than the nearest six) lattice ions make a significant contribution to B_2^0.

The two equations for ΔB_4^4 and ΔB_6^4 depend only on a single unknown, R_1. Solving the equation for ΔB_4^4, we get $R_1 = 2.29$ Å; the equation for ΔB_6^4 cannot be solved exactly. Nevertheless, a self-consistent solution to a set of two nonlinear equations can be obtained. Such a solution gives R_1 equal to 2.30 Å. In this case, the calculated values of the CF parameters B_4^4 and B_6^4 are 1254 and –25 cm^{-1}, respectively. We can see that the square formed by the ions becomes strongly enlarged and that the deviation of the calculated value of the parameter B_6^4 from its experimental value is great (–162 cm^{-1}) with the parameter B_4^4 being described adequately (the deviation is 20 cm^{-1}).

To determine the axial parameters B_4^0 and B_6^0, it is necessary to know t_k and $\bar{B}_k(R_0^{O^{2-}})$, which define the CF induced by the O^{2-} ion substituting for the F^-_6 ion in the TOC. These quantities may be taken from [15], where the CF parameters of rare-earth ions in garnets were interpreted in terms of the SM. In particular, for the Yb^{3+} ion interacting with an O^{2-} ion, the values $t_4 = 16.9$, $\bar{B}_4(R_0^{O^{2-}}) = 71.0$ cm^{-1}, and $t_6 = 22.9$, and $\bar{B}_6(R_0^{O^{2-}}) = 41.0$ cm^{-1} were obtained at the distance $R_0^{O^{2-}} = 2.34$ Å. There is no certainty that the pair of interacting Yb^{3+} and O^{2-} ions in the $KMgF_3$ crystal will

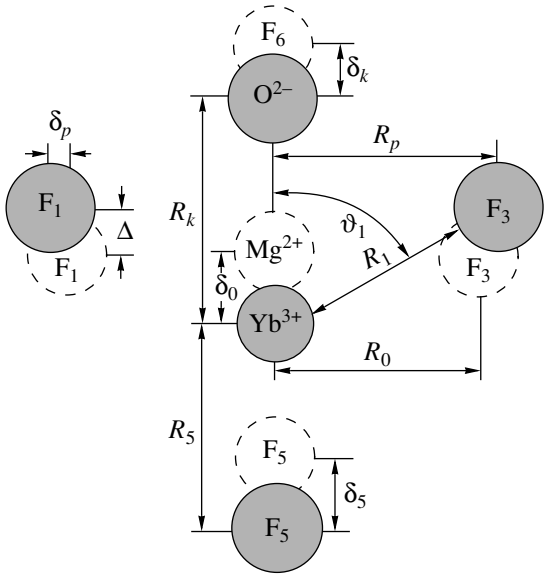

Fig. 2. Structure of the tetragonal oxygen center associated with the Yb^{3+} ion in the $KMgF_3$ crystal (schematic). Dashed circles are the sites of the ions in the impurity-free crystal.

behave as in garnets; however, there is no alternative concept. Substituting the above values for the CF parameters in relation (3) and solving the self-consistent set of four equations (4), we obtain the values of R_1, R_5, and R_k listed in Table 2 (model A). In this model of the tetragonal center, the PI remains at the Mg^{2+} ion site of the host crystal and the F_5 ion recedes from the PI, being displaced by 0.56 Å along the center axis. Each of the four in-plane ions is displaced by 0.31 Å from the center axis. The on-axis oxygen ion is displaced from the Yb^{3+} ion along the center axis by 0.68 Å from the site of the F_6 ion it replaces. The description of the CF parameters (except for B_4^4, B_6^0) turns out to be inadequate (Table 1, model A). For example, the calculated value of the parameter B_4^0 differs from its experimental value (39 cm^{-1}) by 107 cm^{-1}. Moreover, the calculated parameter B_6^4 is opposite in sign to its experimental value.

For this reason, in the further analysis of the tetragonal center structure, we ruled out the condition of unchanged angular coordinates and assumed that the Yb^{3+} ion can leave the four–ion plane and go up or down with respect to this plane. Such deformation of the center is characterized by a single angle ϑ_1. Varying this angle simultaneously with the distances R_1, R_5, and R_k can in principle causes a sign reversal of the parameter B_6^4 and, presumably, improves the description of other quantities. Instead of the set of equations (4) for the CF parameters, we write

$$\begin{aligned}
B_4^0 &= \bar{B}_4(R_k) + \bar{B}_4(R_5) \\
&+ \frac{1}{2}\bar{B}_4(R_1)(35\cos^4\vartheta_1 - 30\cos^2\vartheta_1 + 3), \\
B_4^4 &= \frac{35}{2}\bar{B}_4(R_1)\sin^4\vartheta_1, \\
B_6^0 &= \bar{B}_6(R_k) + \bar{B}_6(R_5) \\
&+ \frac{1}{4}\bar{B}_6(R_1)(231\cos^6\vartheta_1 - 315\cos^4\vartheta_1 + 105\cos^2\theta_1 - 5), \\
B_6^4 &= \frac{63}{4}\bar{B}_6(R_1)\sin^4\vartheta_1(11\cos^2\vartheta_1 - 1).
\end{aligned} \tag{5}$$

When writing this set, we assumed that the CF parameters of the cubic centers as calculated within the SM are exactly equal to their experimental values (this assumption was also used when solving set (4)). In this case, the two equations for B_4^4 and B_6^4 depend on two quantities (R_1, ϑ_1); therefore, their simultaneous solution immediately gives these quantities. We get R_1 = 2.19 Å and $\vartheta_1 = 66.35°$. Thus, the Yb^{3+} ion indeed goes out of the four-ion plane away from the compensating ion, so that the deviation of angle ϑ_1 from 90° is $\Delta\vartheta_1 = -23.65°$. In this case, the planar ions themselves recede from the PI by 0.21 Å. The values B_4^4 = 1274 cm^{-1} and B_6^4 = 137 cm^{-1}, calculated using the determined values of R_1 and ϑ_1, are identical to the experimental values listed in Table 1.

Solution of the set of four equations yields the values of R_k, R_5, R_1, and ϑ_1 listed in Table 2 (model B). By comparing the values of R_k and R_5 with the corresponding distances in the impurity-free crystal (1.987 Å [2]), we can see that, in this deformation model, the on-axis O^{2-} and F_5^- ions become more distant from the Yb^{3+} ion due to the formation of the tetragonal center and all of them are significantly displaced along the center axis in the direction away from the O^{2-} ion toward the PI (Fig. 2). The equations for the parameters B_4^0 and B_6^0 in set (5) require that four planar ions F_{1-4}^- become slightly less distant from the PI (only by 0.001 Å) than follows from the solution of only the two equations and the angular deformation of the center slightly decrease. It should be noted that all the structural factors $K_k^q(\vartheta_1)$ in the equations in set (5) are even functions of the angle ϑ_1. Solution of these equations also yields another reasonable value, $\vartheta_1 = 113.53°$, which corresponds to the angle deviation $\Delta\vartheta_1 = 23.53°$ and for

which all three ions (Yb^{3+}, O^{2-}, F_5^-) are displaced along the axis of the center in the opposite direction. However, we excluded this solution for physical reasons, since it is unlikely that a significant increase in the distance between the O^{2-} ion and the PI will be accompanied by a displacement of the PI itself from the four-ion plane toward the O^{2-} ion. Most likely, the four-ion plane will be displaced from the PI toward the O^{2-} ion, as is the case for the first solution. The values of the CF parameters of the tetragonal center as calculated using the values of R_k, R_5, R_1, and ϑ_1 within model B are listed in Table 1. By comparing them with the experimental values B_k^q (tetr.exp.) (Table 1), we can see that the model of the center structure with angular deformation describes the fourth-order parameters very well and reproduces the sixth-order parameters somewhat worse. This is related particularly to the parameter B_6^0, which was calculated to be positive and large at this deformation of the center. In order to attempt to change the sign of parameter B_6^0 in the model under consideration, we used another calculation version, where only the two equations in set (5) that describe the sixth-order parameters were considered. As a result, we obtained $B_6^0 = -0.64$ cm^{-1} and $B_6^4 = 137$ cm^{-1}, which agree with the experimental values. This was achieved almost at the same distances, $R_k = 2.54$ Å and $R_5 = 2.31$ Å, but at significantly different coordinates of the in-plane fluorine ions, $R_1 = 2.22$ Å and $\vartheta_1 = 42.74°$ ($\Delta\vartheta_1 = 47.26°$). Thus, in order to explain the experimental values of the sixth-order parameters, the displacements of the in-plane ions of the center have to have much larger values; in this case, however, the calculated fourth-order parameters ($B_4^0 = -63$ cm^{-1}, $B_4^4 = 346$ cm^{-1}) differ notably from the experimental ones.

The structure of the tetragonal center as determined within model B is given in Fig. 2, which shows the section of the center by a plane passing through its axis and two in-plane fluorine ions, F_1 and F_3. If we assume that the plane of the four F^- ions is displaced by Δ with respect to its position in the nondeformed crystal during the tetragonal center formation, then, based on the data obtained (Table 2, model B), the Yb^{3+} ion displacement δ_0 with respect to the site of the Mg^{2+} ion substituted by Yb^{3+} is found to be $\delta_0 = R_1\sin(\Delta\vartheta_1) - \Delta = 0.88$ Å $- \Delta$. For the distance R_p from an in-plane F^- ion to the center axis, we obtain $R_p = R_1\cos(\Delta\vartheta_1) = 2.01$ Å. Thus, the displacement of the in-plane ions from the center axis is $\delta_p = R_p - R_0 = 0.03$ Å. The displacement of the O^{2-} compensator from the site of the F_6^- ion substituted by it toward the Yb^{3+} ion is given by $\delta_k = R_0 - R_k + R_1\sin(\Delta\vartheta_1) - \Delta = 0.34$ Å $- \Delta$. The displacement δ_5 of the on-axis F_5^- ion away from the Yb^{3+} ion is $\delta_5 = R_5 - R_0 + R\sin(\Delta\vartheta_1) = 0.76$ Å $- \Delta$.

Unfortunately, we cannot determine the displacement Δ of the four-ion plane on the basis of the CF parameters. Data on this parameter could be obtained by analyzing the constants of the LHFI with the fluorine ion nuclei in the first and more distant coordination shells. In [1], the LHFI with only the nearest neighbor ligands was studied; thus, we have no data on the TOC ion sites in more distant coordination shells.

4. CONCLUSIONS

(1) Substitution of one of the fluorine ions of the nearest octahedral neighborhood of the Yb^{3+} ion by the O^{2-} ion compensating for excess positive-charge causes strong deformation of the $KMgF_3$ lattice in the vicinity of the PI.

(2) Reproduction of these deformations within the center model in which the PI is not displaced from the site of the Mg^{2+} ion substituted by the PI in the crystal host is not adequate; the displacements of the compensating ion and of the on-axis F_5^- ion are unduly large and the CF parameters of the paramagnetic center cannot be interpreted adequately.

(3) It seems likely that the model in which not only the distances between the PI and ligands but also the angular coordinates of planar ions change during the TOC formation is more realistic. The CF parameters calculated on the basis of this model agree well with the experimental values, except for the parameter B_6^0, whose interpretation calls for a larger angular deformation of the center.

Certainly, we recognize that the presented numerical values of the ion displacements are no more than estimates, because the SM is a crude approximation; however, we expect that these results at least qualitatively reproduce the changes in the PI and its neighborhood during the TOC formation.

ACKNOWLEDGMENTS

This study was supported by the Russian Foundation for Basic Research, project no. 02-02-16648.

REFERENCES

1. M. L. Falin, V. F. Latypov, B. N. Kazakov, *et al.*, Phys. Rev. B **61** (14), 9441 (2000).
2. M. M. Abraham, C. B. Finch, J. L. Kolopus, and J. T. Lewis, Phys. Rev. **83**, 2855 (1971).
3. A. A. Antipin, A. V. Vinokurov, M. P. Davydova, *et al.*, Phys. Status Solidi B **81**, 287 (1977).
4. R. D. Shannon and C. T. Prewitt, Acta Crystallogr. B **25**, 925 (1969).

5. D. J. Newman and G. E. Stedman, J. Chem. Phys. **51** (7), 3013 (1969).
6. D. J. Newman, Adv. Phys. **20**, 197 (1971).
7. E. Siegal and K. A. Muller, Phys. Rev. B **19** (1), 109 (1979).
8. H. S. Murrieta, J. O. Rubio, and G. S. Aguilar, Phys. Rev. B **19** (11), 5516 (1979).
9. D. J. Newman and Betty Ng, Rep. Prog. Phys. **52**, 699 (1989).
10. B. N. Kazakov, A. M. Leushin, G. M. Safiullin, and V. F. Bespalov, Fiz. Tverd. Tela (St. Petersburg) **40** (11), 2029 (1998) [Phys. Solid State **40**, 1836 (1998)].
11. K. W. H. Stevens, Proc. Phys. Soc. London, Sect. A **65**, 209 (1952).
12. D. J. Newman, Aust. J. Phys. **31**, 79 (1978).
13. C. Rudowicz, J. Phys. C **20**, 6033 (1987).
14. M. L. Falin, K. I. Gerasimov, V. A. Latypov, and A. M. Leushin, J. Phys.: Condens. Matter **15**, 2833 (2003).
15. M. L. Falin, M. V. Eremin, M. M. Zaripov, *et al.*, J. Phys.: Condens. Matter **2**, 4613 (1990).

Translated by A. Kazantsev

Physics of the Solid State, Vol. 45, No. 12, 2003, pp. 2287–2291. Translated from Fizika Tverdogo Tela, Vol. 45, No. 12, 2003, pp. 2182–2186.

DEFECTS, DISLOCATIONS, AND PHYSICS OF STRENGTH

Trigger Effect of Weak Vibrations in Solids (Rocks)

V. S. Kuksenko*, B. Ts. Manzhikov, K. Tilegenov**, Zh. K. Shatemirov**, and B. É. Émil'bekov****

** Ioffe Physicotechnical Institute, Russian Academy of Sciences, Politekhnicheskaya ul. 26, St. Petersburg, 194021 Russia*
e-mail: victor.kuksenko@mail.ioffe.ru

*** Institute of the Rock Physics and Mechanics, Academy of Sciences of Kyrgyzstan, Bishkek, Kyrgyzstan*

Received February 26, 2003; in final form, May 5, 2003

Abstract—The effect of weak low-frequency vibrations on the process of microfailure was studied. Cylindrical rock samples were subjected to uniaxial compression, during which low-frequency vibrations were periodically applied. The vibrations were weak as compared to the compressive load. Acoustic emission was monitored. The acoustic-emission signal was found to increase sharply after a delay when vibrations were applied for a short time (100–200 s). This effect was explained using the concentration criterion for the formation and development of a site of failure. © *2003 MAIK "Nauka/Interperiodica".*

1. INTRODUCTION

When loaded, solids of different nature undergo nonuniform deformation and microfailure (up to jumpwise behavior) even under constant loads [1, 2]. This is most pronounced upon vibrational loading [3]. This nonuniform behavior is characteristic of various phenomena caused by pulse loading, such as avalanches, landslides, and earthquakes [4, 5], and of the results of special studies into the effect of vibrations on deformation processes. The manifestation of deformation of rock vibrational sensitivity was investigated in [6, 7]. The deformations and deformation rates of loaded samples (natural and artificial samples in both an amorphous and a crystalline state) additionally subjected to vibrations were found to vary anomalously (jumpwise). The anomalous deformation behavior consisted in a sharp deformation jump at the beginning of vibrations and in a reverse jump after their termination. The deformation rate also increased during vibrations. After the termination of vibrations, the deformation characteristics were identical to those measured without applying vibrations [7]. When vibrations were turned on, the level of acoustic emission (AE) substantially decreased as compared to the case where a sample was deformed without vibration. After the vibrations were turned off, the number of acoustic pulses increased to the initial level beginning from the recovery of the deformation characteristics [7].

Pulse action (impacts with a concentrated load) on stick-slip processes was studied in [8, 9]. In those studies, a delayed response of loaded models to impact loads and vibrations was detected. We also observed such a delay and an AE aftereffect [10]. However, as shown in the above brief review, the issue of the initiating action of weak low-frequency vibrations on the deformation of loaded geologic materials remains open in the context of the problems of an active effect of vibrations on stress concentration regions and the estimation of the stability of mechanical systems.

Therefore, in this work, we study AE in rock samples subjected to steady-state uniaxial compression alone or with weak low-frequency vibrations. Particular attention is given to AE in the initial stage of the effect of vibrations, when vibration-induced trigger effects manifest themselves.

2. EXPERIMENTAL

We examined three rock types taken from the following deposits in Kyrgyzstan: Kaindinsk (K) and Sara-Dzhazsk (SD) granites and Chychkansk marble (CM). Cylindrical samples 60 mm high and 30 mm in diameter were subjected to uniaxial compression using a spring rheological press, which provided a constant load for a long period of time. Samples were tested for 25–40 days. In this paper, we present results for three samples. Sample K was loaded stepwise up to failure; fixed loads were 80, 100, 114, 136, and 143 MPa. As the last load was increased, the sample failed. The other samples did not fail during tests. Sample SD was loaded at 22, 29, 36, and 38 MPa, and sample CM was tested at 29, 43, and 57 MPa.

The test duration at each load was several days. In the course of this time, we performed several vibrational sessions alternating with conventional loading of the samples without vibration to reveal the effect of vibrations. Usually, vibrational sessions were conducted in the daytime and tests were continued without vibrations at night. The vibration source was a low-power, five-paddle fan operating at a frequency of rotation of 2400 rpm (40 Hz); it was located at the upper traverse of the press, through which vibrations were transferred to the sample. The pressure in the air flow

1063-7834/03/4512-2287$24.00

created by the fan was varied at a frequency of 200 Hz, and the vibration amplitude was about 1 μm.

AE and microdeformation parameters were recorded during all tests. AE was detected with a wideband damped piezoelectric detector with an active element made of PZT-19 piezoelectric ceramics. The gain of the AE channel was ~2000, and the delay time of the equipment was ~1 ms. To decrease the influence of noise, we record events with certain amplitudes. The threshold of amplitude discrimination was chosen above the noise and fan vibration level. The experimental data were accumulated and processed with a computer. The equipment operated in the waiting mode. A write cycle started once a subsequent AE event satisfying the sampling conditions appeared. Each event was described with six parameters, including the current time counted from the beginning of the experimental session. In one session, 10^2 to 10^5 acoustic signals were recorded. The data were statistically processed using a sliding statistical sample of constant volume (32 events) with a one-event shift. The time at which the last event in a sample occurred was assigned to the whole sample.

3. EXPERIMENTAL RESULTS

We performed 55 ordinary experimental sessions and 57 vibrational sessions. The difference between the AE recorded during a vibrational session and the AE characteristic of the ordinary deformation mode, which was earlier detected in [10], consisted in an increase in the number of low-amplitude signals during the vibrational session; most of them appeared synchronously with vibrations. The AE level during a vibrational session is usually a few times higher than that recorded in an ordinary deformation session without vibrations. However, the specific features of AE are most pronounced in the initial stage of vibrational sessions. Indeed, during an ordinary deformation session, the AE behavior changes only weakly, whereas at the beginning of a vibrational session AE increases abruptly and then significantly decreases. Thereafter, AE is virtually constant for the rest of a vibrational session. The typical time sequences of AE during an ordinary test session and during a vibrational session are shown in Fig. 1. All vibrational sessions can be conventionally divided into three groups differing in the initial stage. In the first group, a vibrational session begins without an increase in the AE amplitude; about 10% of the sessions belong to this first group. In the second group of vibrational sessions, the AE amplitude increases sharply without any delay; such sessions make up about 25% of the total. The third group contains the majority of vibrational sessions; the AE amplitude in this group increases after a certain time delay with respect to the beginning of a vibrational session. The scaled-up parameters of the second and third groups are shown in Figs. 2 and 3.

4. DISCUSSION OF THE RESULTS

The AE spikes at the beginning of vibrational sessions in the given dependences are most likely due to the trigger effect of vibrations on the stressed medium. The initial AE spikes are seen to be significantly higher than the AE background level typical of the rest of the vibrational sessions. The anomalous activation is complex and consists of several alternating short AE rises and drops, which are likely associated with the individual regions in a sample involved in the process, with each region having a different degree of susceptibility to vibrations. The degree of susceptibility of a local volume to vibrations will be high if there are stresses comparable to the material strength in this volume and a relatively high concentration of defects in it. This concentration should be sufficient to form defects of a higher structural level, whose appearance is accompanied by the generation of an acoustic signal that can be reliably recorded because of its high amplitude.

Indeed, according to the modern concepts, structural elements of the lowest level have the highest susceptibility to weak vibrations. The mobility of such elements increases in a vibrational field, which raises the probability of creating point and linear defects. As these defects accumulate, they grow in size and the process of failure involves another structural level and proceeds via a concentration mechanism.

According to the concentration criterion of crack growth [11], the transition of failure to the next structural level takes place when a certain critical concentration of defects N is reached in a loaded material. This concentration depends on the sizes of the forming defects l_i:

$$R = N^{-1/3},$$
$$K = R/l_i = N^{-1/3}/l_i,$$

where R is the mean distance between cracks of the ith rank and K is a dimensionless parameter characterizing the mean defect spacing in terms of the defect sizes.

In this form, the concentration criterion is valid for materials that have no defects prior to loading. Imperfect media, such as rocks, always contain a certain amount N_0 of defects formed earlier. Taking these defects into account, we can write the current concentration of defects as

$$N = N_0 + \dot{N}t,$$
$$K = \frac{(N_0 + \dot{N}t)^{-1/3}}{l_i},$$

where $\dot{N}$ is the rate of defect concentration change.

Whence it follows that the transition of failure (which proceeds at a rate of defect accumulation $\dot{N}$) to the next structural level takes some time. Depending on the vibration parameters (in particular, the vibration

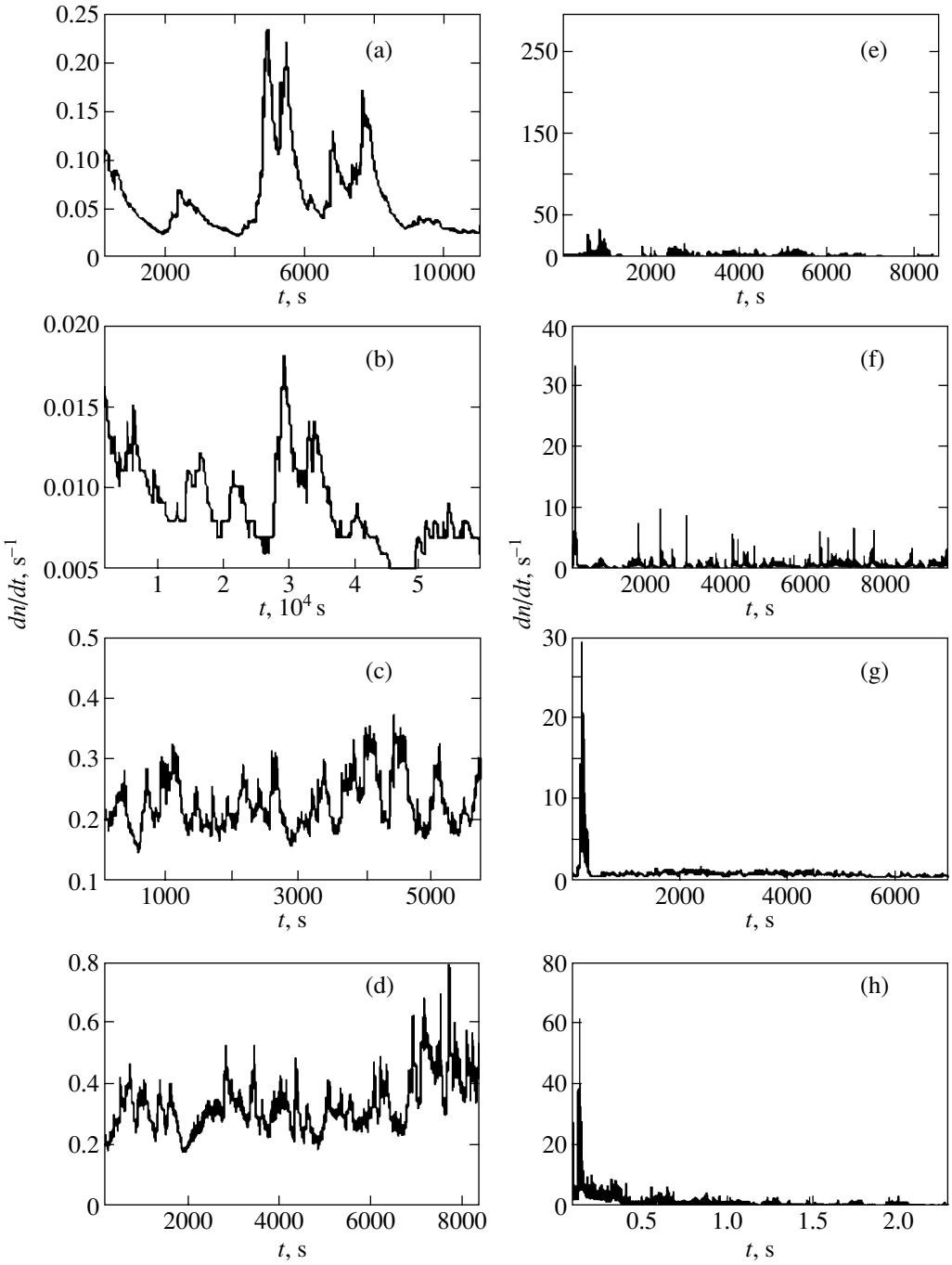

Fig. 1. AE in a session (a–d) without vibrations and (e–h) with vibrations. (a, e) Sample K under a load of 80 MPa; (b, f) sample K, 143 MPa; (c, g) sample SD, 29 MPa; and (d, h) sample CM, 29 MPa.

amplitude), only relatively low structural levels of a loaded material are directly affected by vibrations. Then, this effect extends to higher levels through a rapid accumulation of defects. Because of the finite sensitivity of the equipment and the presence of noise, the effect of vibrations on a certain high structural level can be detected only after the time for which defects are accumulated and failure reaches this structural level according to a concentration scheme. Beginning from this instant, the rate of defect accumulation can be roughly estimated using the AE method. Of course, defects whose acoustic signals do not exceed the noise level and the equipment sensitivity cannot be detected.

The trigger effect of weak vibrations in heterogeneous materials can be explained using the following considerations based on the concepts of the local (differential) strength and life of structural elements making up a material. We assume that the strength distribu-

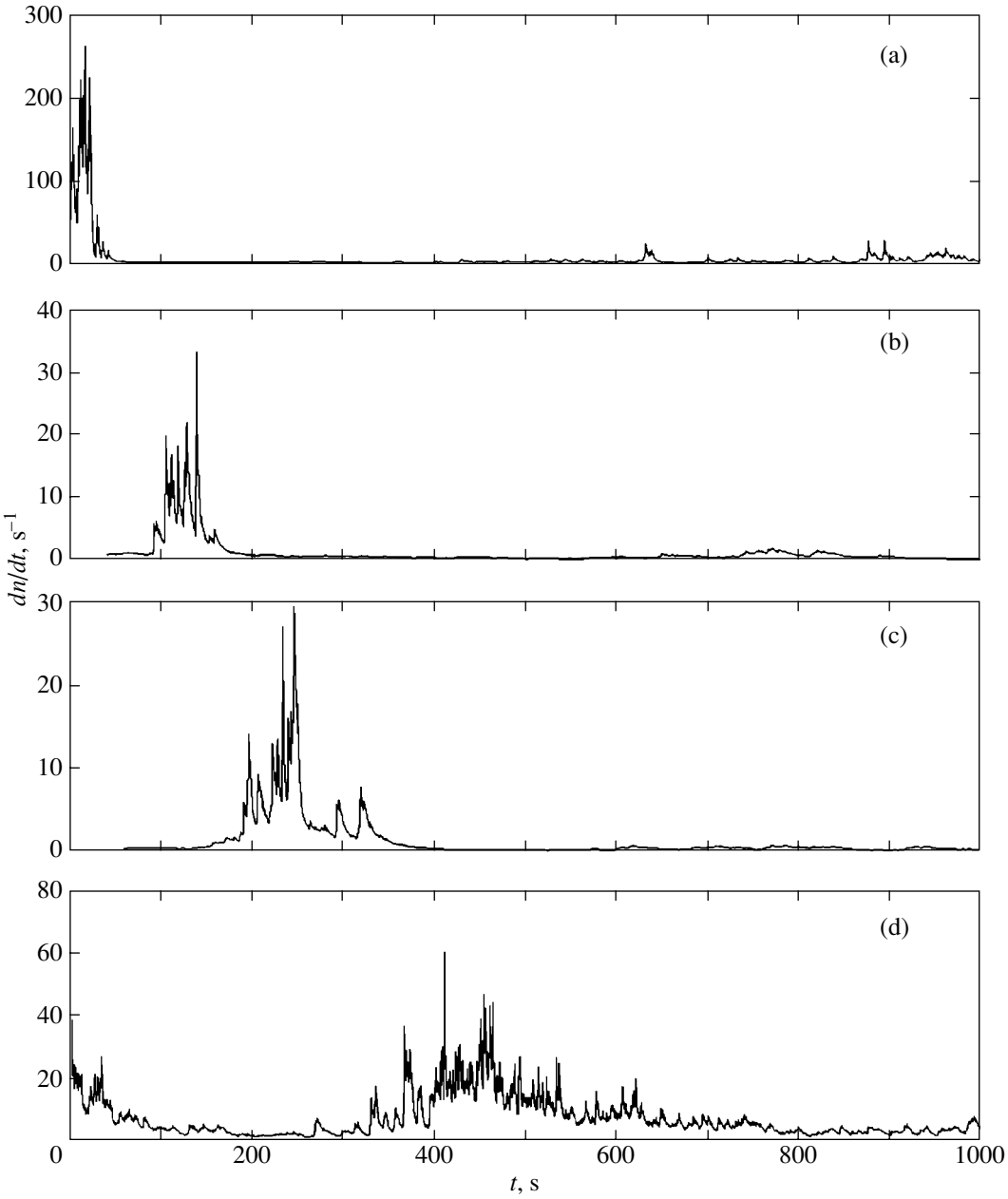

Fig. 2. AE in the initial stage of vibrational sessions: (a) sample SD under a load of 29 MPa; (b) sample K, 143 MPa; (c) sample K, 80 MPa; and (d) sample CM, 29 MPa.

tion of the structural elements is close to being exponential (Fig. 3a). At a given load, only structural elements whose strength is below σ_0 can be involved in the process of failure. Vibrations involve an additional number of structural elements in this process (the region between σ_0 and σ_b in Fig. 3a), which is equivalent to an increase in the load.

According to modern concepts, the mobility of structural elements increases in a vibrational field, which results in a decrease in internal friction, an increase in the probability of defects forming, and an apparent decrease in the strength and life of a material. An increase in the number of defects forming at the beginning of vibrations is accompanied by an increase in the AE activity and, therefore, can be reliably detected. These changes are shown schematically in Figs. 3b and 3c. Here, the instant of time t_0 corresponds to the beginning of vibrations. At this instant, the material transforms jumpwise from the state with apparent strength σ_0 to a new state with strength σ_b. When vibrations are applied to the material, the loading conditions change jumpwise and the portion of structural elements (corresponding to the region between σ_0 and σ_b in Fig. 3a) acquire the new (prefailure) state. These ele-

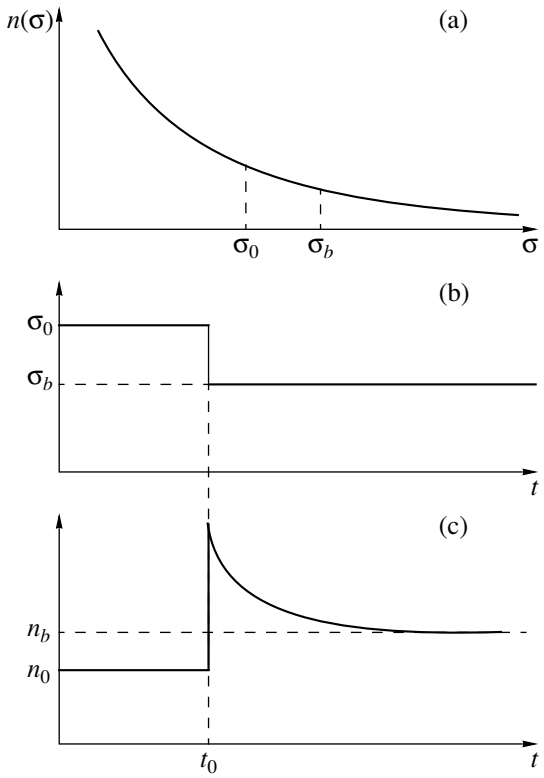

Fig. 3. (a) Hypothetic strength distribution of structural elements, (b) assumed vibration-induced apparent decrease in the strength, and (c) vibration-induced change in the AE signal.

ments fail rapidly, which manifests itself as a trigger increase in the AE activity. However, if vibrations are insufficiently intense, this effect, as noted above, can be detected only after the time it takes for the process of failure to reach a relatively high structural level making it possible to experimentally detect this effect.

Another specific feature of the initial stage of certain vibrational sessions is the deep and long decrease in the AE amplitude after the initial trigger jump (Fig. 2). This decrease is likely caused by intense unloading of the most mechanically unstable regions because of an avalanche mechanical process during the initial activation of failure after vibrations have been turned on. In several cases (especially in marble), the AE decrease is followed by a secondary AE jump, which resembles a transient process developing in the case of weak damping in the system.

5. CONCLUSIONS

Thus, we have revealed the initiating effect of weak low-frequency vibrations on the process of elastic energy release in loaded geologic materials, which manifests itself as a sharp increase in the AE activity at the beginning of vibrational sessions. The increase in the AE activity can proceed with a delay. The high AE activity at the beginning of a vibrational session takes place for a rather short time (100–200 s), after which it drops within about the same time period and the AE amplitude levels off at a magnitude higher than the background level characteristic of an ordinary session without vibrations.

The time delay of the vibrational action is likely associated with the concentration mechanism of failure and depends on the parameters of externally applied vibrations, the imperfection of a material, the conditions for recording signals, and the sensitivity of the equipment employed.

ACKNOWLEDGMENTS

This work was supported in part by the Russian Foundation for Basic Research (project nos. 01-05-64893, 02-05-08003, 02-05-39017), the U.S. Civilian Research and Development Foundation for the Independent States of the Former Soviet Union (CRDF) (grant no. YGI-2316-BI-02), and the International Science and Technology Center (ISTC) (grant no. 1745).

REFERENCES

1. N. N. Peschanskaya and P. N. Yakushev, Fiz. Tverd. Tela (Leningrad) **30** (7), 2196 (1988) [Sov. Phys. Solid State **30**, 1264 (1988)].
2. V. I. Nikolaev and V. V. Shpeĭzman, Fiz. Tverd. Tela (St. Petersburg) **39** (4), 647 (1997) [Phys. Solid State **39**, 565 (1997)].
3. A. B. Lebedev, S. B. Kustov, and B. K. Kardashev, Fiz. Tverd. Tela (Leningrad) **24**, 3169 (1982) [Sov. Phys. Solid State **24**, 1798 (1982)].
4. B. A. Bolt, W. L. Horn, G. A. Makdonald, and R. F. Scott, *Geological Elements* (Springer, Heidelberg, 1977; Mir, Moscow, 1978).
5. K. M. Mirzoev and S. Kh. Negmatulaev, *Forecasting of Earthquakes* (Donish, Dushanbe, 1983), No. 4, p. 365.
6. M. A. Sadovskiĭ, K. M. Mirzoev, S. Kh. Negmatulaev, and N. G. Salomov, Izv. Akad. Nauk SSSR, Fiz. Zemli, No. 6, 32 (1981).
7. K. M. Mirzoev, S. Kh. Negmatulaev, S. D. Vinogradov, T. Yu. Dasturi, and V. I. Starkov, *Modeling and Examinations of Actual Earthquake Origins* (Nauka, Moscow, 1991), p. 143.
8. G. A. Sobolev and A. V. Ponomarev, Vulkanol. Seismol., No. 6, 51 (1997).
9. G. A. Sobolev, A. V. Ponomarev, and A. V. Kol'tsov, Fiz. Zemli, No. 12, 72 (1995).
10. L. M. Bogomolov, B. Manjikov, V. N. Syshev, and T. E. Tullis, EOS Trans. Am. Geophys. Union **81**, 1082 (2000).
11. S. N. Zhurkov, V. S. Kuksenko, V. A. Petrov, *et al.*, Izv. Akad. Nauk SSSR, Fiz. Zemli, No. 6, 8 (1977).

Translated by K. Shakhlevich

Physics of the Solid State, Vol. 45, No. 12, 2003, pp. 2292–2296. Translated from Fizika Tverdogo Tela, Vol. 45, No. 12, 2003, pp. 2187–2191.

DEFECTS, DISLOCATIONS, AND PHYSICS OF STRENGTH

Specific Features of Helium Penetration into Single-Crystal and Nanocrystalline Copper under Deformation in Liquid Helium

O. V. Klyavin, V. I. Nikolaev, L. V. Khabarin, Yu. M. Chernov, and V. V. Shpeĭzman

Ioffe Physicotechnical Institute, Russian Academy of Sciences, Politekhnicheskaya ul. 26, St. Petersburg, 194021 Russia
e-mail: Klyavin@mail.ioffe.ru

Received May 6, 2003

Abstract—This paper reports on experimental data on the penetration of helium atoms into single-crystal and nanocrystalline copper samples subjected to tensile and compressive strains at $T = 4.2$ K, respectively. The dependences of the helium concentration N in the samples on the strain ε and the curves of helium extraction in the temperature range 300–1000 K at different strains ε are determined. It is found that the dependences $N(\varepsilon)$ and $\sigma(\varepsilon)$ correlate qualitatively with each other for single-crystal copper and do not correlate for nanocrystalline copper. This is associated with the different mechanisms of deformation in these samples. The deformation proceeds through the dislocation mechanism in single-crystal copper and through the jumpwise (twinning, rotational) mechanisms in nanocrystalline copper during local heating in regions of plastic shears. These factors are also responsible for the considerable difference between the curves of helium extraction from samples of both types. The curves of helium extraction exhibit two maxima for single-crystal copper and five maxima for nanocrystalline copper samples. The results obtained are discussed in terms of both the dynamic dislocation pipe diffusion and grain-boundary mechanisms of particle penetration from the surrounding medium into copper through different-type moving defects under applied stresses and due to the gradient of the chemical potential at the metal–surrounding medium interface. © *2003 MAIK "Nauka/Interperiodica".*

1. INTRODUCTION

The basic regularities of mechanochemical penetration of particles from an external medium into crystalline materials have been investigated on the basis of dynamic dislocation pipe diffusion for a long time [1–6]. This phenomenon is associated with the penetration of particles from the surrounding medium into a surface layer of strained materials through nucleating and moving dislocations owing to a decrease in the potential barriers in their cores under applied stresses and due to the gradient of the chemical potential at the solid–medium interface. The generality of this phenomenon in single-crystal and polycrystalline materials with lattices of different types has been proved experimentally using the example of a model helium medium in the temperature range 300–0.6 K and also gaseous nitrogen, air with various water contents, and heavy water at $T = 300$ K. In our earlier work [5], we revealed that helium can also penetrate into amorphous materials (eutectic amorphous films) in the course of their deformation in liquid helium. In the initial defect structure of amorphous materials, slip occurs through intercluster boundaries (interlayers). In these materials, regions of local plastic shears are formed, for example, by way of homogeneous nucleation of quasi-dislocations with a quasi-periodic potential (Somigliana dislocations) [7]. This provides viscous plastic flow of amorphous films with a very small coefficient of hardening, which was observed in films down to the liquid-helium temperature [5].

The curves of helium extraction from amorphous films strained at $T = 4.2$ K exhibit several peaks, which are located at temperatures close to the melting point, at this point, and higher temperatures. These findings can be explained by the chemical bonding of helium atoms and atoms of the defect structure of amorphous films due to the formation of excited chemical bonds in the intercluster structure in the course of dynamic transformation during plastic deformation. The presence of chemical bonds between helium atoms and atoms of the crystal lattice was experimentally demonstrated with ionic crystals of lithium fluoride by helium flaw detection [8]. Therefore, in amorphous materials, the phenomenon of dynamic dislocation pipe diffusion, which is characteristic of crystalline materials, transforms into the phenomenon of mechanochemical penetration of particles from the surrounding medium through defects differing from dislocations. In the general case, the carriers that provide the penetration of particles from the surrounding medium into different-type (crystalline, amorphous, polymeric) solids are moving, chemically active, excited nanodefects—localized states of atomic or molecular groups. The electronic structure of these states experiences dynamic transformations due to plastic deformation or other dynamic processes, which result in a change in the energy parameters of the cor-

related interactions between particles of the surrounding medium and solids subjected to external actions of different physical nature.

The main objective of this work was to elucidate how the initial defects in a metal under deformation affect the regularities in the penetration of helium atoms into the metal. For this purpose, we undertook comparative investigations of the penetration of helium atoms into nanocrystalline and single-crystal copper samples.

2. EXPERIMENTAL TECHNIQUE

The copper single crystals (purity, 99.998%) oriented approximately along the [110] axis were grown by the Bridgman method in graphite molds under vacuum. Samples $4 \times 1 \times 30$ mm in size with vanes were extended on an Instron 1342 machine to different strains at a rate of 10^{-4} s^{-1} in liquid helium at $T = 4.2$ K. Nanocrystalline copper (purity, 99.996%) with a mean grain size of 100 nm was prepared by equichannel angular pressing. Samples $4 \times 6 \times 14$ mm in size were cut out with a milling cutter from a large piece. These samples were compressed to different strains at a rate of 10^{-4} s^{-1}. The helium concentration in the strained samples was determined using a high-resolution mass spectrometer (the threshold of sensitivity was approximately equal to 10^9 atoms for ^{4}He [9]). The strained samples were cut by the electric-spark method. We analyzed regions corresponding to the operating length of the samples, regions in the vicinity of the vanes, and face regions in the case of compression.

With the aim of revealing helium traps in differently strained copper samples, the curves of helium extraction were obtained at a constant heating rate (7 K/min) in the temperature range 300–1000 K.

3. RESULTS AND DISCUSSION

3.1. Copper Single Crystals

The samples were extended to different strains up to $\varepsilon = 13\%$. Curve *1* in Fig. 1 depicts the diagram $\sigma(\varepsilon)$, where σ is the applied stress. The initial portions of the curves $\sigma(\varepsilon)$ for different samples at small strains ε are shown by curves *a*, *b*, and *c* in Fig. 1. It is clearly seen from Fig. 1 that these curves are characterized by yield plateaus with a small coefficient of hardening. As the strain increases, the slope of the curve increases twice, because all slip planes of the (110) [110] system for these single crystals successively come into play at large strains. Unlike the stress–strain diagram for nanocrystalline copper (see Section 3.2), the diagram for copper single crystals does not exhibit jumps.

The dependence of the helium concentration N (atoms/cm^2) on the strain of the samples is shown by curve *2* in Fig. 1. The dependences $N(\varepsilon)$ and $\sigma(\varepsilon)$ correlate with each other, except for the initial range in which the slope of the dependence $N(\varepsilon)$ is larger than

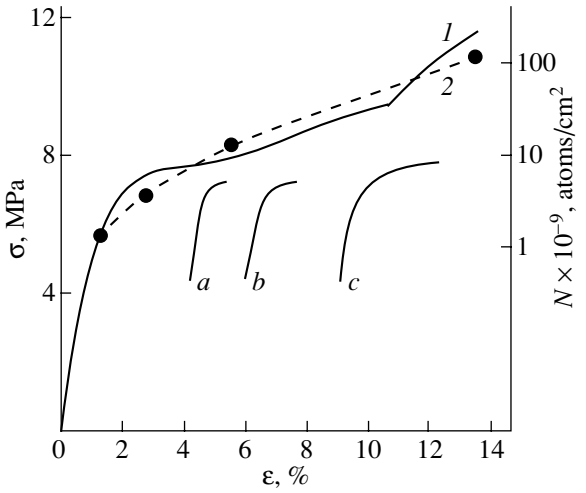

Fig. 1. (*1*) Tensile stress–strain diagram for the copper single crystal at $T = 4.2$ K and (*2*) the dependence of the helium concentration $N(\varepsilon)$ in samples on the plastic strain. (*a*, *b*, *c*) Initial portions of the curves $\sigma(\varepsilon)$ at small strains $\varepsilon = 0.5$–2.5%.

that of the dependence $\sigma(\varepsilon)$. This behavior is associated with the fact that, at strains in the vicinity and at the yield point of the copper single crystals, plastic shears arise from Frank–Read sources in the form of pileups of dislocations. These dislocations have the same sign and move at high velocities, which leads to an increase in the penetration rate of helium into dislocations. In the range of the yield plateau, the dislocation multiplication proceeds as a result of propagation of plastic shears through the mechanism of their cross slip, which is accompanied by a decrease in the dislocation velocity and, hence, in the penetration rate of helium into dislocations. This leads to a weakening of the dependence $N(\varepsilon)$, whose slope becomes constant at larger strains.

The temperature dependence of the amount of extracted helium from the central region of the sample strained to $\varepsilon = 13\%$ is depicted by curve *1* in Fig. 2. The principal broad maximum of helium extraction is located in the range 373–773 K with a peak at $T = 523$ ($T \approx 0.4T_s$, where $T_s = 1356$ K is the melting temperature of copper). Moreover, the dependence exhibits a weak maximum with a peak at $T = 823$ K ($T \approx 0.6T_s$). These two maxima indicate that the strained sample contains helium traps of two types, namely, high- and low-temperature traps. Helium is predominantly contained in the low-temperature traps. The helium concentration in the low-temperature traps is equal to 25×10^{10} atoms/cm^2, whereas the helium concentration in the high-temperature traps is 0.8×10^{10} atoms/cm^2. The ratio of these concentrations is approximately 30 : 1. Defects that form traps for helium atoms in the strained copper single crystals are dislocations and deformation-induced vacancies, which are formed in large amounts when dislocations multiply through the mechanism of double cross slip. Upon heating of the strained

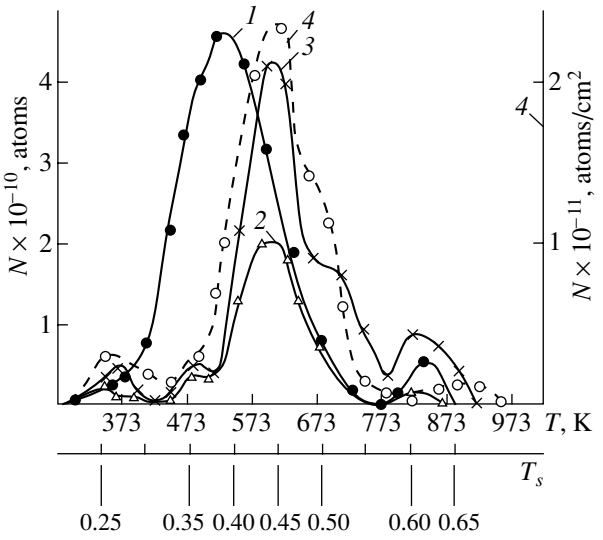

Fig. 2. Curves $N(T)$ of helium extraction from (*1*) the copper single crystal and (*2*–*4*) nanocrystalline copper at ε = (*1*) 13, (*2*) 14, (*3*) 19, and (*4*) 7% (face regions). The heating rate is 7 K/min.

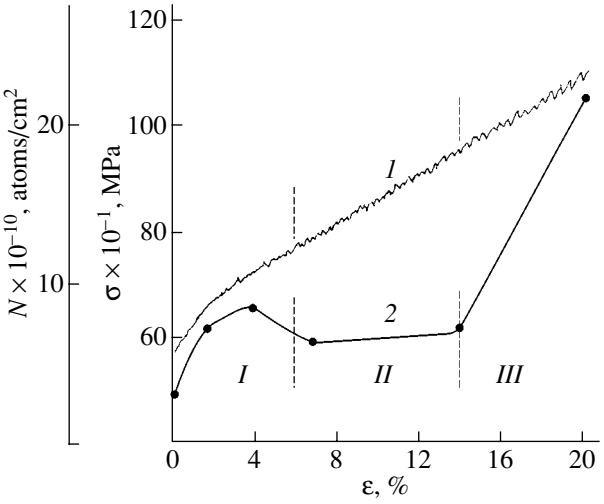

Fig. 3. (*1*) Compression stress–strain diagram for the nanocrystalline copper sample at T = 4.2 K and (*2*) the dependence of the helium concentration N in samples on the plastic strain.

samples to 300 K, vacancies partially emerge from the sample bulk to the outer surface, annihilate with interstitial atoms in dislocation dipoles, and form vacancy pores into which helium atoms penetrate in the course of heating of the samples and their subsequent treatment at 300 K. For the most part, helium is contained in the low-temperature traps located in dislocations and escapes from them through the mechanism of pipe diffusion, migration over divacancies and interstices, and annihilation of short dislocation loops that carry helium to the sample surface due to image forces. It seems likely that the high-temperature maximum is caused by the escape of helium atoms from vacancy pores whose activation energy is higher than that of defects responsible for the low-temperature maximum.

3.2. Nanocrystalline Copper

The compression stress–strain diagram for the sample strained to a maximum degree is presented in Fig. 3 (curve *2*). It can be seen from this figure that the plastic deformation in nanocrystalline copper at T = 4.2 K proceeds in an irregular way with a large constant coefficient of hardening. At small strains $\varepsilon < 5\%$ (Fig. 4, curve *1*), plastic flow occurs through intragrain slip of dislocations generated in nanograins with the most preferred crystallographic orientation. In the range ε = 5–14% (Fig. 4, curve *2*), the diagram exhibits random jumps with irregular amplitudes differing in shape. The appearance of jumps can be associated with mechanical twinning that covers the volume of several nanograins with a similar orientation. A jumpwise plastic deformation due to mechanical twinning is typical of nanocrystalline copper at the liquid-helium temperature [9]. Therefore, we can assume that this process in nanocrystalline copper also takes place in the above strain range. The final portion of the diagram ($\varepsilon > 14\%$) corresponds to the completion of correlated lattice reorientations in nanograins owing to the mechanical twinning and the initiation of the rotational (disclination) intercrystalline mechanism of deformation. The deformation occurs through mesoscopic plastic shears, which manifest themselves in macroscopic jumps with amplitudes as large as several tenths of a percent of the total strain of the sample. This suggests that the kinetics of structural relaxation in nanocrystalline copper is governed by the time evolution, self-organization, and correlation of structural kinetic units of plastic deformation proceeding in the form of jumps. The above mechanism of the dynamic process of structural relaxation in the strained samples is collective and correlated (synergetic) in character. Therefore, the diagram $\sigma(\varepsilon)$ (Fig. 3, curve *2*) can be divided into three portions: portion *I* corresponds to the intragrain dislocation slip, portion *II* is associated with the mechanical twinning, and portion *III* is described by the intercrystalline (rotational) mechanism.

The measured dependence of the helium concentration N in the central regions of the samples on the strain is shown by curve *2* in Fig. 1. At strains smaller than $\varepsilon \approx 4\%$ (portion *I*), the helium concentration N in the strained samples increases by a factor of approximately three as compared to that in the unstrained sample. This is associated with the intragrain dislocation slip, which provides efficient penetration of helium atoms into the nanograin structure of copper at small strains ε. In portion *II* ($\varepsilon \approx$ 5–14%), the helium concentration N remains almost unchanged. In this case, we can assume that helium atoms do not penetrate into the strained

samples owing to the development of mechanical twinning, which manifests itself as irregular jumps of various shape in the dependence $\sigma(\varepsilon)$. Twinning dislocations have no clearly defined core, because they only ensure the reorientation of the crystal lattice, in contrast to lattice dislocations involved in the material transfer due to the slip. Therefore, atomic displacements in twinning dislocations are small compared to those in cores of edge and screw dislocations, whose motion is accompanied by the breaking and formation of bonds between atoms in the lattice and, hence, by a drastic change in the potential barriers between atoms. Consequently, we can expect that helium atoms will not penetrate into moving twinning dislocations, which leads to the appearance of a plateau in the curve $N(\varepsilon)$. A slight decrease in the helium concentration in the strained samples from the maximum to N = const in the curve $N(\varepsilon)$ can be explained by the crossover from intragrain slip to mechanical twinning (Fig. 3, curve *2*). In this case, a number of helium atoms can escape from the sample under deformation as a result of interaction of moving twinning dislocations with immobile intragrain dislocations saturated with helium atoms. Furthermore, as was noted above, the mechanical twinning leads to the cessation of helium penetration into the nanocrystalline copper samples. For this reason, the amount of helium that penetrates into the nanocrystalline copper sample (7×10^{10} atoms/cm^2) turns out to be more than one order of magnitude less than the amount of helium that penetrates into the single-crystal sample (7×10^{11} atoms/cm^2) at $\varepsilon = 13\%$.

At $\varepsilon > 14\%$ (portion *III*), the helium concentration N sharply increases (by a factor of seven) as compared to 30×10^9 atoms/cm^2 in the unstrained sample and reaches 220×10^9 atoms/cm^2. The considerable increase in helium concentration N can be explained by the following factors. Compared to the initial wavy portion of the curve $\sigma(\varepsilon)$, jumps at large strains ε occur more frequently and their amplitude increases drastically (Fig. 4, curves *1*, *2*). This transformation of jumpwise plastic deformation can be associated with the rotational mechanism of nanograin deformation after the mechanical twinning is complete [10]. In this case, the local strain γ in plastic shears in the course of jumpwise deformation also increases appreciably. Moreover, it is known [11] that the jumpwise plastic deformation in crystalline materials at very low temperatures is accompanied by a local heating (with a temperature gradient ΔT up to tens of degrees) in regions of plastic shear [12, 13]. In nanocrystalline copper, an increase in the local strain γ in plastic shears in the case of the rotational mechanism of deformation leads to an increase in the value of ΔT, which, in turn, results in an increase in γ in plastic shears. Therefore, the effect of these two factors is substantially enhanced for the rotational mechanism of deformation and, as a consequence, results in a sharp increase in the rate of penetration of helium into nanocrystalline copper at large strains ε.

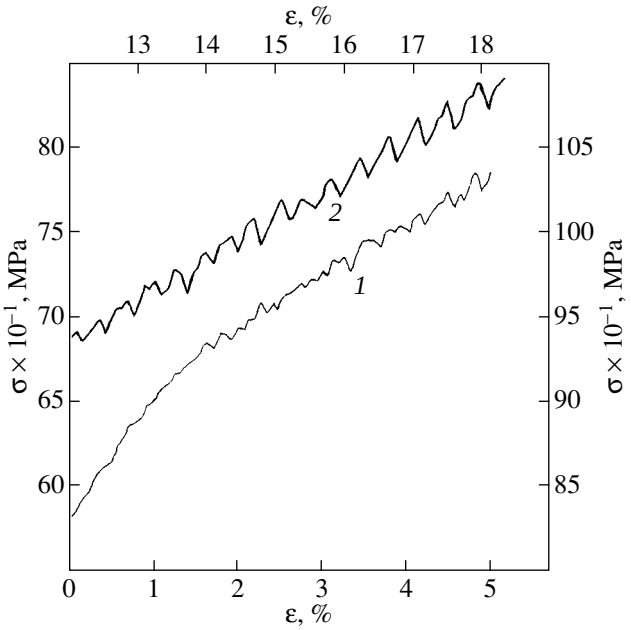

Fig. 4. (*1*) Initial and (*2*) final portions of the compression stress–strain diagram for the nanocrystalline copper sample (Fig. 3) on an enlarged scale.

The absence of correlation between the dependences $N(\varepsilon)$ and $\sigma(\varepsilon)$ for nanocrystalline copper can be explained by the aforementioned sequential crossover from the dislocation (intragrain) mechanism to the mechanical-twinning mechanism and then to the rotational (intercrystalline) mechanism of plastic deformation with an increase in the strain ε.

The curves $N(T)$ of helium extraction for nanocrystalline copper in the range 300–1000 K are depicted in Fig. 2 (curves *2–4*). These curves were obtained for the central regions of the samples at $\varepsilon = 14$ and 19% and also for their face regions at $\varepsilon = 7\%$. The curves exhibit maxima with different heights and widths at $T = 0.25T_s$, $0.35T_s$, $0.45T_s$, $0.5T_s$, $0.6T_s$, and $0.65T_s$. An increase in the strain leads to an increase in the heights of all the maxima (Fig. 2). The principal maximum with a peak at $T = 0.45T_s$ (620 K) is located in the temperature range 470–670 K. The curve $N(T)$ at $\varepsilon = 14\%$ also involves a high-temperature maximum at $T = 0.6T_s$ and two low-temperature maxima at $T = 0.25T_s$ and $0.35T_s$. As the strain ε increases to 19%, one more maximum at $T = 0.5T_s$ arises in the curve $N(T)$. Possibly, the appearance of this maximum is associated with the crossover from the mechanical-twinning mechanism to the rotational (grain-boundary) mechanism of plastic deformation. The crossover is attended by an increase in the helium concentration in the sample [see the dependence $N(\varepsilon)$] and stimulates the formation of new high-temperature traps of helium atoms at $T = 0.5T_s$ (for example, vacancy pores). This maximum is located close to the principal maximum (Fig. 2, curve *3*) and becomes even more pronounced in the curve $N(T)$ for

the face regions of the sample at $\varepsilon = 7\%$ (Fig. 2, curve *4*). For these regions, the high-temperature maximum observed at $T = 0.6T_s$ for the central regions of the samples is shifted to $T = 0.65T_s$ (cf. curves *2–4* in Fig. 2). Furthermore, the height of the principal maximum at $T = 0.6T_s$ for the face regions is more than 30 times greater than that for the central regions of the samples. This finding can be explained by the fact that the compression of the samples gives rise to large, contact, uncontrollable local strains (similar to those observed upon microindentation) in the face regions. These strains are responsible for the drastic increase in the amount of helium atoms that penetrate into the face regions and, hence, in the amount of extracted helium.

For these reasons, the energy traps of helium atoms that manifest themselves in curves $N(T)$ at different temperatures have a different nature and depth depending on the degree and character of deformation of the sample regions.

4. CONCLUSIONS

Thus, we investigated the specific features of the dynamic-dislocation and grain-boundary penetration of helium into single-crystal and nanocrystalline copper samples subjected to tensile and compressive strains in liquid helium at $T = 4.2$ K. The dependences of the helium concentration in the copper samples on the strain and the curves of helium extraction from them were measured for samples with different initial structures. The comparison of the stress–strain diagrams and the dependences of the helium concentration in the samples on the strain revealed a qualitative correlation between them for single-crystal copper and the absence of correlation for nanocrystalline copper. This result was explained by the fundamental difference between the mechanisms of deformation of these samples (the dislocation mechanism for the single crystals and jumpwise twinning and rotational mechanisms for the nanocrystalline copper samples). It was found that the curves of helium extraction from samples of both types differ significantly in the number and location of the maxima of helium liberation.

The results obtained in this study demonstrated that helium traps of different types are formed in the copper samples, depending on their initial structure, which is responsible for the different mechanisms of plastic deformation in liquid helium and, as a consequence, the different curves of helium extraction and helium concentration in the strained samples.

ACKNOWLEDGMENTS

This work was supported by the "Physics of Solid-State Nanostructures" Program of the Ministry of Science and Technology of the Russian Federation.

REFERENCES

1. O. V. Klyavin, N. P. Likhodedov, and A. N. Orlov, Prog. Surf. Sci. **33** (4), 259 (1990).
2. O. V. Klyavin, Fiz. Tverd. Tela (St. Petersburg) **35** (3), 513 (1993) [Phys. Solid State **35**, 261 (1993)].
3. G. I. Shvets, O. V. Klyavin, and G. A. Banshchikov, Fiz. Tverd. Tela (Leningrad) **27** (9), 2618 (1985) [Sov. Phys. Solid State **27**, 1570 (1985)].
4. O. V. Klyavin, B. A. Mamyrin, L. V. Khabarin, and Yu. M. Chernov, Izv. Ross. Akad. Nauk, Ser. Fiz. **63** (9), 1876 (1999).
5. O. V. Klyavin, B. A. Mamyrin, L. V. Khabarin, *et al.*, Fiz. Tverd. Tela (St. Petersburg) **42** (7), 1256 (2000) [Phys. Solid State **42**, 1294 (2000)].
6. O. V. Klyavin, B. A. Mamyrin, L. V. Khabarin, and Yu. M. Chernov, Fiz. Tverd. Tela (St. Petersburg) **44** (2), 291 (2002) [Phys. Solid State **44**, 302 (2002)].
7. A. K. Emaletdinov, R. L. Nurulaev, and N. D. Aleksandrov, in *Abstracts of XXIX International Seminar on Actual Problems of Strength, Chernogolovka* (2002), p. 134.
8. A. I. Kupryazhkin and A. Yu. Kurkin, Fiz. Tverd. Tela (St. Petersburg) **35** (11), 3003 (1993) [Phys. Solid State **35**, 1475 (1993)].
9. O. V. Klyavin, in *Physical Processes of Plastic Deformation at Low Temperatures* (Naukova Dumka, Kiev, 1974).
10. N. I. Noskova and E. G. Volkova, Fiz. Met. Metalloved. **91** (6), 100 (2001).
11. O. V. Klyavin, *Physics of the Crystal Plasticity at Liquid-Helium Temperatures* (Nauka, Moscow, 1987).
12. G. A. Malygin, Fiz. Tverd. Tela (St. Petersburg) **39** (11), 2019 (1997) [Phys. Solid State **39**, 1806 (1997)].
13. O. V. Klyavin, G. A. Malygin, and Yu. M. Chernov, Fiz. Tverd. Tela (St. Petersburg) **38** (1), 191 (1996) [Phys. Solid State **38**, 105 (1996)].

Translated by O. Borovik-Romanova

Physics of the Solid State, Vol. 45, No. 12, 2003, pp. 2297–2302. Translated from Fizika Tverdogo Tela, Vol. 45, No. 12, 2003, pp. 2192–2197.

MAGNETISM AND FERROELECTRICITY

Phase Separation of the Spin System in the $La_{0.93}Sr_{0.07}MnO_3$ Crystal

S. F. Dubunin, V. E. Arkhipov, S. G. Teploukhov, V. D. Parkhomenko, N. N. Loshkareva, and N. I. Solin

Institute of Metal Physics, Ural Division, Russian Academy of Sciences, ul. S. Kovalevskoĭ 18, Yekaterinburg, 620219 Russia

e-mail: dubinin@uraltc.ru

Received March 27, 2003

Abstract—The magnetic state of the manganite $La_{0.93}Sr_{0.07}MnO_3$ in the range 4.2–290 K was studied using elastic neutron scattering. The magnetic state of this compound was found to occupy a particular place in the $La_{1-x}Sr_xMnO_3$ solid-solution system, in which the antiferromagnetic type of order ($LaMnO_3$, T_N = 139.5 K) switches to ferromagnetic ordering ($La_{0.9}Sr_{0.1}MnO_3$, T_C = 152 K) with increasing x. In the transition state, this compound contains large-scale spin configurations of two types. A fractional crystal volume of about 10% is occupied by regions of the ferromagnetic phase with an average linear size of 200 Å, while the remainder of the crystal is a phase with a nonuniform canted magnetic structure. Arguments are presented for the phase separation of the $La_{0.93}Sr_{0.07}MnO_3$ spin system being accounted for by Mn^{4+} ion ordering. © *2003 MAIK "Nauka/Interperiodica".*

1. INTRODUCTION

The acute interest in the magnetic state of complex manganese oxides originates from the rich diversity of their physical properties. Indeed, while the fact nonuniform states (phase separation) can arise that in substances of this class has been known for a long time, it only recently became recognized that this phenomenon can play a crucial part in the formation of their unusual physical properties [1, 2].

A typical complex manganese oxide is represented by the system

$$La_{1-x}Sr_xMnO_3. \quad (1)$$

As the parameter x increases, system (1) transfers from the antiferromagnetic (AFM) type of ordering in $LaMnO_3$ (T_N = 139.5 K [3]) to ferromagnetic (FM) ordering in the manganite $La_{0.9}Sr_{0.1}MnO_3$ (T_C = 152 K [4]). The change in the type of magnetic ordering is the result of competition between the indirect- and double-exchange ($Mn^{4+} \rightleftharpoons O \rightleftharpoons Mn^{3+}$) mechanisms. This phase transition is specific in that it occurs in a narrow compositional interval, $0 < x < 0.1$ (this may take place in the case of strongly correlated systems [2]), so that small changes in the doping level (in the fraction of Mn^{4+} ions) may trigger substantial changes in the spin system of the manganite in the transition region.

We are aware of only one publication [5] on in-depth study of the magnetic state of single-crystal $La_{0.94}Sr_{0.06}MnO_3$ close in composition to the middle of the AFM $\longrightarrow$ FM transition region made using elastic and inelastic neutron scattering. According to [5], the manganite has a canted magnetic structure in which the z and (x, y) spin projections determine the ferromagnetic and antiferromagnetic types of ordering, respectively. This transition spin configuration is nonuniform. Slight deviations of individual components of the canted structure from their average values become manifest in the diffraction pattern of the crystal in the form of small diffuse maxima near the main Bragg reflections. The scale of these nonuniformities was also defined in [5]. Here, we present the most typical correlation lengths $\chi_{[nkl]}$, because they will be of interest further on:

$$\chi_{[010]} = 7 \text{ Å}, \quad \chi_{[101]} = 17 \text{ Å}. \quad (2)$$

To gain a better understanding of the structure of the spin system in the transition region of the manganese oxides (1), we studied the manganite $La_{0.93}Sr_{0.07}MnO_3$ having a doping level larger than that of the crystal studied in [5].

The manganite crystal was grown using the floating-zone technique and consisted of two large, closely spaced single-crystal blocks. The misorientation in a block did not exceed 20′. The sample was a cylinder with linear dimensions d = 4 mm and l = 10 mm. At room temperature, the crystal had orthorhombic structure **O'** with lattice parameters a_0 = 5.58, b_0 = 7.76, and c_0 = 5.55 Å.

Experiments on the elastic scattering of thermal neutrons were performed on a special multidetector diffractometer intended for investigating single crystals. The wavelength of the neutrons striking the sample after passing through a double-crystal monochromator of pyrolytic graphite and strained germanium was λ =

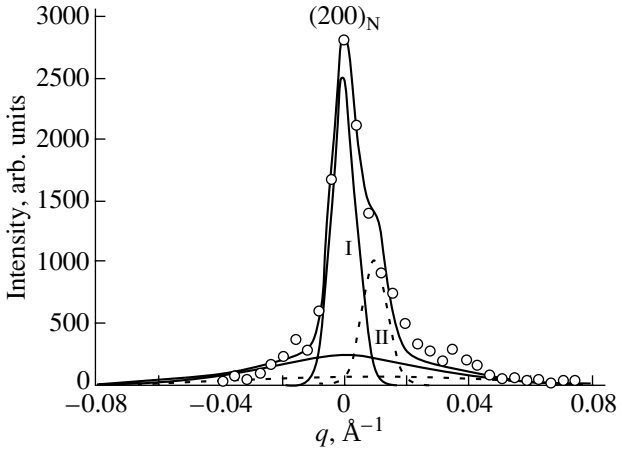

Fig. 1. $(200)_N$ nuclear reflection and analysis of its intensity profile in the neutron scattering pattern of $La_{0.93}Sr_{0.07}MnO_3$, measured at 290 K along the [010] crystallographic direction. Points are experimental data, the thick line is calculation, and thin and dashed lines refer to the contributions from single-crystal blocks I and II to the scattering intensity.

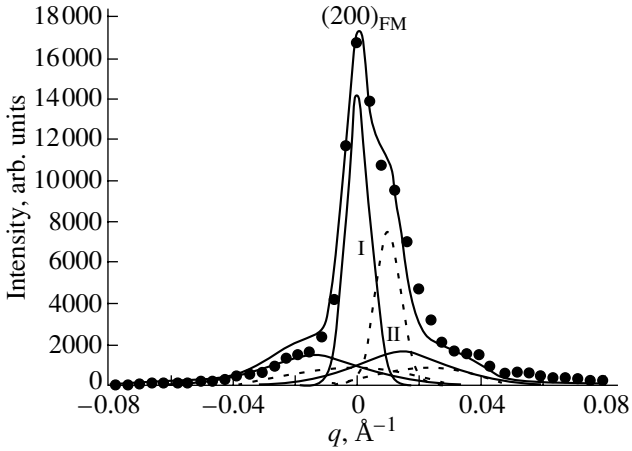

Fig. 2. Ferromagnetic component of the (200) Bragg reflection and its profile analysis in the neutron scattering pattern of $La_{0.93}Sr_{0.07}MnO_3$ measured at 4.2 K along the [010] crystallographic direction. Points are experimental data, the thick line is calculation, and thin and dashed lines refer to the contributions from single-crystal blocks I and II to the scattering intensity.

1.567 Å. By strongly monochromatizing the primary beam and choosing the optimum wavelength of monochromatic neutrons, we succeeded in suppressing multiple diffraction harmonics in the scattering pattern. This feature substantially increases the sensitivity of our technique.

2. RESULTS OF THE EXPERIMENT

The neutron elastic scattering patterns of the $La_{0.93}Sr_{0.07}MnO_3$ single crystal were obtained in the range 4.2–290 K in the a^*b^* reciprocal-lattice plane, which includes nodes of both the antiferromagnetic and ferromagnetic types. The scanning directions of the reciprocal-lattice Bragg nodes were chosen with due account of the instrument resolution of the diffractometer. It is appropriate to note here that the magnetic scattering pattern of $La_{0.93}Sr_{0.07}MnO_3$ measured at 4.2 K turned out to be fairly complex and differs from the one published in [5]. Therefore, the results of our experiment will be presented in an order which we believe to be more convenient for logical construction of the ground-state arrangement of the manganite spin system.

Let us consider first the pattern in the vicinity of the (200) Bragg reflection. The open circles in Fig. 1 show the scattering pattern obtained at the sample temperature of 290 K. The reflection shown in Fig. 1 was scanned in the [010] direction. The instrument resolution is determined in this case by the quality of the sample crystal. Obviously enough, all Bragg reflections in the neutron diffractogram of the oxide obtained at 290 K are of nuclear origin. The thin solid and dashed lines relate to the profile analysis of the observed scattering pattern (R factor = 3%). We readily see that the experimental reflection intensity profile consists of two Gaussians. This means that the sample is made up of two large blocks a very small distance, 0.01 Å^{-1}, apart in the wave-vector space. The halfwidths of the reflections originating from different blocks are also small, not exceeding 0.01 Å^{-1}. Despite the block character of the sample crystal, we clearly have good instrument resolution in the wave vector $q_{[010]}$ in the scanning geometry chosen. This good instrument resolution makes it possible to observe a weak diffuse paramagnetic maximum at the foot of the nuclear Bragg reflection (Fig. 1).

After the sample crystal was cooled to 4.2 K, the intensity of the (200) reflection increased substantially. An increase in the (200) reflection intensity in the neutron diffractogram of $La_{0.93}Sr_{0.07}MnO_3$ at 4.2 K can be associated only with the onset of ferromagnetic ordering in the manganite. In other words, the (200) reflection has a nuclear (N) and a ferromagnetic (FM) component at 4.2 K. Figure 2 displays the intensity and the profile of the ferromagnetic part of the reflection, which were obtained by subtracting the nuclear component of the reflection shown in Fig. 1 from the total scattering intensity profile. Figure 2 also presents the results of a profile analysis of the observed scattering pattern made with due allowance for the block structure of the crystal. (The analysis was conducted assuming the individual components of the $(200)_{FM}$ maximum to have Gaussian shape.)

The good agreement between the experimental data and the results of the profile analysis seen from Figs. 1 and 2 (R factor = 3%) makes it possible to isolate the neutron scattering effects related to one single-crystal block only. Figure 3 presents diffractograms corre-

sponding to single-crystal block I (Fig. 1). The nuclear component $I_{(200)N}$ of the reflection intensity is seen to be substantially weaker in intensity than the ferromagnetic contribution $I_{(200)FM}$. This observation improves the accuracy of numerical estimates of the parameters of the manganite ferromagnetic subsystem, because subsequently we use relations of the type $I_{(200)FM}/I_{(200)N}$ for this purpose.

Thus, the scattering pattern in Fig. 3a obtained at the temperature 4.2 K corresponds to the ground state of the ferromagnetic subsystem of single-crystal $La_{0.93}Sr_{0.07}MnO_3$. This pattern is seen to consist of two fragments, namely, a central maximum, whose half-width is equal to the instrument resolution, and two broadened maxima arranged symmetrically with respect to the center, whose total intensity (114 arbitrary units) differs very little from the integrated intensity (142) of the central peak. In view of their high intensity, the side maxima cannot originate from inhomogeneities in the manganite crystal caused by a modulated deviation of the magnetic-moment densities in clusters from their average values. Indeed, the intensities of the side maxima treated in terms of the modulated-structure model should have been weak relative to that of the central peak, as is the case, for instance, in the neutron diffraction pattern of the $La_{0.94}Sr_{0.06}MnO_3$ manganite [5]. It thus appears that the diffractogram in Fig. 3a indicates the of two large-scale ferromagnetic phases coexistence in the $La_{0.93}Sr_{0.07}MnO_3$ crystal. The central peak indicates the presence of a ferromagnetic phase with long-range order (phase 1), whereas the broadened side maxima suggest the existence of a second ferromagnetic phase of finite size (phase 2). The characteristic linear size L of the regions of phase 2 and the average separation d between the regions can be estimated from the expressions

$$L \cong 2\pi/\Delta q, \quad d = 2\pi/q_m, \tag{3}$$

where $\Delta q = (\Delta q_{obs}^2 - \Delta q_{inst}^2)^{1/2}$ and q_m is the wave vector corresponding to the maximum intensity of the side reflection. The parameters in Eqs. (3) for $La_{0.93}Sr_{0.07}MnO_3$ are

$$L = 200 \text{ Å} \quad \text{and} \quad d = 420 \text{ Å}. \tag{4}$$

It appears reasonable to conjecture that the spin configuration of $La_{0.93}Sr_{0.07}MnO_3$ is actually a mixture of two types of magnetic structure, with one of them being similar to that in the spin system in $La_{0.94}Sr_{0.06}MnO_3$ [5] and the other being similar to the ordering in $La_{0.9}Sr_{0.1}MnO_3$ [4]. In other words, the phase with long-range order is the ferromagnetic component of the canted magnetic structure and (large-scale) phase 2 is a collinear ferromagnetic phase with an average magnetic moment at the manganese sublattice site,

$$\bar{\mu} = 0.93\mu_{Mn^{3+}} + 0.07\mu_{Mn^{4+}}. \tag{5}$$

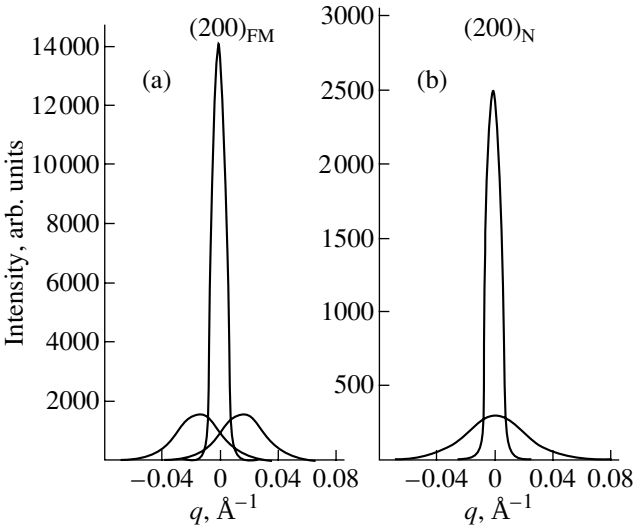

Fig. 3. Neutron scattering patterns from $La_{0.93}Sr_{0.07}MnO_3$ measured along [010]. (a) $(200)_{FM}$ at 4.2 K and (b) $(200)_N$ at 290 K.

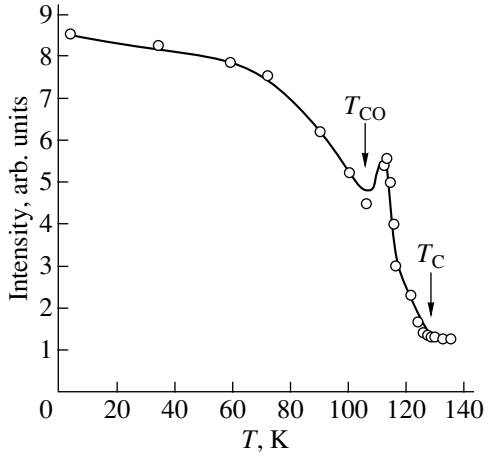

Fig. 4. Temperature dependence of the peak intensity of the $(200)_{FM}$ ferromagnetic reflection in the neutron scattering pattern of $La_{0.93}Sr_{0.07}MnO_3$.

The Curie temperatures of these two phases are apparently similar and, thus, have one effective $T_C \cong 128$ K (Fig. 4). This model allows one to determine the fractional volumes of the magnetic phases in the crystal and the canting angle in phase 1.

The volume fraction c of the collinear ferromagnetic phase was found from the expression

$$(I_{(200)FM2}/I_{(200)N})_{obs} = c[2/3(F_{FM2})^2/(F_N)^2]_{cal}. \tag{6}$$

The experimental values of the intensities $I_{(200)FM2}$ and $I_{(200)N}$ in Eq. (6) were taken from the data in Fig. 3, and the structural amplitude F_{FM2} was calculated using the average magnetic moment given by Eq. (5). The calcu-

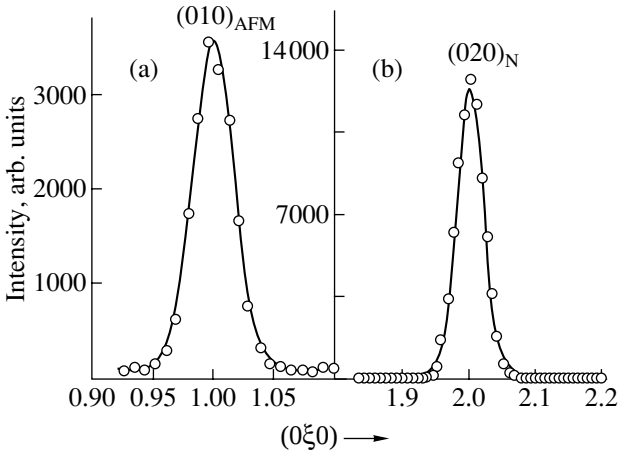

Fig. 5. (a) Antiferromagnetic $(010)_{AFM}$ and (b) nuclear $(020)_N$ reflections in the neutron scattering patterns of $La_{0.93}Sr_{0.07}MnO_3$ measured at 4.2 and 290 K, respectively.

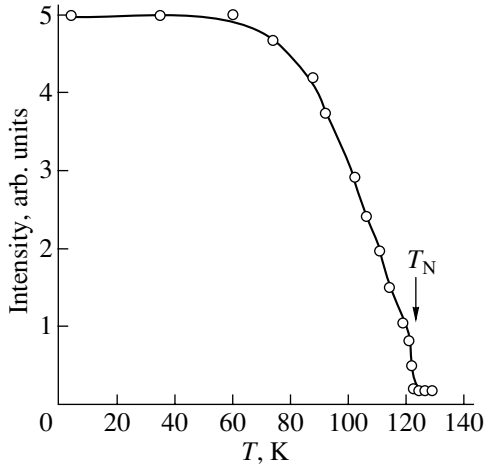

Fig. 6. Temperature dependence of the peak intensity of the $(010)_{AFM}$ antiferromagnetic reflection in the neutron scattering pattern of $La_{0.93}Sr_{0.07}MnO_3$.

lation yielded a value of 0.1 (10%) for c. The remainder of the crystal, $(1 - c) = 0.9$, is occupied, following our model, by the large-scale phase with a canted magnetic structure. The ferromagnetic component of the canted structure coincides, as in [5], with the [010] crystallographic direction, and the antiferromagnetic component of phase 1 lies in the (010) crystal plane. The canting angle φ in magnetic phase 1 was found to be 25°. It was determined using the simple expression

$$\varphi = \arcsin(\mu^z/\bar{\mu}),$$

where

$$\mu^z = 1.7\mu_B, \quad \mu^z \sim F_{FM1},$$
$$F^2_{FM1} = (I_{(200)FM1}/I_{(200)N})_{obs}F^2_N/(1-c). \qquad (7)$$

The fraction of the correlated antiferromagnetic component of phase 1 was derived from the relative intensity of the coherent antiferromagnetic peak, $I_{(010)AF}/I_{(010)N}$. The $(010)_{AF}$ and $(020)_N$ reflections are presented in Fig. 5. Their intensities were measured at crystal temperatures of 4.2 and 290 K, respectively, along the scattering vector $\kappa_{[010]} = 4\pi\sin\theta/\lambda$ (2θ is the scattering angle, λ is the neutron wavelength). The experimental value of μ^{xy} was found to be equal to $0.9\mu_B$, which is substantially smaller than the maximum possible value $\mu_m^{xy} = \bar{\mu}\cos\varphi = 3.6\mu_B$. The noticeable difference between the values of μ^{xy} and μ_m^{xy} implies the presence of a considerable number of frustrated bonds in phase 1, which break the periodicity in orientation of the antiferromagnetic spin component in the crystal. The Néel temperature of the correlated antiferromagnetic component of the canted structure was derived from the temperature dependence of the $(010)_{AF}$ reflection and is 121 K, as can be seen from Fig. 6.

3. DISCUSSION OF RESULTS

To facilitate discussion of the results of this study, the main parameters of the spin systems of the manganites $La_{0.94}Sr_{0.06}MnO_3$ [5] and $La_{0.93}Sr_{0.07}MnO_3$ are listed in the table below. As follows from the tabulated data, a slight increase in the doping level (with the relative fraction of the Mn^{4+} ions increasing by 0.01/0.06 = 0.167) substantially changes the ground-state spin configuration of the manganites. More specifically, the $La_{0.93}Sr_{0.07}MnO_3$ crystal undergoes large-scale phase separation of the spin system. Note that the existence of critical (threshold) carrier densities n_{ci} (i = 1, 2, 3, 4) in $La_{1-x}Sr_xMnO_3$-type compounds is physically quite natural in the quantum version of description of the

Main parameters of the $La_{1-x}Sr_xMnO_3$ manganite spin systems in the vicinity of the AFM ⟶ FM transition

Doping level	Phase 1				Phase 2	
	volume fraction in crystal	canting angle, deg	T_N, K	T_C, K	volume fraction in crystal	T_C, K
x = 0.06 [5]	1	13	129	124	–	–
x = 0.07	0.9	25	121	128	0.1	≅128

AFM ⟶ FM transitions [2]. For instance, above the threshold level n_{c1}, the canted spin configuration becomes energetically preferable (for the collinear AFM structure), whereas at electronic densities above n_{c4} collinear ferromagnetic ordering is a stable state in the crystal.

However, the most important physical factor directly affecting phase separation in the spin system in manganites is charge ordering [2]. Charge ordering sets in in the manganites near definite threshold dopant levels, for instance,

$$x_c = 1/8, 1/4, 1/3, 1/2. \quad (8)$$

Consider the problem of charge ordering in more detail. Charge ordering in the vicinity of stoichiometry, $x = 1/8$, i.e., in the region of comparatively low strontium concentrations in compounds (1), is the most actively discussed in the literature. A positive answer to this problem was given by us in [6] for the particular case of single-crystal $La_{0.85}Sr_{0.15}MnO_3$. We studied magnetic elastic scattering patterns of neutrons in this single crystal in the temperature range 4.2–300 K. It was found that, in addition to the well-known ferromagnetic ordering (T_C = 240 K), this compound has a ferromagnetic superstructure with a wave vector $(010)2\pi/b$, which persists in the crystal at temperatures from 4.2 to 200 K. The ferromagnetic superstructure was shown in [6] to be a direct consequence of charge ordering of the Mn^{3+} and Mn^{4+} ions in this compound, as in the case of $x = 1/8$.

Here, we have assumed that the minimum stoichiometric composition at which charge ordering can take place in the La–Sr manganite system (1) is

$$x_{\min} = 0.0625 = 1/16. \quad (9)$$

The critical threshold in Eq. (9) lies within the compositional interval of interest to us here, $0.06 < x_{\min} < 0.07$ (see table). Figure 7 presents (on the a_0c_0 plane) the model of the superstructure cell of charge ordering in the case of Eq. (9). The filled and open circles identify the positions of the Mn^{4+} and Mn^{3+} ions. The superstructure dimension along the $b_0 = 2b_C$ axis (b_C is the unit cell parameter of the perovskite cube) coincides with that of the original cell. Note that only the Mn^{3+} ions are located at height $(1/2)b_0$, while at the b_0 level the cell has the same pattern as in Fig. 7. The overall dimensions of the superstructure cell were chosen such that only one of the 16 manganese ions in this cell had the 4+ valence, the remaining fifteen being in the 3+ state. The numbering of the eight manganese ions in the a_0c_0 plane is shown in Fig. 7.

Consider now arguments for the existence of Mn^{4+} ordering effects in the manganites under study here.

(1) First, this conclusion follows immediately from theory [2]. It was shown in [2] that a uniform charge-ordered state in the vicinity of a "good" electron density ($n = 1/2$) in manganites with competing exchange couplings is unstable. For instance, for electron densities n close to but higher than 1/2, the ground state of the manganite can break down only into phases with densities

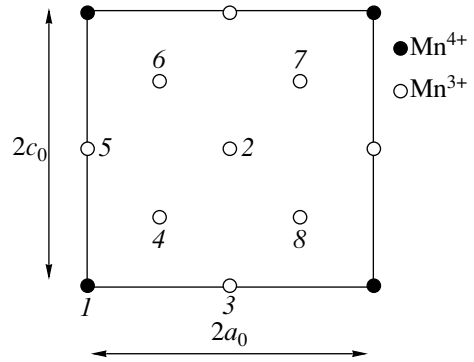

Fig. 7. Unit cell of the charge-ordering superstructure in $La_{0.93}Sr_{0.07}MnO_3$ presented in the a_0c_0 plane (schematic).

$$1/2 < n < n_1 \quad \text{and} \quad n_2 = 1/2. \quad (10)$$

Thus, the separation of the spin system in $La_{0.93}Sr_{0.07}MnO_3$ [in the vicinity of the stoichiometric composition (9)] is not at odds with fundamental theory [2].

(2) The anisotropic scale of the "polaron-type" nonuniformity in $La_{0.94}Sr_{0.06}MnO_3$ (and, hence, as we believe, in phase 1 of $La_{0.93}Sr_{0.07}MnO_3$) is in good agreement with the dimensions of the model superstructure cell in Fig. 7. The dimensions of the charge-ordering cell along the [010] and [101] directions are $b_0 = 7.76$ Å and $2a_0 = 2 \times 5.58\sqrt{2}$ Å = 15.78 Å, respectively which coincides with the correlation lengths in Eq. (2) to within experimental error.

Consider one more point bearing on the spin structure of phase 1. In accordance with Eq. (10), the chemical composition of phase 1 (large-scale canted nonuniform magnetic structure) is determined by parameter (9), which is in excess of the doping level in $La_{0.94}Sr_{0.06}MnO_3$ [5]. It is this factor that accounts, in our opinion, for the canting angle in phase 1 being larger than that in $La_{0.94}Sr_{0.06}MnO_3$ (see table).

(3) The charge ordering in phase 2 manifests itself in the temperature dependence of the peak intensity of the $(200)_{FM}$ ferromagnetic reflection in the diffraction pattern of $La_{0.93}Sr_{0.07}MnO_3$ (Fig. 4). Above 107 K, the intensity is seen to increase sharply. A temperature-induced scattering effect of similar magnitude was observed in $La_{0.85}Sr_{0.15}MnO_3$ at the charge-ordering point T_{CO} = 200 K [6]. The anomalies observed in Fig. 4 and in [6] are, in our opinion, of the same origin and can be assigned to the sharp change that the domain structure undergoes at the charge ordering temperature; more specifically, the scattering factors (which depend on the domain structure of a substance) increase by

$(1 - 2/3) = 1/3$ above the T_{CO} temperature. The change in the type of domain structure, in turn, is triggered by the structural rearrangement of the crystal at the T_{CO} point,

$$Q'(T > T_{CO}) \rightleftharpoons Q^*(T < T_{CO}), \quad (11)$$

where Q' and Q^* refer to the orthorhombic and pseudocubic phases, respectively. The effect of structural rearrangement at T_{CO} was observed earlier in the ferromagnetic manganites $La_{0.9}Sr_{0.1}MnO_3$ [4] and $La_{0.85}Sr_{0.15}MnO_3$. The structural rearrangement (11) at the T_{CO} point may be considered a factor that stabilizes the phase separation in $La_{0.93}Sr_{0.07}MnO_3$ [2].

4. CONCLUSION

Thus, in the manganite $La_{0.93}Sr_{0.07}MnO_3$ with competing exchange couplings, we have observed a large-scale phase separation of the spin system which we believe to originate from ordering of the Mn^{4+} ions in the crystal lattice.

ACKNOWLEDGMENTS

The authors are indebted to Yu.P. Sukhorukov for helpful discussions and to A.M. Balbashev for providing the single crystal for the study.

This study was supported by the Ministry of Industry, Science, and Technology of the Russian Federation (contract no. 40.012.1.1.1150), the state support program for leading scientific schools of the Russian Federation (project no. 00-15-96581), and the Russian Foundation for Basic Research (project no. 02-02-16425).

REFERENCES

1. É. L. Nagaev, Usp. Fiz. Nauk **165**, 529 (1995) [Phys. Usp. **38**, 497 (1995)].
2. M. Yu. Kagan and K. I. Kugel', Usp. Fiz. Nauk **171**, 577 (2001) [Phys. Usp. **44**, 553 (2001)].
3. F. Moussa, M. Hennion, G. Biotteau, and J. Rodriguez-Carvajal, Phys. Rev. B **60** (17), 12299 (1999).
4. V. S. Gaviko, V. E. Arkhipov, A. V. Korolev, *et al.*, Fiz. Tverd. Tela (St. Petersburg) **41** (6), 1064 (1999) [Phys. Solid State **41**, 969 (1999)].
5. M. Hennion, F. Moussa, G. Biotteau, *et al.*, Phys. Rev. B **61** (14), 9513 (2000).
6. S. F. Dubinin, V. E. Arkhipov, S. G. Teploukhov, and Ya. M. Mukovskiĭ, Fiz. Tverd. Tela (St. Petersburg) **45** (1), 113 (2003) [Phys. Solid State **45**, 118 (2003)].

Translated by G. Skrebtsov

Physics of the Solid State, Vol. 45, No. 12, 2003, pp. 2303–2308. Translated from Fizika Tverdogo Tela, Vol. 45, No. 12, 2003, pp. 2198–2203.

MAGNETISM AND FERROELECTRICITY

Microstructure and Properties of Co–Sm–O Nanogranular Films

G. I. Frolov, V. S. Zhigalov, S. M. Zharkov, A. I. Pol'skiĭ, and V. V. Kirgizov

Kirensky Institute of Physics, Siberian Division, Russian Academy of Sciences, Akademgorodok, Krasnoyarsk, 660036 Russia

e-mail: zharkov@iph.krasn.ru

Received April 9, 2003

Abstract—The effect of annealing on the structure and physical properties of Co–Sm–O alloy films prepared using pulsed plasma deposition is investigated. It is found that Co–Sm–O films in the initial state possess superparamagnetic properties due to the presence of small-sized magnetic nanoparticles surrounded by dielectric layers of samarium oxide in the film structure. Upon annealing, the Co–Sm–O films undergo structural transformations and exhibit a number of magnetic properties (including those inherent in both soft and hard magnetic materials). © *2003 MAIK "Nauka/Interperiodica".*

1. INTRODUCTION

In recent years, considerable research attention in materials science has been focused on the structure and properties of nanocomposites with a nanocrystalline structure. A decrease in the crystallite size in solids to a nanometric scale (1–50 nm) leads to a manifestation of a large variety of new properties that are widely used in modern technologies. The parameters of these materials are determined by both the internal properties of nanoparticles and the effects associated with the interparticle interactions. At present, magnetic alloys with a nanocrystalline structure have been extensively used to produce soft and hard magnetic materials [1, 2] and storage media for magnetic memory devices [3, 4].

The majority of soft magnetic materials with a nanocrystalline structure have been prepared through the crystallization of amorphous samples [1]. The great interest expressed by materials scientists in the study and application of soft magnetic nanomaterials stems from the unique combination of their properties, namely, the high magnetic permeability, strong magnetization, and high Curie temperature. However, the possibility of using these alloys in radio-frequency and microwave devices is limited by their high electrical conductivity. An interesting solution of this problem was proposed by Yoon *et al.* [5], who prepared Fe–Sm–O alloy films not only with good soft-magnetic properties but also with high electrical resistance owing to the specific features of the microstructure of the samples produced by magnetron sputtering.

In elaborating the above approach, we studied films prepared through pulsed plasma sputtering of an $SmCo_5$ target under vacuum (at a residual pressure of $\approx 10^{-6}$ Torr) [6]. The specific feature of this technique is the high pulsed condensation rate ($\approx 10^4$ nm/s) at a pulse duration of $\approx 10^{-4}$ s and a high cooling rate of condensates ($\approx 10^7$ K/s). Since a necessary condition for the system to attain a nanocrystalline state is rapid supercooling of the vapors, our technique is an efficient tool for preparing nanocrystalline films.

For our purpose, we prepared 50- to 75-nm-thick films on different substrates (cover glass, NaCl, amorphous sapphire). According to x-ray fluorescence analysis, the changes in the samarium content from sample to sample did not exceed 13–17 at. %. The microstructure and phase composition of the films prepared were examined using transmission electron microscopy (TEM), electron diffraction, and x-ray diffraction. Moreover, we investigated the magnetic properties (coercive force, magnetization) and electrical conductivity of the film samples. For the films deposited onto NaCl and amorphous sapphire substrates, we also studied the effect of thermal annealing (to an annealing temperature $T_{ann} \approx 780$°C) on their structure and physical properties.

Figure 1 shows typical hysteresis loops for Co–Sm–O nanocrystalline films at two temperatures. As can be seen from Fig. 1, the magnetization reversal of the Co–Sm–O film is characterized by an anhysteretic curve at room temperature and a hysteresis loop with $H_C \approx 50$ Oe at $T = 77$ K. This thermal behavior of the hysteresis loop is characteristic of superparamagnetic materials. The measured blocking temperature T_B, i.e., the temperature at which the material undergoes a transition to the superparamagnetic state, is approximately equal to 81 K. The result obtained is rather surprising, because even cobalt and iron nanocrystalline films with a grain size of smaller than 4 nm, which were prepared through either pulsed plasma deposition [6, 7] or cluster deposition [8] and whose anisotropy constant is less

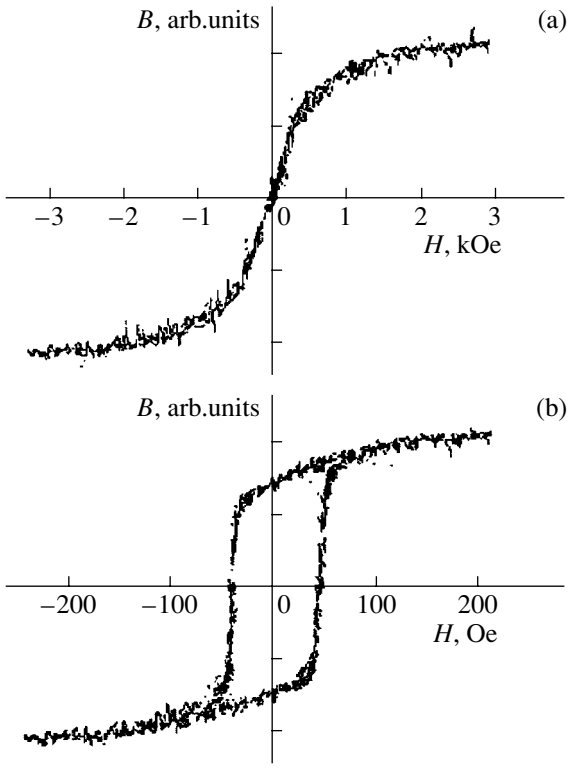

Fig. 1. Hysteresis loops for Co–Sm–O nanocrystalline films at (a) room temperature and (b) liquid-nitrogen temperature. The blocking temperature T_B is approximately equal to 81 K.

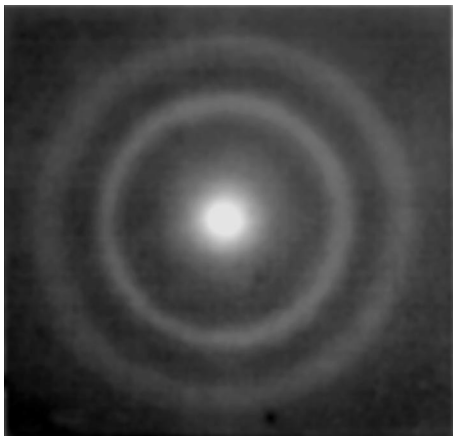

Fig. 2. Electron diffraction pattern of the Co–Sm–O film in the initial state.

than that for Sm–Co alloys, exhibit pure ferromagnetic behavior. In order to elucidate the nature of the observed effects, it was necessary to investigate the structure of the films.

2. FILM STRUCTURE IN THE INITIAL STATE

The microstructure and phase composition of the films prepared were examined using transmission electron microscopy and electron diffraction on a PRÉM-200 transmission electron microscope at an accelerating voltage of 100 kV. For these observations, a film with thickness $d \approx 50$ nm was deposited onto an NaCl substrate. Thereafter, the film was separated from the substrate in water and was then placed on a supporting grid in the electron microscope.

The electron diffraction pattern (Fig. 2) of the Co–Sm–O film in the initial state exhibits two diffuse halos of virtually identical intensity. The interplanar distances corresponding to these diffraction reflections are approximately equal to 2.97 and 2.00 Å. It seems likely that the diffraction peak centered at ≈2.97 Å can be attributed to a phase of Sm_2O_3, namely, the hexagonal modification of Sm_2O_3 (JCPDS card no. 19-1114) with the lattice parameters $a = 3.86$ Å and $c = 6.17$ Å [9]. The diffraction peak centered at ≈2.00 Å can be associated primarily with the hexagonal close-packed (hcp) or face-centered cubic (fcc) phase of cobalt and also with carbon solutions in cobalt [6, 10].

In order to obtain additional information on the original structure of the films, we performed x-ray diffraction investigations. The x-ray diffraction patterns of the films in the initial state exhibited similar reflections, and one of them was used to calculate the mean size of the crystallites. It was assumed that the broadening of the diffraction reflection observed in the x-ray diffraction pattern is caused by the size effect alone. In this case, the crystallite size can be calculated from the Scherrer formula [11]

$$\Delta 2\theta(\text{rad}) = \lambda/(D\cos\theta_0),$$

where $\Delta 2\theta$ is the half-width of the diffraction peak (rad), λ is the radiation wavelength (Å), θ_0 is the diffraction angle (deg), and D is the size of the crystallites in the sample. For the sample studied, we obtained the following diffraction parameters: $\Delta 2\theta \approx 7°$, $\theta_0 = 30°$, and $\lambda = 1.54181$ Å. As a result, we found that, for films in the initial state, the crystallite size is approximately equal to 15 Å. This indicates that the films under investigation have a nanocrystalline structure.

3. TRANSFORMATION OF THE FILM STRUCTURE UPON ANNEALING

The films placed on supporting grids were subjected to multistage annealing under a vacuum of 10^{-5} Torr, during which the films were heat treated for 30 min at each specified temperature in 25 degree intervals up to $T_{ann} = 780°C$.

According to TEM observations, the films subjected to annealing at temperatures $T_{ann} \le 400°C$ contain dense amorphous clusters ranging in size from 0.5 to 1 μm.

However, the electron diffraction patterns of these films are identical to those of the films in the initial state (Fig. 2). Therefore, neither a change in the particle size nor a structural transformation occurs upon annealing of the films at temperatures up to and including 400°C.

After annealing at $T_{ann} > 400$°C, the electron diffraction patterns of the films exhibit diffraction spots associated with polycrystalline particles (Fig. 3a). The results of the analysis of this diffraction pattern are presented in the table. It was found that the film annealed at a temperature of 500°C contains several phases, among which the main phase is samarium oxide Sm_2O_3 with a cubic structure (JCPDS card no. 15-0813) and lattice parameter $a = 10.927$ Å [9]. The electron diffraction pattern exhibits all reflections with high and moderate intensities that are characteristic of this structure. It should be noted that this modification of samarium oxide differs from the hexagonal modification predicted for Sm_2O_3 in the Co–Sm–O film in the initial state. An analysis of the intensities of diffraction reflections $d_{hkl} = 2.063$, 1.779, 1.260, and 1.062 Å revealed the fcc cobalt phase (β-Co) and did not rule out the presence of small amounts of the hexagonal cobalt phase (α-Co, $d_{hkl} = 1.910$ and 1.149 Å) in the film. The microstructure of the film under investigation (see Fig. 3b) consists of larger sized (50–200 nm) denser clusters of samarium oxide and small-sized (10–20 nm) particles of cobalt.

Upon further annealing (up to $T_{ann} = 780$°C), no transformations of the atomic structure are observed. There only occur an increase in the number of structural clusters of samarium oxide per unit area and an insignificant increase in the cluster size (70–250 nm), whereas the size of cobalt nanoparticles remains virtually unchanged (Fig. 3c).

Therefore, we can infer that the structure of the films in the initial state consists of 1.5-nm particles of the cobalt phases separated by layers of samarium oxide. During annealing of the film, the size of cobalt particles increases to 10–20 nm and the hexagonal phase of samarium oxide undergoes a structural transformation into the cubic phase. The maximum size of Sm_2O_3 particles increases to 250 nm.

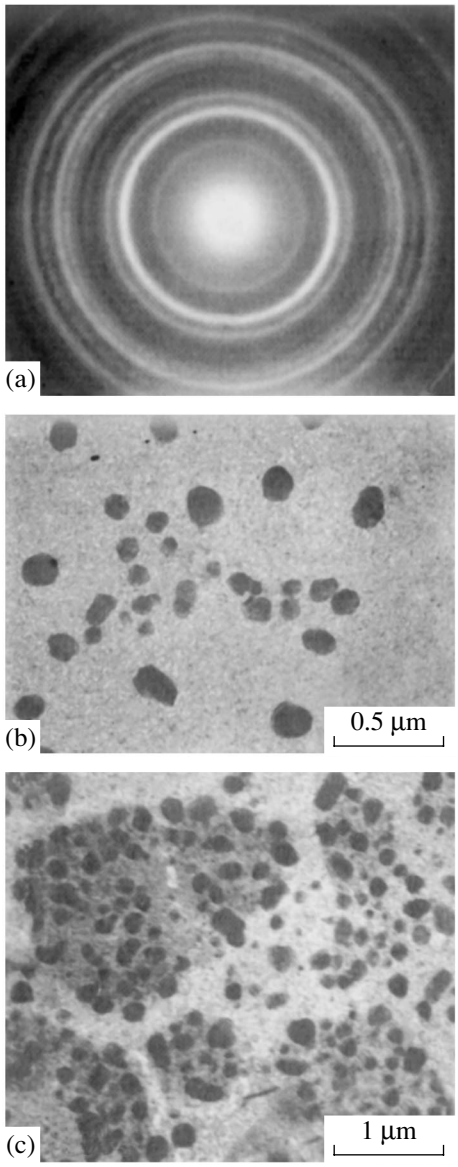

Fig. 3. Electron microscope images of Co–Sm–O films subjected to annealing at different temperatures: (a) electron diffraction pattern of the film annealed at $T_{ann} = 480$°C, (b) electron micrograph of the structure of the film annealed at $T_{ann} = 480$°C, and (c) electron micrograph of the structure of the film annealed at $T_{ann} = 700$°C.

4. EFFECT OF ANNEALING ON THE ELECTRICAL AND MAGNETIC PROPERTIES

Figure 4 shows the dependences of the electrical resistivity, the coercive force, and the saturation magnetization of the studied samples on the annealing temperature. All the measurements were performed at room temperature. The electrical resistivity ρ of the Sm–Co–O films in the initial state (Fig. 4a) is equal to 5×10^{-2} Ω cm, which is approximately four orders of magnitude greater than the values characteristic of metallic film samples ($\approx 5 \times 10^{-6}$ Ω cm) in the polycrystalline state. This confirms our assumption that metallic particles are separated by dielectric layers of samarium oxide in the film structure. An increase in the annealing temperature T_{ann} leads to an increase in the size of metallic particles, which, in turn, brings about a decrease in the electrical resistivity ρ. At an annealing temperature $T_{ann} \geq 600$°C, the electrical resistivity drastically decreases by almost three orders of magnitude as compared to that of the samples in the initial state. This can be associated with the change in the phase composition of the samples and, primarily, with the transfor-

Electron diffraction data for the Co–Sm–O film annealed under vacuum at T_{ann} = 500°C (see the electron diffraction pattern in Fig. 3a)

Co–Sm–O film (experiment)			Sm_2O_3 (JCPDS 15-0813) *la*3 *a* = 10.927 Å			α-Co (JCPDS 05-0727) $P6_3/mmc$ *a* = 2.5031 Å, *c* = 4.0605 Å			β-Co (JCPDS 15-0806) *Fm*3*m* *a* = 3.5447 Å		
No.	*d*, Å	*I*	*d*, Å	Int.	*hkl*	*d*, Å	Int.	*hkl*	*d*, Å	Int.	*hkl*
1	4.493	s	4.460	12	211						
2	3.184	vs	3.155	100	222						
3	2.750	s	2.731	35	400						
4	2.357	w	2.330	4	332						
5	2.161	w	2.143	8	431	2.165	20	100			
6	2.063	av				2.023	60	002	2.047	100	11
7	1.939	s	1.932	40	440	1.910	100	101			
8	1.779	av	1.772	6	611				1.772	40	200
9	1.656	s	1.647	30	622						
10	1.584	w	1.578	8	444						
11	1.498	w	1.487	2	721	1.480	1	102			
12	1.365	vw	1.366	4	800						
13	1.260	s	1.254	6	662	1.252	80	110	1.253	25	220
14	1.120	av	1.115	6	844	1.149	80	103			
15	1.061	av	1.071	4	1020	1.066	80	112	1.069	30	311

Note: *d* is the interplanar distance determined in the diffraction experiment, and *I* stands for the relative intensity of the diffraction reflections [the designations used for reflections are as follows: vs = very strong, s = strong, av = average, w = weak, vw = very weak]. The tabulated data for Sm_2O_3, α-Co, and β-Co are taken from [9].

mation of the microstructure, which manifests itself in the formation of large-sized particles of samarium oxide due to their rapid growth and, consequently, in the destruction of separating dielectric layers. As a result, the metallic grains form a galvanic contact.

As the annealing temperature changes, the coercive force exhibits a very complex behavior (Fig. 4b). The dependence of the coercive force of the studied samples on the annealing temperature can be divided into three portions with different values of H_C. The hysteresis loops typical of these three portions are shown in Fig. 5. The first portion of the temperature dependence of the coercive force is represented by an anhysteretic curve. This thermal behavior of the coercive force indicates that the samples are in a superparamagnetic state (Fig. 5a). The coercive force in the second portion, which lies in the annealing temperature range T_{ann} = 300–400°C, is characterized by a hysteresis loop with small values of H_C = 0.1–2 Oe (Fig. 5b). In this case, the uniaxial anisotropy field reaches H_K = 5 Oe. The appearance of the hysteresis loop can be explained by an increase in the size of cobalt nanoparticles. In the third portion ($T_{ann} \geq 400$°C), the thermal behavior of the coercive force H_C has two specific features: the coercive force first increases abruptly to 250 Oe, then decreases, and again exhibits a jump to ≈450 Oe. An analysis of the electron microscope images (Fig. 3b) revealed that, at annealing temperatures $T_{ann} \geq 400$°C, the nanocrystalline structure transforms into a polycrystalline structure and the size of cobalt nanoparticles increases by approximately one order of magnitude. As a rule, this transformation of the structure is accompanied by an increase in the coercive force H_C.

It should be noted that, as the annealing temperature increases over the entire range under investigation, the saturation magnetization J_S increases by a factor of approximately three (Fig. 4c). It seems likely that this phenomenon can be associated not only with the structural transformation but also with the phase transitions occurring in the films upon annealing. As was shown in our previous studies [6, 10, 12], which were performed with nanocrystalline cobalt films prepared according to the same technique, the film samples contain dissolved carbon in small amounts and also the metastable phases Co_3C and Co_2C, which are not ferromagnetic at room temperature. The decomposition of the carbide phases and, correspondingly, the increase in the saturation magnetization occur at the same temperatures (see [10]) at which, in our case, the saturation magnetization J_S of the films exhibits the first two features (at 250 and 400°C). In the temperature range 600–700°C, the saturation magnetization J_S undergoes a jump due to the formation of the structure consisting of a polycrystalline cobalt matrix with Sm_2O_3 inclusions. As was noted

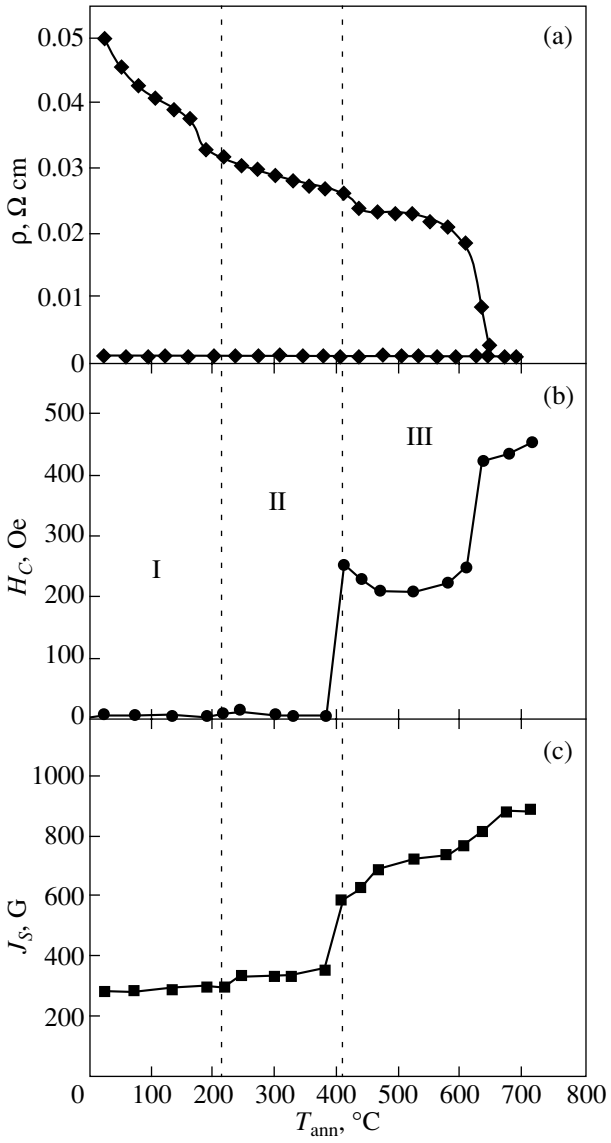

Fig. 4. Dependences of (a) the electrical resistivity, (b) the coercive force, and (c) the saturation magnetization on the annealing temperature for the Co–Sm–O film.

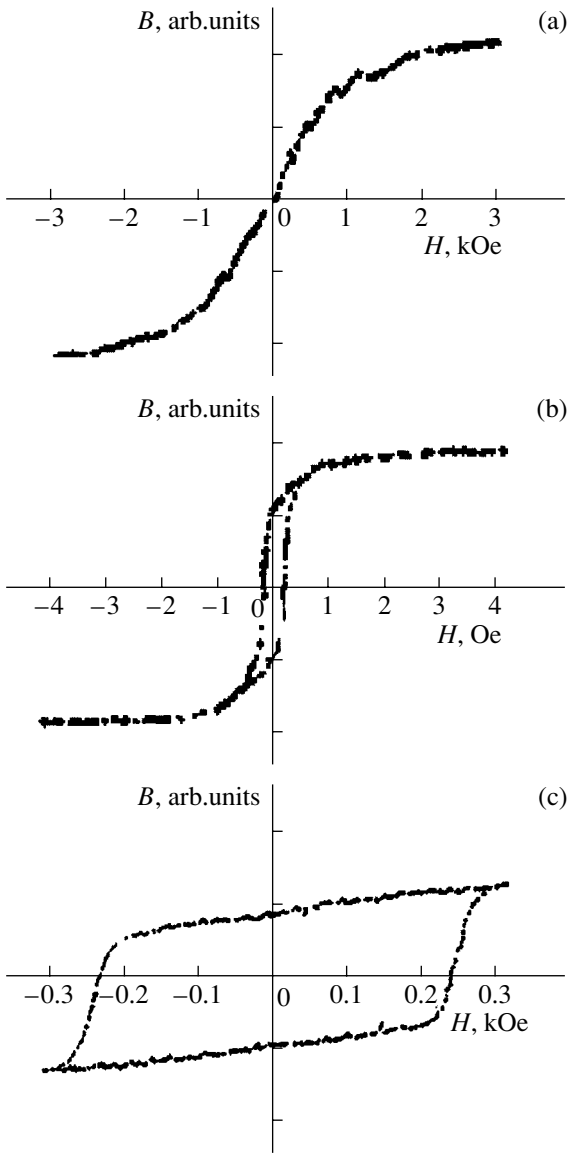

Fig. 5. Characteristic hysteresis loops for Co–Sm–O films (a) in the initial state and after annealing at (b) T_{ann} = 300°C and (c) T_{ann} = 480°C.

above, this transformation of the structure is accompanied by a number of effects: the electrical resistivity ρ drastically decreases by almost three orders of magnitude, and the coercive force H_C increases.

Let us now consider the specific features of the superparamagnetic state of the studied films prior to annealing. According to Been and Levingston [13], 3*d*-metal nanoparticles with sizes $D < 9$ nm at room temperature should be in a superparamagnetic state. However, numerous experiments have demonstrated that nanogranular films with a high content of the magnetic phase exhibit a ferromagnetic order even when the particle size is less than 5 nm [6, 8, 14, 15]. The existence of ferromagnetic order in nanogranular films can be explained both by the effects of dipole–dipole interactions between particles and by the suppression (blocking) of their magnetic state due to strong induced anisotropy. For nanogranular samples, this anisotropy is determined by a complex structure of nanoparticles with a 3*d* metal nucleus at the particle center surrounded by a passivated shell consisting of oxides or metal carbides [16, 17].

The superparamagnetic state observed in our films can be associated with a decrease in the size of nanoparticles ($D \approx 1.5$ nm), on the one hand, and with an increase in the contribution from a nonmagnetic phase (Sm_2O_3) in the bulk of grain boundaries, on the other.

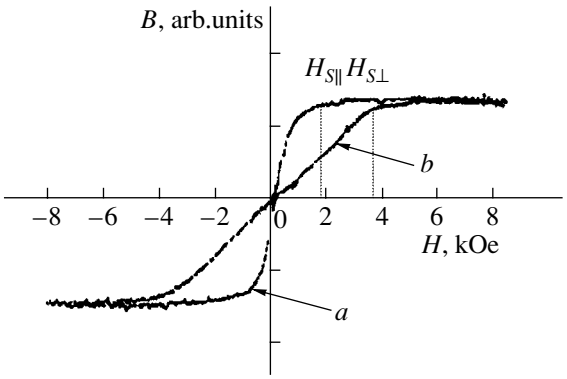

Fig. 6. Magnetization curves for a Co–Sm–O film in the initial state at $T = 300$ K in a magnetic field applied (*a*) parallel to the film plane and (*b*) perpendicular to the film plane.

As a result, the exchange interaction between nanoparticles becomes weaker.

In order to evaluate the role played by the dipole–dipole interaction, we obtained the magnetization curves for film samples at $T = 300$ K in a magnetic field applied in two directions (parallel and perpendicular to the plane of the film) (Fig. 6). As can be seen from Fig. 6, the magnetization curves are characterized by shape anisotropy. From analyzing the magnetization curves, we can assess the factors responsible for demagnetization in the plane of the film ($N_\|$) and along the normal to this plane ($N_\perp$). In a magnetic field applied perpendicular to the film plane (Fig. 6, curve *b*), the magnetization reaches saturation at a magnetic field strength $H_{S\perp} \approx 3.8$ kOe. Since the saturation magnetization of the films in the initial state is estimated as $J_S \approx 300$ G (Fig. 4c), we obtain $N_\perp = H_{S\perp}/J_S = 3.8 \times 10^3/3 \times 10^2 \approx 4\pi$ and, correspondingly, $N_\| \approx 0$. Therefore, we can state that, for our samples, the magnetic moment lies in the film plane. At the same time, the magnetization can reach saturation in the film plane only in a sufficiently strong field ($H_{S\|} \approx 1$ kOe), which suggests a strong anisotropy of disordered superparamagnetic cobalt particles.

5. CONCLUSIONS

Thus, it was found that the dependences of the electrical resistivity, the coercive force, and the saturation magnetization on the annealing temperature of Co–Sm–O films exhibit a nonmonotonic behavior. This indicates that the structural transformations of the films subjected to annealing have a complex character. However, all the structural and magnetic data obtained in this study demonstrated that no phases of $SmCo_5$ are not formed in the films studied, because the high chemical activity of samarium particles under vacuum at a residual pressure of 10^{-6} Torr leads to their oxidation.

The Co–Sm–O alloy films prepared in this work are of interest both for the study of the supermagnetism phenomenon in samples with a high content of the magnetic phase and for practical use as soft-magnetic (with a high electrical resistance) and hard-magnetic materials.

ACKNOWLEDGMENTS

This work was supported by the Russian Foundation for Basic Research (project no. 03-02-16052) and the 6th Competition of Research Projects of Young Scientists of the Russian Academy of Sciences (1999) (project no. 56).

REFERENCES

1. G. Herzer, Scr. Metall. Mater. **33** (10/11), 1741 (1995).
2. M. E. McHenry and L. E. Laughlin, Acta Mater. **1**, 223 (2000).
3. M. H. Kryder, W. Messner, and L. K. Garley, J. Appl. Phys. **79** (8), 4485 (1996).
4. G. I. Frolov, Zh. Tekh. Fiz. **71** (12), 50 (2001) [Tech. Phys. **46**, 1537 (2001)].
5. T. S. Yoon, Y. Li, W. S. Cho, and C.-O. Kim, J. Magn. Magn. Mater. **237**, 288 (2001).
6. V. S. Zhigalov, G. I. Frolov, and L. I. Kveglis, Fiz. Tverd. Tela (St. Petersburg) **40** (11), 2074 (1998) [Phys. Solid State **40**, 1878 (1998)].
7. G. I. Frolov, V. S. Zhigalov, L. I. Kveglis, *et al.*, Fiz. Met. Metalloved. **88** (2), 85 (1999).
8. J. P. Perez, V. Dupuis, J. Tuaillon, *et al.*, J. Magn. Magn. Mater. **145** (1–2), 74 (1995).
9. Powder Diffraction File, Inorganic, Card No. 15-0813 (Sm_2O_3), 19-1114 (Sm_2O_3), 05-0727 (α-Co), 15-0806 (β-Co) (JCPDS International Center for Diffraction Data, Swarthmore, PA, USA).
10. G. I. Frolov, V. S. Zhigalov, and V. K. Mal'tsev, Fiz. Tverd. Tela (St. Petersburg) **42** (2), 326 (2000) [Phys. Solid State **42**, 334 (2000)].
11. A. Guinier, *Théorie et Technique de la Radiocristallographie* (Dunod, Paris, 1956; Fizmatgiz, Moscow, 1961).
12. R. S. Iskhakov, S. V. Stolyar, L. A. Chekanova, *et al.*, Pis'ma Zh. Éksp. Teor. Fiz. **72** (6), 457 (2000) [JETP Lett. **72**, 316 (2000)].
13. C. P. Been and J. D. Levingston, J. Appl. Phys. **30**, 120S (1959).
14. J. Tuallon, V. Dupuis, P. Melionon, *et al.*, Philos. Mag. A **76**, 493 (1997).
15. G. I. Frolov, O. A. Bayukov, V. S. Zhigalov, *et al.*, Pis'ma Zh. Éksp. Teor. Fiz. **61** (1), 61 (1995) [JETP Lett. **61**, 63 (1995)].
16. J. P. Chen, C. M. Sornsen, K. J. Klabunde, and G. C. Hadjipanayis, Phys. Rev. B **51**, 11527 (1995).
17. S. T. Woods, J. R. Kirtley, Shouheng Sun, and R. H. Koch, Phys. Rev. Lett. **87**, 137205 (2001).

Translated by O. Borovik-Romanova

Physics of the Solid State, Vol. 45, No. 12, 2003, pp. 2309–2312. Translated from Fizika Tverdogo Tela, Vol. 45, No. 12, 2003, pp. 2198–2203.

MAGNETISM AND FERROELECTRICITY

Surface and Volume Phase States of $Fe_{1-x}Ga_xBO_3$ Crystals in the Vicinity of the Néel Point

A. S. Kamzin and R. G. Glyantsev

Ioffe Physicotechnical Institute, Russian Academy of Sciences, Politekhnicheskaya ul. 26, St. Petersburg, 194021 Russia

Received April 14, 2003

Abstract—The behavior of the magnetic system of a surface layer of macroscopic $Fe_{1-x}Ga_xBO_3$ crystal (x = 0, 0.3) in the vicinity of the Néel temperature T_N was studied. The studies were made by a method involving simultaneous gamma, x-ray, and electron Mössbauer spectroscopy that made it possible to obtain information simultaneously from surface layers and from the bulk of a macroscopic crystal. It was found that the temperature $T_N(L)$ at which a thin layer at a depth L from the surface switches to a disordered state is lower than T_N for the bulk and is lower the closer this layer is to the surface. In the vicinity of T_N, a nonuniform state is observed in which the bulk of the crystal is magnetically ordered and the surface layer is disordered. The transition temperature $T_N(L)$ decreases from T_N to its surface value within a surface layer of a "critical" thickness. © *2003 MAIK "Nauka/Interperiodica".*

The processes occurring at the surface of macroscopic crystals in phenomena of fundamental importance, such as phase transitions at the critical temperature in the bulk of a crystal, have been attracting the interest of researchers since the late 1960s. A theoretical basis for describing the processes observed on the surface in the critical temperature region was developed in [1, 2]. It was shown, for instance, that the transition temperature of a thin surface layer to the paramagnetic state may either coincide with the Curie (or Néel) point for the crystal bulk or exceed it [1, 2]. Those publications were followed by numerous theoretical and experimental papers (see [3–9] and references therein). The experimental studies made on thin Gd films revealed that the transition temperature of a thin surface layer is higher than the point at which bulk samples undergo magnetic ordering [6]. At the same time, another experiment [5] showed the magnetic ordering temperature of a surface layer of a PdFe alloy to be lower than the Curie point for the bulk of the sample, which disagrees with the theoretical analysis. Simultaneous studies of the properties of the surface and the bulk of macrocrystals have shown that magnetic disordering in the surface layer of weakly ferromagnetic materials [7] and hexagonal ferrites [8] occurs at temperatures below the critical points of transitions in these compounds. Nevertheless, the experimental data available to date on the influence of the surface on the magnetic properties of the near-surface layer in crystals are inadequate. Moreover, in order to establish the relation between the phenomena on the surface and in the bulk of a crystal, one has to investigate profiles of the variation in the crystal properties with distance from the surface (by layer-by-layer analysis) and compare the properties of surface layers of macroscopic samples with those of the bulk.

The present communication offers information obtained in simultaneous experimental studies of the surface and volume magnetic properties of bulk $Fe_{1-x}Ga_xBO_3$ crystals in the vicinity of the phase transition at the Néel temperature. As iron ions are being replaced by diamagnetic gallium ions, the Néel point shifts below room temperature. Therefore, the studies were conducted by simultaneous gamma, x-ray, and electron Mössbauer spectroscopy (SGXEMS) [10] with the use of a low-temperature system [11] to extend the application area of SGXEMS from room temperature down to 10 K. The essence of SGXEMS consists in that it permits a Mössbauer study of layers within less than 300 nm from the surface, as well as of the bulk of a macrocrystal, by obtaining spectra for radiations with different mean free paths in the material, more specifically, of the conversion and Auger electrons (CAE), x rays, and gamma rays (GR). The SGXEMS is unique in that (i) the information from the bulk and the surface of a crystal is extracted simultaneously and (ii) using the Mössbauer effect in SGXEMS for probing both the surface and the bulk makes it possible to directly compare the corresponding experimental data.

The SGXEMS spectrometer used in this study was computer-controlled in the dialogue mode. The temperature was maintained to within 0.1 K. The gamma-ray source was Co^{57} embedded in a rhodium matrix. An iron foil was employed to calibrate the velocity of the gamma-ray source motion. The theoretical spectra were fitted using the least squares method to experimental points with the use of special codes developed for processing Mössbauer spectra. Mössbauer studies in the vicinity of the magnetic ordering point present

1063-7834/03/4512-2309$24.00

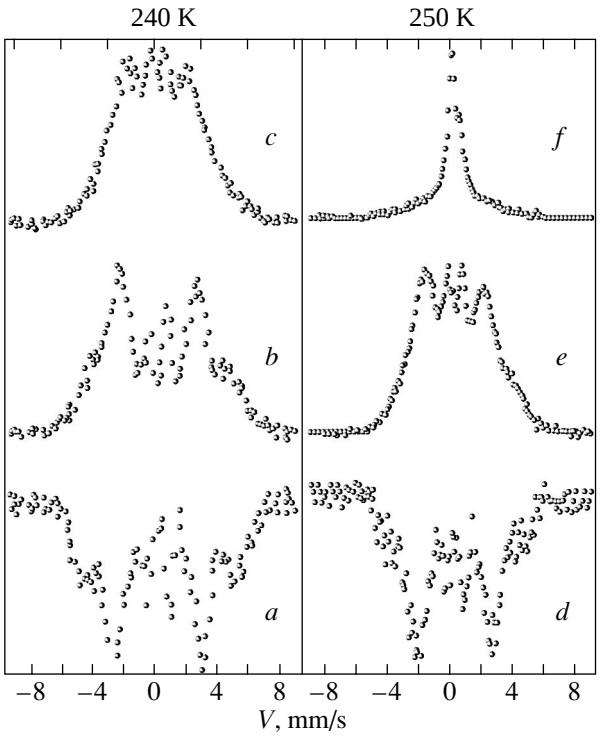

Fig. 1. Mössbauer spectra of $Fe_{0.7}Ga_{0.3}BO_3$ obtained by measuring the number of (*a*, *d*) gamma quanta, as well as conversion and Auger electrons from a surface layer of thickness (*b*, *e*) 200 nm and (*c*, *f*) 40 nm at 240 K (left) and 250 K (right).

certain difficulties if the iron ions in a sample are capable of occupying two or more inequivalent positions. In this case, the lines of the Zeeman sextuplets are difficult to resolve in the critical-temperature region; this factor substantially degrades the accuracy with which the values of the effective magnetic field can be extracted from experimental spectra and, hence, the quality of the data obtained. If, however, the magnetic structure of a crystal is generated by iron ions occupying equivalent positions, the Mössbauer spectrum consists of one Zeeman sextuplet only, thus facilitating its treatment greatly in the critical temperature region.

The above features accounts for our choice of $Fe_{1-x}Ga_xBO_3$ for the study; this compound preserves a simple magnetic structure as Fe ions are substituted for by ions of gallium up to $x = 0.45$ [12–17]. $Fe_{1-x}Ga_xBO_3$ crystals possess orthorhombic symmetry. The magnetic structure of $Fe_{1-x}Ga_xBO_3$ (for $x \le 0.45$) consists of two magnetic sublattices, which are formed by iron ions occupying two equivalent positions in octahedral sites and coupled antiferromagnetically at temperatures below the Néel point [12–16]. The crystal symmetry (point group D_{3D}^6) allows the existence of a weak ferromagnetic moment in the basal plane perpendicular to the [111] threefold axis, which was confirmed experimentally in [18, 19]. The phase transition occurring at the Néel temperature in bulk $FeBO_3$ crystals has been studied extensively, which allowed us to compare our experimental data with those from the available publications. The critical indices for bulk $FeBO_3$ were determined in [20, 21].

For the study, we selected single-crystal plates about 80 μm thick grown through spontaneous crystallization from a melt solution [13, 17]. The major faces of the plates coincided with the (111) basal plane. In studies of the properties of surface layers, the surface treatment of the samples is critical. The single crystals were prepared using two techniques, namely, (i) mechanical polishing with fine-grained powders and weak etchants and (ii) chemical polishing with a 1 : 1 mixture of the H_3PO_4 and H_2SO_4 acids at room temperature for about 50 h. Note that the experimental results were reproducible only in the second case.

Figure 1 displays some of the Mössbauer spectra obtained using SGXEMS. The spectra measured by detecting GRs at temperatures below the Néel point consist of one Zeeman sextuplet. At temperatures $T \le T_N$, the sextuplet line intensity ratio is 3 : 4 : 1 : 1 : 4 : 3, which argues for the plates being correctly oriented. When the crystals were heated to above the Néel temperature, the gamma resonance spectra transformed in the following manner. The separation between the Zeeman sextuplet lines decreased, and the spectra obtained as the Néel point was approached contained both the Zeeman and paramagnetic lines (we call such spectra mixed). At the Néel temperature, the lines collapse to form a paramagnetic doublet. Note that $FeBO_3$ produced mixed spectra in a very narrow temperature interval near T_N, whereas mixed spectra in $Fe_{0.7}Ga_{0.3}BO_3$ appear at temperatures fairly far from the Néel point.

The Mössbauer spectra obtained by detecting CAEs far from the Néel temperature are similar to those for the gamma rays. When a crystal is heated, the conversion-electron Mössbauer spectra transform into a paramagnetic doublet similarly to as occurs with the gamma resonance spectra but at different temperatures.

An analysis of the experimental spectra obtained by measuring the radiations emitted from layers located at a depth L from the surface shows that they can be divided into three groups corresponding to the temperature regions (1) $T \le T_S(L)$, (2) $T \ge T_N(L)$, and (3) $T_S(L) < T < T_N(L)$, respectively.

The experimental spectra taken at temperatures $T \le T_S(L)$ consist of one well-resolved Zeeman sextuplet. All the sextuplet lines have a close to natural width, which implies that the crystal is in a magnetically ordered state Γ_M. In the temperature region $T \ge T_N(L)$, the experimental spectra consist of one quadrupole doublet. This means that the layers under study and the bulk of the crystal are in the paramagnetic state Γ_P. No lines corresponding to hyperfine Zeeman splitting are observed in this phase. In the experimental spectra obtained at temperatures $T_S(L) < T < T_N(L)$ (Fig. 2), the Zeeman background is overlaid by lines resembling the

paramagnetic doublet of the Γ_P phase. We denote this phase by Γ_S and call such spectra mixed. As the temperature is increased from $T_S(L)$ to $T_N(L)$, the outer lines of the Zeeman sextuplets decrease in intensity until they disappear altogether. The inner sextuplet lines grow in intensity as the temperature increases from $T_S(L)$ to $T_N(L)$.

Figure 2 shows a phase diagram of regions Γ_M, Γ_S, and Γ_P based on the experimental spectra. The boundaries of these regions were determined as follows. The position of the $T_S(L)$ line (lines *2*, *4* in Fig. 2) was found by extrapolating the temperature dependences of the inner (analogous to paramagnetic) lines in the experimental spectra to zero. The $T_N(L)$ phase boundary (lines *1*, *3* in Fig. 2) was located by the following techniques used in Mössbauer spectroscopy to find the Néel temperature: (1) The experimental spectra obtained in the phase transition region and containing only the quadrupole lines due to the paramagnetic phase, with no Zeeman splitting lines present, were selected; the temperature at which the Zeeman lines disappeared was taken as the Néel point. (2) The temperature dependence of the number of detected quanta was found by temperature scanning. In this case, the gamma-radiation source is either fixed or moves with a constant velocity. As one approaches $T_N(L)$ from the low-temperature side, the number of quanta measured by the detector increases, as seen in Fig. 3. At the $T_N(L)$ point, the curve saturates and the number of detected quanta no longer varies with a further increase in temperature (Fig. 3). Both methods yielded the same value of $T_N(L)$.

The experimental spectra were used to derive the hyperfine-interaction parameters. The temperature dependences of the effective magnetic field H_{eff} are displayed in Fig. 3, which shows that H_{eff} at the sites of the iron ion nuclei in the surface layer decreases faster with increasing temperature than at the sites of the iron ion nuclei in the bulk of the crystal. To check the reproducibility of the results in terms of temperature, the spectra were measured repeatedly and in different directions on the temperature scale. An analysis of the data obtained showed the results to be reproducible.

As seen from the phase diagram in Fig. 2, the paramagnetic state is separated from the magnetically ordered state by region Γ_S, in which mixed spectra are observed. As one approaches the surface of the sample, the $T_S(L)$ boundary of phase state Γ_S shifts toward lower temperatures. The phase boundary $T_N(L)$, as is evident from Fig. 2, implies that the temperature of the paramagnetic transition decreases with decreasing distance from the crystal surface. In $FeBO_3$, the transition to the disordered state in a surface layer ~40 nm thick occurs at a temperature ~0.2 K lower than T_N for the bulk of the sample. In $Fe_{0.7}Ga_{0.3}BO_3$, where 30% of the iron ions are replaced by diamagnetic ions, the difference between the paramagnetic transition temperatures in

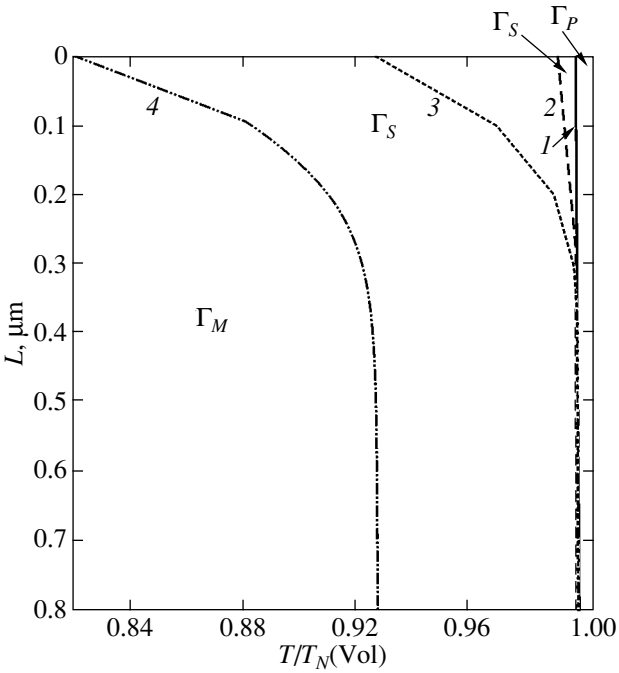

Fig. 2. Phase diagram of the states of $FeBO_3$ and $Fe_{0.7}Ga_{0.3}BO_3$ in the vicinity of the Néel temperatures. The numbers *1* and *3* denote the boundaries $T_N(L)$, and *2* and *4*, $T_S(L)$ for $FeBO_3$ and $Fe_{0.7}Ga_{0.3}BO_3$, respectively. The temperature scale is normalized against the Néel temperatures of the crystals.

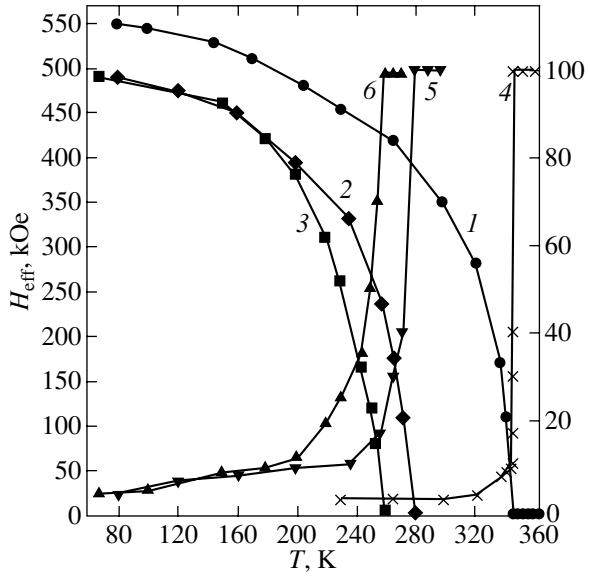

Fig. 3. Temperature dependences of the effective magnetic fields at the sites of the iron ion nuclei located (*1*, *2*) in the bulk of the $FeBO_3$ and $Fe_{0.7}Ga_{0.3}BO_3$ crystals, respectively, and (*3*) in the 40-nm-thick surface layer of the $Fe_{0.7}Ga_{0.3}BO_3$ crystal. Temperature dependences of the number (*4*, *5*) of detected gamma quanta and (*6*) of the conversion and Auger electrons at zero Mössbauer source velocity.

the surface layer and in the bulk of the crystal increases up to 20 K.

The experimental data obtained suggest the following scenario for the transition of a macroscopic crystal to the paramagnetic state. As a bulk crystal is heated, the paramagnetic state appears on its surface at a temperature less than T_N for the bulk of the crystal, which should be assigned to the surface ions lacking some magnetic bonds. As the temperature is raised further, the paramagnetic phase spreads into the bulk of the crystal. After T_N has been reached, thermal energy destroys magnetic ordering in the remaining bulk.

The smoothness with which the $T_N(L)$ and $T_S(L)$ boundaries shift as the surface is approached can be accounted for in the following way. It was shown in [22] that the effective magnetic field (or magnetization) in $FeBO_3$ decreases smoothly toward the crystal surface at temperatures that are far enough from the Néel point. Hence, the surface layer of the crystals under study can be divided into a number of thin layers in which the exchange interaction energy decreases as one approaches the surface and the value of $T_N(L)$ depends on the depth L of the given layer from the surface.

The transition temperature $T_N(L)$ varies within a surface layer of "critical" thickness. In layers located deeper than this critical thickness, the paramagnetic transition occurs at the temperature T_N for the bulk of the crystal. In the temperature interval from $T_N(L)$ to T_N, the crystal resides in a nonuniform state in which the material in the bulk is magnetically ordered whereas the sample surface is paramagnetic.

ACKNOWLEDGMENTS

This study was supported by the Russian Foundation for Basic Research, project no. 01-02-17889.

REFERENCES

1. M. I. Kaganov and A. N. Omel'yanchuk, Zh. Éksp. Teor. Fiz. **61** (4), 1679 (1971) [Sov. Phys. JETP **34**, 895 (1972)].
2. D. Mills, Phys. Rev. B **3**, 3887 (1971).
3. J. Mathon, Rep. Prog. Phys. **51**, 1 (1988).
4. T. Kaneyoshi, J. Phys.: Condens. Matter **3**, 4497 (1991).
5. R. D. McGrath, R. M. Mirzababayev, and J. C. Walker, Phys. Lett. A **67** (2), 149 (1978).
6. C. Rau, Appl. Phys. A **49**, 579 (1989).
7. A. S. Kamzin and L. A. Grigor'ev, Zh. Éksp. Teor. Fiz. **105** (2), 377 (1994) [JETP **78**, 200 (1994)]; Fiz. Tverd. Tela (St. Petersburg) **36** (5), 1271 (1994) [Phys. Solid State **36**, 694 (1994)].
8. A. S. Kamzin and V. L. Rozenbaum, Pis'ma Zh. Éksp. Teor. Fiz. **67** (11), 940 (1998) [JETP Lett. **67**, 991 (1998)]; Pis'ma Zh. Éksp. Teor. Fiz. **69** (1), 52 (1999) [JETP Lett. **69**, 57 (1999)]; Fiz. Tverd. Tela (St. Petersburg) **41** (3), 468 (1999) [Phys. Solid State **41**, 420 (1999)].
9. A. S. Kamzin, B. Stahl, E. Kankeleit, *et al.*, Pis'ma Zh. Éksp. Teor. Fiz. **71** (10), 643 (2000) [JETP Lett. **71**, 442 (2000)]; B. Stahl, E. Kankeleit, R. Gellert, *et al.*, Phys. Rev. Lett. **84** (24), 5632 (2000).
10. A. S. Kamzin and L. A. Grigor'ev, Pis'ma Zh. Tekh. Fiz. **16** (16), 38 (1990) [Sov. Tech. Phys. Lett. **16**, 616 (1990)].
11. A. S. Kamzin and D. B. Vcherashniĭ, Pis'ma Zh. Tekh. Fiz. **28** (9), 22 (2002) [Tech. Phys. Lett. **28**, 365 (2002)].
12. L. Bernal, C. W. Struck, and J. G. White, Acta Crystallogr. **16** (8), 849 (1963).
13. L. V. Velikanov, A. S. Prokhorov, E. G. Rudashevskiĭ, and V. N. Seleznev, Zh. Éksp. Teor. Fiz. **66** (5), 1847 (1974) [Sov. Phys. JETP **39**, 909 (1974)].
14. R. C. Le Craw, R. Wolfe, and J. W. Nielsen, Appl. Phys. Lett. **14** (11), 352 (1969).
15. J. C. Joubert, T. Shiek, W. B. White, and R. Roy, Mater. Res. Bull. **3**, 671 (1968).
16. O. A. Bayukov, V. P. Ikonnikov, M. P. Petrov, *et al.*, in *Proceedings of International Conference on Magnetism (MKM-73)* (Moscow, 1974), Vol. 3, p. 313.
17. A. S. Kamzin, L. P. Ol'khovik, and E. V. Snetkova, Fiz. Tverd. Tela (St. Petersburg) **45** (11), 2025 (2003) [Phys. Solid State **45**, 2128 (2003)].
18. M. P. Petrov, G. A. Smolenskiĭ, A. P. Paugurt, *et al.*, Fiz. Tverd. Tela (Leningrad) **14** (1), 109 (1972) [Sov. Phys. Solid State **14**, 87 (1972)].
19. M. Eibschutz and M. E. Lines, Phys. Rev. B **7** (11), 4907 (1973).
20. D. M. Wilson and S. Broersma, Phys. Rev. B **14** (5), 1977 (1976).
21. A. L. Irshinskiĭ, V. P. Ozhogin, V. M. Cherepanov, and S. S. Yakimov, Zh. Éksp. Teor. Fiz. **76** (3), 1111 (1979) [Sov. Phys. JETP **49**, 563 (1979)].
22. A. S. Kamzin, B. Stahl, R. Gellert, *et al.*, Pis'ma Zh. Éksp. Teor. Fiz. **71** (4), 197 (2000) [JETP Lett. **71**, 134 (2000)].

Translated by G. Skrebtsov

Physics of the Solid State, Vol. 45, No. 12, 2003, pp. 2313–2319. Translated from Fizika Tverdogo Tela, Vol. 45, No. 12, 2003, pp. 2208–2214.

MAGNETISM AND FERROELECTRICITY

Spin-Wave Dispersion in Two-Layer Magnetic Films

A. M. Zyuzin, S. N. Sabaev, and A. V. Kulyapin

Mordovian State University, ul. Bol'shevistskaya 68, Saransk, 430000 Russia

e-mail: zyuzinam@mrsu.ru

Received February 11, 2003; in final form, April 17, 2003

Abstract—The change in spin-wave resonance spectra in multilayer magnetic films occurring under the gradual transformation of a spin-pinned layer from the reactive medium into a dispersive state or vice versa is studied. Spatial spin-wave dispersion associated with the spin-pinned layer is established to occur. This dispersion is most markedly pronounced in films with a mixed mechanism of spin pinning. The dispersion observed allows the so-called effect of "repulsion" of spin-wave modes to be accounted for. *© 2003 MAIK "Nauka/Interperiodica".*

1. INTRODUCTION

In most theoretical and experimental papers dedicated to spin-wave resonance (SWR), the spectra are studied in the case where an external dc field **H** is directed normally or parallel to the film plane [1–4]. The SWR spectra for such orientations can satisfactorily be explained in terms of the commonly used models [5–8], which assume that the pinning of spins is caused by the surface anisotropy or by a dynamic mechanism. Angular variations of SWR spectra in two-layer films in which the dynamic mechanism of spin pinning operates were studied in [9–12]. This spin-pinning mechanism implies that the change in the angle between the external field and the film causes a change in the region of excitation of harmonic standing spin-wave (SW) modes. For normal and parallel field orientations, these modes are excited in different layers. The authors of those papers observed the so-called "repulsion" of modes, the mechanism of which is still poorly understood.

In spite of the large number of publications on SWR, there is still a lack of studies concerning the features of SWR spectra, in particular, their transformation in the case when the spin-pinned (SP) layer gradually transforms from the state of a reactive medium into a dispersive state [13] or vice versa. In this paper, we report the results of such studies performed on multilayer films with dissipative [14, 15] and mixed mechanisms of spin pinning.

2. EXPERIMENT

Single-crystal garnet-ferrite films grown through liquid-phase epitaxy on (111)-oriented gadolinium gallium garnet substrates were used in the experiments. Multilayer films were obtained through the successive growth of layers from various fluxes. The thickness h of films was measured using the interference method and was also estimated from the time of complete etching.

The saturation magnetization of layers was determined from the intensity and the width of the uniform ferromagnetic resonance measured on the corresponding single-layer analogs [16]. The method for determining the crystallographic directions $\langle 100\rangle$ and $\langle 111\rangle$ and the cubic anisotropy field H_{k1} is described in [17]. The parameters of the films studied are listed in the table (γ is the gyromagnetic ratio, $H_k^{\text{eff}} = (2K_u/M) - 4\pi M_s$ is the effective uniaxial-anisotropy field, $\alpha = \Delta H\gamma/\omega$ is the Gilbert damping parameter, with ΔH being the half-width of the absorption line and ω being the angular frequency of a microwave field).

SWR spectra were recorded with the aid of an RÉ-1301 radiospectrometer. The microwave-field frequency $\omega/2\pi$ was 9.34×10^9 Hz. The samples were placed in crossed dc and ac magnetic fields. The intensity of the dc magnetic field was measured with the aid of an NMR magnetometer.

As a parameter most susceptible to variations in the resonance fields of SW modes we used the difference between the resonance fields $H_0 - H_n$ of the zeroth and nth modes. This quantity is usually used to construct dispersion curves, $H_0 - H_n = f(n)$. In processing the results of measurements using numerical methods, we took into account the mutual interrelation of closely spaced absorption peaks and resonance fields of SW modes, which were determined experimentally as the half-sum of the fields corresponding to the extrema of the derivative of the SW mode absorption line.

It is known [13] that, if the excited SWR spectrum is observed in the range of magnetic fields H lower than the field H_{02} of uniform resonance in an SP layer, this layer is dispersive for spin waves. The eigenfrequency of uniform spin oscillations in such a layer (the eigenfrequency of uniform precession) $\omega_{02} = \gamma_2 H_{02}$ is lower than the frequency of the ac magnetic field ω. Conversely, if the spectrum is observed in the range of fields $H > H_{02}$, an SP layer is a reactive (elastic)

Parameters of two-layer films

Sample	Layer	Composition	h, μm	γ, 10^7 Oe^{-1} s^{-1}	α	$4\pi M_s$, G	H_k^{eff}, Oe	H_{k1}, Oe
1	1*	$Y_{2.98}Sm_{0.02}Fe_5O_{12}$	0.98	1.76	0.003	1740	–1715	–82
	2*	$Er_{2.58}La_{0.42}Fe_{3.95}Ga_{1.05}O_{12}$	1.2	1.66	0.84	450	–78	–93
2	1*	$Y_{2.98}Sm_{0.02}Fe_5O_{12}$	0.69	1.76	0.003	1740	–1715	–82
	2*	$Sm_{0.45}Er_{2.55}Fe_5O_{12}$	1.8	1.38	0.2	1330	96	–120
3	1*	$Y_{2.98}Sm_{0.02}Fe_5O_{12}$	0.51	1.76	0.003	1740	–1715	–82
	2*	$Sm_{1.2}Lu_{1.8}Fe_5O_{12}$	1.4	1.76	0.12	1760	790	–135

Note: 1* denotes the layer of the excitation of harmonic SW modes and 2* is the spin-pinned layer.

medium and $\omega_{02} > \omega$. Thus, in order to transform an SP layer from one state into the other, one needs to change either the microwave frequency ω or the frequency of uniform precession $\omega_{02} = \gamma_2 H_{02}$ by changing uniform-resonance the field H_{02}. The magnitudes of the uniform-resonance fields for the excitation layer (H_{01}) and the SP layer (H_{02}) depend on the values of the effective anisotropy fields H_k^{eff} in the layers, the gyromagnetic ratios γ_1 and γ_2, the angle between the external field **H** and the film plane, and the temperature T. As follows from the data given above, the films under study have different values of H_k^{eff} and γ in the layers. The uniform-resonance field in the excitation layer (the layer with low damping) is considerably higher than that in the SP layer in the case of perpendicular orientation and is lower than that in the SP layer in the case of parallel orientation. Because of this, and also due to the fact that, for any direction of **H**, harmonic standing SWs are excited by a microwave field in the layer with low α, the SP layer is a reactive medium for SWs in the case of perpendicular orientation and a dispersive medium in the case of parallel orientation in the fields corresponding to the excited SWR spectrum. The SP layer can be gradually transformed from a dispersive into a reactive state in two different ways: by changing the angle θ_H between **H** and the normal to the film plane or by changing the temperature. As the angle θ_H is increased, the fields H_{01} and H_{02} approach each other. At a certain value of θ_H, the field H_{01} becomes equal to H_{02} and then the properties of the SP layer change from reactive to dispersive.

The second way the SP layer can be transformed is as follows. If the temperature coefficients of the fields H_{01} and H_{02} have opposite signs (due to the opposite signs of H_k^{eff} in the layers) and the values of γ in the layers are different, then the increase in temperature will cause intersection of the $H_{01}(T)$ and $H_{02}(T)$ dependences and, as a consequence, the above transformation will take place.

One of the factors responsible for the angular dependence of $H_0 - H_n$ and for an increase in the slope of the dispersion curve at intermediate (between easy and hard) directions of magnetization is connected with the change in the equilibrium orientation of the magnetization **M** due to a change in the magnitude of the dc magnetic field during the recording of the SWR spectrum [18]. The contribution to the difference $H_0 - H_n$ caused by a variation in the equilibrium orientation of the magnetization **M** can be calculated from the dispersion relation [13]

$$\left(\frac{\omega}{\gamma}\right)^2 = \left[H\cos(\theta_H - \theta_M) + H_k^{eff}\cos^2\theta_M - H_{k1}a(\theta_M) + \frac{2A}{M}k^2\right]\left[H\cos(\theta_H - \theta_M) + H_k^{eff}\cos 2\theta_M - H_{k1}b(\theta_M) + \frac{2A}{M}k^2\right], \quad (1)$$

where

$$a(\theta_M) = (3 - 16x - 3y)/16, \quad b(\theta_M) = -(x + 3y)/4,$$

$$x = (2^{3/2}\sin 2\theta_M - \cos 2\theta_M)/3,$$

$$y = -(2^{5/2}\sin 4\theta_M - 7\cos 4\theta_M)/9.$$

Expression (1) is written for the excitation and SP layers and allows one to correlate the wave numbers in these layers. The values of the angle θ_M were calculated from the condition of equilibrium orientation of the magnetization **M**:

$$2H\sin(\theta_H - \theta_M) = H_k^{eff}\sin 2\theta_M + H_{k1}\left[\frac{1}{12}\sin 2\theta_M + \frac{7}{24}\sin 4\theta_M + \sqrt{2}\sin^2\theta_M - \frac{4\sqrt{2}}{3}\sin^4\theta_M\right]. \quad (2)$$

In Eqs. (1) and (2), A is the exchange constant, k is the wave number of an SW mode, and θ_M and θ_H are the angles between the normal to the film plane and the vectors **M** and **H**, respectively, reckoned in the (110) plane from normal [111] to the film plane along the shortest possible path towards crystallographic direction [001]. Note that, when the vector **H** lies in the

(110) plane, the vector **M** also lies in this plane. This simplified method of calculation assumes that spins are completely pinned at the interface between the layers; the wave numbers are taken to be equal to $k_1 = (n + 1/2)\pi/h_1$, where h_1 is the thickness of the excitation layer. The calculation results are shown in Figs. 1a–3a (dashed lines). It can be seen that the difference $H_0 - H_n$ increases significantly in the angle range $10° \le \theta_H \le 70°$.

We obtained the following experimental results. The difference $H_0 - H_n$ exhibits a pronounced dependence on the angle θ. In Figs. 1b–3b, the angular variations of the uniform-resonance fields $H_{01}(\theta_H)$ and $H_{02}(\theta_H)$ are also shown for the excitation and SP layers. In the samples with a dominating dissipative mechanism of spin pinning, the increase in θ_H causes a gradual increase and a subsequent decrease in the difference $H_0 - H_n = f(\theta_H)$ (points in Fig. 1a). In addition, in the range $15° < \theta_H < 40°$, the experimental $H_0 - H_n = f(\theta_H)$ dependence deviates from the dashed line calculated from Eqs. (1) and (2). This deviation of the experimental dependence from the calculated dependence becomes more and more pronounced as the damping parameter in the SP layer decreases (Fig. 2a); this effect manifests itself the most for high-order modes.

For the samples with still smaller values of α_2 (sample 3), a pronounced specific feature is observed in the experimental angular dependences. As follows from Fig. 3a, the amplitude of $H_0 - H_n$ angular variations increases with the mode index. As can be seen, the deviation of the difference $H_0 - H_n$ from the calculated dashed line towards smaller values is significantly larger than the deviation towards larger values. Furthermore, the angular dependences of $H_0 - H_n$ for the modes with $n > 4$ show a discontinuity caused by the fact that, in a certain θ_H range, the modes with an index higher than four become unobservable in SWR spectrum in this sample. Such anomalous behavior was also observed in the temperature dependences of $H_0 - H_n = f(T)$ for the samples showing intersection of the temperature dependences of the uniform-resonance fields H_{0i} for the excitation and SP layers, i.e., for the samples in which the transformation of the SP layer from the reactive into a dispersive state occurred (Fig. 4). For the samples showing no intersection of the $H_{01}(T)$ and $H_{02}(T)$ curves, the $H_0 - H_n = f(T)$ dependences were monotonic (Fig. 5). The smooth decrease in $H_0 - H_n$ with increasing T takes place, because the exchange constant A decreases more rapidly than the magnetization [19]. We note that the SWR spectra at various temperatures were recorded for perpendicular orientation of **H** with respect to the film surface, where there is no disorientation of the **M** and **H** vectors and, consequently, the effect of a change in the equilibrium orientation of **M** and in the disorientation of the $\mathbf{M}_1$ and $\mathbf{M}_2$ vectors in layers [11] on the difference between the resonance fields is absent. Note also that the mutual influence of the peaks of SW modes and of the zeroth mode

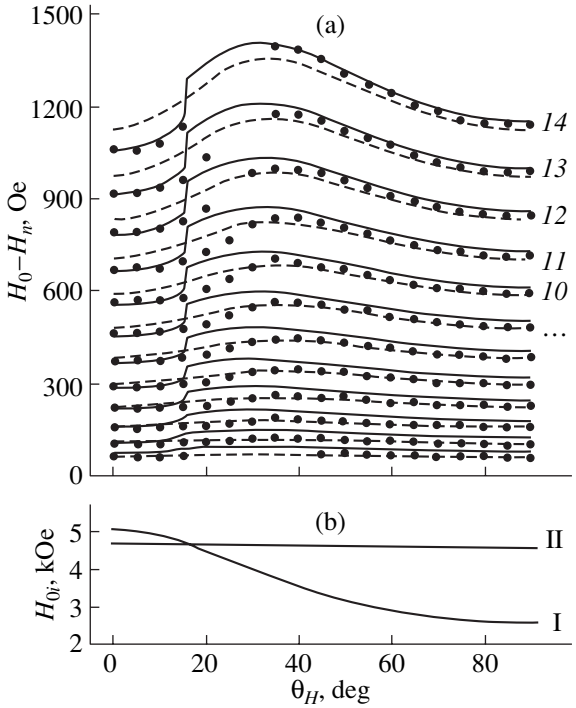

Fig. 1. (a) Angular variation of $H_0 - H_n$ for sample 1. Numbers on the curves are the mode indices. The experimental data are shown by points, calculations based on Eqs. (1) and (2) by dashed lines, and those based on Eqs. (1)–(6) by solid lines. (b) Angular variations of the uniform-resonance field in (I) the excitation and (II) spin-pinned layers.

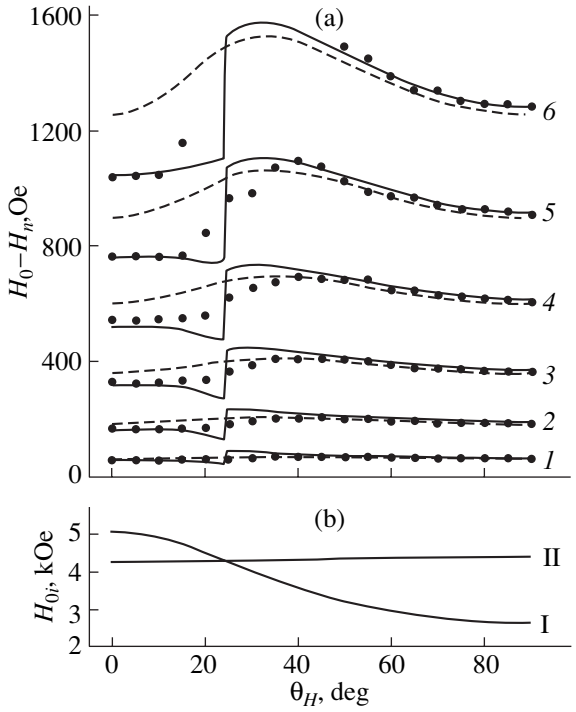

Fig. 2. The same as in Fig. 1 but for sample 2.

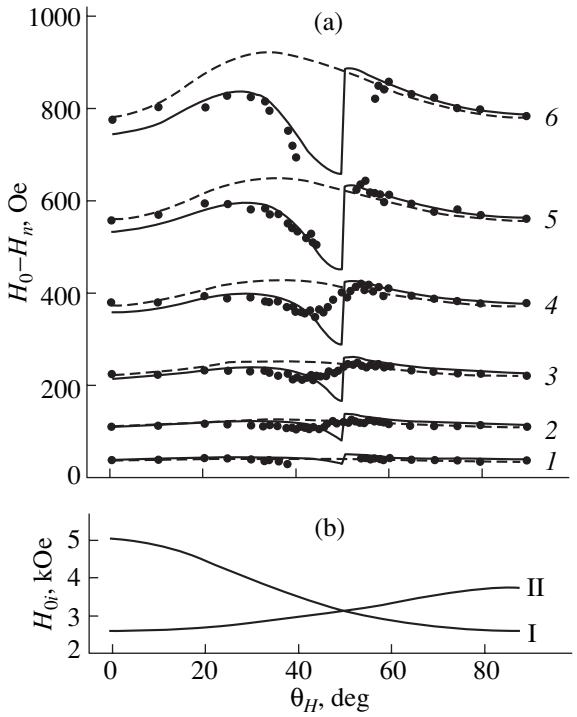

Fig. 3. The same as in Fig. 1 but for sample 3.

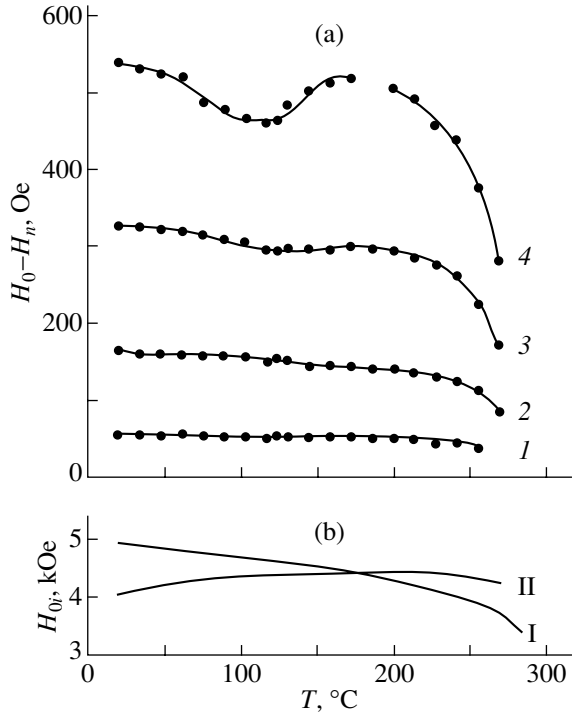

Fig. 4. Temperature dependences (a) of $H_0 - H_n$ for sample 1 and (b) of the uniform-resonance field in (I) the excitation and (II) SP layers.

of the SP layer could not be responsible for the observed features in the angular and temperature dependences of $H_0 - H_n$ [20]. Calculation with due regard for the influence of the peak with a larger width and with a low intensity from the SP layer on the resonance field of the *n*th SW mode shows that the resulting correction is not larger than 3–5 Oe, which is much smaller than the possible change in $H_0 - H_n$.

As follows from Figs. 1a–4a, the $H_0 - H_n = f(\theta_H)$ and $H_0 - H_n = f(T)$ dependences are similar to the dispersion curves that are observed near absorption bands and possess intervals of normal and anomalous dispersion. We also observed a pronounced increase in damping (linewidth of SW modes; Fig. 6) in the range of angles corresponding to a sharp change in the $H_0 - H_n$ versus θ_H (or T) dependence, which is caused by the increased effect of the region of SW damping in the layer with large α on the standing-SW energy dissipation [15]. The specific feature of the observed type of dispersion is that it is caused not by the properties of the medium in which a harmonic wave is excited but by the state of the boundary region. Therefore, this dispersion can be considered a type of spatial dispersion of SWs.

3. CALCULATION OF THE SPIN-WAVE RESONANCE SPECTRUM

In order to determine the quantitative characteristics of the dispersion observed and the character of the transformation of SW modes that occurs when θ_H is change, we calculated the SWR spectra taking into consideration not only the variation of the equilibrium orientation of **M** but also the change in the properties of the SP layer from dispersive to reactive taking place as the angle θ_H or temperature is varied.

In calculating the SWR spectra, we used Eqs. (1) and (2), the exchange boundary conditions [12]

$$\frac{m_1}{M_1} = \frac{m_2}{M_2}\bigg|_{z = h_1}, \quad \frac{A_1}{M_1}\frac{\partial m_1}{\partial z} = \frac{A_2}{M_2}\frac{\partial m_2}{\partial z}\bigg|_{z = h_1} \tag{3}$$

(m_1 and m_2 are the time-dependent components of the magnetization in the SP and excitation layers, respectively), and additional conditions that take into account the SW damping in the layer with a large value of α (SP layer):

$$\begin{aligned}
&\frac{2A_1}{M_{01}}\frac{\partial m_{1y}}{\partial z}\bigg|_{z = h_1} + b_{11}\int\limits_{h_1}^{h_1 + h_2} m_{2y}dz + b_{12}\int\limits_{h_1}^{h_1 + h_2} m_{2x}dz = 0,\\
&\frac{2A_1}{M_{01}}\frac{\partial m_{1x}}{\partial z}\bigg|_{z = h_1} + b_{22}\int\limits_{h_1}^{h_1 + h_2} m_{2x}dz + b_{21}\int\limits_{h_1}^{h_1 + h_2} m_{2y}dz = 0,
\end{aligned} \tag{4}$$

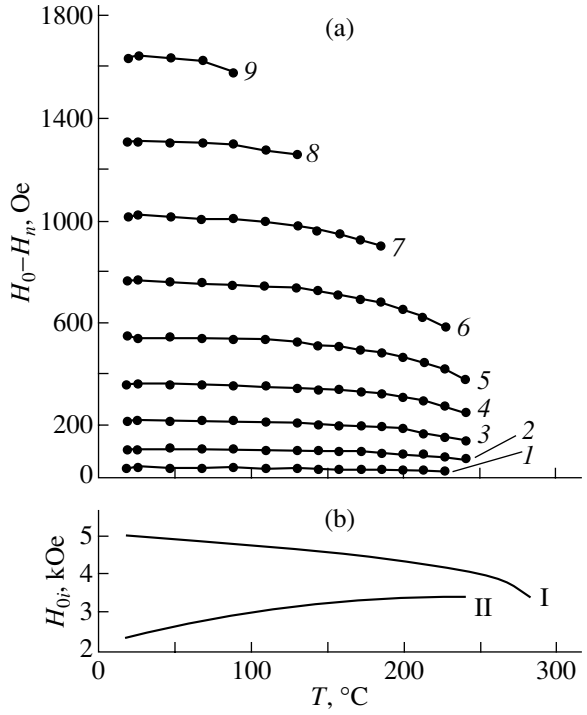

Fig. 5. The same as in Fig. 4 but for sample 3.

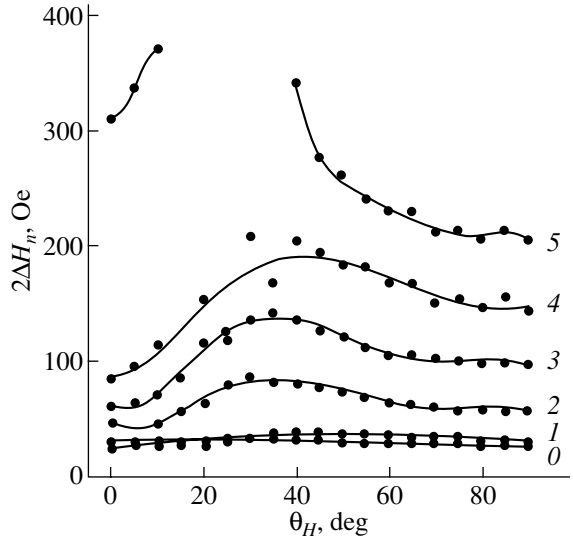

Fig. 6. Angular variations of the linewidth $2\Delta H(\theta_H)$ of SW modes for sample 2. Numbers on the curves are the SW mode indices.

where

$$b_{11} = H\cos(\theta_H - \theta_M) + H_{k2}^{\text{eff}}\cos 2\theta_M + \frac{i\alpha_2\omega}{\gamma_2},$$

$$b_{22} = H\cos(\theta_H - \theta_M) + H_{k2}^{\text{eff}}\cos^2\theta_M + \frac{i\alpha_2\omega}{\gamma_2}, \quad (5)$$

$$b_{12} = -b_{21} = \frac{i\omega}{\gamma_2},$$

h_1 and h_2 are the thicknesses of the excitation and SP layers, respectively, and the z axis is directed normally to the film plane. These additional conditions were obtained by integrating the equation of motion of the magnetization over a region having the shape of a disk, one of whose bases is located in the excitation layer near the interface between the layers and the other is beyond the free surface of the SP layer [13]. These conditions are a consequence of the equality of the torque moment exerted by the exchange field near the interface of the layers and the torque moment (including dissipation effects) due to a damping spin wave propagating in the SP layer.

In addition, we used the following expression relating the real (k_2') and imaginary (k_2'') parts of the wave number in the SP layer [5]:

$$k_2'' = \frac{\alpha_2\omega M_2}{4\gamma_2 A_2}\frac{1}{k_2'}. \quad (6)$$

The spin wave was approximated by a harmonic wave in the excitation layer and by a damping harmonic wave in the SP layer. The solutions for several values of the angle θ_H are shown in Fig. 7a (the points of intersection of curves *1–4* with the family of $\tan(k_1h_1)$ curves). It can be seen that with increasing θ_H the wave numbers of all SW modes decrease; they decrease to a greater extent for modes with higher indices, which explains the decrease in the difference $H_0 - H_n$. Figure 7b shows the configurations of several SW modes for $\theta_H = 0°$ (the SP layer is a reactive medium), $\theta_H = 40°$ and 55° (the SP layer is located in the region of transformation from the reactive into a dispersive state), and $\theta_H = 90°$ (the SP layer is a dispersive medium). It is seen that, when H_{01} and H_{02} approach each other, the configuration of the nth mode tends to transform into the $(n-1)$th mode; however, in the region of transformation of the SP layer from the reactive into a dispersive state, a drastic transformation of modes takes place and is accompanied by the formation of a node located in the excitation layer near the interface of the layers. When H_{01} and H_{02} become equal, the set of solutions undergoes a jumplike change. The values of k_1 for all modes, including the zeroth mode, abruptly increase. As an example, Fig. 7a shows the transformation for the mode with $n = 5$. As a result of this transformation, the difference $H_0 - H_n$ increases in a. The solid lines in Figs. 1–3 show the calculated angular variations of $H_0 - H_n$. It can be seen that the calculations agree quite satisfactorily with the experimental data. The increase in damping parameter α ($\alpha = \Delta H\gamma/\omega$) and, consequently, the increase in the linewidth in the SP layer widen the range of the fields corresponding to the transformation of the SP layer

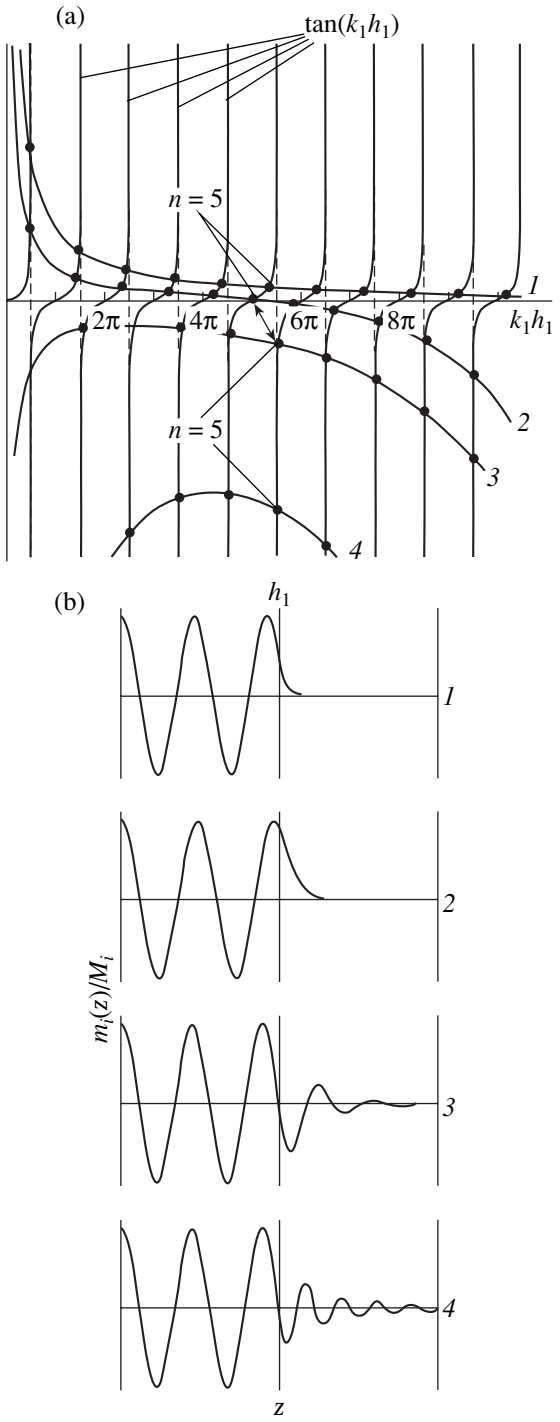

Fig. 7(a). Graphical solution of the system of equations (1)–(6) for sample 3 and (b) the distribution of normalized time-varying magnetization $m_i(z)/M_i$ (i is the number of layer) for the mode with $n = 5$ for various values of θ_H: (*1*) 0°, (*2*) 40°, (*3*) 55°, and (*4*) 90°.

from the reactive into a dispersive state. This, in turn, leads to the spreading of the observed discontinuity in the $H_0 - H_n = f(\theta_H)$ curves.

4. DISCUSSION

The nature of the observed SW dispersion, in our opinion, consists in the following. In the case of the simultaneous operation of dissipative and dynamic mechanisms of spin pinning (mixed mechanism), where the dissipative mechanism is quite important, the exponentially decaying SW in the SP layer is excited, for any orientation of **H**, by the standing SW localized in the layer with small α; this SW, in turn, is exited by the microwave field. If the SP layer is in the reactive state, the eigenfrequency of spin precession ω_{02} in this layer is higher than the frequency of the standing harmonic wave in the excitation layer, which is equal, at resonance, to the frequency of the microwave field ω ($\omega_{02} > \omega$, $H_{02} < H_{01}$). Therefore, the exponentially decaying spin wave (whose oscillations are forced and also occur at the frequency ω) in the SP layer tends to be ahead, in phase, of the harmonic wave localized in the excitation layer and tries to carry along and extend the latter. This process results in a reduction of the wave numbers and in a difference between the resonance fields $H_0 - H_n$. When the SP layer becomes dispersive ($\omega_{02} < \omega$, $H_{02} > H_{01}$), the situation is reversed: the decaying spin wave in the SP layer lags in phase and compresses the harmonic standing wave in the excitation layer. This causes, although to a lesser degree, an increase in the difference $H_0 - H_n$. When H_{01} and H_{02} approach each other, the amplitude of time-varying magnetization m_{02} in the SP layer increases and the influence of spin oscillations in the SP layer on the value of k_1 becomes stronger. At the same time, the increase in m_{02} loosens spin pinning; consequently, high-order modes are no longer excited in the spectrum.

As θ_H increases further, the difference $H_{02} - H_{01}$ increases and the precession amplitude in the SP layer decreases and strengthens the pinning of spins, thereby favoring the appearance of high-order modes.

It should be noted that the observed dispersion also takes place in the case of dynamic spin pinning, when the layer in the reactive state plays the part of the SP layer. As the angle θ_H is changed, the region of excitation of harmonic modes shifts from one layer to the other. The effect of dispersion in this case reveals itself in the repulsion between SW modes localized in the excitation layer and the zeroth mode in the SP layer (or the FMR mode, according to the terminology used in [10, 11]). In [10, 11], it is shown that both the first and the second layer can be the excitation layer, depending on the range of angles. However, as was mentioned above, in both situations, the excitation layer is a reactive medium; therefore, the wave numbers of the excited SW modes decrease in both angle ranges. This reveals itself in spectra as a shift of the peaks of SW modes towards higher fields or as their repulsion from the zeroth mode of the SP layer. Thus, in the case of dynamic pinning, only one part of the dispersion curve will be observed. In the case of the dissipative or mixed

mechanism of pinning, as was mentioned above, at any orientation of **H** with respect to the film plane or at any temperature, the region of excitation of standing harmonic modes is the layer with low damping. Therefore, the wave numbers of SW modes shift towards lower values if the SP layer is in the reactive state ($H_{02} < H_{01}$) and to higher values if the SP layer is in the dispersive state ($H_{02} > H_{01}$). As a consequence, the peaks of SW modes in both cases are shifted in field from the absorption peak of the SP layer. The consideration of such dispersion of SW is of great importance for correct determination of the exchange interaction constant from the SW spectrum, since from the type of state (dispersive or reactive) of the SP layer and the position of the resonance frequency (eigenfrequency of precession) for this layer with respect to microwave frequency one can find the values of the wave numbers of SW modes and, consequently, the slope of the $H_0 - H_n = f(n^2)$ dependence, from which the value of A is determined. Obviously, the effect of this factor should be taken into account in recording and analyzing the SWR spectra for any orientation of **H** with respect to the film plane.

5. CONCLUSIONS

Thus, the results of this study allows one to come to the following conclusions:

(1) SW spatial dispersion caused by the effect of the SP layer is established in multilayer films. Dispersion is most pronounced in films with a mixed spin-pinning mechanism when the SP layer transfers from the reactive state to a dispersive state and vice versa.

(2) This type of spatial dispersion can explain the so-called effect of repulsion of SW modes observed in previous studies.

(3) In determining of the exchange interaction constant from the SWR spectra, one should take into account the significant effect of spatial dispersion on the wave numbers of excited SW modes.

REFERENCES

1. C. H. Wolts, J. Zebrowski, and K. Komenou, J. Appl. Phys. **50** (9), 5878 (1979).
2. R. N. Nosov and D. I. Sementsov, Fiz. Tverd. Tela (St. Petersburg) **42** (8), 1430 (2000) [Phys. Solid State **42**, 1471 (2000)].
3. A. V. Pomyalov and P. E. Zil'berman, Radiotekh. Radioélektron., No. 1, 94 (1986).
4. V. F. Dmitriev and B. A. Kalinikos, Zh. Tekh. Fiz. **57** (11), 2212 (1987) [Sov. Phys. Tech. Phys. **32**, 1336 (1987)].
5. A. G. Gurevich and G. A. Melkov, *Magnetic Oscillations and Waves* (Nauka, Moscow, 1994).
6. Yu. A. Korchagin, R. G. Khlebopros, and N. S. Chistyakov, Fiz. Tverd. Tela (Leningrad) **14** (7), 2121 (1972) [Sov. Phys. Solid State **14**, 1826 (1972)].
7. M. Jirsa, Phys. Status Solidi B **113**, 679 (1982).
8. B. Hoekstra, R. P. van Stapele, and J. M. Robertson, J. Appl. Phys. **48** (1), 382 (1977).
9. S. L. Vysotskiĭ, G. T. Kazakov, M. L. Kats, and Yu. A. Fillimonov, Fiz. Tverd. Tela (St. Petersburg) **35** (5), 1190 (1993) [Phys. Solid State **35**, 606 (1993)].
10. A. M. Grishin, V. S. Dellalov, V. F. Shkar, *et al.*, Phys. Lett. A **140** (3), 133 (1989).
11. N. K. Dan'shin, V. S. Dellalov, M. A. Kol'tsov, *et al.*, Zh. Éksp. Teor. Fiz. **110** (3), 938 (1996) [JETP **83**, 517 (1996)].
12. A. L. Sukstanskiĭ and G. I. Yampol'skiĭ, Fiz. Tverd. Tela (St. Petersburg) **42** (5), 866 (2000) [Phys. Solid State **42**, 889 (2000)].
13. A. M. Zyuzin, S. N. Sabaev, V. V. Radaĭkin, and A. V. Kulyapin, Fiz. Tverd. Tela (St. Petersburg) **44** (5), 893 (2002) [Phys. Solid State **44**, 932 (2002)].
14. A. M. Zyuzin and A. G. Bazhanov, Zh. Éksp. Teor. Fiz. **112** (10), 1430 (1997) [JETP **85**, 778 (1997)].
15. A. M. Zyuzin, A. G. Bazhanov, S. N. Sabaev, and S. S. Kidyaev, Fiz. Tverd. Tela (St. Petersburg) **42** (7), 1279 (2000) [Phys. Solid State **42**, 1317 (2000)].
16. A. M. Zyuzin, V. N. Van'kov, and V. V. Radaĭkin, Pis'ma Zh. Tekh. Fiz. **17** (23), 65 (1991) [Sov. Tech. Phys. Lett. **17**, 848 (1991)].
17. A. M. Zyuzin, V. V. Radaĭkin, and A. G. Bazhanov, Zh. Tekh. Fiz. **67** (2), 35 (1997) [Tech. Phys. **42**, 155 (1997)].
18. A. M. Zyuzin, Fiz. Tverd. Tela (Leningrad) **31** (7), 109 (1989) [Sov. Phys. Solid State **31**, 1161 (1989)].
19. A. M. Zyuzin and A. G. Bazhanov, Pis'ma Zh. Éksp. Teor. Fiz. **63** (7), 528 (1996) [JETP Lett. **63**, 555 (1996)].
20. A. M. Zyuzin and V. V. Radaĭkin, in *Proceedings of XIII School–Seminar on New Magnetic Materials for Microelectronics, Astrakhan* (1992), Part 1, p. 253.

Translated by A. Zalesskiĭ

Physics of the Solid State, Vol. 45, No. 12, 2003, pp. 2320–2327. Translated from Fizika Tverdogo Tela, Vol. 45, No. 12, 2003, pp. 2215–2221.

MAGNETISM AND FERROELECTRICITY

Effect of Magnetocrystalline Anisotropy on the Temperature Characteristics of Magnetostatic Waves in Ferromagnetic Films

V. V. Shagaev

Research Institute of Electronic Engineering Materials, Kaluga, 248650 Russia

e-mail: met@postklg.ru

Received February 11, 2003; in final form, May 15, 2003

Abstract—The temperature dependence of the eigenfrequencies of magnetization oscillation in a single-crystal film is shown to depend strongly on the temperature dependence of the magnetocrystalline anisotropy field. The conditions are considered under which the temperature coefficient of the ferromagnetic resonance frequency in a film with cubic anisotropy changes sign as the orientation of the magnetization vector is changed from the ⟨111⟩ to the ⟨100⟩ direction. The spectrum of surface magnetostatic waves is investigated experimentally in {110}-oriented yttrium iron garnet films. It is established that, due to magnetic anisotropy of the ferrite, the temperature dependence of the long-wavelength limit of the frequency spectrum becomes nonmonotonic when a film of this material is magnetized along the ⟨100⟩ axis. © *2003 MAIK "Nauka/Interperiodica".*

1. INTRODUCTION

The spectrum of magnetostatic spin waves (MSWs) in anisotropic ferromagnetic films has been well studied both theoretically and experimentally [1–8]. However, the temperature variations of the spectrum were considered mainly within an isotropic model [9, 10], and the variations of the frequencies were assumed to be due to the temperature dependence of the saturation magnetization of the material of a film. Such an approach is justified, in part, by the fact that yttrium iron garnet (YIG, $Y_3Fe_5O_{12}$), which is used extensively in spin-wave electronics, is a weakly anisotropic material. For example, at temperature $T = 295$ K, the saturation magnetization $4\pi M_0$ is equal to 1750 G, the effective cubic-anisotropy field H_c is –42 Oe, and their temperature coefficients are $d(4\pi M_0)/dT = -4.0$ G/K and $dH_c/dT = 0.4$ Oe/K [11]. The parameters H_c and dH_c/dT are relatively small and can be treated as small corrections in calculating the temperature-dependent MSW characteristics. The main contribution to the temperature dependence comes from the derivative $d(4\pi M_0)/dT$.

The effect of magnetic anisotropy on the temperature dependence of the ferromagnetic resonance (FMR) frequency was considered in [12, 13], where an orientational method for stabilizing the parameters of ferrite-based high-frequency devices was discussed. The problems that were treated in those papers are very specific, and the results obtained there give but a rough idea of the magnitude and mechanisms of the effect of crystalline anisotropy on the temperature variations of the MSW frequencies in films. Furthermore, only the case of cubic anisotropy was analyzed in [12, 13].

In this paper, we consider the effect of magnetic anisotropy on the temperature dependence of the eigenfrequencies of magnetization oscillation in ferromagnetic single-crystal films. The effect of crystalline anisotropy on the temperature characteristics of surface MSWs is investigated in detail on the example of cubic-ferrite films.

In general, the temperature variations of the MSW spectrum in a ferromagnetic film can be studied theoretically on the basis of dispersion relations and the equations from which the equilibrium magnetization direction is determined. By differentiating these equations with respect to temperature, the most general expressions for the frequency temperature coefficient (FTC) can be derived after certain mathematical manipulation. However, we will not proceed this way but restrict our consideration to a few specific cases in which the equations mentioned above are simplified and the effect of magnetoctystalline anisotropy on the frequency temperature dependence has a clear physical interpretation.

2. THE FREQUENCY TEMPERATURE COEFFICIENT OF UNIFORM FERROMAGNETIC RESONANCE

We consider the effect of crystallographic anisotropy on the FTC of free magnetization oscillation in a film through the example of the FMR frequency. We note that, in the exchange-free approximation, the FMR frequency is the long-wavelength limit of the MSW spectrum. Below (in discussing the experimental data), we will derive a simple relation between the tempera-

ture coefficient of any frequency of the surface MSW spectrum and the FTC of uniform FMR.

We will consider a ferromagnetic film in the coordinate system *xyz* with the *z* axis parallel to the equilibrium magnetization vector $\mathbf{M}_0$ and with the *y* axis parallel to the plane of the film (Fig. 1). The magnetocrystalline anisotropy of the material of the ferromagnetic film can be described by the tensor of effective demagnetizing factors N_{ij}^c of ($i, j = x, y, z$). We also take into account uniaxial anisotropy, which usually arises in epitaxially grown films. For uniaxial anisotropy with the axis normal to the film plane, the nonzero components of the corresponding tensor N_{ij}^u are [14]

$$N_0 N_{xx}^u = -H_u \cos^2\theta,$$

$$M_0 H_{zz}^u = -H_u \sin^2\theta,$$

$$M_0 N_{xz}^u = -H_u \sin\theta\cos\theta,$$

where θ is the angle between $\mathbf{M}_0$ and the film plane and $H_u = 2K_{u1}/M_0$ is the uniaxial-anisotropy field, with K_{u1} being the first uniaxial-anisotropy constant, which characterizes the anisotropy energy density $W_a^u = K_{u1}\cos^2\theta$.

The tensor N_{ij}^c depends on the crystal symmetry of the ferromagnetic material. In order to decrease the number of independent components of this tensor, we consider the case where the vector $\mathbf{M}_0$ is directed along a crystallographic symmetry axis of the ferromagnetic film. Let us derive the relations that follow from the invariance of the magnetocrystalline anisotropy energy density W_a^c under symmetry transformations.

For small deviations $\mathbf{m}$ of the magnetization vector from the *z* axis ($\mathbf{M} = \mathbf{M}_0 + \mathbf{m}$, where $\mathbf{M}_0 \parallel z$, $m_z = 0$), we have

$$W_a^c = \frac{1}{2}\sum_{i,j} N_{ij}^c M_i M_j. \quad (1)$$

To a rotation of vector $\mathbf{m}$ about the symmetry axis (of order n_s) through angle $2\pi/n_s$ corresponds the following transformation of the components of the magnetization vector:

$$M_i \longrightarrow \sum_j R_{ij} M_j,$$

$$\hat{R} = \begin{pmatrix} \cos\frac{2\pi}{n_s} & \mp\sin\frac{2\pi}{n_s} & 0 \\ \pm\sin\frac{2\pi}{n_s} & \cos\frac{2\pi}{n_s} & 0 \\ 0 & 0 & 1 \end{pmatrix}.$$

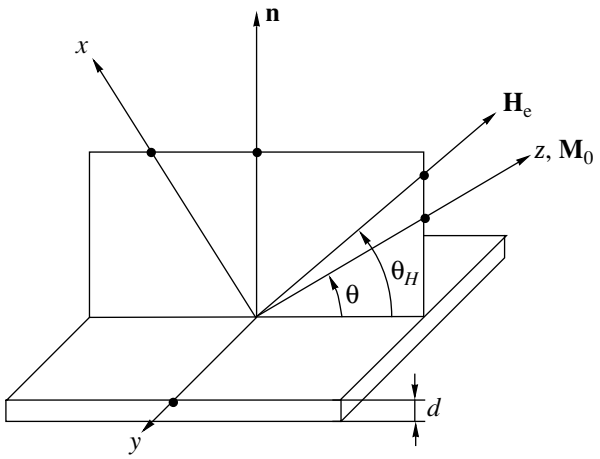

Fig. 1. Ferromagnetic film (schematic).

Therefore, W_a^c takes the form

$$W_a^c = \frac{1}{2}\sum_{i',j',i,j} N_{i'j'}^c R_{i'i} R_{j'j} M_i M_j. \quad (2)$$

By comparing Eqs. (1) and (2), we obtain the condition of the energy density invariance:

$$N_{ij}^c = \sum_{i',j'} N_{i'j'}^c R_{i'i} R_{j'j}. \quad (3)$$

From Eq. (3) for $n_s \geq 3$, it follows that

$$N_{xy}^c = N_{xz}^c = N_{yz}^c = 0, \quad N_{xx}^c = N_{yy}^c. \quad (4)$$

We note that at $n_s = 2$, i.e., if the magnetization vector is parallel to a twofold rotation axis, Eq. (3) imposes no restriction on the components N_{xy}^c, N_{xx}^c, and N_{yy}^c. In what follows, we consider the case of $n_s \geq 3$ and make use of Eqs. (4).

The frequency of uniform FMR can be found, using a standard method [14], to be

$$f_{\mathrm{FMR}}^2 = g^2[H_{ez} + M_0(N_{xx}^c - N_{zz}^c) + 4\pi M_{\mathrm{eff}}\cos 2\theta] \times [H_{ez} + M_0(N_{yy}^c - N_{zz}^c) + 4\pi M_{\mathrm{eff}}\sin^2\theta] - (gM_0 N_{xy}^c)^2. \quad (5)$$

Here, *g* is the gyromagnetic ratio and H_{ez} is the projection of the external dc magnetic field $\mathbf{H}_e$ onto the direction of magnetization vector $\mathbf{M}_0$. In Eq. (5), we also introduced the parameter $4\pi M_{\mathrm{eff}} = 4\pi M_0 - H_u$ and used the expressions presented above for the effective demagnetizing factors of normal uniaxial anisotropy (for any value of angle θ).

The FTC is defined as

$$\alpha_{FMR} = \frac{1}{f_{FMR}}\frac{df_{FMR}}{dT}.$$

Using Eqs. (5) and (4), the formulas for the derivatives $d\theta/dT$ and dH_{ez}/dT derived in the Appendix, and simple algebra, the coefficient α_{FMR} can be found to be

$$\begin{aligned}\alpha_{FMR} - \frac{1}{g}\frac{dg}{dT} &= \frac{1}{2H_{in} + 4\pi M_{eff}(1+\cos 2\theta)} \\ &\times \left\{\left[\frac{H_{in}(3\cos 2\theta - 1) + 4\pi M_{eff}(1+\cos 2\theta)}{2H_{in} + 4\pi M_{eff}(1+\cos 2\theta)}\right]\right. \\ &+ \frac{d(4\pi M_{eff})}{dT}\frac{dM_0(N^c_{xx} - N^c_{zz})}{dT} \\ &\left. + \left[\frac{2H_{in} + 4\pi M_{eff}(1+\cos 2\theta)}{2H_{in}}\right]\frac{dM_0(N^c_{yy} - N^c_{zz})}{dT}\right\},\end{aligned} \tag{6}$$

where

$$H_{in} = H_{ez} - 4\pi M_{eff}\sin^2\theta + M_0 N^c_t,$$

$$N^c_t = N^c_{xx} - N^c_{zz} = N^c_{yy} - N^c_{zz}.$$

In the same notation, the FMR frequency can be rewritten in the form

$$f^2_{FMR} = g^2 H_{in}(H_{in} + 4\pi M_{eff}\cos^2\theta).$$

In deriving Eq. (6), it was taken into account that, while the coefficients N^c_{xx} and N^c_{yy} are equal, their temperature derivatives are generally different and should be calculated separately.

The parameters H_{in} and θ can be expressed in terms of the external field H_e and angle θ_H between the direction of this field and the film plane by using the relations

$$H_e = \sqrt{(4\pi M_{eff}\sin\theta\cos\theta)^2 + (H_{in} + 4\pi M_{eff}\sin^2\theta - M_0 N^c_t)^2},$$

$$\tan(\theta_H - \theta) = \frac{4\pi M_{eff}\sin\theta\cos\theta}{H_{in} + 4\pi M_{eff}\sin^2\theta - M_0 N^c_t}.$$

We note that Eq. (6) can be used to analyze the FMR temperature characteristics in both weakly and highly anisotropic films. In deriving Eq. (6), no restrictions were imposed on the values of parameters $M_0 N^c_{ij}$ and their temperature derivatives.

3. ANALYSIS OF THE FREQUENCY TEMPERATURE COEFFICIENT IN FILMS WITH CUBIC ANISOTROPY

In the case of a film with cubic anisotropy, the coefficients N^c_{ij} in Eq. (6) can be found from W^c_a, which is invariant under cubic-symmetry transformations and is expressed in terms of the components of the magnetization vector $\mathbf{M}_0$ as [15]

$$W^c_a = -\frac{K_{c1}}{2M_0^4}\sum_p M^4_{0p}. \tag{7}$$

Here, K_{c1} is the first cubic-anisotropy constant (which is generally larger than the coefficients of the other possible invariants) and summation is performed over the components of the vector $\mathbf{M}_0$ along the axes p = [100], [010], [001].

In the case of $\mathbf{M}_0 \parallel z$, Eq. (7) gives the following expressions for the coefficients $M_0 N^c_{ii}$ [14]:

$$\begin{aligned}M_0 N^c_{xx} &= -6H_c\sum_p \beta^2_{xp}\beta^2_{zp}, \\ M_0 N^c_{yy} &= -6H_c\sum_p \beta^2_{yp}\beta^2_{zp}, \\ M_0 N^c_{zz} &= -2H_c\sum_p \beta^4_{zp},\end{aligned} \tag{8}$$

where $H_c = K_{c1}/M_0$ is the effective cubic-anisotropy field and β_{ip} are the cosines of the angles between the coordinate axes $i = x, y, z$ and the crystallographic axes p = [100], [010], [001].

If the equilibrium magnetization vector is directed along a threefold or fourfold axis of a cubic crystal (axes $\langle 111\rangle$ and $\langle 100\rangle$, respectively), then it follows from Eqs. (8) that

$$\begin{aligned}M_0 N^c_t \equiv M_0(N^c_{xx} - N^c_{zz}) &= M_0(N^c_{yy} - N^c_{zz}) \\ &= \begin{cases} 2H_c, & \mathbf{M}_0 \parallel \langle 100\rangle \\ -\frac{4}{3}H_c, & \mathbf{M}_0 \parallel \langle 111\rangle. \end{cases}\end{aligned} \tag{9}$$

In order to calculate the temperature derivatives $dM_0(N^c_{xx} - N^c_{zz})/dT$ and $dM_0(N^c_{yy} - N^c_{zz})/dT$ involved in Eq. (6), we use the equation

$$\frac{dM_0(N^c_{ii} - N^c_{zz})}{dT} = \frac{\partial(M_0 N^c_t)}{\partial H_c}\frac{dH_c}{dT} + \frac{dM_0(N^c_{ii} - N^c_{zz})}{d\theta}\frac{d\theta}{dT}. \quad (10)$$

Here, the partial derivative in the first term is calculated using Eq. (9) and the derivative dH_c/dT is a material parameter of a ferromagnetic film. The derivative $d\theta/dT$ in the second term is given by Eq. (A6) from the Appendix. The derivatives $dM_0(N^c_{xx} - N^c_{zz})/d\theta$ and $dM_0(N^c_{yy} - N^c_{zz})/d\theta$, as calculated using Eqs. (8), have the form

$$\frac{dM_0(N^c_{ii} - N^c_{zz})}{d\theta} = 0, \quad \mathbf{M}_0 \parallel \langle 100\rangle,$$

$$\frac{dM_0(N^c_{xx} - N^c_{zz})}{d\theta} = -\frac{dM_0(N^c_{yy} - N^c_{zz})}{d\theta} = 2\sqrt{2}H_c\cos 3\nu, \quad \mathbf{M}_0 \parallel \langle 111\rangle.$$

In deriving the last formula, the parameters β_{ip} were expressed in terms of angles ν and τ, which define the orientation of the coordinate system *xyz* relative to crystallographic axes $[11\bar{2}]$, $[\bar{1}10]$, and [111] (Fig. 2). This formula takes into account the symmetry of the axis along which the vector $\mathbf{M}_0$ is directed. Indeed, the right-hand side is invariant under the transformation $\nu \longrightarrow \nu + 2\pi/3$, which characterizes a threefold axis. Therefore, the angle ν can be reckoned from the *y* axis [which is the line of intersection of the film plane and crystallographic plane (111)] to any of the $[10\bar{1}]$, $[\bar{1}10]$, and $[0\bar{1}1]$ directions.

Upon making the substitutions indicated above, Eq. (10) takes the form

$$\frac{dM_0(N^c_{xx} - N^c_{zz})}{dT} = \frac{dM_0(N^c_{yy} - N^c_{zz})}{dT} = 2\frac{dH_c}{dT}, \quad \mathbf{M}_0 \parallel \langle 100\rangle, \quad (11)$$

$$\frac{dM_0\left(N^c_{\left\{\begin{smallmatrix}xx\\yy\end{smallmatrix}\right\}} - N^c_{zz}\right)}{dT} = -\frac{4}{3}\frac{dH_c}{dT} \mp \frac{H_c 2\sqrt{2}\cos 3\nu \sin 2\theta}{2H_{\text{in}} + 4\pi M_0(1+\cos 2\theta)}\frac{d(4\pi M_0)}{dT}, \quad \mathbf{M}_0 \parallel \langle 111\rangle. \quad (12)$$

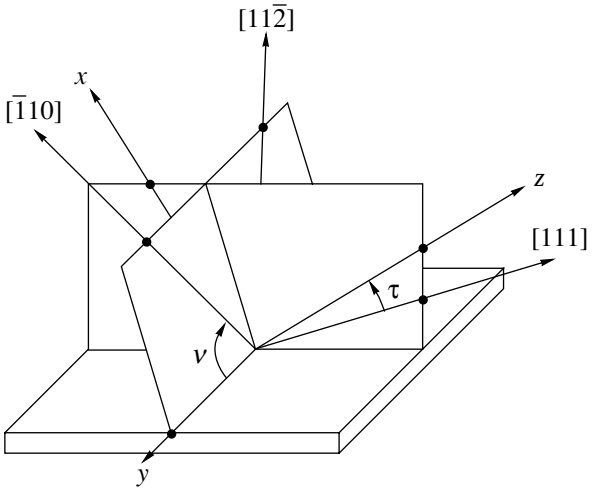

Fig. 2. Orientation of the coordinate system *xyz* with respect to the crystallographic axes.

We use Eqs. (11) and (12) to transform the general equation (6). We also introduce dimensionless quantities and put $dg/dT = 0$ for simplicity (the contribution from the derivative dg/dT to the FTC is of no interest to us here, because, according to Eq. (6), this derivative is independent of the parameters H_c and $4\pi M_{\text{eff}}$ and their temperature derivatives). After straightforward algebra, we obtain

$$\frac{\alpha_{\text{FMR}}}{\alpha_M} = \frac{1}{4\tilde{f}^2_{\text{FMR}}}\left[A + B\frac{H_c}{4\pi M_{\text{eff}}} + C\frac{dH_c/dT}{d(4\pi M_{\text{eff}})/dT}\right], \quad (13)$$

where

$$\alpha_M = \frac{1}{4\pi M_{\text{eff}}}\frac{d(4\pi M_{\text{eff}})}{dT}, \quad \tilde{f}_{\text{FMR}} = \frac{f_{\text{FMR}}}{4\pi M_{\text{eff}} g},$$

$$A = 2\tilde{H}_{\text{in}}\left(1 - 3\tilde{H}_{\text{in}}\frac{1-\cos 2\theta}{2\tilde{H}_{\text{in}} + 1 + \cos 2\theta}\right),$$

$$B = \frac{R_{\langle nml\rangle}\sin 2\theta}{2\tilde{H}_{\text{in}} + 1 + \cos 2\theta},$$

$$C = \tilde{N}_{\langle nml\rangle}(4\tilde{H}_{\text{in}} + 1 + \cos 2\theta),$$

$$R_{\langle 111\rangle} = 2\sqrt{2}\cos 3\nu, \quad R_{\langle 100\rangle} = 0,$$

$$\tilde{N}_{\langle 100\rangle} = 2, \quad \tilde{N}_{\langle 111\rangle} = -\frac{4}{3}.$$

Here,

$$\tilde{H}_{\text{in}} = \frac{H_{\text{in}}}{4\pi M_{\text{eff}}} = \sqrt{\frac{\cos^4\theta}{4} + \tilde{f}^2_{\text{FMR}}} - \frac{\cos^2\theta}{2}. \quad (14)$$

In deriving Eq. (13), it was assumed that $\mathbf{M}_0 \parallel \langle 111\rangle$ or $\mathbf{M}_0 \parallel \langle 100\rangle$, but the crystallographic orientation of the film can be arbitrary. Using Eq. (14), we can obtain

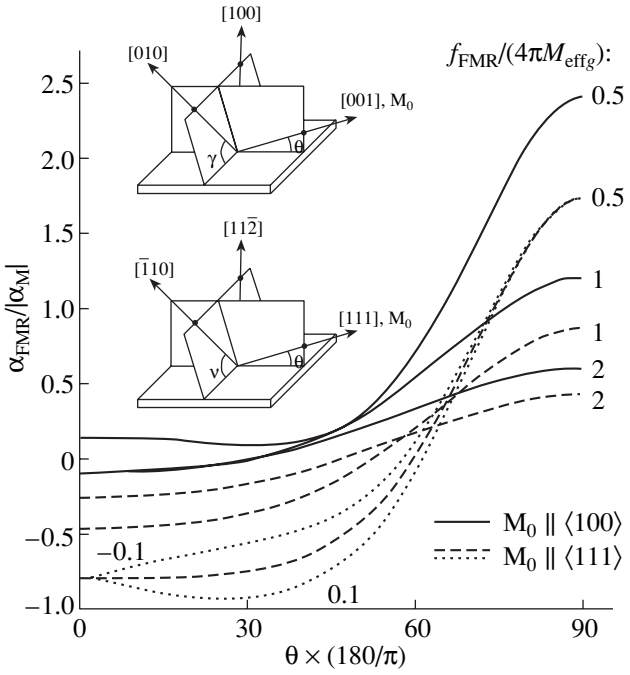

Fig. 3. Dependences of the temperature coefficient of the FMR frequency on the magnetization orientation with respect to the film plane and the crystallographic axes. The crystallographic orientation of the film is defined by angles θ and γ in the case of $\mathbf{M}_0 \parallel [001]$ (upper inset) and by angles θ and ν in the case of $\mathbf{M}_0 \parallel [111]$ (lower inset). For $\mathbf{M}_0 \parallel [001]$, the temperature coefficient is independent of angle γ. For $\mathbf{M}_0 \parallel [111]$, the dependence on angle ν in the computing formula is through the ratio $H_c\cos 3\nu/(4\pi M_{\text{eff}})$. This ratio is equal to zero for dashed curves and to ±0.1 for dotted curves. In computing, it was assumed that $dg/dT = 0$, $dH_c/dT = -0.1\,d(4\pi M_{\text{eff}})/dT$, and $|\alpha_M| = |d(4\pi M_{\text{eff}})/dT|(4\pi M_{\text{eff}})^{-1}$.

explicit analytical dependences of the coefficients *A*, *B*, and *C* on θ and $\tilde{f}_{FMR}$. Such dependences, as calculated from Eq. (13), are exemplified in Fig. 3. It can be seen that the effect of magnetic anisotropy on the FTC is significant even in the case where H_c and dH_c/dT are small in comparison with $4\pi M_{\text{eff}}$ and $d(4\pi M_{\text{eff}})/dT$, respectively.

It follows from Eq. (13) that, at a given value of the FMR frequency, its temperature coefficient depends on the orientation of $\mathbf{M}_0$ with respect to both the film plane and the crystal lattice. According to Fig. 3, the difference in value between the FTCs for $\mathbf{M}_0 \parallel \langle 111\rangle$ and $\mathbf{M}_0 \parallel \langle 100\rangle$ is maximum for θ = 0 and increases with decreasing frequency f_{FMR}. The frequency f_{FMR} in Fig. 3 is measured in units of $4\pi M_{\text{eff}}g$. In the case of $f_{FMR}/4\pi M_{\text{eff}}g = 0.5$, the values of the FTC for small values of θ are opposite in sign for the [111] and [100] magnetization vector directions (crystallographic sign reversal of the FTC). This feature is due to the fact that anisotropy of the FTC is associated with anisotropy of both H_c and dH_c/dT and that the latter quantity enters into Eq. (13) with opposite sign for $\mathbf{M}_0 \parallel \langle 111\rangle$ and $\mathbf{M}_0 \parallel \langle 100\rangle$. We note that, in the case of in-plane magnetization, the dependence of the FTC sign on the crystallographic orientation of $\mathbf{M}_0$ arises only because of the temperature dependence of the magnetic anisotropy field. Indeed, from Eq. (13), it follows that, for $dH_c/dT = 0$ and θ = 0, the sign of α_{FMR} coincides with that of α_M.

In an anisotropic ferromagnetic film with in-plane magnetization, the conditions of the FTC sign reversal are derived from Eq. (13) to be

$$\alpha_{FMR,\langle 100\rangle} < 0, \quad \alpha_{FMR,\langle 111\rangle} > 0,$$
$$\frac{dH_c/dT}{d(4\pi M_{\text{eff}})/dT} < -\frac{\tilde{H}_{in,\langle 100\rangle}}{2(1+2\tilde{H}_{in,\langle 100\rangle})}, \tag{15}$$

$$\alpha_{FMR,\langle 100\rangle} > 0, \quad \alpha_{FMR,\langle 111\rangle} < 0,$$
$$\frac{dH_c/dT}{d(4\pi M_{\text{eff}})/dT} > \frac{3\tilde{H}_{in,\langle 111\rangle}}{4(1+2\tilde{H}_{in,\langle 111\rangle})}. \tag{16}$$

Here, subscripts with angular brackets indicate the crystallographic orientation of $\mathbf{M}_0$. As an example, we consider a {110}-oriented single-crystal film of a material for which $dH_c/dT > 0$ and $d(4\pi M_{\text{eff}})/dT < 0$. If, in addition,

$$\frac{dH_c}{dT} \geq \frac{1}{4}\left|\frac{d(4\pi M_{\text{eff}})}{dT}\right|,$$

then inequalities (15) are satisfied for any value of $\tilde{H}_{in,\langle 100\rangle}$. Otherwise (as in YIG), from the last of inequalities (15), it follows (after simple algebra) that

$$H_e < H_0,$$
$$H_0 = -2\left[4\pi M_{\text{eff}}\frac{dH_c/dT}{d(4\pi M_{\text{eff}})/dT + 4dH_c/dT} + H_c\right]. \tag{17}$$

Using the values of the magnetic parameters presented above for YIG, we obtain $H_0 \approx 667$ Oe.

Thus, the theory developed in this paper predicts that, in anisotropic films, there is a threshold field H_0 below which crystallographic reversal of the sign of the FTC takes place.

4. EXPERIMENTAL STUDY OF THE TEMPERATURE CHARACTERISTICS OF SURFACE MAGNETOSTATIC WAVES

We studied YIG films grown on {110}-oriented gadolinium gallium garnet single-crystal substrates. MSWs were excited and detected through the use of a microstrip package, on which the sample under study was mounted. The dispersion relation (dependence of the frequency *f* on wave number *k*) was determined using an interference technique similar to that used in [16]. A film was magnetized by an in-plane magnetic

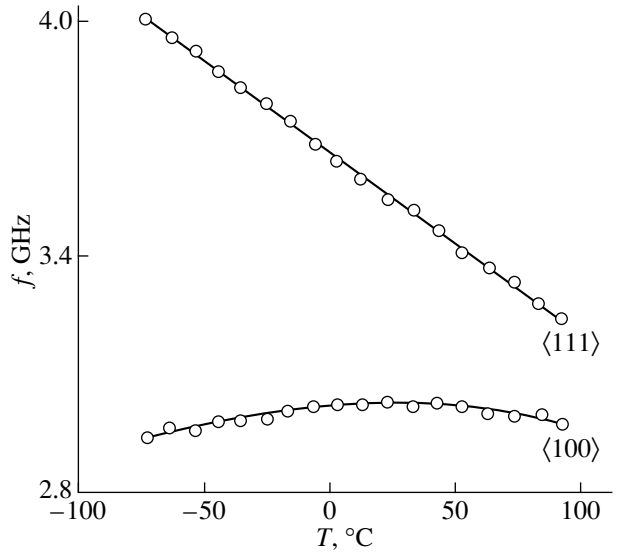

Fig. 4. Experimental temperature dependences of the frequency of long-wavelength surface MSWs in a {110}-oriented YIG film in the cases where the external in-plane field is directed along ⟨100⟩ and ⟨111⟩; H_e = 600 Oe.

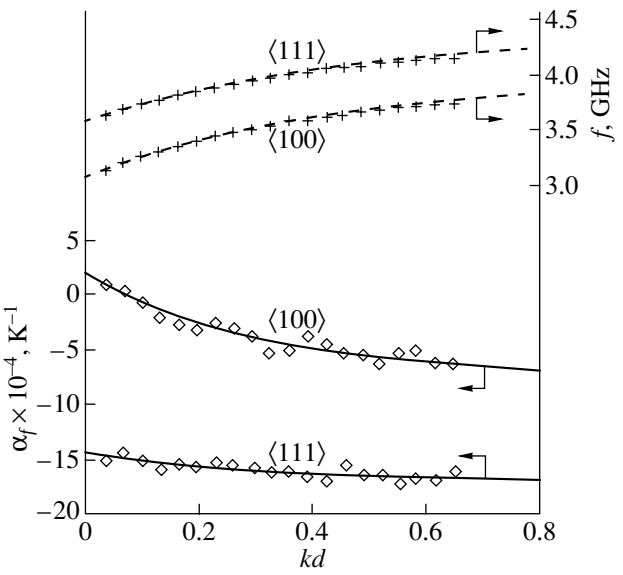

Fig. 5. Experimental (symbols) and theoretical (solid curves) $f(kd)$ and $\alpha_f(kd)$ dependences for surface MSWs in a {110}-oriented in-plane-magnetized YIG film of thickness d = 10.5 μm at T = 12°C. The external magnetic field H_e = 600 Oe was directed along the ⟨100⟩ and ⟨111⟩ axes. Film parameters: $4\pi M_{eff}$ = 1830 G, H_c = –42 Oe, $d(4\pi M_{eff})/dT$ = –4.2 G/K, and dH_c/dT = 0.46 Oe/K.

field directed along the microstrip transducers. This geometry allows one to investigate MSWs with a wave vector perpendicular to the external magnetic field. The orientation of the magnetic field with respect to the crystal lattice was varied by rotating the YIG film under a compression spring. Measurements were performed for $\mathbf{H}_e \parallel \langle 100\rangle$ and $\mathbf{H}_e \parallel \langle 111\rangle$. The sample orientations corresponding to these geometries were determined using experimentally measured angular dependences of the MSW frequencies; the minima and maxima in these dependences corresponded to the orientations $\mathbf{H}_e \parallel \langle 100\rangle$ and $\mathbf{H}_e \parallel \langle 111\rangle$, respectively.

Figure 4 shows measured temperature dependences of the MSW frequency in the long-wavelength limit (k = 0). It is worth noting that the $f_{\langle 100\rangle}(T)$ dependence is nonmonotonic. Analysis based on the $H_c(T)$ and $4\pi M_{eff}(T)$ dependences obtained for YIG films by using the technique described in [17] shows that an increase in the frequency ($df_{\langle 100\rangle}/dT > 0$) is observed in the temperature range where inequality (17) is valid.

Using experimental $f^{(1)}(k_n d)$ and $f^{(2)}(k_n d)$ dependences (where d is the film thickness, k_n are wave numbers, as determined following the technique described in [16]) for two temperatures T_1 and T_2 that are close to each other, we determined the wave-number dependence of the FTC (Fig. 5) from the formula

$$\alpha_f(k_n d) = \frac{2}{f^{(1)}(k_n d) + f^{(2)}(k_n d)} \frac{f^{(2)}(k_n d) - f^{(1)}(k_n d)}{T_2 - T_1}.$$

The FTC thus found was compared with the theoretical $\alpha_f(kd)$ dependence calculated with inclusion of the effect of magnetocrystalline anisotropy on the FTC. The calculation was based on the dispersion relation of MSWs in ferromagnetic films with cubic and uniaxial anisotropy. However, the exact dispersion relation [17] gives the $f(kd)$ dependence in an implicit form and can be found only by separately including the effects of the saturation magnetization $4\pi M_0$ and of the uniaxial anisotropy field H_u. For this reason, we used the approximate dispersion relation

$$f^2_{appr}(kd) = f^2_{FMR} + \frac{(4\pi M_{eff} g)^2}{4}[1 - \exp(-2kd)]. \quad (18)$$

An elementary analysis shows that Eq. (18) is the zeroth approximation in the expansion of the exact dispersion relation in a power series in $H_u/4\pi M_{eff} \ll 1$. The difference between the exact and the approximate dispersion relation is given by

$$\max\left\{\frac{f^2(kd) - f^2_{appr}(dk)}{(4\pi M_{eff} g)^2}, 0 < kd < \infty\right\} \approx 0.1\frac{H_u}{4\pi M_{eff}}.$$

The approximate dispersion relation gives exact expressions for the FMR frequencies in the limits of k = 0 and ∞.

From Eq. (18), we obtain an explicit analytical expression for the FTC

$$\alpha_f = \frac{f_{\mathrm{FMR}}^2}{f^2}\alpha_{\mathrm{FMR}} + \left(1 - \frac{f_{\mathrm{FMR}}^2}{f^2}\right)\alpha_M.$$

From this formula, it follows that the effect of the crystallographic anisotropy on the FTC decreases in magnitude with decreasing wavelength.

In accordance with the geometry of the experiment, we used the formula

$$f_{\mathrm{FMR}}^2 = g^2(H_e + \tilde{N}_{\langle nml\rangle}H_c) \times (H_e + \tilde{N}_{\langle nml\rangle}H_c + 4\pi M_{\mathrm{eff}}),$$

where the values of coefficients $\tilde{N}_{\langle nml\rangle}$ are given above [after Eq. (13)] and $g = 2.8$ MHz/Oe, which is typical of YIG. The values of $4\pi M_{\mathrm{eff}}$, H_c, and their derivatives $d(4\pi M_{\mathrm{eff}})/dT$ and dH_c/dT were derived from the best fit of the calculated dispersion relations (shown in Fig. 5) to the experimental data. These fitted parameters are presented in the caption under Fig. 5, and they agree well with the values typical of YIG films.

As seen from Fig. 5, FTC anisotropy in {110}-oriented YIG films is significant in spite of the fact that $4\pi M_0$ and $d(4\pi M_0)/dT$ are much larger than H_c and dH_c/dT, respectively. Analysis of the calculated dependences shows that the dominant contribution to the anisotropy comes from the derivative dH_c/dT rather than from the parameter H_c itself.

APPENDIX: TEMPERATURE DERIVATIVES OF THE ANGLES DEFINING THE ORIENTATION OF THE STATIC MAGNETIZATION VECTOR IN A FERROMAGNETIC SINGLE-CRYSTAL FILM

In the static case, the Landau–Lifshitz equation has the form

$$[\mathbf{M}(T), \mathbf{H}_{\mathrm{eff}}(T)] = 0. \quad \text{(A1)}$$

The deviation of the magnetization $\mathbf{M}(T)$ with temperature from its initial orientation $\mathbf{M}(T_0)$ can be described by a two-component vector $\mathbf{m}(T)$, which satisfies the condition $\mathbf{m}(T_0) = 0$ and $m_z(T) = 0$ in the coordinate system xyz with $z \parallel \mathbf{M}(T_0)$. Therefore, we have $\mathbf{M}(T) = M_z(T)\mathbf{e}_z + \mathbf{m}(T)$, where $\mathbf{e}_z$ is a unit vector parallel to the z axis. In Eq. (A1), $\mathbf{H}_{\mathrm{eff}}$ is the effective magnetic field, which is the variational derivative of the energy of the magnet with respect to the magnetic moment. In the exchangeless magnetostatic approximation, by using a standard method [14], we obtain

$$\mathbf{H}_{\mathrm{eff}} = \mathbf{H}_e - 4\pi(\mathbf{Mn})\mathbf{n} - (\overleftrightarrow{N}^c + \overleftrightarrow{N}^u)\mathbf{M}. \quad \text{(A2)}$$

where the tensors $\overleftrightarrow{N}^c$ and $\overleftrightarrow{N}^u$ allow for crystallographic and uniaxial anisotropy. From Eq. (A1), it follows that

$$H_{\mathrm{eff},x}(T_0) = H_{\mathrm{eff},y}(T_0) = 0. \quad \text{(A3)}$$

By differentiating Eq. (A1) with respect to T and taking into account Eq. (A3), we obtain

$$H_{\mathrm{eff},z}(T_0)\frac{dm_x}{dT} = M_z(T_0)\frac{dH_{\mathrm{eff},x}}{dT},$$
$$H_{\mathrm{eff},z}(T_0)\frac{dm_y}{dT} = M_z(T_0)\frac{dH_{\mathrm{eff},y}}{dT}. \quad \text{(A4)}$$

Let the vector $\mathbf{M}(T_0)$ be directed along a symmetry axis of order three or higher. Therefore, we can use Eqs. (4) in calculating the projections of the vector $\mathbf{H}_{\mathrm{eff}}$ and their temperature derivatives from Eqs. (A2). In a static external field, $d\mathbf{H}_e/dT = 0$ and, hence, at $T = T_0$, we have

$$\frac{dH_{\mathrm{eff},x}}{dT} = -4\pi\left(n_x\frac{dm_x}{dT} + n_z\frac{dM_0}{dT}\right)n_x - (N_{xx}^u + N_{xx}^c)\frac{dm_x}{dT} - \frac{d(M_0N_{zz}^u)}{dT},$$
$$\frac{dH_{\mathrm{eff},y}}{dT} = -N_{yy}^c\frac{dm_y}{dT},$$
$$H_{\mathrm{eff},z} = H_{ez} - 4\pi M_0 n_z^2 - M_0(N_{zz}^u + N_{zz}^c).$$

Here, n_x and n_z are the projections of a normal to the film plane ($n_y = 0$). In deriving these expressions, it was taken into account that $N_{xy}^u = N_{yz}^u = N_{yy}^u = 0$ for normal uniaxial anisotropy and that $M_z(T) = M_0(T)$ for $\mathbf{m} = 0$. Substituting these expressions into Eqs. (A4) gives

$$[H_{ez} + 4\pi M_0(n_x^2 - n_z^2) + M_0(N_{xx}^u - N_{zz}^u + N_{xx}^c - N_{zz}^c)]\frac{dm_x}{dT} = -M_0\left[n_xn_z\frac{d(4\pi M_0)}{dT} + \frac{d(M_0N_{xz}^u)}{dT}\right],$$
$$\frac{dm_y}{dT} = 0. \quad \text{(A5)}$$

Using the relations

$$n_x = \cos\theta, \quad n_z = \sin\theta, \quad \frac{dm_x}{dT} = M_0\frac{d\theta}{dT},$$
$$M_0N_{xz}^u = -H_u(T)\sin\theta(T_0)\cos\theta(T_0),$$

we obtain, after simple algebra, the expression

$$\frac{d\theta}{dT} = -\frac{\sin\theta\cos\theta}{H_{ez} + 4\pi M_{\mathrm{eff}}\cos 2\theta + M_0N_t^c}\frac{d(4\pi M_{\mathrm{eff}})}{dT}, \quad \text{(A6)}$$

where, according to Eqs. (4), $N_t^c = N_{xx}^c - N_{zz}^c = N_{yy}^c - N_{zz}^c$.

From Eqs. (A3) and (A5), it follows that $H_{ey} = 0$ and that infinitely small deviations of the magnetization vector from its initial direction with temperature are rotations in the plane containing the vectors **n** and $\mathbf{H}_e$. We take these results into account in calculating the derivative dH_{ez}/dT. [It is obvious that the projection of $\mathbf{H}_e$ onto the vector $\mathbf{M}(T)$ is also characterized by the temperature dependence of $H_{ez}(T)$.] From the character of the deviations of the vector **M** with temperature, it follows that

$$\frac{dH_{ez}}{dT} = H_{ex}\frac{d\theta}{dT}.$$

Using Eqs. (A3) and (A2), we find H_{ex} and obtain the final expression

$$\frac{dH_{ez}}{dT} = 4\pi M_{\text{eff}} \sin\theta\cos\theta\frac{d\theta}{dT}. \qquad \text{(A7)}$$

We note that, in deriving Eqs. (A6) and (A7), no restrictions were imposed on the magnetocrystalline anisotropy field.

REFERENCES

1. B. Schneider, Phys. Status Solidi B **51** (1), 325 (1972).
2. S. N. Bajpai, I. Rattan, and N. C. Srivastava, J. Appl. Phys. **50** (4), 2887 (1979).
3. R. A. Lemons and B. A. Auld, J. Appl. Phys. **52** (12), 7360 (1981).
4. O. A. Chivileva, A. G. Gurevich, and L. M. Émiryan, Fiz. Tverd. Tela (Leningrad) **29** (1), 110 (1987) [Sov. Phys. Solid State **29**, 61 (1987)].
5. I. V. Zavislyak, V. M. Talalaevskiĭ, and L. V. Chevnyuk, Fiz. Tverd. Tela (Leningrad) **31** (5), 319 (1989) [Sov. Phys. Solid State **31**, 906 (1989)].
6. P. E. Zil'berman, V. M. Kulikov, V. V. Tikhonov, and I. V. Shein, Radiotekh. Élektron. (Moscow) **35** (5), 986 (1990).
7. A. S. Beregov and E. V. Kudinov, Élektron. Tekh., Ser. 1: Élektron. SVCh, No. 6(400), 8 (1987).
8. G. M. Dudko, G. T. Kazakov, A. G. Sukharev, *et al.*, Radiotekh. Élektron. (Moscow) **35** (5), 966 (1990).
9. Yu. K. Fetisov, Zh. Tekh. Fiz. **57** (12), 2393 (1987) [Sov. Phys. Tech. Phys. **32**, 1451 (1987)].
10. A. N. Slavin and Yu. K. Fetisov, Zh. Tekh. Fiz. **58** (11), 2210 (1988) [Sov. Phys. Tech. Phys. **33**, 1343 (1988)].
11. Yu. M. Yakovlev and S. Sh. Gendelev, *Ferrite Monocrystals in Radioelectronics* (Sovetskoe Radio, Moscow, 1975).
12. S. V. Belyakov and O. A. Gorodaĭkina, Élektron. Tekh., Ser. 1: Élektron. SVCh, No. 7(391), 28 (1986).
13. L. V. Lutsev and I. L. Berezin, Élektron. Tekh., Ser. 1: Élektron. SVCh, No. 6(420), 3 (1989).
14. A. G. Gurevich, *Magnetic Resonance in Ferrites and Antiferromagnets* (Nauka, Moscow, 1973).
15. L. D. Landau and E. M. Lifshitz, *Course of Theoretical Physics*, Vol. 8: *Electrodynamics of Continuous Media*, 2nd ed. (Nauka, Moscow, 1982; Pergamon, Oxford, 1984).
16. B. N. Gusev, O. A. Chivileva, A. G. Gurevich, *et al.*, Pis'ma Zh. Tekh. Fiz. **9** (2), 159 (1983) [Sov. Tech. Phys. Lett. **9**, 70 (1983)].
17. V. V. Shagaev, Fiz. Tverd. Tela (St. Petersburg) **40** (11), 2089 (1998) [Phys. Solid State **40**, 1892 (1998)].

Translated by Yu. Epifanov

Physics of the Solid State, Vol. 45, No. 12, 2003, pp. 2328–2333. Translated from Fizika Tverdogo Tela, Vol. 45, No. 12, 2003, pp. 2222–2226.

MAGNETISM AND FERROELECTRICITY

Size Effect in Nanocrystalline Manganites $La_{1-x}A_xMnO_3$ (A = Ag, Sr)

A. E. Teplykh*, S. G. Bogdanov*, É. Z. Valiev*, A. N. Pirogov*, Yu. A. Dorofeev*, A. A. Ostroushko, A. E. Udilov**, V. A. Kazantsev*, and A. E. Kar'kin***

**Institute of Metal Physics, Ural Division, Russian Academy of Sciences, ul. S. Kovalevskoĭ 18, Yekaterinburg, 620219 Russia*
e-mail: pirogov@uraltc.ru

***Institute of Physics and Applied Mathematics, Ural State University, Yekaterinburg, 620083 Russia*

Received February 25, 2003; in final form, May 20, 2003

Abstract—Nanocrystalline samples of the manganites $La_{0.9}Ag_{0.1}MnO_3$, $La_{0.7}Ag_{0.3}MnO_3$, and $La_{0.7}Sr_{0.3}MnO_3$ were synthesized through pyrolysis and isothermally annealed. The atomic, subatomic, and magnetic structures of these manganites were studied using magnetic, x-ray, and neutron diffraction measurements. Increasing the annealing temperature from 600 to 1200°C coarsens the grains from 30–40 to 600–700 nm in size. All the samples studied have rhombohedral structure and are ferromagnets. The Curie temperature decreases for the samples doped by silver and increases for the samples doped by strontium as the anneal temperature is increased. The magnetization of the Mn ions increases with nanoparticle size in all the three systems, which indicates the presence of a size effect. © *2003 MAIK "Nauka/Interperiodica".*

1. INTRODUCTION

The manganites $La_{1-x}A_xMnO_3$, which exhibit colossal magnetoresistance, have recently been attracting heightened interest (see, e.g., [1, 2]). Studies performed on ceramic and single-crystal samples revealed a number of remarkable properties of these manganites, such as the charge, orbital, and spin ordering; a metal–insulator transition; etc. A correlation has been found to exist between the parameters describing the crystal structure of the manganites and the parameters characterizing their magnetic properties. It was shown, in particular, that the Curie temperature T_C depends on the Mn–O–Mn bond angle $\Theta_{Mn-O-Mn}$.

The origin of the manganite magnetoresistance is assigned [3] to three carrier-scattering processes. One of them, the critical scattering from magnetization fluctuations, provides the major contribution to magnetoresistance at temperatures close to T_C. The other two processes, the inter- and intragrain scattering, are significant for $T < T_C$. Intergrain scattering involves domain walls, which coincide, as a rule, with grain boundaries. This scattering is absent in perfect single crystals [4] and is observed in microcrystalline samples already in a weak external magnetic field; this mechanism is most probably associated with interdomain carrier tunneling [5]. Intragrain scattering is observed at higher fields and is due to the ordering of magnetic moments, which form a spin-glass-type state in the absence of a field. This effect originates apparently from the grain crystalline (and magnetic) structure being heavily defected.

Therefore, in order to elucidate the mechanism responsible for the colossal magnetoresistance in the manganites, it appears reasonable to study nanocrystalline samples in which the particle size is comparable to the domain dimensions. Nanocrystalline manganites are also of interest from the application viewpoint, because they feature higher values of the low-field magnetoresistance compared to those for ceramic samples [6] and, hence, can be used in magnetic sensors.

The available scarce publications on nanocrystalline manganites show that the properties of these compounds can change substantially with decreasing particle size. For instance, samples of $La_{2/3}Sr_{1/3}MnO_3$ with particles L = 30 nm in size and smaller do not exhibit metallic conduction [6], unlike the corresponding ceramic samples. According to [7], spontaneous magnetization σ of $La_{0.85}Sr_{0.15}MnO_3$ increases approximately twofold as L decreases from 1000 to 20 nm. By contrast, a decrease in σ by about two times was observed to occur in the manganites $La_{1-x}A_xMnO_3$ (A = Ca, Sr; $x \approx 0.3$) [7, 8]. The conclusion was drawn in [7] that the growth of σ and T_C in nanocrystalline $La_{0.85}Sr_{0.15}MnO_3$ and the decrease in these quantities in $La_{0.65}Sr_{0.35}MnO_3$ are related to the change in the bond angle $\Theta_{Mn-O-Mn}$. The values of this angle were calculated for samples annealed at various temperatures with inclusion of only the variation in the lattice parameters with the anneal temperature. Possible variation of the coordinates of the oxygen atoms was neglected, because no neutron diffraction measurements were conducted in [7]. Another opinion on the reasons for the variation in σ was put forward in [8], where it was suggested that the decrease in σ in $La_{0.67}Ca_{0.33}MnO_3$ could be associated with the increase in the fractional volume

of the amorphous phase existing in nanocrystalline samples at low anneal temperatures.

This study was aimed at establishing the relation connecting the magnetic moment and the Mn–O–Mn bond angle with the size of nanoparticles in the manganites $La_{1-x}Ag_xMnO_3$ (x = 0.1, 0.3) and $La_{0.7}Sr_{0.3}MnO_3$ with the use of neutron diffraction data. Note that we are not aware of any neutron diffraction studies on the magnetic state of nanocrystalline manganites.

2. SAMPLES AND EXPERIMENTAL TECHNIQUES

The starting nanocrystalline manganites $La_{1-x}Ag_xMnO_3$ with x = 0.1 and 0.3 and $La_{0.7}Sr_{0.3}MnO_3$ were prepared through pyrolysis. The weighted lanthanum and silver nitrates (and of strontium in the case of $La_{0.7}Sr_{0.3}MnO_3$) were dissolved under heating in a 10 wt % solution of polyvinyl alcohol, and the required amount of a manganese nitrate solution was added. The solution thus obtained was vaporized, and the solid residue left was calcined to complete the synthesis and subsequent sintering. All samples were prepared from the same solution. To vary the particle size, annealing was carried out for 4 h at temperatures T_a ranging from 600 to 1200°C for samples doped by silver and from 700 to 1300°C for samples doped by strontium. To reach a constant value of the oxygen off-stoichiometry in different samples, the samples were subjected to a normalizing anneal at 700°C.

Structural characterization was performed on a DRON-UM-1 diffractometer with CuK_α radiation (filtered by a pyrographite crystal) in the diffracted beam at 293 K. The magnetization of the $La_{0.9}Ag_{0.1}MnO_3$ samples was measured with an MPMSR5-XL SQUID magnetometer (Quantum Design). The Curie temperatures of $La_{0.7}Ag_{0.3}MnO_3$ and $La_{0.7}Sr_{0.3}MnO_3$ were derived from data on the ac susceptibility in a field of 10 Oe and at a frequency of 1 kHz.

The neutron diffraction measurements were conducted on D-2 and D-3 diffractometers operating at neutron wavelengths λ = 0.180 and 0.243 nm, respectively. X-ray and neutron diffraction patterns were calculated with the Fullprof code [9].

The particle size was derived from neutron small-angle scattering scans ($\lambda \approx 0.45$ nm) obtained with a D-6 diffractometer. Plexiglas was used to reduce the measured intensities on cross sections. The D-2, D-3, and D-6 diffractometers were installed in horizontal channels of an IVV-2M reactor.

3. EXPERIMENTAL RESULTS

3.1. Crystal Structure at 293 K

The x-ray diffraction patterns of nanocrystalline samples of $La_{0.9}Ag_{0.1}MnO_3$, $La_{0.7}Ag_{0.3}MnO_3$, and $La_{0.7}Sr_{0.3}MnO_3$ obtained at 293 K were found to be similar. An analysis of the patterns revealed all the manganites studied by us to have rhombohedral structure (space group $R\bar{3}c$). The diffractograms of the silver-doped samples showed, in addition to the reflections of the main phase, weak reflections due to metallic silver. Unfortunately, we did not succeed in determining the silver content in the manganites. Qualitative estimates suggest that the main phase in $La_{0.7}Ag_{0.3}MnO_3$ contains more silver than that in $La_{0.9}Ag_{0.1}MnO_3$.

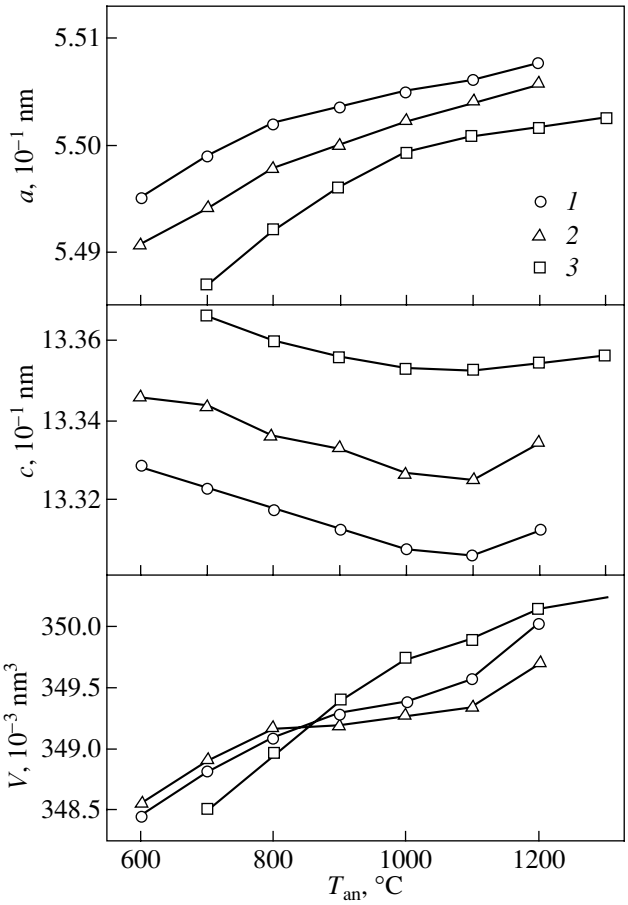

Fig. 1. The lattice parameters and unit cell volume of the manganites (*1*) $La_{0.9}Ag_{0.1}MnO_3$, (*2*) $La_{0.7}Ag_{0.3}MnO_3$, and (*3*) $La_{0.7}Sr_{0.3}MnO_3$ plotted vs. annealing temperature.

Figure 1 displays the dependence of the unit cell parameters a and c (based on the hexagonal notation for the $R\bar{3}c$ group) on annealing temperature for three groups of samples. An increase in the temperature T_a is seen to cause an expansion of the lattice in the basal plane and its contraction along the hexagonal axis in all samples. These lattice changes are approximately of the same relative magnitude, $\Delta a/a \approx \Delta c/c \approx 0.2\%$. On the whole, this brings about a certain increase in the unit cell volume ($\Delta V/V \approx 0.5\%$) with increasing T_a. Figure 1

Characteristics of nanoparticles of manganites $La_{0.9}Ag_{0.1}MnO_3$, $La_{0.7}Ag_{0.3}MnO_3$, and $La_{0.7}Sr_{0.3}MnO_3$ derived from small-angle neutron-scattering data

T, °C	$La_{0.9}Ag_{0.1}MnO_3$			$La_{0.7}Ag_{0.3}MnO_3$			$La_{0.7}Sr_{0.3}MnO_3$		
	D_S	*L*, nm	*c**	D_S	*L*, nm	*c**	D_S	*L*, nm	*c**
600	2	36	0.16	2.5	36	0.16	–	–	–
700	2	36	0.16	2.3	33	0.19	2.1	30	0.22
800	2.1	60	0.15	2.1	36	0.12	2.1	50	0.14
900	2.1	60	0.09	2.1	60	0.12	2.1	60	0.10
1000	2.2	400	0.14	2.3	400	0.15	2.1	140	0.11
1100	2.2	400	0.14	2.4	400	0.11	2.1	180	0.18
1200	2	600	0.17	2.4	700	0.14	2	200	0.16
1300	–	–	–	–	–	–	2	300	0.12

Note: D_S is the fractal dimensionality of the surface, *L* is the particle size, and *c** is the fractional volume of particles of the solid phase.

also shows that doping with silver somewhat decreases the parameter *a* and increases the parameter *c*.

3.2. Small-Angle Neutron Scattering

Small-angle neutron-scattering scans were made to determine the size of the particles in the nanocrystalline samples under study. While the scattering curves obtained featured the same pattern of the intensity vs. scattering-angle dependence, they nevertheless differed slightly in the cross-section magnitude and the shape and slope of the curves, which was caused by differences in the dimensions and concentration of the particles and in the properties of their surface. For $q > 0.5\ \text{nm}^{-1}$, the experimental points can be fitted to the $d\Sigma/d\Omega \sim q^{-n}$ law, where $d\Sigma/d\Omega$ is the scattering cross section from a unit sample volume, $q = 4\pi\sin\theta/\lambda$, and θ is the scattering angle. Knowing the exponent *n*, one can determine the nanoparticle surface dimensionality D_S, because $D_S = 6 - n$. The values of D_S obtained are listed in the table. The fact that D_S is other than 2 indicates the fractal nature of the rough surface of the particles. As seen from the table, the $La_{0.7}Ag_{0.3}MnO_3$ samples have a clearly pronounced fractal surface. To describe the experimental $d\Sigma/d\Omega = f(q)$ curves, we used the Debye–Porod relation [10]

$$\frac{d\Sigma}{d\Omega} = \frac{8\pi\rho^2 c^* r^3}{(1 + A(qr)^2)^{\frac{6-D_S}{2}}}, \quad (1)$$

where *A* is an interpolation coefficient defined as

$$A^{\frac{6-D_S}{2}} = \frac{2}{\Gamma(5-D_S)\sin\left(\frac{\pi}{2}(D_S-1)\right)}, \quad (2)$$

ρ is the neutron-scattering amplitude density, *r* is the correlation length, *c** is the volume fraction of scattering particles, and $\Gamma(x)$ is the gamma function.

By fitting the curves calculated using Eqs. (1) and (2) to the experimental $d\Sigma/d\Omega = f(q)$ curves, we found the particle dimensions $L = 2r$ and the fractional volume of scattering particles (see table). We readily see that the particle size changes relatively weakly with an increase in T_a from 600 to 900°C and grows sharply as T_a is increased from 900 to 1000°C.

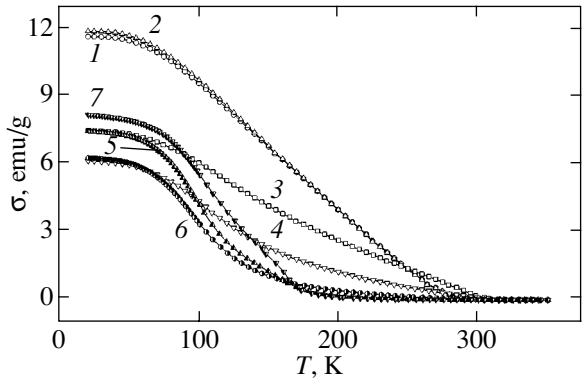

Fig. 2. Temperature behavior of the magnetization of $La_{0.9}Ag_{0.1}MnO_3$ samples measured in a field of 100 Oe. T_a: (*1*) 600, (*2*) 700, (*3*) 800, (*4*) 900, (*5*) 1000, (*6*) 1100, and (*7*) 1200°C.

3.3. Magnetic Measurements

Figure 2 shows the temperature behavior of the magnetization of $La_{0.9}Ag_{0.1}MnO_3$ samples measured in an external field of 100 Oe. We clearly see that, for the samples annealed at $T_a \le 900$°C, the magnetization vanishes at higher temperatures than for the samples annealed at $T_a \ge 1000$°C. By identifying the inflection point on the $\sigma(T)$ curve with T_C, we obtain $T_C \approx 130$ K in the former case and $T_C \approx 90$ K in the latter. The Curie temperatures of all samples studied by us are presented in Fig. 3. We readily see that, in contrast to the behavior

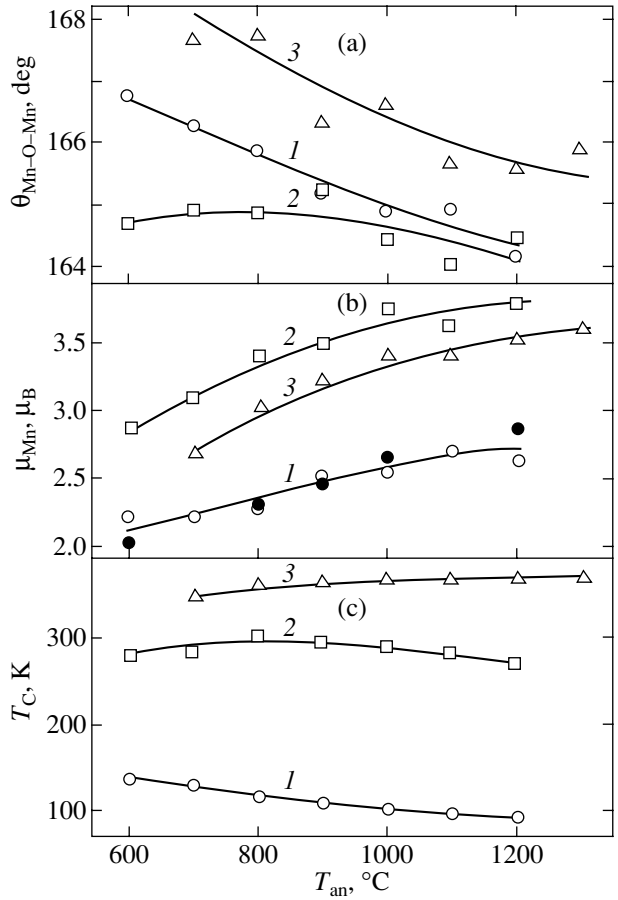

Fig. 3. (a) Mn–O–Mn bond angle, (b) average magnetic moment of the Mn ion, and (c) Curie temperature for the manganites (*1*) $La_{0.9}Ag_{0.1}MnO_3$ (open circles are the neutron diffraction data, filled circles represent magnetic measurements), (*2*) $La_{0.7}Ag_{0.3}MnO_3$, and (*3*) $La_{0.7}Sr_{0.3}MnO_3$ plotted vs. annealing temperature.

of T_C in $La_{0.9}Ag_{0.1}MnO_3$, the value of T_C of the strontium-doped sample increases with T_a.

Figure 3 also displays the dependence of the spontaneous magnetic moment per Mn ion (μ_{Mn}) in $La_{0.9}Ag_{0.1}MnO_3$ on the annealing temperature. The magnetic moment μ_{Mn} is seen to grow monotonically as T_a increased.

3.4. Magnetic Ground State

As an illustration, Fig. 4 presents neutron diffraction patterns (measured at 4.2 K) of $La_{0.9}Ag_{0.1}MnO_3$ samples annealed at T_a = 600 and 1200°C. The difference in the reflection intensities is connected primarily with the difference in the volume density of the samples (which is about fivefold). All the nanocrystalline manganites studied by us have rhombohedral structure at 4.2 K. The magnetic unit cell coincides in size with the crystal cell, which indicates that the wave vector of the magnetic structure is **k** = 0. The magnetic moments of the

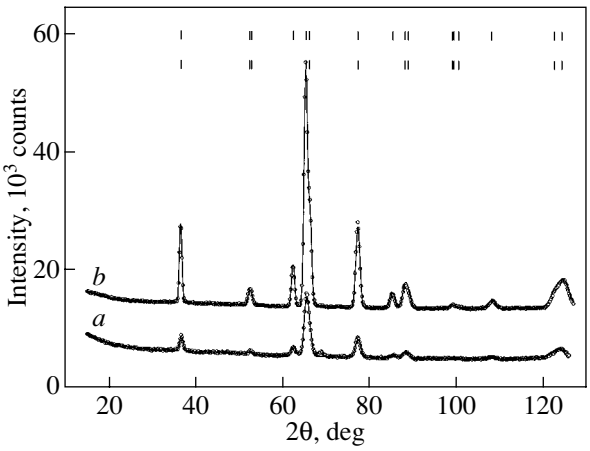

Fig. 4. Neutron diffraction patterns measured at 4.2 K (symbols) and calculated (lines) for $La_{0.9}Ag_{0.1}MnO_3$ samples annealed at (a) 600 and (b) 1200°C. Bars indicate the angular positions of the reflections.

Mn ions (μ_{Mn}) are ferromagnetically coupled and oriented parallel to the *a*–*b* plane. The dependence of the moment μ_{Mn} on the annealing temperature is shown graphically in Fig. 3. We readily see that μ_{Mn}, as well as σ, grows monotonically as T_a increased. The moment μ_{Mn} is also seen to increase with T_a in the other two groups of samples, $La_{0.9}Ag_{0.3}MnO_3$ and $La_{0.9}Sr_{0.3}MnO_3$.

4. DISCUSSION OF THE RESULTS

The nanocrystalline samples studied by us were prepared through pyrolysis, whereas those discussed in [7] were prepared using the sol-gel techniques. Nevertheless, the dependence of the size of $La_{0.7}Sr_{0.3}MnO_3$ nanoparticles on the annealing temperature presented here is in good agreement with the relation established in [7] for $La_{0.65}Sr_{0.35}MnO_3$. This suggests that the coarsening of particles in the manganites $La_{1-x}Sr_xMnO_3$ with $x \approx 0.3$ depends only weakly on the actual method used to prepare nanoparticles. On the other hand, as seen from the table, an increase in the annealing temperature of silver-doped nanocrystalline samples brings about a considerably more intense (for T_a > 900°C) growth in the size of particles than in the case of Sr-doped samples. This suggests that the coarsening of nanoparticles depends on the dopant. It is quite possible that the dopant affects the formation of the nanoparticle surface as well, because the dimensionalities D_S in $La_{0.7}Ag_{0.3}MnO_3$ and $La_{0.7}Sr_{0.3}MnO_3$ differ considerably.

As already mentioned, our $La_{0.7}Sr_{0.3}MnO_3$ samples annealed at T_a = 700–1300°C contain only one (rhombohedral) phase. In this T_a interval, the $La_{0.65}Sr_{0.35}MnO_3$ samples studied in [7] underwent a structural transition from the orthorhombic phase to

coexisting orthorhombic and rhombohedral phases. The difference in the structural states of the samples studied in [7] may result from the oxygen off-stoichiometry Z (notation taken from [7]). The estimates of Z derived from the neutron diffraction patterns show that in our samples Z is slightly in excess of three ($Z \approx 3.06(7)$), whereas the samples studied in [7] were oxygen-deficient ($Z \approx 2.99$).

The increase in the unit cell volume with T_a observed by us (Fig. 1) correlates with the idea that the lattice unit cell of nanoparticles expands as their size increases.

As seen from Fig. 3, T_C of silver-doped samples increases with the dopant concentration. This behavior of T_C is observed in ceramic samples doped, for instance, by calcium or strontium and is accounted for by the increased number of ferromagnetically coupled Mn^{4+}–Mn^{3+} pairs. This is apparently also valid in our case. The fact that T_C of strontium-doped samples is higher than that of silver-containing manganites can be attributed to the presence of a larger number of Mn^{4+}–Mn^{3+} pairs in the former.

The average magnetic moment of Mn ions in the three groups of nanocrystalline samples (Fig. 3) and, hence, the magnetization increase with annealing temperature, i.e., with increasing nanoparticle size. This behavior of the magnetization was observed earlier in $La_{0.65}Sr_{0.35}MnO_3$ [7] and $La_{0.67}Ca_{0.33}MnO_3$ [8]. Magnetization was found to increase with coarsening of the nanoparticles, for instance, in studies of the oxide systems $NiFe_2O_4$ [11] and $CoFe_2O_4$ [12], where this effect was assigned to the spin arrangement on the surface of the particles being noncollinear. The magnitude of σ was observed to decrease with increasing nanoparticle size in $La_{0.85}Sr_{0.15}MnO_3$ [7].

Following the double-exchange model, the behavior of the spontaneous magnetization (and of T_C) in nanocrystalline samples was assumed in [7] to originate from the Mn–O–Mn bond angle being dependent on T_a. In the double-exchange model [12], the magnitude of ferromagnetic coupling increases with the overlap of the e and p_σ orbitals of the Mn and O ions, respectively:

$$W \approx \nu^2 \cos\phi \cos(\theta_{ij}/2), \qquad (3)$$

where ν is the covalency parameter, $(2\pi - \phi) = \theta_{Mn–O–Mn}$, and θ_{ij} is the angle between the spins of the nearest neighbor Mn ions. Because in [7] the coordinates of the O ions were not refined, the variation in the $\theta_{Mn–O–Mn}$ angle was caused by the variation in the interatomic distances with increasing T_a. If the Mn–O–Mn bond angle increases with T_a, one might also expect the T_C to increase, as is the case in $La_{0.65}Sr_{0.35}MnO_3$. By contrast, a decrease in this angle with an increase in T_a should bring about a decrease in T_C, which is exactly what occurs in $La_{0.85}Sr_{0.15}MnO_3$.

We attempted to interpret the $\mu_{Mn}(T_a)$ and $T_C(T_a)$ relations obtained for the nanocrystalline $La_{0.9}Ag_{0.1}MnO_3$, manganites $La_{0.7}Ag_{0.3}MnO_3$, and $La_{0.7}Sr_{0.3}MnO_3$ along these lines. Figure 3 displays the annealing-temperature dependence of the angle $\theta_{Mn–O–Mn}$ derived for these three groups of samples from x-ray and neutron diffraction data. The silver-doped manganites are seen to exhibit a correlation between T_C and the angle $\theta_{Mn–O–Mn}$; indeed, as T_a is increased, both quantities decrease in $La_{0.9}Ag_{0.1}MnO_3$ and show a small maximum in $La_{0.7}Ag_{0.3}MnO_3$. On the other hand, an increase in T_a in $La_{0.7}Sr_{0.3}MnO_3$ samples is accompanied by an increase in T_C, although the angle $\theta_{Mn–O–Mn}$ decreases. It cannot be ruled out that in the latter system the decrease in T_C through the decrease in the $\theta_{Mn–O–Mn}$ angle is offset by the increase in T_C because of the angle θ_{ij} decreasing as the annealing temperature is increased. This suggestion appears only natural in connection, for instance, with the conclusion [13] that the spins on the surface of nanoparticles are noncollinear. Because the number of nearest neighbors of Mn ions on the nanoparticle surface is less than that inside the particles, the average angle θ_{ij} for the magnetic moments of ions on the surface should be larger than that for ions inside the particles. As T_a increases (and, hence, the nanoparticle size grows), the contribution due to the internal magnetic moments grows faster than that from the surface moments; this should be accompanied by a decrease in the average value of θ_{ij}. The decrease in θ_{ij} should give rise to an increase in the magnetization of the Mn ions, an effect that, as seen from Fig. 3, does indeed occur in the three groups of samples studied by us. This gives us grounds to suggest that the increase in magnetization is connected with nanoparticle coarsening, which implies the observation of a size effect.

The magnetization and, hence, μ_{Mn} in $La_{0.7}Sr_{0.3}MnO_3$ annealed at high T_a are close to those observed in ceramic samples [2]. The lower values of μ_{Mn} in the $La_{0.7}Sr_{0.3}MnO_3$ system as compared to those in $La_{0.7}Ag_{0.3}MnO_3$ may be assigned to the higher content of Mn^{4+} ions in the samples of the former system. An increase in the Mn^{4+} concentration increases both the number of ferromagnetic (Mn^{3+}–Mn^{4+}) and antiferromagnetic (Mn^{4+}–Mn^{4+}) pairs. Therefore, starting from a certain concentration of Mn^{4+} ions, the effect of the antiferromagnetic Mn^{4+}–Mn^{4+} pairs will dominate and this will give rise to a decrease in magnetization.

5. CONCLUSIONS

Thus, the nanocrystalline manganites $La_{0.9}Ag_{0.1}MnO_3$, $La_{0.7}Ag_{0.3}MnO_3$, and $La_{0.7}Sr_{0.3}MnO_3$ studied here crystallize in a rhombohedral structure and have a collinear ferromagnetic structure with wave vector $\mathbf{k} = 0$ at 4.2 K. The average magnetic moment of the manganese ion increases with nanoparticle size, which

is possibly associated with the noncollinearity of the Mn ion spins at the particle surface.

ACKNOWLEDGMENTS

This study was supported by the Russian Foundation for Basic Research (project no. 00-02-16211) the Administration of the Sverdlovsk oblast (project no. Ural-01-02-96412), and the program "Neutron Studies of Condensed Media" (project no. 40.012.1.1.11.50).

REFERENCES

1. Yu. A. Izyumov and Yu. N. Skryabin, Usp. Fiz. Nauk **171** (2), 121 (2001) [Phys. Usp. **44**, 109 (2001)].
2. J. M. D. Coey, M. Viret, and S. Von Monlar, Adv. Phys. **48** (2), 167 (1999).
3. A. E. Kar'kin, D. A. Shulyatev, A. A. Arsenov, *et al.*, Zh. Éksp. Teor. Fiz. **116** (2), 671 (1999) [JETP **89**, 358 (1999)].
4. H. Y. Hwang, S.-W. Cheong, N. P. Ong, and B. Batlog, Phys. Rev. Lett. **77**, 2041 (1996).
5. M. Auslender, A. E. Kar'kin, E. Rozenberg, and G. Gorodetsky, J. Alloys Compd. **314**, 163 (2000).
6. M. B. Salamon and M. Jaime, Rev. Mod. Phys. **73**, 583 (2001).
7. N. Zhang, W. Yang, W. Ding, *et al.*, Solid State Commun. **109**, 537 (1999).
8. R. D. Sanchez, J. Rivas, C. Vazquez-Vazquez, *et al.*, Appl. Phys. Lett. **68** (1), 134 (1996).
9. J. Rodriguez-Carvayal, Physica B (Amsterdam) **192**, 55 (1993).
10. P. Debye, H. R. Andreson, and H. Brumberger, J. Appl. Phys. **28**, 679 (1957).
11. R. N. Panda, J. C. Shin, and T. S. Chin, J. Magn. Magn. Mater. **257**, 79 (2003).
12. J. Topfer and J. B. Godenough, J. Solid State Chem. **130**, 117 (1997).
13. S. Prasad and N. S. Gajbhiye, J. Alloys Compd. **265**, 87 (1998).

Translated by G. Skrebtsov

Physics of the Solid State, Vol. 45, No. 12, 2003, pp. 2334–2337. Translated from Fizika Tverdogo Tela, Vol. 45, No. 12, 2003, pp. 2227–2229.

MAGNETISM AND FERROELECTRICITY

A Manifestation of Magnetism of Bismuth in Iron Garnet Films

V. F. Shkar'*, V. P. Denisenkov, A. M. Grishin**, A. A. Yalali**, S. I. Khartsev**, E. I. Nikolaev*, and V. N. Sayapin***

** Donetsk Physicotechnical Institute, National Academy of Sciences of Ukraine, Donetsk, 83114 Ukraine*
e-mail: Shkar@donapex.net.ua

*** Department of Condensed Matter Physics, Royal Institute of Technology, S-10044 Stockholm, Sweden*

Received January 16, 2003; in final form, May 23, 2003

Abstract—Bismuth iron garnet films prepared through electron-beam and laser-induced evaporation on (001)-oriented substrates of scandium gallium gadolinium garnet are investigated using ferromagnetic resonance. It is assumed that the additional minima observed in the angular dependence of the resonance field can be associated with the magnetic moment of bismuth ions. © *2003 MAIK "Nauka/Interperiodica".*

1. INTRODUCTION

The considerable interest expressed by researchers in iron garnet films containing bismuth stems from the fact that these films are characterized by an appreciable Faraday effect, which makes it possible to use them in magneto-optic devices [1]. It has been assumed that, since bismuth ions, like yttrium ions, are diamagnetic, they should not deteriorate the magnetic and dynamic characteristics of yttrium iron garnet after the substitution of bismuth for yttrium. Consequently, completely substituted bismuth iron garnet, like yttrium iron garnet, at room temperature should have the saturation magnetization $4\pi M$ = 1760 G and the ferromagnetic resonance linewidth $\Delta H \approx 0.5$ Oe. Since these films exhibit a Faraday effect, they can be widely used in spin-wave magneto-optical electronics.

However, in actual practice, bismuth iron garnets possess somewhat worse magnetic and essentially worse dynamic characteristics. For bismuth iron garnet films at room temperature, the saturation magnetization falls in the range 1500–1650 G and the ferromagnetic resonance linewidth is approximately equal to 25–30 Oe, depending on the technique of film preparation employed [2, 3]. Therefore, in the structure of bismuth iron garnets, the bismuth ions are likely not diamagnetic (magnetic ions located at dodecahedral interstitial sites bring about a broadening of the resonance line [4]).

One of the initial materials used in synthesizing bismuth iron garnet is bismuth oxide. This compound was traditionally considered to be diamagnetic. However, results obtained by a number of authors have demonstrated that the magnetic and electrical properties of bismuth oxide are considerably more complex. In particular, ^{209}Bi NQR studies of powder and single-crystal samples of the α modification of bismuth oxide revealed a splitting of all resonance lines in the absence of an external magnetic field [5–7]. This experimental fact was interpreted as a manifestation of local magnetic fields of the order of 150–200 G in the α modification of bismuth oxide [5, 7, 8].

Volkozub *et al.* [9] and Kharkovskii *et al.* [10] investigated the temperature and field dependences of the magnetization of the α modification of bismuth oxide on an SQUID magnetometer and revealed three magnetic subsystems, namely, ordered, paramagnetic, and diamagnetic subsystems. The effective magnetic moment estimated from the temperature dependences of the magnetization was approximately equal to 0.1 μ_B/at.

It was also established that, at low temperatures, this compound exhibits a linear magnetoelectric effect: the electric polarization of a single-crystal sample was induced by an external magnetic field. It was assumed that there is a close relationship between the electrical and magnetic properties; however, the mechanism of this mutual influence is as yet unknown. These unusual properties of bismuth oxide persist up to room temperature. It was inferred that the nature of these properties is more complex than that of magnetism of rare-earth and transition metal compounds, because bismuth atoms do not contain inner unfilled *d*- or *f*-electron shells [11].

In order to answer the question as to whether these unusual magnetic properties of bismuth are retained in bismuth iron garnets, we investigated the temperature and angular dependences of the ferromagnetic resonance spectra of bismuth iron garnet films prepared through magnetron deposition and laser-induced evaporation. The present paper reports on the results of these investigations.

1063-7834/03/4512-2334$24.00

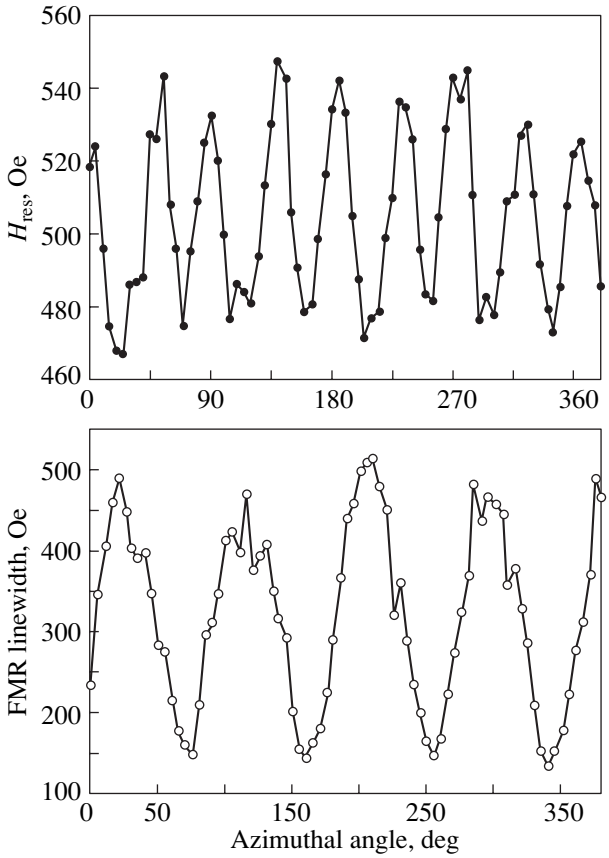

Fig. 1. Angular dependences of the resonance field and the ferromagnetic resonance linewidth in the film plane at room temperature for sample **1**.

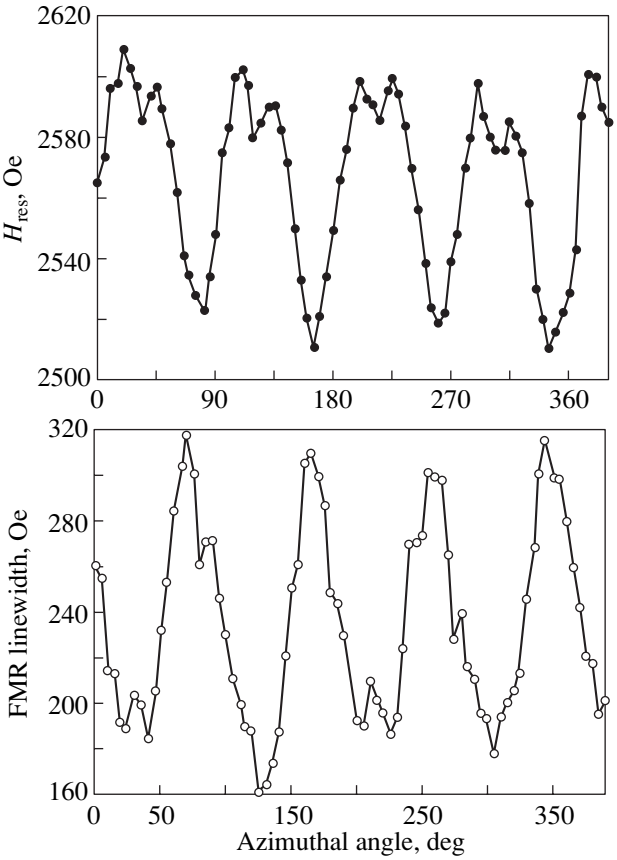

Fig. 2. Angular dependences of the resonance field and the ferromagnetic resonance linewidth in the film plane at room temperature for sample **2**.

2. SAMPLES AND THE FERROMAGNETIC RESONANCE RADIOSPECTROMETER

Samples of bismuth iron garnet were obtained by evaporation on (001)-oriented substrates of scandium gallium gadolinium garnet. Sample **1** was prepared through electron-beam evaporation and had a thickness of 630 nm ($4\pi M$ = 1500 G, ΔH = 35 Oe). Sample **2** was obtained by pulsed laser-induced evaporation and had a thickness of approximately 1 μm ($4\pi M$ = 630 Oe, ΔH = 25 Oe). The technique for preparing these films was described in detail in [2, 3]. The characteristics of the samples were determined by standard methods [1].

The ferromagnetic resonance radiospectrometer made it possible to investigate the magnetic resonances in two mutually perpendicular planes, i.e., provided measurements with respect to both the polar and azimuthal angles. The temperature dependences of the ferromagnetic resonance was examined using an insert with a microstrip structure in the form of a meander. The sample was located on a rotating device and was tightly pressed to the microstrip. The insert was placed in a cryostat with provision for varying the sample temperature. The magnetic part of the nuclear magnetic resonance spectrometer (Bruker) was used as an external-magnetic-field source. The experimental setup was computer controlled, which made it possible to determine the resonance fields and widths of the ferromagnetic resonance lines in automatic mode.

A rectangular waveguide was also used as a measuring cell at room temperature. In this case, the sample was placed in the homogeneous region of the microwave magnetic field of the waveguide. This made it possible to compare the ferromagnetic resonance spectra recorded for different measuring cells (the meander and the waveguide), which is important for analyzing these spectra. The results of the experiment demonstrated that the ferromagnetic resonance spectra were of identical shape in both cases.

3. RESULTS AND DISCUSSION

The ferromagnetic resonance was investigated using bismuth iron garnet films prepared through electron-beam (sample **1**) and laser-induced (sample **2**) evaporation on (001)-oriented substrates of scandium gallium gadolinium garnet.

Figures 1 and 2 depict the angular dependences of the resonance field and the ferromagnetic resonance

linewidth in the film plane at room temperature for samples **1** and **2**, respectively.

As can be seen from these figures, the anisotropy of the ferromagnetic resonance linewidth differs from the anisotropy of the resonance field in that the resonance field exhibits additional minima along the hard magnetic axes. These minima are also observed at a temperature of 77 K. The theoretical calculations demonstrated that these minima are not related to the cubic magnetocrystalline anisotropy.

Ferromagnetic resonance in iron garnets has been studied thoroughly and is one of the reliable methods for determining the magnetic and dynamic characteristics of iron garnet films [1, 4].

When analyzing the mechanisms of relaxation observed in both pure yttrium iron garnet and yttrium iron garnet with rare-earth impurities, proper allowance must be made for the fact that the magnetocrystalline anisotropy entails the anisotropy of the ferromagnetic resonance linewidth, for which the minimum linewidths correspond to the hard magnetic axes [4].

The studied samples in the (001) plane, which is the plane of the film, are characterized by the ⟨001⟩ and ⟨011⟩ crystallographic axes; consequently, the cubic crystalline anisotropy should manifest itself in the anisotropy of both the resonance field and the ferromagnetic resonance linewidth [4].

Let us now assume that bismuth ions are nonmagnetic and that, by analogy with yttrium iron garnets, the anisotropy in bismuth iron garnets is governed only by the magnetic iron ions. Under these conditions, the resonance field should exhibit minima in the case when the external magnetic field is oriented along the ⟨011⟩ axes and maxima when the field is oriented along the ⟨001⟩ axes [4], because, at room temperature, the cubic anisotropy for yttrium iron garnets is determined only by the first constant and has negative sign. However, as can be seen from Figs. 1 and 2, the above correlation between the linewidth and the resonance field is not observed for the yttrium iron garnet films under investigation: the anisotropy of the linewidth for bismuth iron garnets is similar to that for yttrium iron garnets, whereas the resonance field has additional minima along the hard magnetic axes. For sample **1**, the additional minima are comparable to the main minima. Consequently, the bismuth iron garnet films should possess a source of additional magnetic anisotropy that manifests itself in the case of anisotropy of the resonance field and is absent for anisotropy of the linewidth, which is not specific to even magnetic rare-earth iron garnets at room temperature. At low temperatures, the rare-earth subsystem is magnetically ordered and the ions with strong spin–orbit coupling in yttrium iron garnets with impurities affect the ferromagnetic resonance. For some ions, this effect manifests itself in the form of additional maxima in the angular dependences of the resonance field and the linewidth [4, 12–14].

Therefore, it can be assumed that, as in the α modification of bismuth oxide, the bismuth ions in iron garnets can occur in a paramagnetic state. Consequently, the ferrimagnetic ensemble of the iron sublattice magnetizes the bismuth sublattice in a direction antiparallel to its own net magnetization (as is the case with the rare-earth sublattice at low temperatures [15]). This accounts for the underestimated value of the saturation magnetization of bismuth iron garnets (as compared to that of yttrium iron garnets), which is observed in the experiment. As was shown in [9, 10], the effective magnetic moment is equal to 0.1 μ_B/at. Bi and the net magnetization of the iron sublattice is 5.9 μ_B [16], which, at room temperature, corresponds to 1760 G for yttrium iron garnets. In this case, the saturation magnetization for bismuth iron garnets should be equal to 5.6 μ_B (three bismuth ions per formula unit), which corresponds to 1670 G. In [5, 7, 8], the local magnetic fields of bismuth were found to be of the order of 150–200 G, which corresponds to 1160–1310 G for bismuth iron garnets.

It is obvious that, since the environment of bismuth in the garnet structure differs from the environment typical of the monoclinic structure of the α modification of bismuth oxide, the above calculations are approximate. However, they determine the range of possible values of the magnetization of bismuth iron garnets. The existence of such a range is quite possible, especially when it is taken into account that, as in bismuth oxide [9, 10], bismuth in iron garnets can form several magnetic subsystems.

As a consequence, one possible ordering (as in sample **1**) should lead to a saturation magnetization of 1500 G and additional minima with a depth of the order of 70 Oe, whereas another ordering (as in sample **2**) should result in a saturation magnetization of 1650 G and minima with a depth of 10–20 Oe.

It was established earlier that, in substituted yttrium iron garnet films prepared through liquid-phase epitaxy on (111)-oriented substrates of gallium gadolinium garnet, bismuth gives rise to uniaxial magnetic anisotropy along the [111] axis normal to the film plane [1]. It seems likely that the uniaxial anisotropy in these films has the same origin as the additional minima of the resonance field in bismuth iron garnet films.

4. CONCLUSIONS

Thus, we made the assumption that, as in the α-modification of bismuth oxide, bismuth ions in iron garnets exhibit magnetic properties.

ACKNOWLEDGMENTS

We would like to thank Nabuyasu Adachi for supplying the samples used in our experiments.

This work was supported in part by the Scientific and Technical Center of Ukraine, project no. 1583.

REFERENCES

1. *Bubble-Based Elements and Devices: A Reference Book*, Ed. by N. N. Evtikhiev and B. N. Naumov (Radio i Svyaz', Moscow, 1987).
2. N. Okuda, T. Katayama, H. Kobayashi, and N. Kobayashi, J. Appl. Phys. **67** (9), 4944 (1990).
3. N. Adachi, V. P. Denysenkov, S. I. Khartsev, *et al.*, J. Appl. Phys. **88** (5), 2734 (2000).
4. A. G. Gurevich and G. A. Melkov, *Magnetic Oscillations and Waves* (Nauka, Moscow, 1994).
5. A. A. Boguslavskiĭ and G. K. Semin, Zh. Fiz. Khim. **53** (1), 33 (1979).
6. G. K. Semin, A. V. Prygin, and A. A. Boguslavskiĭ, Izv. Akad. Nauk SSSR, Ser. Fiz. **49** (7), 1412 (1985).
7. E. A. Kravchenko and V. G. Orlov, Z. Naturforsch. A **49** (2), 418 (1994).
8. N. E. Ainbinder, G. A. Volgina, E. A. Kravchenko, *et al.*, Z. Naturforsch. A **49** (2), 425 (1994).
9. A. V. Volkozub, O. V. Snigirev, V. G. Orlov, *et al.*, Fiz. Tverd. Tela (Leningrad) **33** (8), 2506 (1991) [Sov. Phys. Solid State **33**, 1415 (1991)].
10. A. I. Kharkovskii, V. I. Nizhankovskii, E. A. Kravchenko, and V. G. Orlov, Z. Naturforsch. A **51** (3–4), 665 (1996).
11. V. G. Orlov, A. A. Bush, S. A. Ivanov, and V. V. Zhurov, Fiz. Tverd. Tela (St. Petersburg) **39** (5), 865 (1997) [Phys. Solid State **39**, 770 (1997)].
12. J. F. Dillon, Jr. and J. W. Nielsen, Phys. Rev. **120** (1), 105 (1960).
13. J. F. Dillon, Jr. and J. W. Nielsen, Phys. Rev. Lett. **3** (1), 30 (1959).
14. A. G. Gurevich, A. N. Ageev, and M. I. Klinger, J. Appl. Phys. **41** (3), 1295 (1970).
15. R. Pauthenet, J. Appl. Phys. **30** (4), 290S (1959).
16. C. Kittel, *Introduction to Solid State Physics*, 5th ed. (Wiley, New York, 1976; Nauka, Moscow, 1978).

Translated by O. Moskalev

Physics of the Solid State, Vol. 45, No. 12, 2003, pp. 2338–2341. Translated from Fizika Tverdogo Tela, Vol. 45, No. 12, 2003, pp. 2230–2232.

MAGNETISM AND FERROELECTRICITY

Optical Spectra of Lithium Niobate

T. P. Myasnikova and A. É. Myasnikova

Rostov State University, ul. Zorge 5, Rostov-on-Don, 344090 Russia

e-mail: rochal@phys.rnd.runnet.ru

Received May 20, 2003

Abstract—The specific features revealed in the optical spectra of lithium niobate crystals at temperatures of 90 and 120–125°C can be attributed to the change in the electronic subsystem and the related isostructural transformation of the crystal lattice. In the near-IR range, the optical absorption spectra of lithium niobate crystals exhibit bands (1.43 eV) assigned to polarons of large radius with a binding energy of 0.48 eV. The decrease observed in the absorption coefficient at the maxima of these bands with an increase in the temperature to 160°C can be explained by the decay of polarons of large radius at these temperatures. © *2003 MAIK "Nauka/Interperiodica".*

1. INTRODUCTION

Crystals of lithium niobate $LiNbO_3$ have been intensively studied in recent years. It has been found that lithium niobate undergoes a ferroelectric phase transition at a temperature of 1140°C. A number of authors have suggested that the electrical characteristics and optical properties of this crystal exhibit anomalies in the temperature range 20–200°C [1, 2]. However, there is no consensus of opinion among researchers regarding not only the nature of these anomalies but also the mere fact of their existence.

The purpose of this work was to elucidate the nature of the anomalies observed in the absorption spectra of lithium niobate crystals in the temperature range 20–180°C. Analysis of the absorption spectra is a sufficiently sensitive and effective method for studying phase transitions in ferroelectrics, specifically in crystals of barium titanate and lead scandium niobate [3, 4].

2. SAMPLE AND EXPERIMENTAL TECHNIQUE

The objects of our investigation were commercial lithium niobate single-crystal plates cut out parallel (*YZ* section) and perpendicularly (*XY* section) to the ferroelectric axis with thicknesses of 0.105 and 0.1025 cm, respectively. The absorption spectra were recorded on an SF-14 spectrophotometer in the visible range (400–750 nm) and on an IKS-14A infrared spectrometer in the near-IR range (3800–14 200 cm^{-1}) at temperatures ranging from 16 to 160°C. The temperature was regulated using a VRT-3 temperature controller with an accuracy of 0.1 K. The light incident on the sample in the SF-14 spectrophotometer was polarized perpendicularly to the slit.

3. RESULTS AND DISCUSSION

In the visible range, the optical spectra of the *YZ* section of the lithium niobate crystal contain two absorption bands with maxima at 402 and 685 nm and the spectra of the *XY* section of the lithium niobate crystal exhibit two absorption bands with maxima at 470 and 685 nm. According to the results obtained by Shirmer *et al.* [5], the first band can be assigned to the $Nb_{Li}^{3+}\,Nb_{Nb}$ bipolarons of small radius and the second band can be attributed to the Nb_{Li}^{3+} polarons of small radius. The long-wavelength absorption edge of the first band follows the Urbach rule. As can be seen from Fig. 1a, the parameter of the Urbach rule σ, which characterizes the slope of the linear dependence of the logarithm of the absorption coefficient K on the incident radiant energy [$\sigma = (\Delta \ln K/\Delta\hbar\omega)kT$), has resonance minima at temperatures of 90.125 and 160°C upon heating of the lithium niobate crystal (*YZ* section) and at temperatures of 125 and 80°C upon cooling. The electron–phonon interaction constant is determined to be $g = 145$ in the heating cycle at temperatures below and above 125°C, $g = 131$ in the cooling cycle at temperatures above 125°C, and $g = 170$ in the cooling cycle at temperatures below 125°C. The energy of the effective phonon associated with the electron transition at a temperature above 125°C is equal to 417 cm^{-1}, and the energy of the effective phonon attributed to the electron transition below 125°C is 386 cm^{-1}. The parameter of the Urbach rule σ for the *XY* section of the lithium niobate crystal has minima at temperatures of 90.120 and 130°C in the heating cycle and at temperatures of 130, 110, and 80°C in the cooling cycle. The electron–phonon interaction constant is estimated as $g = 37$ at a temperature below 90°C and as $g = 21$ above 90°C. The energy of the effective phonon is 500 cm^{-1}. The specific

1063-7834/03/4512-2338$24.00

features observed in the temperature dependences of the parameter of the Urbach rule at temperatures close to 90 and 120°C correlate with the changes revealed by Kamentsev *et al.* [6] in the domain structure and electrical conductivity at these temperatures.

The temperature dependence of the energy location of the absorption edge E_g^K of the first band (*YZ* section) at the absorption coefficient $\ln K = 3.91$ is characterized by the following features: during heating of the crystal, the energy E_g^K abruptly decreases by 0.06 and 0.075 eV at temperatures close to 90 and 125°C, respectively (see Fig. 1a, curve *1*). For the *XY* section of the lithium niobate crystal, the energy of the absorption edge E_g^K of the first band at the absorption coefficient $\ln K = 1.26$ decreases by 0.1 and 0.125 eV at temperatures close to 90 and 120°C, respectively. These findings allowed us to assume that, at temperatures of 90 and 120–125°C, the electronic structure undergoes a transformation, which, in turn, leads to an isostructural transformation of the crystal lattice and domain structure, because similar changes are usually due to an interband electron–phonon interaction that results in a shift of the absorption bands and an isostructural transformation of the crystal lattice [7].

The second absorption band (at 685 nm) has a bell-shaped form. In this case, both sections are characterized by similar temperature dependences of the integrated intensity I_∞, which slightly increases in the temperature range 90–130°C and sharply increases at temperatures above 160°C (Fig. 1b).

In the near-IR spectral range, the spectrum of the *YZ* section of the lithium niobate crystal exhibits a bell-shaped absorption band with the center at 11500 cm^{-1} and a half-width of 1.26 eV at a temperature of 100°C. The contour of this band is such (Fig. 2a) that the absorption coefficient at high frequencies is substantially larger than that at low frequencies. This is an indication of the formation of a polaron of large radius with a binding energy $\hbar\omega/3 = 0.48$ eV [8]. It should be noted that the formation of a polaron with such a high binding energy in lithium niobate crystals due to the Fröhlich electron–phonon interaction alone seems to be unlikely, because the width of the conduction band is relatively large (of the order of 2 eV [9]). However, the inclusion of the vibronic interaction at the instant a carrier appears in the conduction band can explain such a large value of the binding energy of the polaron. The occurrence of an excess electron in a spatial region (the region of carrier localization in a polaron of large radius), according to the Hartree–Fock scheme, leads to a transformation of the whole system of electronic single-particle states of the lattice ions, including the core electrons. As a result, the arrangement of the ions changes and the energy of the system decreases due to the vibronic interaction. A study of clusters of different sizes within the Hartree–Fock formalism demonstrated

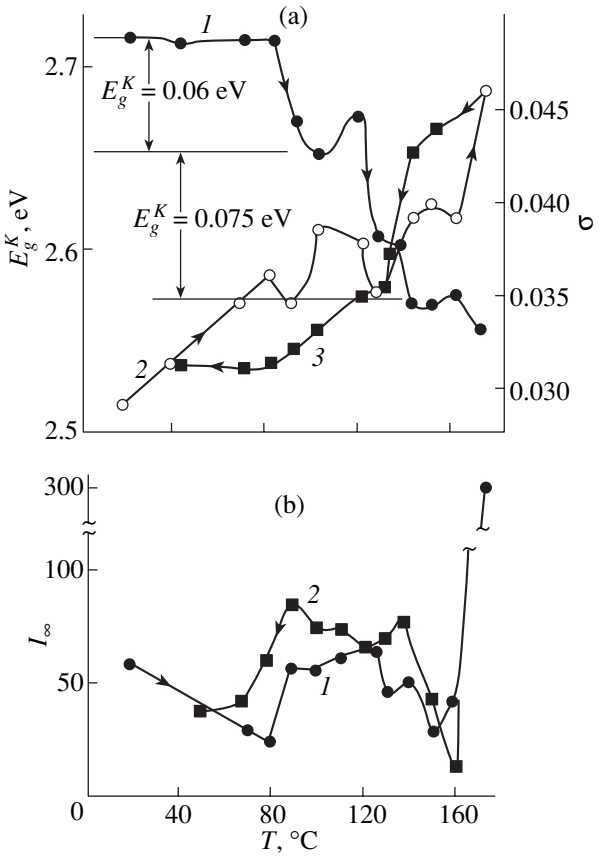

Fig. 1. (a) Temperature dependences of (*1*) the energy location of the long-wavelength absorption edge E_g^K at the absorption coefficient $\ln K = 3.91$ and (*2*, *3*) the parameter of the Urbach rule σ upon (*2*) heating and (*3*) cooling of the lithium niobate crystal (*YZ* section). (b) Temperature dependences of the integrated intensity I_∞ of the absorption band at $\lambda_{max} = 685$ nm upon (*1*) heating and (*2*) cooling of the lithium niobate crystal (*YZ* section).

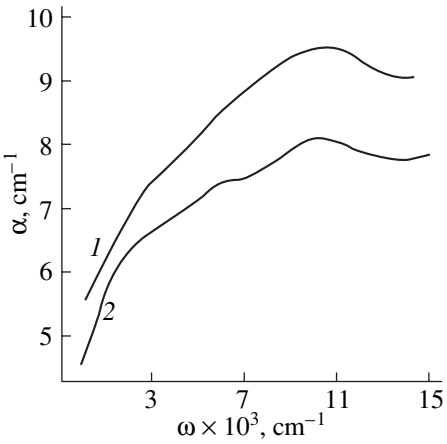

Fig. 2. Absorption spectra of lithium niobate crystals in the near-IR range: (*1*) the *YZ* section at 110°C and (*2*) the *XY* section at 80°C.

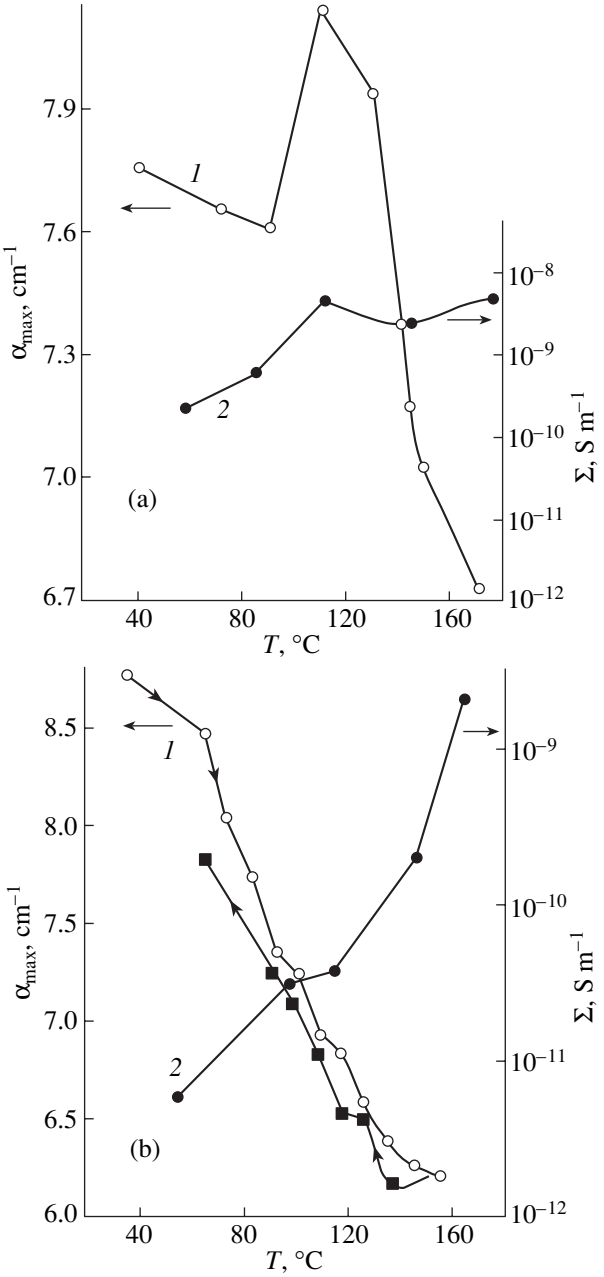

Fig. 3. Temperature dependences of (*1*) the absorption coefficient α_{max} at the maximum of the absorption band at a frequency of 11500 cm^{-1} and (*2*) the electrical conductivity Σ [6]: (a) the *YZ* section and (b) the *XY* section.

that the smaller the size of the cluster, i.e., the higher the density of the distribution of an excess electron in the system of electronic single-particle states, the more pronounced the effect of the transformation of this system. A similar dependence of the vibronic interaction energy on the size of the region of carrier localization was described in [10–12]. Consequently, the vibronic interaction leads to a decrease in the polaron radius; i.e., the binding energy of the polaron increases. The increase in the binding energy of the polaron in lithium niobate crystals due to the vibronic interaction can be evaluated taking into account the fact that, in the temperature range 90–130°C, the interband electron–phonon interaction decreases the band gap by approximately 0.1–0.225 eV (as follows from the shift in the energy location of the absorption edge E_g^K). This decrease in the band gap can be considered the lower limit of reduction of the polaron level for the conduction electron due to the vibronic interaction, because the density of the electron distribution in the polaron is substantially higher than the mean density of carriers in the conduction band. This estimate agrees with that obtained for the contribution of the vibronic interaction to the binding energy of the vibronic exciton with charge transfer in perovskite ferroelectrics [13].

It can be seen from Fig. 3a that, as the temperature increases, the absorption coefficient α_{max} at the maximum of the absorption band with the center at 11500 cm^{-1} for the *YZ* section first decreases and then reaches a maximum at a temperature of 110°C. It is interesting to note that the temperature dependence of the electrical conductivity of the *YZ* section of the lithium niobate crystal [6] exhibits a maximum at a temperature of approximately 112°C against the background of a general increase in the conductivity with an increase in the temperature. For the *XY* section of the lithium niobate crystal, the absorption band centered at 11500 cm^{-1} is also observed in the near-IR range (Fig. 2, curve *2*). The absorption coefficient α_{max} of the band at 11500 cm^{-1} for the *XY* section of the lithium niobate crystal decreases with an increase in the temperature in the range from 80 to 160°C. The temperature behavior of the absorption coefficient is in agreement with the temperature dependence of the electrical conductivity of the *XY* section, which rapidly increases in the aforementioned temperature range [6] (Fig. 3b). Possibly, the temperature range 80–160°C corresponds to the decay of polarons of large radius. The decay of the polaron state at temperatures considerably lower than the binding energies of the polaron can be explained by the fact that, even at these temperatures, the mean thermal velocity of polarons is higher than the minimum phase velocity of the phonons. In this supersonic motion, the polaron loses its phonon shell (polarization coat); i.e., it decays [14]. The variations observed in the spectra in the temperature range 150–160°C agree with the changes in the unit cell parameters at these temperatures [1].

REFERENCES

1. I. G. Ismailzade, V. I. Nesterenko, and F. A. Mirishli, Kristallografiya **13** (1), 33 (1968) [Sov. Phys. Crystallogr. **13**, 25 (1968)].
2. G. A. Smolenskii, N. N. Krainik, N. P. Kruchua, *et al.*, Phys. Status Solidi **13** (2), 309 (1966).
3. T. P. Myasnikova, S. G. Gakh, R. Ya. Evseeva, and A. V. Alferov, Neorg. Mater. **37**, 355 (2001).

4. K. G. Abdulvakhidov, I. V. Mardasova, T. P. Myasnikova, *et al.*, Fiz. Tverd. Tela (St. Petersburg) **43** (3), 489 (2001) [Phys. Solid State **43**, 508 (2001)].
5. O. J. Shirmer, O. Thiemann, and M. Wohlecke, J. Phys. Chem. Solids **52** (1), 185 (1991).
6. V. P. Kamentsev, A. V. Nekrasov, B. B. Ped'ko, and V. M. Rudyak, Izv. Akad. Nauk SSSR, Ser. Fiz. **47** (4), 791 (1983).
7. V. M. Fridkin, *Ferroelectric Semiconductors* (Nauka, Moscow, 1976; Consultants Bureau, New York, 1980).
8. D. Emin, Phys. Rev. B **48** (18), 13691 (1993).
9. I. Sh. Akhmadullin, V. A. Golenishchev-Kutuzov, S. A. Migachev, and S. P. Mironov, Fiz. Tverd. Tela (St. Petersburg) **40** (7), 1307 (1998) [Phys. Solid State **40**, 1190 (1998)].
10. F. S. Ham, Phys. Rev., Sect. A **138** (6), 1727 (1965).
11. G. D. Watkins and F. S. Ham, Phys. Rev. B **1** (10), 4071 (1970).
12. S. Kohne, O. F. Schrimer, H. Hesse, *et al.*, J. Supercond. **12** (1), 193 (1999).
13. V. S. Vikhnin and S. Kappkhan, Fiz. Tverd. Tela (St. Petersburg) **40** (5), 907 (1998) [Phys. Solid State **40**, 834 (1998)].
14. É. N. Myasnikov and A. É. Myasnikova, Zh. Éksp. Teor. Fiz. **116** (4), 1386 (1999) [JETP **89**, 746 (1999)].

Translated by O. Moskalev

Physics of the Solid State, Vol. 45, No. 12, 2003, pp. 2342–2347. Translated from Fizika Tverdogo Tela, Vol. 45, No. 12, 2003, pp. 2233–2237.

LATTICE DYNAMICS AND PHASE TRANSITIONS

Euler Instability of Bidirectional Shape Memory Effect in a Titanium Nickelide Strip

G. A. Malygin

Ioffe Physicotechnical Institute, Russian Academy of Sciences, Politekhnicheskaya ul. 26, St. Petersburg, 194021 Russia

e-mail: malygin.ga@mail.ioffe.ru

Received May 20, 2003

Abstract—The mechanism for the Euler instability of the bidirectional shape memory effect in a titanium nickelide strip is discussed in terms of the diffuse martensitic transformations. The shape instability and a plastic jerk of a strip that are observed in the temperature range of a forward and the reverse martensitic transformation are due to the additional bending moment that arises in the case where the ends of the strip are fixed (with the use of hinges) and the strip can only rotate about them. *© 2003 MAIK "Nauka/Interperiodica".*

1. INTRODUCTION

The bidirectional shape memory effect (SME) arises in thin strips [1, 2] and plates [3] of titanium nickelide (TiNi) enriched with nickel (as compared with its equiatomic composition) when a strip or a plate is preliminarily subjected to a special thermomechanical treatment, namely, to bending and annealing in this state at 600–800 K. After such a treatment, differently oriented coherent intermetallic Ti_3Ni_4 precipitates arise in the compressed and stretched layers of a strip (or a plate) [4–6] and the strip remains bent elastically after removing the external bending stress. Experiment shows that, in the temperature range of the two-step phase transformation $B2 \longrightarrow R \longrightarrow B19'$, microstrains produced by precipitates relax and the strip bends in the direction opposite to that of the initial bending. In the course of the reverse martensitic transformation, the initial direction of the strip bending is restored. Therefore, the bidirectional SME takes place.

In [7], the stress field produced by a single disk-shaped Ti_3Ni_4 precipitate in the matrix was calculated and the average stress in the compressed layer of a strip (plate) was found as a function of the volume concentration of Ti_3Ni_4 particles in the alloy. These results were used in [8] to analyze the mechanism of the bidirectional SME occurring in a thin strip (plate) of titanium nickelide in terms of the theory of diffuse martensitic transformations (DMTs) [9, 10]. It was assumed in [8] that the ends of a strip are free, i.e., that the strip is not subjected to external forces and bending moments. In this paper, we consider the case where the ends of a strip are fixed (with the use of hinges). Therefore, as the SME takes place, the distance between the strip ends remains unchanged and the strip is subjected to an additional bending moment. This moment is analogous to a bending moment that arises when compressive stresses are applied to a bar along its length and, under certain critical conditions, give rise to Euler instability of elastic strains in the bar or, in the case of a fixed thin bimetallic strip (plate), to an elastic jerk of the strip [11, 12]. Experimental studies of the bidirectional SME have shown [2, 3] that a jerk of an arch-shaped titanium nickelide strip with its ends kept fixed with the use of hinges takes place when the strip is heated in the temperature range of the two-step martensitic transformation $B19' \longrightarrow R \longrightarrow B2$ and the M and R martensites disappear, respectively. It is clear that this effect is of considerable interest for practical application, because it enhances the functional capabilities of shape memory alloys by narrowing the switching temperature range of relays and sensing devices.

In this paper, based on the results obtained in [8], we analyze the conditions under which the Euler instability of the bidirectional SME arises in a thin arch-shaped strip of titanium nickelide. In Section 2, we consider the extra stresses that arise due to the SME in a strip when its ends are fixed. The changes in the radius of curvature and in the bending deflection of the strip caused by these extra bending stresses are analyzed in Section 3. The conditions under which the Euler instability of the SME and a jerk of the strip occur are discussed in Section 4.

2. BENDING STRESSES IN A STRIP

As in [8], we consider a titanium nickelide strip $2h$ thick by b wide by $2l$ long and assume that $2h \ll b \ll 2l$. Upon annealing, the bending radius of the strip is $R_0 > 2l$. The ends of the strip are assumed to be fixed with the use of hinges, so that the distance between the ends remains unchanged when the SME occurs. The

1063-7834/03/4512-2342$24.00

additional curvature of the strip caused by fixing the ends of the strip is [11, 12]

$$R_G^{-1}(x, T) = -\frac{M(x, T)}{EJ}, \qquad M(x, T) = W_0(x, T)P(T), \tag{1}$$

where $M(x, T)$ is the bending moment, $W_0(x, T)$ is the deflection of the free strip under the SME conditions, $P(T) = EA\varepsilon(T)$ is the longitudinal compressive force applied to the ends of the strip, $\varepsilon(T) = [l_0 - L_0(T)]/l$ is the additional tensional strain due to the confinement of the strip motion, $2L_0(T)$ is the distance between the ends of the free strip [8], $2l_0$ is the distance between the fixed ends of the strip ($2l_0 < 2l$), $A = 2hb$ is the strip cross-sectional area, $J = b(2h)^3/12$ is the moment of inertia of the strip cross section, E is the elastic modulus, T is the temperature, and x is the coordinate along the chord connecting the fixed ends of the strip. When the problem of the Euler instability of the bidirectional SME is solved exactly, the strip deflection $W(x, T)$ is the sought rather than given quantity and can be calculated numerically, e.g., by using an iterative technique. The deflection $W_0(x, T)$ of the free strip can be taken as a zeroth approximation. In what follows, we restrict our consideration to the first approximation.

The bending moment $M(x, T)$ causes additional elastic stresses, which produce plastic (martensitic) deformation in the strip. By substituting $M(x, T)$ into the condition for the balance of the bending moments applied to the strip, we can find, as in [8], the stress distribution over the length and thickness (along the y axis) of the strip:

$$\sigma(x, y, T) = \sigma_0'(x, y) - \sigma_p(x, y, T), \tag{2a}$$

$$\sigma_0'(x, y, T) = \frac{1}{2}E|\varepsilon_0|\left(\frac{3y}{2h} \pm 1\right) - \frac{3}{2}\frac{M(x, T)}{bh^2}\frac{y}{h}, \tag{2b}$$

$$\sigma_p(x, y, T) = E\left(\varepsilon_p(x, y, T) + \frac{1}{2}\tilde{\varepsilon}_p(x, T) - \frac{3}{2}\tilde{\tilde{\varepsilon}}(x, T)\frac{y}{h}\right). \tag{2c}$$

Here, $\sigma_0'(x, y, T)$ are the elastic stresses due to the strip bending under the action of the moment $M(x, T)$ and the internal stresses due to the anisotropically distributed Ti_3Ni_4 particles in the strip [8] (ε_0 is the elastic strain of the strip caused by these particles) and $\sigma_p(x, y, T)$ is the martensitic stress relaxation due to the formation of the R and M martensites. The strains averaged over the strip thickness,

$$\tilde{\varepsilon}_p(x, T) = \frac{1}{2h}\int_{-h}^{h}\varepsilon_p(x, y, T)dy, \qquad \tilde{\tilde{\varepsilon}}_p(x, T) = \frac{1}{h^2}\int_{-h}^{h}\varepsilon_p(x, y, T)ydy, \tag{3}$$

depend on the martensitic-strain distribution in the strip:

$$\varepsilon_p(x, y, T) = [\varepsilon_R\varphi_R(\sigma_0'(x, y, T), T) + \varepsilon_M\varphi_M(\sigma_0'(x, y, T), T)\operatorname{sgn}[\sigma_0'(x, y, T)], \tag{4}$$

where φ_R and φ_M are the volume fractions of the R and M martensites, respectively; $\varepsilon_R = n_R m_R f\xi_R$, $\varepsilon_M = n_M m_M f\xi_M$, ξ_R, and ξ_M are the shear strains associated with the lattice transformations into the R and M martensites; f is the volume concentration of Ti_3Ni_4 particles in the strip; m_R and m_M are the orientation factors; and n_R and n_M are the numbers of equivalent orientations of R- and M-martensite particles (with the same orientation factors).

According to the theory of DMTs, if there are two types of martensite, then their volume fractions φ_R and φ_M at temperature T and stress $\sigma_0'(x, y, T)$ are given by [8]

$$\varphi_R = \frac{\exp(-\Delta U_R/kT)}{1 + \exp(-\Delta U_R/kT) + \exp(-\Delta U_M/kT)}, \tag{5a}$$

$$\varphi_M = \frac{\exp(-\Delta U_M/kT)}{1 + \exp(-\Delta U_R/kT) + \exp(-\Delta U_M/kT)}, \tag{5b}$$

$$\frac{\Delta U_R}{kT} = B_R(t - 1 - m_R a_R|S_0'(\bar{x}, \bar{y}, t)| \pm \tau_{fR}/\tau_R), \tag{5c}$$

$$\frac{\Delta U_M}{kT} = B_M(ct - 1 - m_M a_M|S_0(\bar{y})| \pm \tau_{fM}/\tau_M), \tag{5d}$$

$$\frac{\sigma_0'(x, y, T)}{E|\varepsilon_0|} = S_0'(\bar{x}, \bar{y}, t) = \frac{1}{2}\left(\frac{3}{2}\bar{y} \pm 1\right) + 3\frac{W_0(\bar{x}, t)}{h}\frac{|\varepsilon(t)|}{|\varepsilon_0|}\bar{y}, \tag{5e}$$

where $t = T/T_R$, $\bar{y} = y/h$, $\bar{x} = x/L_0$, $c = T_R/T_M$, $a_R = \xi_R|\varepsilon_0|(E/q_R)$, $a_M = \xi_M|\varepsilon_0|(E/q_M)$, $\tau_R = q_R/\xi_R$, and $\tau_M = q_M/\xi_M$. Here, the parameters B_R and B_M characterize the degree of diffuseness of the corresponding phase transformations in terms of temperature, τ_{fR} and τ_{fM} characterize the hysteresis of these transformations, T_R and T_M are the characteristic temperatures, and q_R and q_M are the specific heats of these transformations.

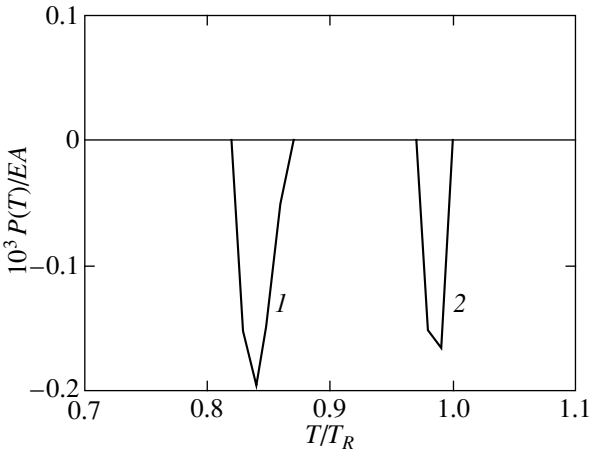

Fig. 1. Temperature dependence of the compressive forces applied to a strip of titanium nickelide under the confined-SME conditions on (*1*) cooling and (*2*) heating.

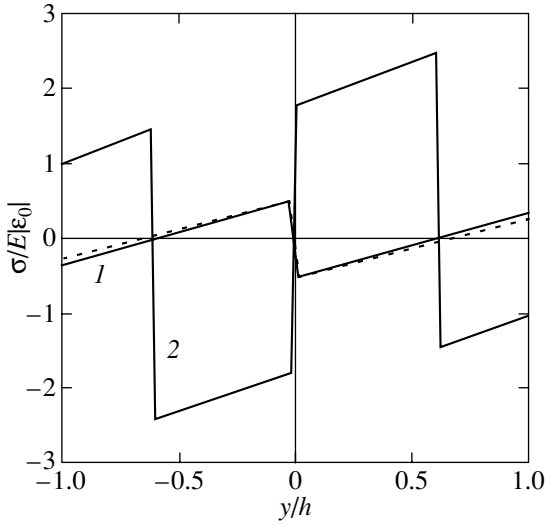

Fig. 2. Elastic-stress distribution over the strip thickness under the nonconfined (dotted line) and confined (line *1*) SME conditions and after martensitic stress relaxation (line *2*).

Figure 1 shows the temperature dependence of the compressive force $P(T)$ that is applied to the strip due to the ends of the strip being fixed:

$$\frac{P(T)}{EA} = \varepsilon(T) = \frac{l_0 - L_0(T)}{l},$$
$$L_0(T) = R_0(T)\sin\frac{l}{R_0(T)}, \quad (6)$$

where $R_0(T)$ is the radius of curvature of the free strip under the SME conditions [8]. The calculations were performed for the same values of the parameters of the strip and martensitic transformations as those used in [8]. The elastic compressive strain of the strip is maximum when the strip becomes linear: $\varepsilon_m = (l_0 - l)/l = -2 \times 10^{-4}$. For strains close to ε_m, as seen from Fig. 1, the compressive force is nonzero only within fairly narrow temperature ranges for both the forward and reverse martensitic transformations. Outside these ranges, the ends of the strip are actually free.

Figure 2 shows the elastic-stress distribution over the strip thickness in the middle of the strip ($x = 0$) as calculated from Eq. (5e) for $T = 0.84T_R$ upon cooling for the free (dotted line) and for the confined strip (curve *1*). In Eq. (5e), the deflection of the free strip under the SME conditions is given by [8]

$$W_0(x, T) = R_0(T)[\sqrt{1 - (x/R_0(T))^2} - \sqrt{1 - (L_0(T)/R_0(T))^2}]. \quad (7)$$

It can be seen that, when the ends of the strip are fixed, the bottom strip layer is subjected to elastic compression, which is changed to tension (curve *2*) after martensitic relaxation of the elastic stresses. Curve *2* in Fig. 2 shows the stress distribution as calculated from Eq. (2a); this equation accounts for the stress relaxation mentioned above and should be combined with Eq. (2c), in which $\tilde{\varepsilon}_p(x, T) = 0$.

3. CONFINED SHAPE MEMORY EFFECT

With allowance for the internal bending moments (due to the anisotropic distribution of Ti_3Ni_4 particles) and the external bending moments (due to the confinement of the strip motion), the total curvature of the strip is

$$R^{-1}(x, T) = R_0^{-1} + R_e^{-1} + R_p^{-1}(x, T) + R_G^{-1}(x, T), \quad (8a)$$

where R_0^{-1} is the initial curvature of the strip (upon its annealing); $R_e^{-1} = -(3/4h)|\varepsilon_0|$ and $R_p^{-1} = -(3/2h)\tilde{\tilde{\varepsilon}}_p(x, T)$ are the changes in the curvature due to the elastic [8] and martensitic [see Eqs. (2)–(5)] stress relaxation, respectively; and $R_G^{-1}(x, T)$ is the elastic contribution to the curvature due to the ends of the strip being fixed. For numerical calculations, it is convenient to represent Eq. (8a) in the reduced form

$$\frac{R_0}{R(x, T)} = 1 - \frac{3R_0}{2h}\left(\frac{1}{2}|\varepsilon_0| + \tilde{\tilde{\varepsilon}}_p(x, T)\right) + 3\left(\frac{R_0}{h}\right)^2\frac{W_0(x, T)}{R_0}|\varepsilon(T)|. \quad (8b)$$

Figures 3a and 3b show the calculated temperature dependences of the reduced curvature in the middle of the strip ($x = 0$) upon cooling and heating, respectively, for $R_0/h = 3 \times 10^2$, $l/R_0 = 0.5$, and the other parameters

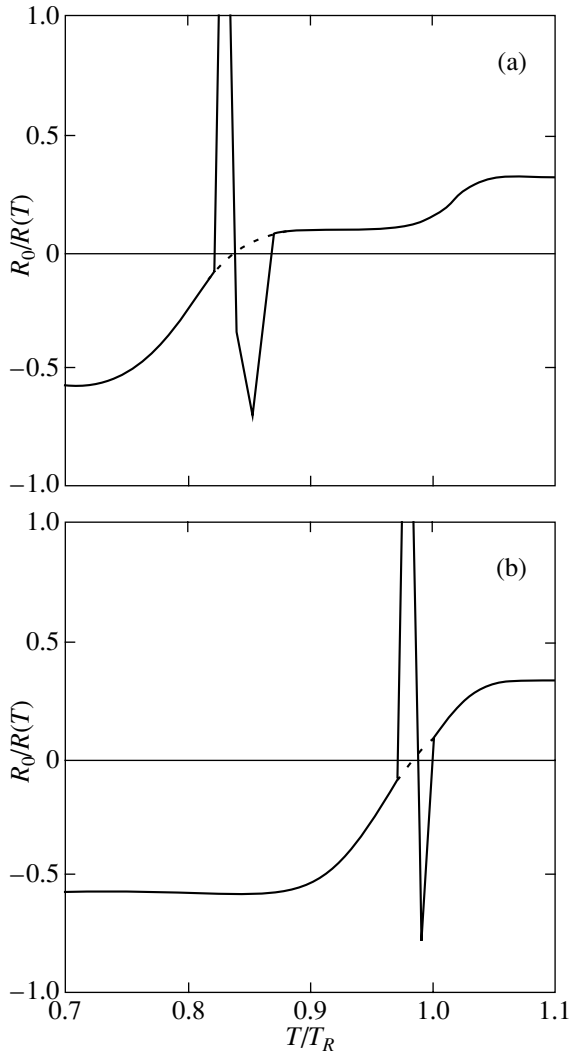

Fig. 3. Temperature dependence of the reduced strip curvature [calculated from Eq. (8b)] under the confined-SME conditions on (a) cooling and (b) heating.

being the same as those in [8]. The dotted lines represent the temperature dependence of the curvature of the free strip [8]. It can be seen that, in the narrow temperature ranges where the curvature of the free strip under the SME conditions is close to zero, the curvature of the confined strip sharply changes sign and magnitude because of the compressive force applied to its ends. Therefore, the strip undergoes the Euler instability in these temperature ranges. Outside these ranges, the strip curvature takes on the values characteristic of the SME in the free strip.

In order to trace the changes in the strip shape in the region of the shape instability, we use the well-known equation relating the radius of curvature of a strip to the coordinate derivatives of the strip deflection $W(x, T)$:

$$R^{-1}(x, T) = -\frac{W''}{(1 + W'^2)^{3/2}}, \qquad (9)$$

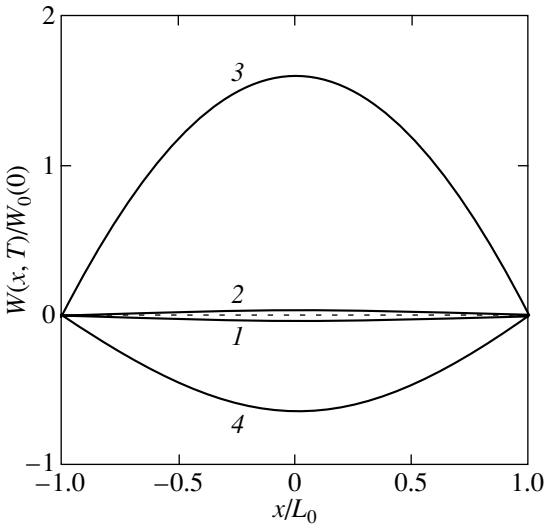

Fig. 4. Strip shape variation on heating under (*1*, *2*) the nonconfined- and (*3*, *4*) confined-SME conditions: (*1*, *3*) $T = 0.98T_R$ and (*2*, *4*) $0.99T_R$.

where $W' = dW/dx$ and $W'' = dW'/dx$. The minus sign in Eq. (9) signifies that the curvature is positive when the strip is convex upward. The angle of rotation of strip cross sections is $\Omega(x, T) = W'(x, T)$. We assume that strip cross sections remain planar upon unstable deformation of the strip. Integrating Eq. (9) once, we obtain

$$\frac{\Omega}{(1 + \Omega^2)^{1/2}} = \omega(x, T),$$

$$\omega(x, T) = \omega_1(T) - \int_{-L_0(T)}^{x} \frac{dx}{R(x, T)}, \qquad (10)$$

$$\omega_1(T) = \int_{-L_0(T)}^{0} \frac{dx}{R(x, T)},$$

where $\omega_1(T)$ is a constant of integration, which can be found from the condition $\Omega(x, T) = 0$ for $x = 0$, and $2L_0(T)$ is the distance between the ends of the strip. From the first of equations (10), it can be seen that, at small values of the angle of rotation of strip cross sections ($\Omega \ll 1$), we have $\Omega(x, T) \approx \omega(x, T)$.

It follows from Eq. (10) that, in general, $\Omega = \omega/\sqrt{1 - \omega^2}$; therefore, the strip deflection as a function of coordinate x and temperature T is given by

$$W(x, T) = \int_{-L_0(T)}^{x} \frac{\omega(x, T)dx}{\sqrt{1 - \omega^2(x, T)}}. \qquad (11)$$

For $\omega(x, T) = x/R_0(T)$, i.e., in the case of the SME in a free strip, Eq. (11) reduces to Eq. (7). The strip deflection upon heating as calculated from Eq. (11) is shown

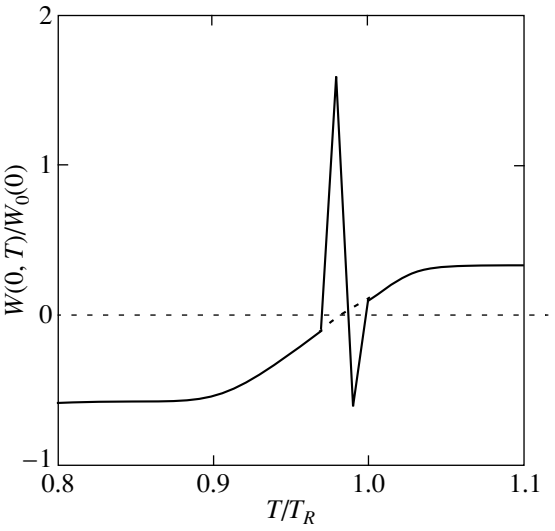

Fig. 5. Temperature evolution of the maximal strip deflection upon heating under the confined-SME conditions.

in Fig. 4 for the free (curves *1*, *2*) and the confined strip (curves *3*, *4*) at temperatures $0.98T_R$ (curves *1*, *3*) and $0.99T_R$ (curves *2*, *4*). At these temperatures, as seen from Fig. 3, the curvature and deflection of the strip with its ends kept fixed vary sharply upon the reverse martensitic transformation $B19' \longrightarrow R \longrightarrow B2$.

At temperature $0.98T_R$, the deflection in the middle of the strip ($x = 0$) is equal to $-0.1W_0(0)$ (Fig. 4, curve *1*) and $1.58W_0(0)$ (curve *3*) for the free and the confined strip, respectively, where $W_0(0) = R_0(1 - \cos\theta_0) \approx 0.12R_0$ is the strip deflection and $2\theta_0 = 2l/R_0$ is the full bending angle of the strip upon its annealing. Therefore, for a strip of length $2l = 20$ mm [2], the deflection increases from –0.24 to 3.8 mm after the ends of the strip become fixed. Such a sharp change of the strip deflection in magnitude and sign within the narrow temperature range $(0.97–0.98)T_R$ (of width ≈3 K for T_R = 300–320 K) indicates that the strip jerks as the temperature is varied under the bidirectional-SME conditions.

Figure 5 shows the full evolution of the maximal strip deflection $W(0, T)$ as the temperature is increased. It is seen that a small deviation from the temperature at which the strip curvature is zero produces a large deflection of the titanium nickelide strip. This effect can be used to significantly enhance the functional capabilities of relays and sensing devices based on such strips.

4. EULER INSTABILITY OF THE SHAPE MEMORY EFFECT

The elastic Euler instability of a bar of a rectangular cross section is purely elastic in character and arises when the following criterion is satisfied [11, 12]:

$$P_c \geq EJ\left(\frac{\pi}{2l}\right)^2, \qquad (12)$$

where $P_c = AE\varepsilon_c$ is the critical force applied to the bar and ε_c is the critical strain. For the thin strip considered above, we have $\varepsilon_c \geq 0.2(h/l)^2 \approx 4.4 \times 10^{-5}$. For zero curvature (i.e., when the strip becomes linear), the elastic compressive strain of the strip was calculated to be $\varepsilon_m = -2 \times 10^{-4}$, which is significantly larger in magnitude than the critical strain ε_c.

Due to the Euler instability, a strip of titanium nickelide first undergoes a small elastic deflection and then its deflection becomes plastic and large (but limited in magnitude; see Fig. 4, curves *3*, *4*). The deflection and a plastic jerk of a strip are caused by the thermodynamic driving force of the structural phase transition and by the stresses applied to the strip.

The criterion for the strip losing its stability is the inequality $|\varepsilon(T)| > |\varepsilon_c|$, where $\varepsilon(T)$ is the compressive strain that arises in the strip under the bidirectional-SME conditions and is given by Eq. (6). Using Eq. (6), we represent this criterion in the form

$$\frac{R_0(T)}{R_0}\sin\left(\theta_0\frac{R_0}{R_0(T)}\right) > \theta_0[1 - |\varepsilon_m| + |\varepsilon_c|], \qquad (13a)$$

$$\frac{R_0}{R_0(T)} = 1 - \frac{3R_0}{2h}\left(\frac{1}{2}|\varepsilon_0| + \bar{\bar{\varepsilon}}_p(T)\right). \qquad (13b)$$

Here, $R_0/R_0(T)$ and $\varepsilon_p(T)$ are the reduced curvature and the compressive strain [analogous to that in Eq. (4)], respectively, of the free strip under the SME conditions [8]. Since $R_0/R_0(T) \ll 1$ when the instability occurs, we can use the approximation $\sin x \approx x - x^3/6$ in inequality (13a) and represent this criterion in the form

$$\frac{3R_0}{2h}\left(\frac{1}{2}|\varepsilon_0| + \bar{\bar{\varepsilon}}_p(T)\right) > 1 \mp \sqrt{6}\theta_0^{-1}\sqrt{|\varepsilon_m| - |\varepsilon_c|}. \qquad (14)$$

For given values of the parameters R_0/h, $|\varepsilon_m|$, and $|\varepsilon_c|$, criterion (14) determines the critical temperatures T_- and T_+ at which the instability occurs and disappears, respectively.

5. CONCLUSION

Thus, based on the theory of DMTs, we have shown that the plastic instability of the bidirectional SME depends on the geometric parameters of a titanium nickelide strip, the bending angle of the strip upon its initial annealing, the concentration of Ti_3Ni_4 particles, and on the structural and thermodynamic parameters of the martensitic transformation that determine the strains ε_0 and $\bar{\bar{\varepsilon}}_p(T)$.

REFERENCES

1. N. Nishida and T. Honma, Scr. Metall. **18** (11), 1293 (1984).
2. M. A. Khusainov, Vestn. Novgor. Univ., No. 10, 34 (1998).
3. M. A. Khusainov, Zh. Tekh. Fiz. **67** (6), 118 (1997) [Tech. Phys. **42**, 692 (1997)].
4. T. Honma, in *Shape Memory Alloy-86*, Ed. by Ch. Youyi, T. Y. Hsu, and T. Ko (China Academic, Guilin, 1986), p. 83.
5. D. Y. Li and L. Q. Chen, Acta Mater. **45** (2), 471 (1997).
6. L. Bataillard, J. E. Bidaux, and R. Gotthardt, Philos. Mag. A **78** (2), 327 (1998).
7. G. A. Malygin, Fiz. Tverd. Tela (St. Petersburg) **45** (8), 1491 (2003) [Phys. Solid State **45**, 1566 (2003)].
8. G. A. Malygin, Fiz. Tverd. Tela (St. Petersburg) **45** (9), 1700 (2003) [Phys. Solid State **45**, 1784 (2003)].
9. G. A. Malygin, Fiz. Tverd. Tela (St. Petersburg) **36** (5), 1489 (1994) [Phys. Solid State **36**, 815 (1994)].
10. G. A. Malygin, Usp. Fiz. Nauk **171** (2), 187 (2001) [Phys. Usp. **44**, 173 (2001)].
11. L. E. Andreeva, *Elastic Elements of Devices* (Mashinostroenie, Moscow, 1981).
12. A. S. Vol'mir, *Stability of Deformed Systems* (Nauka, Moscow, 1967).

Translated by Yu. Epifanov

Physics of the Solid State, Vol. 45, No. 12, 2003, pp. 2348–2351. Translated from Fizika Tverdogo Tela, Vol. 45, No. 12, 2003, pp. 2238–2241.

LOW-DIMENSIONAL SYSTEMS AND SURFACE PHYSICS

Intensity of Intersubband Electron Scattering by Polar Optical Phonons in Semiconductor Quantum Wires with Account of Energy Level Broadening

D. V. Pozdnyakov and V. M. Borzdov

Belarussian State University, ul. F. Skarina 4, Minsk, 220050 Belarus

e-mail: borzdov@bsu.by

Received April 2, 2003

Abstract—An approach describing the effect of energy level broadening in semiconductor quantum wires on the intensity of intersubband electron scattering by polar optical phonons is suggested. As a broadening mechanism, scattering by atomic thermal vibrations and by the roughness of the confining surfaces of a quantum system is considered. It is shown that in this case the dependence of the intensity of intersubband scattering of electrons on their kinetic energy has no singularities. © *2003 MAIK "Nauka/Interperiodica".*

1. INTRODUCTION

Modern technological methods in micro- and nanoelectronics make it possible to create nanoscale semiconductor device structures whose operation principles are based on quantum effects. Due to this, the development of fundamentally new high-speed and energy-saving devices has become possible [1, 2]. Accordingly, much attention is paid to theoretical and experimental studies on quantum wires. From the point of view of device application, the most important direction of research is the study of electron transport in such structures, in particular, its numerical modeling. One of the most promising methods is Monte Carlo calculations [3]. Correct application of this method is possible only if rigorous expressions for charge carrier scattering intensities are known for the basic scattering mechanisms.

In this paper, we consider quantum wires of polar semiconductors, where the main electron scattering mechanism is scattering by polar optical phonons, which, to a great extent, is determined by the specific features of the density of states in a one-dimensional system [4]. In particular, this gives rise to the appearance of singular points in the dependence of the carrier scattering intensity on carrier energy [5, 6]. Since the intensity of phonon scattering diverges at these points, various contradictions arise in describing of the character and value of the conductance of quantum wires. For example, it was shown in [4] that under certain conditions a quantum wire can, in principle, have zero conductance; this, however, is not actually observed. In our paper, we attribute this contradiction to the fact that the calculations in [4] use the parameters for an idealized quantum structure for which the density of states is determined under the assumption of a discrete energy spectrum with infinitely narrow energy levels, whereas in real quantum wires the levels have a finite width.

The aim of this paper is to calculate the density of states for a quantum wire with broadened energy levels and to study the effect of this broadening on the intensity of intersubband electron scattering by polar optical phonons. We assume that the level broadening is mainly due to thermal atomic vibrations of the crystal lattice and to roughness of the semiconductor quantum structure surfaces forming a two-dimensional quantum well [5].

2. DENSITY OF STATES

According to [4], the density of states for a quantum wire in the case of infinitely narrow energy levels is given by

$$n(E) = \frac{\sqrt{2}}{\pi}\frac{\sqrt{m_d}}{\hbar ab}\sum_{\mu}\sum_{\nu}\frac{U(E-E_{\mu\nu})}{\sqrt{E-E_{\mu\nu}}}, \qquad (1)$$

where m_d is the density-of-states effective mass of an electron in the quantum wire, E is the average total energy of an electron, $E_{\mu\nu}$ is the energy of the corresponding quantum state ($\{\mu, \nu\} = 1, 2, 3, \ldots$), a and b are the height and the width of the quantum wire in the y and z directions, respectively, and U is a step function.

Let us consider a diagonal electron effective mass tensor. For a one-dimensional case, we have

$$m_d = m_x, \qquad (2)$$

$$E = E_{\mu\nu} + \frac{\hbar^2 k_x^2}{2m_x}, \qquad (3)$$

1063-7834/03/4512-2348$24.00

$$E_{\mu\nu} = E_\mu + E_\nu = \frac{\pi^2\hbar^2}{2}\left(\frac{\mu^2}{m_y a^2} + \frac{\nu^2}{m_z b^2}\right), \quad (4)$$

where m_x, m_y, and m_z are the electron effective masses in the x, y, and z directions, respectively, and k_x is the component of the wave vector of an electron in the x direction.

In accordance with [1, 7, 8], we consider Lorentzian broadening of energy levels described by a modified Lorentzian probability density function $f(\varepsilon, E)$ that takes into account the overlap of the levels. In our case, this function has the form

$$f(\varepsilon, E) = \frac{g(\eta)}{\pi}\frac{\eta E}{(E-\varepsilon)^2 + (\eta E)^2}, \quad (5)$$

$$\eta = \frac{\Delta E}{E}, \quad (6)$$

where ε is the total energy of an electron, ΔE is the average deviation of ε from E (the half-width of the Lorentzian), η is the broadening coefficient, and $g(\eta)$ is a function that takes into account the overlap of energy levels. Then, with allowance for broadening, according to the mean value theorem, the density of states for a quantum wire assumes the form

$$N(E) = \int_0^\infty n(\varepsilon) f(\varepsilon, E) d\varepsilon. \quad (7)$$

Now, let us determine the function $g(\eta)$. Taking into account that, for $\Delta E \longrightarrow +\infty$, the density of states for a quantum wire must uniformly converge to the three-dimensional density of states $G(E)$, we can write the following equation:

$$G(E) = \int_0^\infty G(\varepsilon) f(\varepsilon, E) d\varepsilon. \quad (8)$$

Solving this equation with respect to $g(\eta)$ and substituting the explicit form of the function $G(E)$ [9], we arrive at the following result:

$$g(\eta) = \sqrt{2}\frac{\sqrt{\sqrt{1+\eta^2} - 1}}{\eta}. \quad (9)$$

Now, we calculate the broadening coefficient η in the z direction by correlating this coefficient with small variations of the width of the quantum wire produced by atomic thermal vibrations of the crystal lattice. In this case, the following relation holds:

$$\eta = \eta_\nu = \frac{\Delta E_\nu}{E_\nu} = 1 - \frac{b^2}{(b+\Delta b)^2} \approx \frac{2\Delta b}{b}. \quad (10)$$

For the quantum system, this relation determines the broadening of the energy level E_ν due to spatial fluctuations Δb related to time fluctuations of the width of the quantum wire. By analogy with Eq. (10), the resulting broadening coefficient for the quantum wire in the presence of two spatial deviations Δa and Δb can be written as

$$\eta = \eta_{\mu\nu} = \frac{\Delta E_\mu + \Delta E_\nu}{E_{\mu\nu}} \approx \frac{2\Delta a}{a}\frac{E_\mu}{E_{\mu\nu}} + \frac{2\Delta b}{b}\frac{E_\nu}{E_{\mu\nu}}. \quad (11)$$

Next, we consider the magnitude of these spatial fluctuations. Obviously, they are determined by the relative displacements of atomic planes due to thermal atomic vibrations of the crystal lattice [10]. Hence, the root-mean-square deviation of the interatomic distance corresponds to time-dependent spatial displacements and the following equalities are valid:

$$\Delta a = \Delta b = \sigma, \quad (12)$$

where σ is the root-mean-square deviation of the interatomic distance with respect to the equilibrium value for the system with one degree of freedom.

According to [10, 11], we can write down the following expressions:

$$\sigma = \sqrt{\frac{E_0}{M_1\omega^2}} + \sqrt{\frac{E_0}{M_2\omega^2}}, \quad (13)$$

$$E_0 = \frac{\hbar\omega}{2}\left(1 + \exp\left(-\frac{\hbar\omega}{k_B T}\right)\right)\left(1 - \exp\left(-\frac{\hbar\omega}{k_B T}\right)\right)^{-1}, \quad (14)$$

where E_0 is the average atomic vibrational energy for the case of one degree of freedom, M_1 and M_2 are the atomic masses for the different types of particles in a crystal lattice with a basis (for a primitive lattice, we have $M_1 = M_2$), ω is the optical phonon angular frequency, and T is the lattice temperature. Combining Eqs. (13) and (14), we obtain

$$\sigma = \left(\frac{\hbar}{M\omega}\right)^{1/2}\left(1 + \exp\left(-\frac{\hbar\omega}{k_B T}\right)\right)^{1/2} \times\left(1 - \exp\left(-\frac{\hbar\omega}{k_B T}\right)\right)^{-1/2}, \quad (15)$$

$$M = \frac{2M_1 M_2}{(\sqrt{M_1} + \sqrt{M_2})^2}. \quad (16)$$

Now, we take into account additional broadening of the energy levels due to the presence of surface roughness. In particular, following paper [5], we can easily derive an expression similar to Eq. (11). However, we note that the authors of [5] assumed that the characteristic roughness scale is appreciably greater than the electron wavelength, whereas we are interested in the region near the energy levels, where this assumption is not valid. Moreover, roughness scales of the order of interatomic distance are of much greater practical interest, in particular, for short quantum wires. We perform our calculation of broadening for precisely this case.

We assume that the roughness height is distributed according to the normal law [12]. Next, we take into account that, e.g., according to [11], the mean particle lifetime τ_ν on the energy level E_ν is related to the level half-width by

$$\Delta E_\nu = \frac{\hbar}{2\tau_\nu}. \tag{17}$$

Using Eqs. (10) and (17), it is easy to calculate the deterministic phase shift of an electronic wave for the time τ_ν with respect to the unperturbed state corresponding to the absence of surface roughness; this shift is equal to l/2 rad. If the electron wavelength is significantly greater than the characteristic roughness scale, then it is necessary to pass from the deterministic phase shift to a random one with normal distribution. In this case, for the mean lifetime of a particle on an energy level, the root-mean-square deviation of the phase of an electronic wave determined by the surface roughness is $\pi/2$ rad.

Therefore, we can calculate the energy level broadening produced by the surface roughness from the phase shifts for electronic waves. Using this argument, we arrive at the following result:

$$\eta_\nu = \frac{1}{\nu\pi}\left(\frac{b}{2\nu\delta_z}\right)^{-2}, \tag{18}$$

where δ_z is the root-mean-square deviation of the rough surface from the plane perpendicular to the z axis. Moreover, since the electronic states corresponding to the phase shift $\pm\nu\pi$ rad are equivalent, it can be shown that Eq. (18) must be replaced by a more accurate expression,

$$\eta_\nu = \frac{1}{\nu\pi}\left(\left(\frac{b}{2\nu\delta_z}\right)^2 + 3\exp\left(-\frac{2}{5}\left(\frac{b}{2\nu\delta_z}\right)^2\right)\right)^{-1}. \tag{19}$$

Using Eqs. (10)–(12) and (19), the total broadening coefficient can be found to be

$$\begin{aligned}\eta_{\mu\nu} = &\left[\frac{2\sigma}{a} + \frac{1}{\mu\pi}\left(\left(\frac{a}{2\mu\delta_y}\right)^2\right.\right.\\ &\left.\left. + 3\exp\left(-\frac{2}{5}\left(\frac{a}{2\mu\delta_y}\right)^2\right)\right)^{-1}\right]\frac{E_\mu}{E_{\mu\nu}}\\ &+\left[\frac{2\sigma}{b} + \frac{1}{\nu\pi}\left(\left(\frac{b}{2\nu\delta_z}\right)^2\right.\right.\\ &\left.\left. + 3\exp\left(-\frac{2}{5}\left(\frac{b}{2\nu\delta_z}\right)^2\right)\right)^{-1}\right]\frac{E_\nu}{E_{\mu\nu}},\end{aligned} \tag{20}$$

where δ_y is the root-mean-square deviation of the rough surface from the plane perpendicular to the y axis. Simplifying expression (7) and using Eq. (20), we obtain

$$N(E) = \frac{\sqrt{2}}{\pi}\frac{\sqrt{m_d}}{\hbar ab}\sum_\mu\sum_\nu F_{\mu\nu}(E), \tag{21}$$

$$\begin{aligned}F_{\mu\nu}(E) = &\frac{E}{\sqrt{(E_{\mu\nu}-E)^2 + (\eta_{\mu\nu}E)^2}}\\ &\times\frac{\sqrt{\sqrt{1+\eta_{\mu\nu}^2}-1}}{\sqrt{(E_{\mu\nu}-E) + \sqrt{(E_{\mu\nu}-E)^2 + (\eta_{\mu\nu}E)^2}}}.\end{aligned} \tag{22}$$

Equations (21) and (22) describe the density of states for a quantum wire in the presence of energy level broadening due to the perturbation of the quantum system by thermal lattice vibrations and by roughness of the confining surface.

3. SCATTERING INTENSITY

Let us write the intensity of intersubband electron scattering by polar optical phonons in a polar-semiconductor quantum wire using the results from paper [5]. In the formulas from that paper, we replace the density of final states calculated without regard for energy level broadening by the density of final states in the presence of broadening. In addition, we take into account the conservation of the total electron momentum and not only the conservation of its longitudinal component as in [5]; this is done in order for the scattering intensity in a quantum wire to reduce to that in the bulk semiconductor as a and b tend to infinity. In this case, the intersubband scattering intensity of electrons in a quantum state with energy $E_{\mu\nu}$ with phonon emission/absorption (denoted by the superscripts "e/a," respectively) is given by

$$\begin{aligned}W^{\{e/a\}}(E_x) = &\alpha^{\{e/a\}}\sum_{\mu'}\sum_{\nu'} I(q_+^{\{e/a\}})F_{\mu'\nu'}\\ &\times(E_x + E_{\mu\nu} \mp \hbar\omega)U(E_x + E_{\mu\nu} - E_{\mu'\nu'} \mp \hbar\omega)\\ &+\alpha^{\{e/a\}}\sum_{\mu'}\sum_{\nu'} I(q_-^{\{e/a\}})F_{\mu'\nu'}\\ &\times(E_x + E_{\mu\nu} \mp \hbar\omega)U(E_x + E_{\mu\nu} - E_{\mu'\nu'} \mp \hbar\omega),\end{aligned} \tag{23}$$

where

$$\begin{aligned}\alpha^{\{e/a\}} = &\left(\frac{2}{\pi}\right)^4\left(\frac{1}{\varepsilon_\infty} - \frac{1}{\varepsilon_s}\right)\\ &\times\left(N_{ph} + \frac{1}{2} \pm \frac{1}{2}\right)\frac{e^2\omega\sqrt{2m_d}}{\hbar ab},\end{aligned} \tag{24}$$

$$I(q_\pm) = \sum_{i=1}^{\infty}\sum_{j=1}^{\infty}\frac{P_{ij}^2}{q_\pm^2 + \left(\frac{i\pi}{a}\right)^2 + \left(\frac{j\pi}{b}\right)^2}, \tag{25}$$

$$q_+^{\{e/a\}} = k_x + \frac{\sqrt{2m_d(E_x + E_{\mu\nu} - E_{\mu'\nu'} \mp \hbar\omega)}}{\hbar}, \tag{26}$$

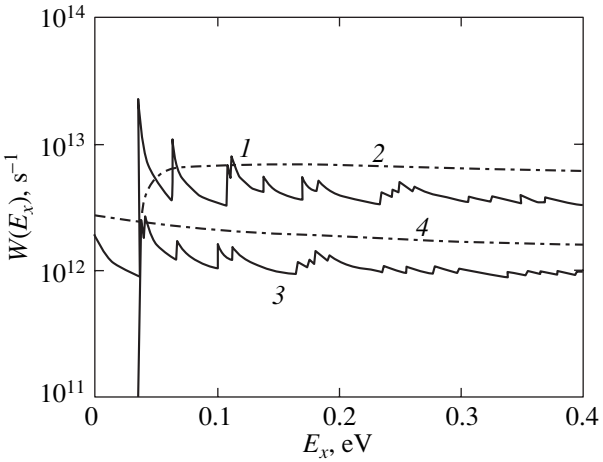

Dependence of the intensity of intersubband electron scattering W on the electron kinetic energy E_x for (*1*, *2*) emission and (*3*, *4*) absorption of polar optical phonons (*1*, *3*) in a quantum wire and (*2*, *4*) in a bulk semiconductor. T = 300 K, $\mu = \nu = 1$, a = 15 nm, b = 25 nm, δ_y = 0.53 nm, and δ_z = 0.88 nm.

$$q_{-}^{\{e/a\}} = k_x - \frac{\sqrt{2m_d(E_x + E_{\mu\nu} - E_{\mu'\nu'} \mp \hbar\omega)}}{\hbar}, \quad (27)$$

$$P_{ij} = \int_0^\pi \sin(\mu y)\sin(\mu' y)\sin(iy)dy \times \int_0^\pi \sin(\nu z)\sin(\nu' z)\sin(jz)dz, \quad (28)$$

E_x is the electron kinetic energy, ε_∞ and ε_s are the optical and static dielectric permittivities of the polar semiconductor, N_{ph} is the number of phonons, and e is the electron charge.

4. DISCUSSION OF THE RESULTS

Comparison of our results with the results from [5] shows that, because of the conservation of transverse components of the electron momentum in scattering, the particle scattering probability reduces by a factor of four. This is due to the fact that a transverse component of a de Broglie electron wave can interact only with the codirectional component of the corresponding transverse phonon mode; otherwise, the momentum is not conserved. A similar effect of a decrease in electron scattering probability at resonant levels in a one-dimensional quantum well has been discussed already in [13].

As an example, in the figure, we plot the dependence of the intensity $W(E_x)$ of intersubband scattering of electrons in the ground state by polar optical phonons in a gallium arsenide quantum wire; this dependence was calculated using Eq. (23) at T = 300 K for the same parameters of the quantum system as in [5]. For comparison, in the same figure, we plot the dependence of the intensity $W(E_x)$ of intersubband scattering of electrons in the ground state by polar optical phonons in bulk gallium arsenide (the quantum wire with a cross section of $10^{-3} \times 10^{-3}$ m). We note that, in the limiting case of a bulk semiconductor, our results completely coincide with the results of calculations in [14].

5. CONCLUSIONS

Thus, in this paper, we have calculated the intensity of electron intersubband scattering by polar optical phonons in semiconductor quantum wires with energy levels of finite width. It has been shown that the dependence of the scattering intensity on carrier kinetic energy has no singularities. In the limiting case where the transverse dimensions of the quantum wire tend to infinity, this dependence reduces to that for a bulk semiconductor [14], whereas asimilar calculation using the results from [5] overestimates the scattering intensity by a factor of four.

REFERENCES

1. A. S. Tager, Élektron. Tekh., Ser. 1: Élektron. SVCh **9**, 21 (1987).
2. L. Worschech, S. Reitzenstein, and A. Forchel, Appl. Phys. Lett. **77** (22), 3662 (2000).
3. V. M. Borzdov, F. F. Komarov, A. V. Homich, and O. G. Zhevnyak, Phys. Low-Dimens. Semicond. Struct., No. 10, 63 (1997).
4. D. Calecki, J. Phys. C: Solid State Phys. **19**, 4315 (1986).
5. R. Mickevicius, V. V. Mitin, K. W. Kim, *et al.*, J. Phys.: Condens. Matter **4**, 4959 (1992).
6. V. M. Borzdov, V. O. Galenchik, F. F. Komarov, *et al.*, Phys. Low-Dimens. Semicond. Struct., No. 11/12, 21 (2002).
7. P. Roblin and W.-R. Liou, Phys. Rev. B **47** (4), 2146 (1993).
8. N. Zou, Q. Chen, and M. Willander, J. Appl. Phys. **75** (3), 1829 (1994).
9. V. L. Bonch-Bruevich and S. G. Kalashnikov, *Physics of Semiconductors*, 2nd ed. (Nauka, Moscow, 1990).
10. P. V. Pavlov and A. F. Khokhlov, *Physics of Solids* (Vysshaya Shkola, Moscow, 2000).
11. A. S. Davydov, *Quantum Mechanics*, 2nd ed. (Nauka, Moscow, 1973; Pergamon, Oxford, 1976).
12. E. X. Ping and H. X. Jiang, Phys. Rev. B **40** (17), 11792 (1989).
13. V. M. Borzdov and D. V. Pozdnyakov, Vestn. Belloruss. Gos. Univ., Ser. 1 **1**, 26 (2002).
14. V. M. Ivashchenko and V. V. Mitin, *Simulation of Kinetic Phenomena in Semiconductors. The Monte Carlo Method* (Naukova Dumka, Kiev, 1990).

Translated by I. Zvyagin

Physics of the Solid State, Vol. 45, No. 12, 2003, pp. 2352–2356. Translated from Fizika Tverdogo Tela, Vol. 45, No. 12, 2003, pp. 2242–2246.

LOW-DIMENSIONAL SYSTEMS AND SURFACE PHYSICS

Size Effect in Nuclear Spin–Lattice Relaxation and Atomic Mobility for Molten Gallium Particles

C. Tien*, E. V. Charnaya, P. Sedykh**, and Yu. A. Kumzerov*****

**Department of Physics, National Cheng Kung University, Tainan, 701 Taiwan*

***Fock Institute of Physics, St. Petersburg State University, ul. Pervogo Maya 100, Petrodvorets, St. Petersburg, 198504 Russia*

e-mail: charnaya@paloma.spbu.ru

****Ioffe Physicotechnical Institute, Russian Academy of Sciences, Politekhnicheskaya ul. 26, St. Petersburg, 194021 Russia*

Received April 30, 2003

Abstract—The spin–lattice relaxation rate of gallium isotopes in a melt was shown by NMR to increase considerably with a decrease in gallium particle size. The dominant relaxation mechanism of gallium embedded in an synthetic opal matrix changes from magnetic dipole to electrical quadrupole. The increase in the correlation time of atomic motion in gallium particles with a decrease in their size was estimated. For gallium in opal, the correlation time was found to increase by more than an order of magnitude. It was shown that a variation in atomic mobility becomes noticeable already in gallium particles about 5 μm in size. © *2003 MAIK "Nauka/Interperiodica".*

1. INTRODUCTION

The influence of size effects on various physical properties of materials, including atomic mobility, relaxation phenomena, and liquid fluidity, in confining systems has been recently attracting considerable interest [1]. It has been shown that rotational and translational diffusion, nucleation kinetics, and glass formation processes in liquids filling porous matrices can undergo considerable changes [2–5]. These changes depend primarily on the size of the pores determining the dimensions of the embedded nanoparticles, as well as on the wettability of the inner surface of porous matrices, on the pore geometry, the length of molecular chains in polymers, etc. NMR is known to yield valuable information on dynamics in condensed media and has found wide application in studies of the mobility of liquids inserted into nanosized pores [2, 3, 6, 7]. The technique employed in those studies primarily involved measurement of nuclear relaxation under application of a magnetic field gradient. Nevertheless, studies of size effects in the mobility of metal melts were started only recently, despite the fact that, in a number of low-melting metals, such as gallium, mercury, and indium, confining geometry has currently been found to noticeably affect many other physical properties, in particular, the crystal structure, superconducting characteristics, and the melting–crystallization phase transitions (see [8–11] and references therein). A decrease in atomic mobility, first observed to occur in liquid gallium incorporated in nanosized pores [12], manifested itself in an increase in the nuclear spin relaxation rate by a few times due to enhancement of the role of the quadrupole contribution. However, these studies [12] are currently the only ones in this area. Furthermore, they dealt solely with nanosized gallium particles, which did not permit one to reveal the characteristic dimensions at which size effects in atomic mobility become noticeable in a gallium melt. On the other hand, measurements of quasi-elastic neutron scattering [13] suggest a decrease in the atomic diffusion coefficient in thin films of liquid gallium on aluminum particles to a level less than 10^{-5} cm^2/s (compared with 3×10^{-5} cm^2/s for a bulk melt), which made its accurate determination impossible. These data permit the suggestion that size effects start to noticeably influence the atomic mobility in liquid gallium for particles with dimensions considerably in excess of 100 nm.

The goal of the present study was to investigate the correlation times of atomic motion in liquid gallium for single particles about 50 and 5 μm in size and particles embedded in pores of synthetic opal, using NMR.

2. EXPERIMENT

The studies were performed on three gallium samples differing in particle dimensions. Sample 1 consisted of small particles about 50 μm in size obtained by grinding solid gallium and wrapped in cotton wool. Sample 2 was gallium in drops on cotton wool filaments about 5 μm in size. In this case, gallium particles could be considered isolated. Sample 3 was a synthetic opal consisting of closely packed silica spheres 250 nm in diameter. Purely geometric considerations supported by electron microscopy suggest the existence of pores with characteristic dimensions on the order of 100 and

50 nm in such opals. Gallium was pressure-injected in the liquid state. The pore filling factor by gallium was approximately 20% of the total pore volume.

The measurements were conducted on an Avance-400 NMR pulsed spectrometer (Bruker). Gallium has two isotopes, ^{69}Ga and ^{71}Ga, with slightly different abundances. Both isotopes have a spin of 3/2 and different values of the gyromagnetic ratio γ_n and quadrupole moment Q (Q = 0.168 and 0.106 barn and $\gamma_n = 6.44 \times 10^{-7}$ and 8.18×10^{-7} rad T^{-1} s^{-1} for ^{69}Ga and ^{71}Ga, respectively). This offers the possibility of separating the magnetic and electrical quadrupole contributions to nuclear spin relaxation. The resonance frequency was 122 MHz for ^{71}Ga and 96 MHz for ^{69}Ga.

The melting point of bulk gallium is 303 K, but gallium can be readily supercooled below room temperature; for this reason, we carried out all measurements on liquid gallium at room temperature (294 K), as in [12]. Note also that the melting temperature of small particles in porous matrices is considerably lower than that in bulk gallium [10, 11].

The spin–lattice relaxation rate of both isotopes in the samples was measured using an inversion recovery procedure. We also measured the NMR line by using the precession signal following a 90° pulse.

3. RESULTS AND DISCUSSION

Figure 1 displays the restoration of nuclear spin magnetization with time following a 180° inverting pulse measured on both gallium isotopes in the samples under study. The NMR line shape is shown in Fig. 2. Table 1 lists the calculated NMR linewidths. As seen from Fig. 1, the recovery of NMR signals in gallium particles 50 and 5 μm in size (samples 1, 2) is faster for the ^{71}Ga isotope, which has a larger gyromagnetic ratio and a smaller quadrupole moment, whereas for gallium in opal the NMR signal for the ^{69}Ga isotope, which has a larger quadrupole moment, takes less time to be restored. This shows that, as the gallium particle size decreases, the dominant spin–lattice spin relaxation mechanism switches from magnetic dipole to electrical quadrupole, in full agreement with the data quoted in [12].

As is well known, nuclear spin relaxation in bulk liquid gallium proceeds as competition between two mechanisms, namely, the magnetic mechanism involving the interaction of nuclear magnetic moments with conduction electrons and the quadrupole mechanism based on the coupling of nuclear quadrupole moments with dynamic gradients of electric fields generated during thermal motion of atoms in the melt [14, 15]. As a result of the high atomic mobility in bulk liquid gallium, the quadrupole contribution to the relaxation is insignificant, thus making the interaction with conduction electrons dominant. It was shown in [12] that, because of the atomic mobility in molten gallium nanoparticles embedded in porous matrices being consider-

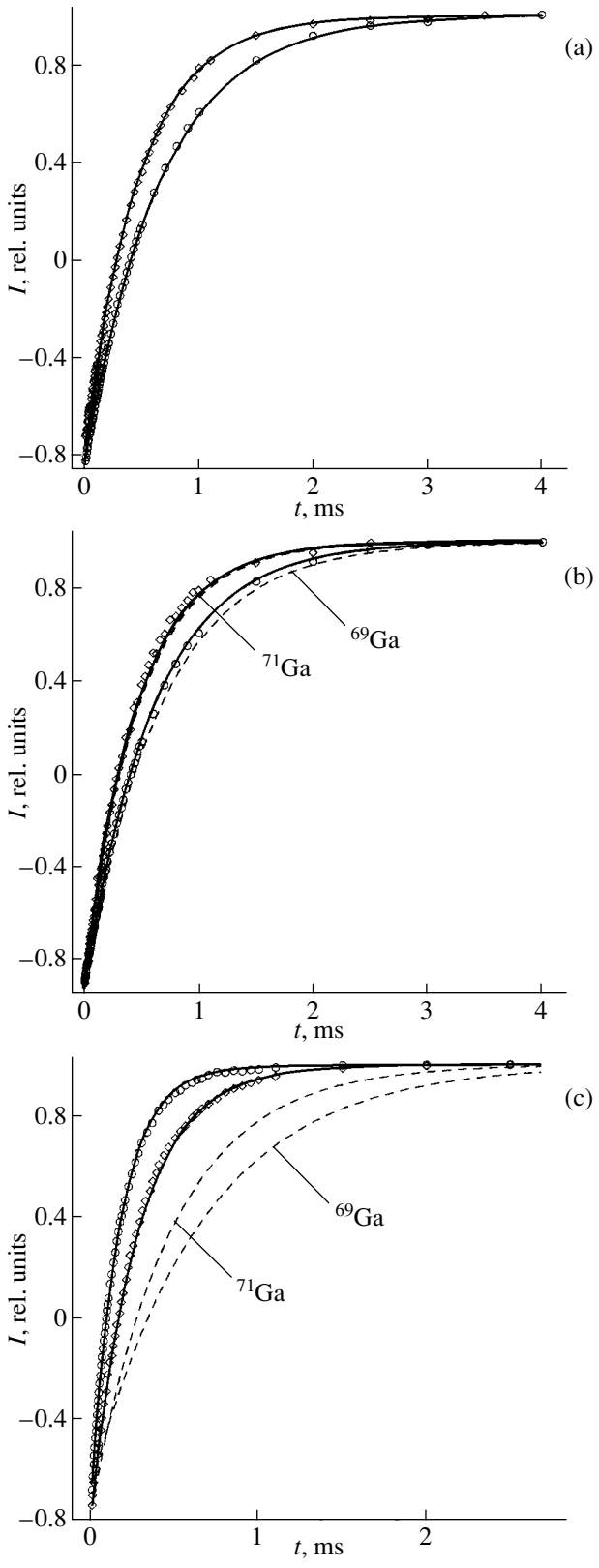

Fig. 1. Integrated intensity I of the NMR signal of the isotopes ^{71}Ga (diamonds) and ^{69}Ga (circles) after the 180° inverting pulse plotted vs. time t for samples (a) 1, (b) 2, and (c) 3. Solid lines are plots of Eq. (2) with τ_c given in Table 2, and dashed lines are those calculated with the correlation times for sample 1.

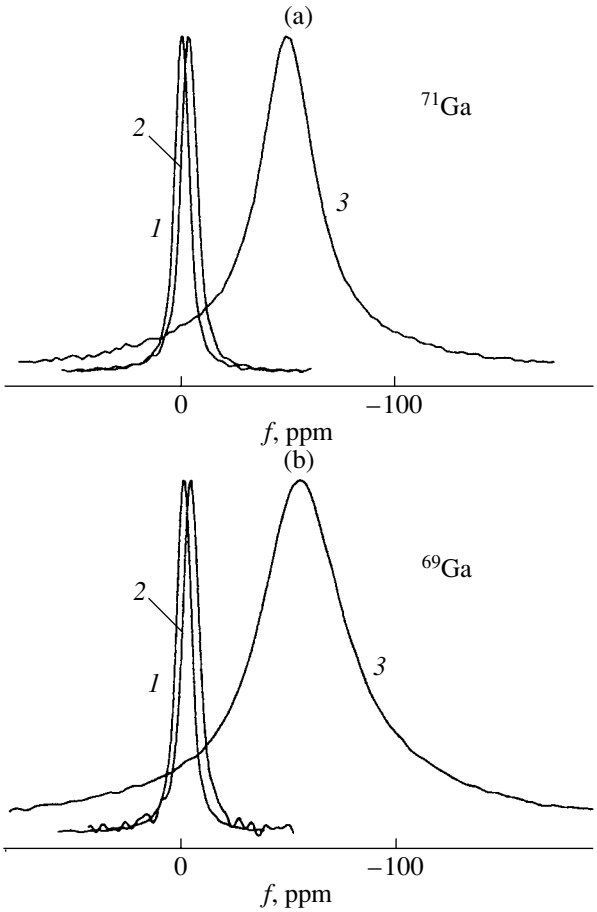

Fig. 2. NMR line shape for the isotopes (a) ^{71}Ga and (b) ^{69}Ga in the samples studied. Sample numbers are given by the figures, on the curves.

ably lower, the spectral density of the electric-field gradient correlation function at the Larmor frequency increases, which brings about a substantial acceleration of the quadrupole relaxation. It can be suggested that fast spin–lattice relaxation in gallium incorporated in opal pores could also be assigned to an increase in the quadrupole relaxation rate caused by the slowing down of atomic diffusion. This suggestion is corroborated by the substantial broadening of the resonance lines for the opal-incorporated gallium, which is larger for ^{69}Ga; this shows a noticeable acceleration of transverse spin relaxation associated with the increase in the quadrupole contribution. The results presented in Figs. 1 and 2 and Table 1 also clearly reveal, however, a certain acceleration of longitudinal relaxation and broadening of the resonance line in sample 2 as compared with sample 1, which implies a change in the atomic diffusion rate with a decrease in gallium particle size down to 5 μm.

Table 1. NMR FWHM δ for gallium isotopes in the samples studied

NMR FWHM	Sample 1	Sample 2	Sample 3
δ(*ppm*), ^{71}Ga	8.2 ± 0.1	9.2 ± 0.2	32.0 ± 0.5
δ(*ppm*), ^{69}Ga	8.2 ± 0.1	9.0 ± 0.2	50.0 ± 0.5

A quantitative assessment of the variation of the spin relaxation rate in liquid gallium with particle size can be approached by analyzing the expression for the recovery of the nuclear magnetization signal in the case of quadrupole spin–lattice relaxation of nuclei with spin 3/2 [16]:

$$\frac{M(t)}{M_0} = 1 - b\left[\frac{4}{5}\exp\left(-2\left(\frac{eQ}{\hbar}\right)^2 J_{-22}(2\omega_0)t\right) + \frac{1}{5}\exp\left(2\left(\frac{eQ}{\hbar}\right)^2 J_{-11}(\omega_0)t\right)\right]. \quad (1)$$

Here, $M(t)$ and M_0 are the time-dependent (t) and equilibrium magnetizations, respectively; $1 - b$ is the relative magnetization immediately following the inverting pulse; e is the electron charge; ω_0 is the Larmor frequency; and $J_{-ii}(\omega)$ are the spectral densities of the correlation function of electric field gradients at the site of a nucleus. In the case of fast atomic motion, where the approximation of strong resonance-line narrowing is valid, the exponents in Eq. (1) reduce to $-C\tau_c t$ [17], where C is a constant proportional to Q^2 and τ_c is the correlation time. The magnetization restoration process is described by a single exponent, and $C\tau_c$ is equal to the inverse quadrupole spin–lattice relaxation time T_{1Q}^{-1}. According to the atomic diffusion rate in bulk liquid metals, the correlation time should be of the order of 10^{-12} s [17].

In general (in particular, for viscous liquids), the relaxation, in accordance with Eq. (1), does not follow a simple exponential pattern. To simplify the consideration of the general case, we assume that the correlation function in Eq. (1) can be presented in the form $\exp(-t/\tau_c)$. Then, the arguments of the exponentials in Eq. (1) reduce to $-C\tau_c t/(1 + k^2\omega_0^2\tau_c^2)$, where $k = 1, 2$. Now, the total gallium relaxation process, including magnetic relaxation through interaction with the conduction electrons characterized by the time T_{1m}, can be described by the relation

$$\frac{M(t)}{M_0} = 1 - b\left[\frac{4}{5}\exp\left(-\frac{C\tau_c t}{1 + 4\omega_0^2\tau_c^2}\right) + \frac{1}{5}\exp\left(-\frac{C\tau_c t}{1 + \omega_0^2\tau_c^2}\right)\right]\exp\left(-\frac{t}{T_{1m}}\right). \quad (2)$$

As seen from Eq. (2), the quadrupole relaxation rate can be affected by variations in the C factor and in the correlation time. The correlations of electric-field gradient fluctuations at zero frequency, which determine the quantity C, depend on the melt structure [17]. Experi-

mental studies of the structure of various liquids embedded in porous matrices have shown that it does not vary at least down to pore sizes of about 4 nm [1]. This is in agreement with x-ray diffraction patterns of molten gallium in nanoporous matrices [11]. It thus appears unlikely that the factor C could increase to the extent that it could account for the switching of the character of longitudinal relaxation and resonance-line broadening from magnetic to quadrupole for a gallium melt in opal. Therefore, following [12], one can suggest that the variations in the quadrupole contribution to the spin–lattice relaxation rate are associated primarily with variations in the atomic-motion correlation time τ_c.

On the other hand, the magnetic relaxation time T_{1m} due to interaction with the conduction electrons is connected with the Knight shift of a resonance line through the Korringa relation $T_{1m}TK_s^2 = \text{const}/(\gamma_n K)$, where T is the temperature, K_s is the Knight shift, and K is a factor taking into account correlation effects and exchange in the conduction electron system. As follows from Fig. 2, the Knight shift differs little in the samples studied (for opal, by about 1%, and for 5-μm particles, by about 0.1% relative to the NMR signal in sample 1); therefore, it appears reasonable to suggest that the magnetic relaxation time likewise depends only weakly on the dimensions of gallium nanoparticles and, as a result, this dependence may be neglected.

Assuming that the longitudinal relaxation is described by Eq. (2) and that only the correlation time τ_c depends on the dimensions of the gallium particles, we calculated the nuclear magnetization restoration curves for both gallium isotopes in the three samples studied using the magnetic relaxation time and the factor C for the ^{71}Ga isotope (T_{1m}^{71}, C_{71}) and the correlation times τ_{c1}, τ_{c2}, and τ_{c3} as fitting parameters. The magnetic relaxation time and the magnitude of C for the ^{69}Ga isotope were derived from the relations between the gyromagnetic ratios and quadrupole moments: $T_{1m}^{69} = T_{1m}^{71}(\gamma_n^{71})^2/(\gamma_n^{69})^2$ and $C_{69} = C_{71}Q_{69}^2/Q_{71}^2$. In view of the large dimensions of the gallium particles in sample 1, it was also assumed that the time τ_{c1} should be of the order of 10^{-12} s, as for bulk gallium. The results of the calculations are presented in Fig. 1 for the set of parameters listed in Table 2. As is evident from Table 2, the atomic-motion correlation times in the gallium melt for particles 5 μm in size and in the opal vary considerably as compared to that for particles measuring 50 μm. For the opal, the correlation time increases by more than an order of magnitude, which corresponds to a noticeable decrease in the atomic mobility. For particles about 5 μm in size, the correlation time increases by only a factor 1.5; however, even this increase is evidence of a noticeable change in the diffusion rate. Thus, size effects in the atomic mobility in a gallium melt become manifest already for particle sizes of about 5 μm.

Table 2. Atomic-motion correlation times τ_c, magnetic relaxation time T_{1m}, and factor C for the two gallium isotopes in the samples studied

Sample number	τ_c, 10^{-12} s	T_{1m}^{71}, 10^{-6} s	T_{1m}^{69}, 10^{-6} s	C_{71}, 10^{12} s^{-2}	C_{69}, 10^{12} s^{-2}
1	9.2				
2	14	505	815	10.55	30.50
3	150				

It should be pointed out that the values of T_{1m}, as well as of the product $C\tau_{c1}$, which is the inverse quadrupole relaxation time in the limit of a strong narrowing of the NMR line, is derived for both isotopes unambiguously from the restoration curves. The values thus obtained agree, on the whole, with the data presented in [14, 15] for bulk gallium. The values of C and of the correlation times are, however, somewhat ambiguous, which should possibly be assigned to our approximation concerning the shape of the correlation function. Figure 1 and Table 2 present the values which best fit the experimental values. It should be stressed that the ambiguity in determining of the correlation times can affect the quantities themselves but not the relative magnitude of the correlation times obtained for different samples and, hence, cannot change our main conclusion that atomic mobility decreases with decreasing size of molten gallium particles.

4. CONCLUSIONS

To sum up, we have measured the longitudinal spin relaxation rate and the NMR line shape for two gallium isotopes in molten gallium particles of various sizes. The correlation time of atomic motion (which characterizes the atomic mobility) for gallium incorporated in pores of synthetic opal is shown to increase by more than an order of magnitude. The dominant spin relaxation switches from magnetic, based on the interaction of nuclear dipole moments with conduction electrons, to quadrupole relaxation, which involves dynamic electric field gradients induced by thermal motion at the sites of nuclei. The magnetic mechanism remains dominant for gallium particles about 5 μm in size, but the quadrupole relaxation increases through an increase in the correlation time by a factor of about 1.5. This means that the decrease in atomic mobility in molten gallium particles becomes noticeable as their dimensions decrease to 5 μm.

ACKNOWLEDGMENTS

This study was supported by the program "Integration" (project no. A0147) and the State Committee on Science of Taiwan (grant no. 91-2112-M-006-017).

REFERENCES

1. *Dynamics in Small Confining Systems*, Ed. by J. M. Drake, G. S. Grest, J. Klafter, and R. Kopelman (MRS, Warrendale, Pennsylvania, 1999).
2. S. Granic, Science **253**, 1374 (1991).
3. S. Stapf, R. Kimmich, and R.-O. Seitter, Phys. Rev. Lett. **75**, 2855 (1995).
4. S. H. Anastasiadis, K. Karatasos, G. Vlachos, *et al.*, Phys. Rev. Lett. **84**, 915 (2000).
5. H. K. Christenson, J. Phys.: Condens. Matter **13**, R95 (2001).
6. J.-P. Korb, L. Malier, F. Cros, *et al.*, Phys. Rev. Lett. **77**, 2312 (1996).
7. M. Weber, A. Klemm, and R. Kimmich, Phys. Rev. Lett. **86**, 4302 (2001).
8. K. M. Unruh, T. E. Huber, and C. A. Huber, Phys. Rev. B **48**, 9021 (1993).
9. C. Tien, C. S. Wur, K. J. Lin, *et al.*, Phys. Rev. B **61**, 14833 (2000).
10. B. F. Borisov, E. V. Charnaya, T. Loeser, *et al.*, J. Phys.: Condens. Matter **11**, 10259 (1999).
11. E. V. Charnaya, C. Tien, K. J. Lin, and Yu. A. Kumzerov, Phys. Rev. B **58**, 11089 (1998).
12. E. V. Charnaya, T. Loeser, D. Michel, *et al.*, Phys. Rev. Lett. **88**, 097602 (2002).
13. H. Konrad, C. Karmonik, J. Weissmüller, *et al.*, Physica B (Amsterdam) **234–236**, 173 (1997).
14. A. L. Kerlin and W. G. Clark, Phys. Rev. B **12**, 3533 (1975).
15. J. M. Titman, Phys. Rep. **33**, 1 (1977).
16. P. S. Hubbard, J. Chem. Phys. **53**, 985 (1970).
17. J. Bosse, D. Quitmann, and C. Wetzel, Phys. Rev. A **28**, 2459 (1983).

Translated by G. Skrebtsov